CHEMIA

STUDIA
UNIVERSITATIS BABEŞ-BOLYAI

CHEMIA

4/2014

S T U D I A

UNIVERSITATIS BABEŞ–BOLYAI

CHEMIA

4

CUPRINS – CONTENT – SOMMAIRE – INHALT

UPLC-QTOF-ESI(+) MS AND DIRECT MS INJECTION USED TO FINGERPRINT RESTING AND STIMULATED SALIVA PROFILES: PRELIMINARY RESULTS

IULIA CLARA BADEA[a], MARIA CRISAN[a], RALUCA POP[a, b], ALEXANDRU FLORIN BADEA[a], CARMEN SOCACIU[b, *]

ABSTRACT. A rapid and reliable profiling of resting and stimulated saliva by two advanced techniques, LC-QTOF-ESI (+) MS and direct injection mass spectrometry (DIMS) was performed. Male and female healthy volunteers (n=12) were randomly selected, their resting, and stimulated saliva being collected, before and after chewing stimulation with parafin. Base peak chromatograms of saliva methanolic extracts (BPC) were recorded, the main peaks were identifed and the MS data (m/z values) were used to identify specific biomarkers. The biostatistic analysis made by Principal Component Analysis was applied to discriminate between samples' profile. The comparative UPLC-QTOF-ESI(+)MS fingerprints, before and after storage at -20ºC showed similar data with DIMS analysis, but the later one identified a larger range of molecules, without a preliminary separation by UPLC. Around 10 major biomarkers were identified, mainly phosspholipid derivatives, showing quantitative differences among the resting and stimulated saliva. Such preliminary results will be used for early diagnosis and monitoring therapy's effects in dental pathology.

Keywords: resting and stimulated saliva, metabolomics, UPLC-QTOF-MS, direct MS injection

INTRODUCTION

Saliva is a complex mixture, of crevicular or gingival fluids, derived from the gingival sulcus, desquamated oral epithelial cells and microorganisms, i.e. viruses, fungi, bacteria and endotoxins [1-3] as well a large number of inorganic electrolytes and organic components [4]. Salivary glands produce

[a] *University of Medicine and Pharmacy "Iuliu Hatieganu", 12, Victor Babes Street, Cluj-Napoca, Romania.*
[b] *Research Centre on Applied Biotechnology in Diagnosis and Molecular Therapy, 12G Trifoiului Street, Cluj-Napoca, Romania.*
* *Corresponding author: carmen.socaciu@usamvcluj.ro*

90% of slight acidic (pH 6–7) secretions and 10% fluids from labial, buccal or palatal salivary glands [4-6]. Saliva components may represent a "mirror" of the body's health or pathological condition, by its qualitative or quantitative composition [7-8] reflecting the organs function in the body [9-10]. Saliva proteins bind up to 80% of carbohydrates (i.e., MUC5B mucins), mainly sialic acid, but also galactose, mannose, aminosugars, glycolipids (i.e., neutral and sulphated glyceroglucolipids), neutral lipids (i.e. free fatty acids, cholesteryl esters, triglycerides and cholesterol), as well phospholipids (i.e. phosphatidyl-ethanolamine, phosphatidylcholine), [11-12] as well amylase, mucin, lysozyme, IgA, lactoferrin, peroxidase, metalloproteases, glycoproteins, and lipoproteins [13]. The nonproteic components of saliva are uric acid, bilirubin, creatinine, glucose, cholesterol, hormones and fatty acids [14-17] representing good diagnosis biomarkers.

Recently, the salivary biomolecules were identified by omics' technologies, including genomics, transcriptomics, proteomics and metabolomics [18-21].

Saliva is an appropriate diagnostic fluid with interesting perspectives for personalized therapy [22-25]. The metabolic profiling of saliva in patients with primary Sjögren's syndrome was recently reported by Mikkonen et al. [26]. By metabonomic analysis, saliva proved to be an adequate biofluid for chronic periodontitis signature as well [27, 28].

Saliva can be collected without exogenous stimulation (resting saliva) or by stimulation, which is influenced by olfactory stimulus, exposure to light, diurnal and seasonal factors [29]. Beside these factors, important differences have been reported in analyte levels, relating to collection and sample processing. It is therefore important to use appropriate methods in order to standardize the collection of saliva, use of specific inhibitors or additives after collection and storage [29].

Recently, the salivary metabolome was established based on a protein precipitation and UHPLC–IM–MS technique, before and after exercise-induced physiological stress [30]. Recently, a metabolic fingerprinting in saliva of smokers and nonsmokers was validated by GC-TOF-MS technique [31] identifying 13 altered metabolites in smokers, such as tyramine, adenosine, and glucose-6-phosphate, linked to detrimental perturbations of smoking.

The aim of this study was to apply two rapid and reliable screening protocols, to find metabolic biomarkers in resting and stimulated saliva of healthy subjects. The UPLC-QTOF-ESI(+)MS technique was applied in parallel with a direct injection mass spectrometry (DIMS) to fingerprint the methanolic saliva extracts and their stability, after 1 year storage. The principal component analysis (PCA) was applied to evaluate qualitative and quantitative modifications of saliva biomarkers, considering comparatively the statistical buckets of resting *versus* stimulated saliva.

RESULTS AND DISCUSSION

The "omics" technology applied to saliva proved to reflect a complete set of small metabolites using liquid- or gas- chromatography coupled with mass spectrometry (LC-MS, GC-MS) [32] to be used in translational and clinical applications, including personalized dentistry and medicine [32-36].

Most attention was given to separation and identification protocols to find appropriate saliva biomarkers of diagnosis and disease monitoring [13] the low concentrations (picograms to nanograms) of different metabolites in saliva need sensitive equipments and protocols [37-39].

1. Comparative UPLC-QTOF-ESI(+)MS fingerprints based on Base Peak chromatograms, registered before and after storage

Fig. 1 shows comparatively the Base Peak Chromatograms (BPC) of a resting saliva extract compared with a stimulated saliva based on the UPLC-QTOF ESI(+)MS analysis. Around 32 minor and major peaks with high similarity

Fig. 1. The profiles of Base Peak Chromatograms (BPC) of a resting sample (up) compared with a stimulated sample (down), based on the UPLC-QTOF ESI(+) MS analysis
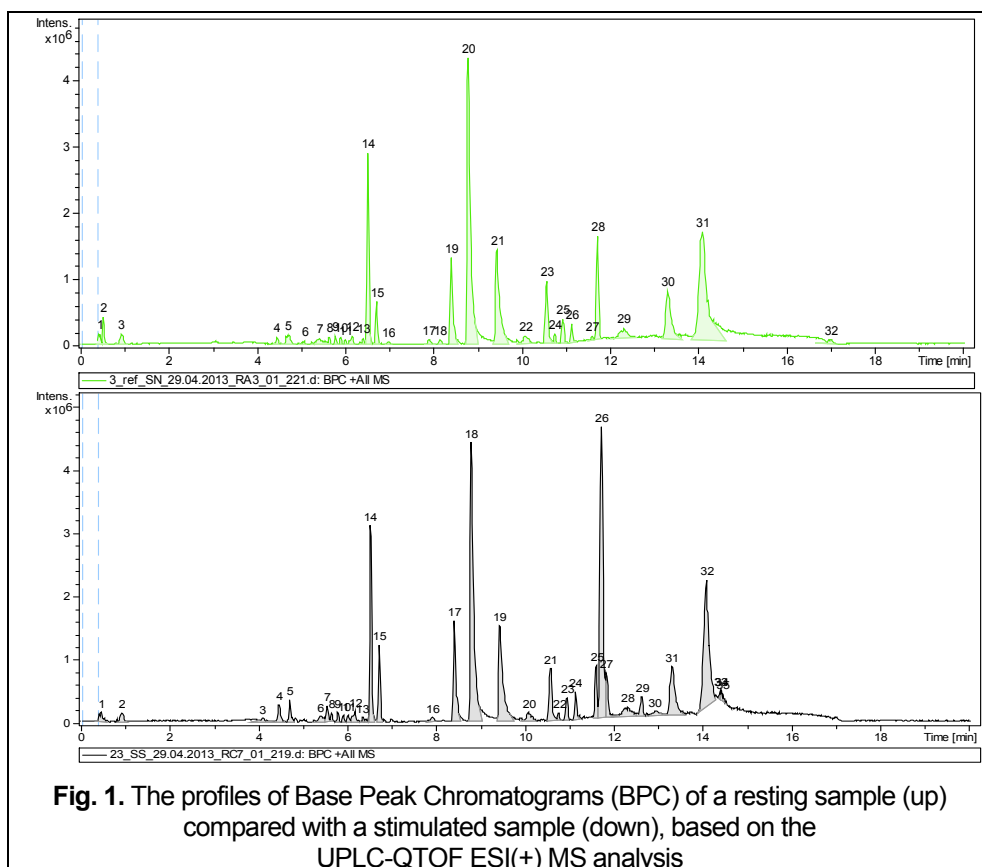
were identified, as follows: at t_R= 2-6.5 min includes minor peaks followed by 2 major peaks from 6.5-6.7 min (nr. 14 and 15). Between t_R= 8.4-9.4 3 major peaks (nr. 19, 20, 21) followed by many peaks between 10.6 to 13.0 min. (21, 26 for resting saliva and 23, 28 for stimulated saliva. Only 2 peaks (30, 31) were observed after 13.3 min. The identification of these peaks is presented in Table 1.

There were identified peaks corresponding to Phospholipids (LysoPC (18:2) (11), (LysoPE 16:0) (15), Oleoyl glycine (14), Oleamide (28 /NSS; 27/ SS), N-Lauroyl-glycine (21/ NSS; 19/ SS), Heptanoylcarnitine (19/NSS; 17/SS), peptides like asparaginyl-proline or prolyl-asparagine (/ 20/NSS;18/SS) and tyrosyl-arginine or argynil-tyrosine (31/NSS; 32/ SS), as well Hydroxyglutaric acid (23/NSS; 21/SS) and 12-ketodeoxycholic acid (30/NSS; 31/SS).

When the BPC from the same patient saliva (NSS *vs* SS) were compared, quantitative but not qualitative differences, were seen (data not shown). In SS samples there were noticed increased peak areas for 26 and 27 (Fig.1; table 1) corresponding to oleamide and monoacylglicerol C16:0, respectively.

Table 1. Tentative identification of peaks identified in resting (NSS) and simulated saliva (SS) by LC-QTOF-ESI(+) MS analysis, in the t_R range from 6 to 14.1 min. Minor peaks (mP) and bolded marks for main peaks are represented.

t_R (min.)	NSS		SS		Tentative identifications by Mass Spectrometry
	Peak nr.	m/z [M+1]	Peak nr.	m/z [M+1]	
6.00	**11**	**520.3555**	**11**	**520.3573**	**Lyso PC 18:2(9Z,12Z)**
6.40	mP	742.4768	mP	742.4768	PE(18:2(9Z,12Z)/18:1(9Z); PE (18:0/18:3(9Z,12Z,15Z)) PC(15:0/18:3(6Z,9Z,12Z))
6.50	14	340.2771	14	340.2777	Oleoyl glycine
6.70	15	453.3653	15	453.3662	Lyso PE 16:0(9Z,12Z)
7.00	mP	171.1573	mP	171.1575	2-Undecen-1-ol
7.90	mP	213.1565	mP	213.1566	Methyl (E)-2-dodecenoate
8.22	mP	227.1363	mP	227.1367	Ammonium citrate, dibasic
8.42	19	274.2883	17	274.2886	Heptanoylcarnitine
8.81	20	230.2607	18	230.2607	Asparaginyl-Proline or Prolyl-Asparagine
9.43	21	258.2929	19	258.2933	N-Lauroylglycine
10.11	mP	286.325	mP	286.3252	Myristoylglycine
10.60	23	149.0308	21	149.0309	L-2-Hydroxyglutaric acid
11.28	mP	331.268	**27**	**331.268**	**MG (16:0)**
11.71	28	282.294	**26**	**282.2946**	**Oleamide**
11.95	mP	353.269	**mP**	**353.269**	**MG (18:3)**
13.30	30	391.3047	31	391.3048	12-Keto-deoxycholic acid
14.10	31	338.3598	32	338.3599	Tyrosyl-Arginine or Arginyl-Tyrosine

Fig. 2 presents the BPC fingerprints of SS samples after 1 year storage of saliva at -20ºC (A1), or stored as methanol extract (A2).

These modifications shows a general decrease of components in the stored methanol extract comparing with saliva storage, up to 2 times, dependent on the individual molecules, as it is visible in Fig.2 and Fig.3.

Fig. 2. Comparative BPC fingerprints of SS samples analyzed after 1 year storage at -20ºC, as saliva (up, A1) or as methanolic saliva extract (down, A2).

Fig. 3. Comparative evolution of the BPC peak areas for samples A1 *vs* A2, which show differences after 1 year storage of methanol extract (A2) *vs* saliva storage (A1).
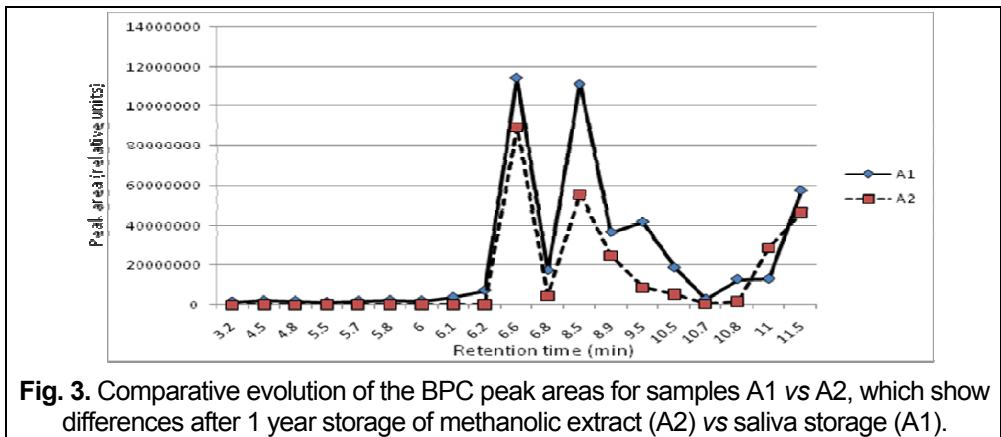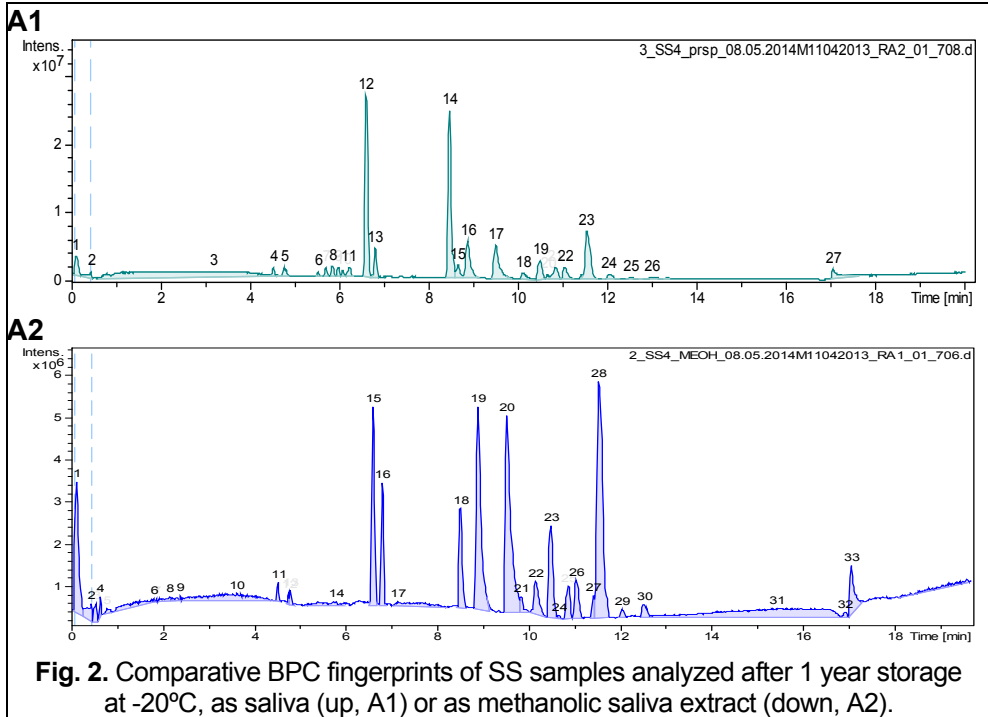
2. Principal Component Analysis (PCA) to discriminate differences between saliva groups

According to Fig. 4, PCA scores and loadings considering the 5 principal components from each group, with a statistical relevance of > 70%, were determined for the t_R range from 10 to 12.3 min.

Fig. 4. PCA analysis of NSS *vs* SS samples, considering 5 principal components separated at t_R from 10 to 12.3 min. The scores (left) shows the good clustering of NSS samples and SS samples. The loadings (right) shows the m/z values of responsible molecules for discriminations between NSS and SS samples.
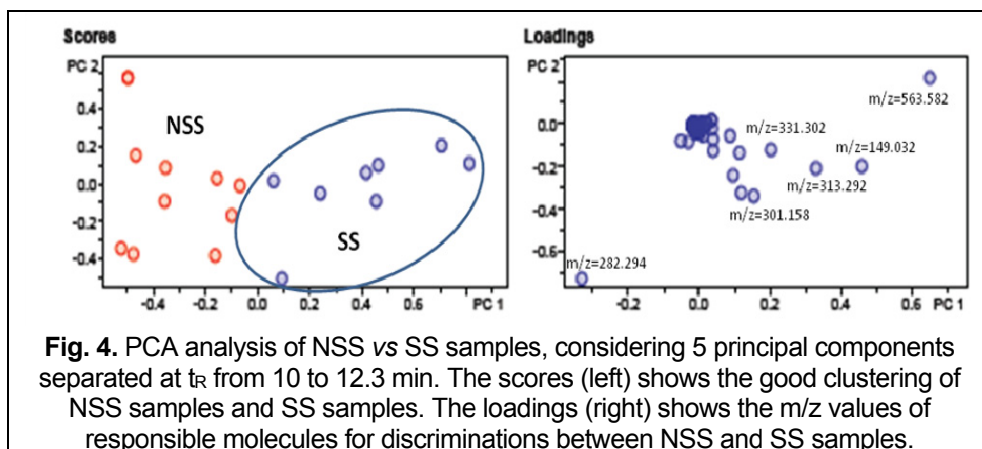
There were identified differences between NSS (circles) and SS (triangle) samples, at t_R=11.28 and 11.95 min, corresponding to MG(16:0/0:0/0:0) and MG(0:0/18:3/0:0), respectively. The scores (left) shows the good discriminations between the NSS and SS groups. The loadings (right) shows the m/z values of the molecules responsible for the discriminations, the most significant differences being noticed for m/z values of 563.582, 282.294, 301.158, 313.292, 331.302 and 149.032 (right).

3. Evaluation and identification of saliva (NSS or SS) molecules by direct, shotgun DIMS analysis

Fig. 5 represents the comparative MS spectra of saliva samples, obtained by DIMS for m/z ranges from 100 to 1000 (upper left), 75-250 (upper right), 250-430 (lower left) and 350-555 (lower right).

The DIMS analysis can identify more molecules than UPLC-QTOF-ESI(+)MS, and m/z values higher than 391, up to 742.47 corresponding mainly to polar PA, PC and PE, SM, DG lipids. Meanwhile, one should consider that UPLC-QTOF-ESI(+)MS analysis was done on methanolic saliva extract, which contain more polar molecules having smaller m/z values, e.g. lyso derivatives of phospholipids, and monoglycerides (MG).

Fig. 5. Comparative mass spectra of saliva samples, obtained by DIMS for the whole range m/z = 100-1000 (upper left), and for different m/z ranges: 75-250 (upper right), 250-430 (lower left) and 350-555 (lower right).
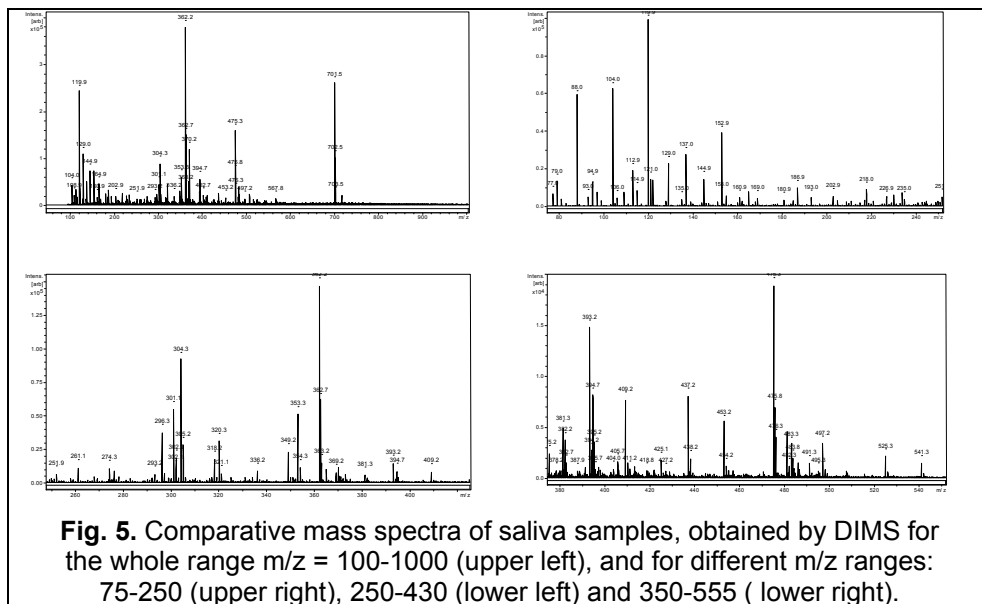
Finally this metabolomics fingerprinting proved to provide rapid and accurate measurements of saliva, in agreement with other authors [40].

CONCLUSIONS

Considering the objectives and results of these experiments, using in parallel two advanced technologies (UPLC-QTOF-ESI(+)MS and shotgun DIMS analysis) we can conclude that metabolomic fingerprinting of resting *vs* stimulated saliva can be achieved fast and in a reliable manner, supporting the identification of main biomarkers, which can be confirmed the Human Metabolomic Databases.

The DIMS analysis allows a larger and more detailed identification of the most relevant small metabolites, offering a fast and reliable picture of the saliva samples, without preliminary separation. By both methods, quantitative, more than qualitative differences were noticed between samples.

According to our studies, saliva investigations have several advantages considering the simple and noninvasive collection, easily handled, low risk for hazardous results, easy to be stored and processed, with lower costs. The saliva analysis is simple, low cost and rapid, easy to storend reliable in time, keeping constant its composition. Such investigations can have good relevance for the utilization of saliva as a diagnostic fluid, for clinical application.

Future research will focus on the identification and validation of saliva biomarkers for systemic diseases, to change the perception that saliva is only useful for the diagnosis of oral diseases, but a mirror of the whole body health.

EXPERIMENTAL SECTION

Collection of saliva. Male and female healthy volunteers were randomly selected from patients of the Prevention Department of the University of Medicine and Pharmacy „Iuliu Hatieganu" in Cluj-Napoca (period April-May 2013) The study was approved by the university Ethics Committe, the inclusion criterion was the clinicaly healthy patient, mean age of 23.1, including 8 females and 4 males.

The sample collection was made in the morning, the subjects did not eat within 60 minutes prior to sample collection. For saliva recovery, alcohol, caffeine, and dairy products were not avoided.

The stimulated saliva (SS) was collected after chewing stimulation with parafin. The whole saliva was collected by drooling it into a vial, allowing to accumulate in the mouth and then expectorate it into a special cup used for saliva testing. A volume of 1 ml saliva was introduced in an Eppendorf vial containing 1 ml of Natrium azide solution 1%, in order to avoid microbial development. All saliva-azide samples were homogenized by a vortex mixer for 1 min. and stored at -20ºC before analysis.

Sample preparation. Aliquots of 1 ml saliva (NSS or SS) were mixed with 1 ml methanol (HPLC grade, Merck) and kept 15 min at -20ºC, for protein precipitation. After centrifugation at 10.000×g, for 10 min., the supernatant was filtered through nylon filters (0.25 µm) to cut-off molecules with molecular weight > 1000 Da. The methanolic extracts were kept at -20ºC before analysis. To check the stability and reproductibility of the samples and their fingerprints, the UPLC-QTOF-MS analysis was repeated 1 year after storage of raw saliva (A1) or methanolic extract (A2).

UPLC–QTOF(ESI+)MS analysis. Aliquots of 5 µl of NSS and SS methanolic extracts were subjected to chromatographic separation on a Thermo Scientific UPLC UltiMate 3000 system equipped with a quaternary pump delivery system Dionex UltiMate 3000 and autosampler. The separation was made with the Thermo Scientific Acclaim C18 column (3µm, 2.1x 250 mm) using a gradient elution program. The column temperature was set at 40°C. The mobile phases were 0.1% formic acid in water (A) and 0.1% formic acid in acetonitrile (B). The flow rate was set at 0.5 mL·min⁻¹. The elution program consisted on a linear gradient from 1% B to 15% B (0 - 3 min), 15% to 50% B (3-6 min), 50% to 95% B (6-9 min) and isocratic 95% B for more 6 min,

returning to initial conditions at min. 15, then kept isocratic for more 5 min with 1% B. The molecules released succesively from UPLC column were introduced automatically into the mass spectrometer using electrospray injection.

The mass spectrometry was performed on a Bruker Daltonics MaXis Impact Q-TOF operating in positive ion mode (ESI+). The mass range was set between 50-1000 m/z. The nebulizing gas pressure was set at 0.4 bar, the drying gas flow at 4 L/min, the drying gas temperature at 200 ºC. Before each chromatographic run, a calibration solution of sodium formate was injected.

Shotgun Direct Infusion Mass Spectrometry (DIMS). The saliva were directly infused into the same mass spectrometer using a KD Scientific syringe pump (Holliston, USA). The flow was set at 3 µl / min, infusion time of 2 min per sample. The results were expressed as MS peaks intensities (x 10^5) at different m/z ranges.

Statistical Analysis. The control of the UPLC-QTOF-MS instrument was done using TofControl 3.2 and Data Analysis 4.1 (Bruker Daltonics). The biostatistic processing used Profile Analysis 5.1 (Bruker Daltonics) which provided Principal Component Analysis (PCA).

AKNOWLEDGMENTS

REFERENCES

1. W.M. Edgar, *Br Dent J*, **1992**, *172*, 305.
2. S.P. Humphrey, R.T. Williamson, *J Prosthetic Dentistry*, **2001**, *85*, 162.
3. E. Kaufman, I.B. Lamster, *Crit Rev Oral Biol Med*, **2002**, *13*, 197.
4. M. Navazesh, S.K. Kumar, *J Am Dent Assoc*, **2008**, *139*, 35S.
5. M. Navazesh, *Ann NY Acad Sci*, **1993**, *694*, 72.
6. Y. Zhang, J. Sun, C.C. Lin, E. Abemayor, M.B. Wang, D.T.W. Wong, *OHDM*, **2014**, *13*, 200.
7. V. de Almeida Pdel, A.M. Gregio, M.A. Machado, A.A. de Lima, L.R. Azevedo, *J Contemp Dent Pract*, **2008**, *9*, 72.
8. F. Ahmadi Motamayel, P. Davoodi, M. Dalband, S.S. Hendi, *DJH*, **2013**, *1*, 1.
9. M. Greabu, M. Battino, M. Mohora, *J Med Life*, **2009**, *2*, 124.
10. D.P. Lima, D.G. Diniz, S.A.S. Moimaz, D.H. Sumida, A.C. Okamoto, *Intl J Infect Dis*, **2010**, *14*, e184.

11. T.K. Fabian, P. Fejerdy, P. Csermely, "Saliva in health and disease, chemical biology of", Wiley Encyclopedia of Chemical Biology, John Wiley & Sons, Inc., **2008**, 1.
12. E. Neyraud, M. Tremblay-Franco, S. Gregoire, O. Berdeaux, C. Canlet, *Metabolomics*, **2013**, *9*, 213.
13. B. Cuevas-Córdoba, J. Santiago-García, *OMICS A J Integrative Biol*, **2014**, *18*, 87.
14. B.L. Slomiany, V.L. Murty, A. Slomiany, *Progress in Lipid Res,* **1985**, *24*, 311.
15. B. Larsson, G. Olivecrona, T. Ericson, *Arch Oral Biology*, **1996**, *41*, 105.
16. M. Soukup, I. Biesiada, A. Henderson, *Diabetol Metab Syndr*, **2012**, *4*, 1.
17. O. Brinkmann, N. Spielmann, D.T. Wong, *Dentistry today*, **2012**, *31*, 56.
18. I. Takeda, C. Stretch, P. Barnaby, *NMR Biomed*, **2009**, *22*, 577.
19. A. Zhang, H. Sun, P. Wang, Y. Han, X. Wang, *J Proteomics*, **2012**, *75*, 1079.
20. A. Zhang, H. Sun, X. Wang, *Applied Biochem & Biotechnol*, **2012b**, *168*, 1718.
21. N.J. Bonne, D.T.W. Wong, *Genome Medicine*, **2012**, *4*: 2.
22. C.F. Streckfus, L.R. Bigler, *Oral Dis*, **2002**, *8*, 69.
23. C.K. Yeh, N.J. Christodoulides, P.N. Floriano, *Tex Dent J*, **2010**, *127*, 651.
24. N. Spielmann, D. Wong, *Oral Dis*, **2011**, *17*, 345.
25. D. Malamud, *Dent Clin North Am*, **2011**, *55*, 159.
26. J.W. Mikkonen, M. Herrala, P. Soininen, R. Lappalainen, L. Tjäderhane, H. Seitsalo, R. Niemelä, S.A. Tuula, M. Kullaa, S. Myllymaa, *Metabolomics*, **2013**, *3*, 1.
27. M. Aimetti, S. Cacciatore, A. Graziano, L. Tenori, *Metabolomics,* **2012**, 8, 465.
28. Y. Huang, M. Zhu, Z. Li, R. Sa, Q. Chu, Q. Zhang, H. Zhang, W. Tang, M. Zhang, H. Yin, *Free Rad Biol and Med*, **2014**, *70*, 223.
29. S. Chiappin, G. Antonelli, R. Gatti, E.F. de Palo, *Clin Chim Acta*, **2007**, *383,* 30.
30. A. Malkar, N.A. Devenport, H.J. Martin, P. Patel, M.A. Turner, P. Watson, R.J. Maughan, H.J. Reid, B.L. Sharp, C.L.P. Thomas, J.C. Reynolds, C.S. Creaser, *Metabolomics*, **2013**, *9*, 1192.
31. D.C. Mueller, M. Piller, R. Niessner, M. Scherer, G. Scherer, *J Proteome Res* **2014**, *13*, 1602.
32. M. Sugimoto, J. Saruta, C. Matsuki, M. To, H. Onuma, M. Kaneko, T. Soga, M. Tomita, K. Tsukinoki, *Metabolomics*, **2013**, *9*, 454-4.
33. L. Caporossi, A. Santoro, B. Papaleo, *Biomarkers,* **2010**, *15*, 475.
34. D.T.W. Wong, *Operative Dentistry*, **2012**, *37*, 562
35. Q. Wang, P. Gao, F. Cheng, X. Wang, Y. Duan, *Talanta*, **2014a**, *119*, 299.
36. Q. Wang, P. Gao, X. Wang, Y. Duan, *Clin Chim Acta*, **2014b**, *427*, 79.
37. B. Álvarez-Sánchez, F. Priego-Capote, M.D. Luque de Castro, *J Chromatogr A,* **2012**, *1248*, 178.
38. V. Bessonneau, B. Bojko, J. Pawliszyn, *Bioanalysis*, **2013**, *5*, 783-792.
39. M. del Nogal Sánchez, E. Hernández García, J.L. Pérez Pavón, B. Moreno Cordero, *Anal Chem,* **2012**, *84*, 379.
40. F. Wei, D.T. Wong, *Chinese J Dental Res*, **2012**, *15*, 7.

A COMPARATIVE STUDY OF THREE METHODS OF EXTRACTION OF MYCOTOXINS FROM BEER

COSMIN IONASCU[a], VASILE OSTAFE[b,*]

ABSTRACT. Three sample preparation methods: solvent extraction, solid-phase extraction (SPE) and stir bar sorptive extraction (SBSE) to assess the occurrence of 11 mycotoxins in beer (pale, dark and non-alchoolic) samples were compared. In order to select the best extraction procedure, the sample matrix effects and the effect of the dilution of the sample were investigated by addition of the analytes before and after the extraction procedure was carried out. The study revealed that SPE (with Oasis HLB cartridge) procedure offered the best results compared with the other two extraction methods: relative standard errors under 16% and recovery of the analytes better than 85%. An Ultrahigh Performance Liquid Chromatography coupled with Mass Spectrometry (UPLC-MS/MS) method was used to identify and confirm the mycotoxins.

Keywords: mycotoxins, extraction method, SPE, matrix effects, sample dilution effect

INTRODUCTION

Mycotoxins are toxic secondary metabolites formed by certain *Aspergillus* spp., in particular *A. flavus* and *A. parasiticus*, which produce them on many plant products [1]. They have been detected as natural contaminants of barley, maize and sorghum malts [2]. Mycotoxins can survive the technological steps of beer production to the extent of 18–20% of the amount initially found in malt or corn grits; most of the losses occurred in the malt mash, boiled wort and final fermentation steps [3].

Maximum levels for mycotoxins in beer have been established by European Commission [4, 5] and classified by IARC [6].

---

[a] *Department of Biology - Chemistry, Faculty of Chemistry, Biology, Geography, West University of Timisoara, 16 Street Pestalozzi, Timisoara 300115, Romania*
[b] *Advanced Research Environmental Laboratories, Multidisciplinary Research Platform "Nicholas Georgescu - Roegen", 4 Street Oituz, Timisoara 300086, Romania*
* *Corresponding author: e-mail: vostafe@cbg.uvt.ro*

Beer is a complex matrix and for this reason, extraction procedures for mycotoxins from beer has to be carefully studied [7].

UPLC-MS/MS is a powerful technique used to analyze many types of chemical residues in food and feed products [8]. The chromatographic separation has to be preceded by an efficient sample treatment technique in order to reduce, as much as possible, the sample matrix effects on the separation, detection and quantification steps. The most common techniques for preparation of the samples for UPLC-MS/MS procedures are solvent addition [9], solid phase extraction [10], liquid phase microextraction [11] and accelerated solvent extraction [12]. Used more rarely, but with very good results, is the stir bar sorptive extraction method [13]. The main drawback of these techniques is the fact that these procedures have to be optimized for each compound of interest, the results not being able to be transferred to other analytes. To compensate for the sample matrix effects the use of internal standards will be the first option, but the cost of this approach as well as their commercial availability for every analyte prevent their application in multi-residue extraction procedures.

In this context, the main objective of this work was to compare the performances of three sample preparation methods (directly solvent addition to the beer, solid-phase extraction (SPE) with Oasis HLB SPE cartridge and SBSE (stir bar sorptive extraction)) used for the confirmation and quantization of 11 microtoxins by a UPLC-MS/MS method.

Representative mycotoxins (Table 4) were selected based on the published reports and the frequency of appearance of these compounds in beer samples [14].

RESULTS AND DISCUSSION

The present work focus on the optimization of the sample extraction method of 11 mycotoxins from beer. The optimization of chromatographic separation and MS detection were presented in another report [15], where, beside the information presented in experimental section and especially in Table 5, there were determined the linear range (0.15 – 10 ppb for aflatoxins G1, G2, B1, B2 and OTA, 1,5 – 100 ppb for FB1, FB2, T-2 and ZEA and 15 – 1000 ppb for DON and HT-2), the repeatability and intermediary precision (with relative standard deviations smaller than 13%), accuracy, limit of detection (smaller than 1.2 ppb) and limit of quantification (smaller than 3.5 ppb).

As it can be seen in Table 4 the logP values for the 11 mycotoxins considered in this study differ from -1.41 for DON until +4.39 from FB2 that make a difficult task to find the optimal extraction conditions for all the analytes.

Due to the complexity of composition of the beer, the sample matrix effects must be evaluated in order to obtain a correct quantification of mycotoxins. It was also taken into account that the influence of the matrix upon the estimation of the concentration of the analytes can be reduced by dilution of the raw samples [16]. Sample matrix effects may include any change in the analyte ionization process due to co-elution of the analyte with contaminants from the sample. Matrix-matched calibration curves are used for compensation of the sample matrix effects, considering that all the analytes will be equally affected [17]. Sample matrix may induce changes in the MS/MS signal, changes that can be constant and independent of the quantity of the analyte from the sample, variable and proportional with the quantity of the analyte, or a combination between the two [18].

To extract and concentrate the studied mycotoxins from beer three methods of sample preparation were used: (a) addition of solvent; (b) SPE and (c) SBSE and a comparison regarding the yield of extraction and sample matrix effect were made. The effect of dilution of the sample was also studied. To simplify the graphs only 3 of the 11 studied mycotoxins were presented: DON (logP = -1.41), AFB1 (logP = 0.45) and FB2 (logP = 4.39).

As it can be seen from Figure 1 when the method with solvent addition for sample preparation is applied to a mixture of analytes made in purified water, the percent of yield of recovery of the analytes is between 85 and 95%. When the same procedure is applied to a sample of beer fortified with the same concentration of analytes, the yield of recovery decrease until 45% in case of DON when no dilution of sample was applied. In case of dilution of the sample the percent of recovery is constantly better for all the analytes.
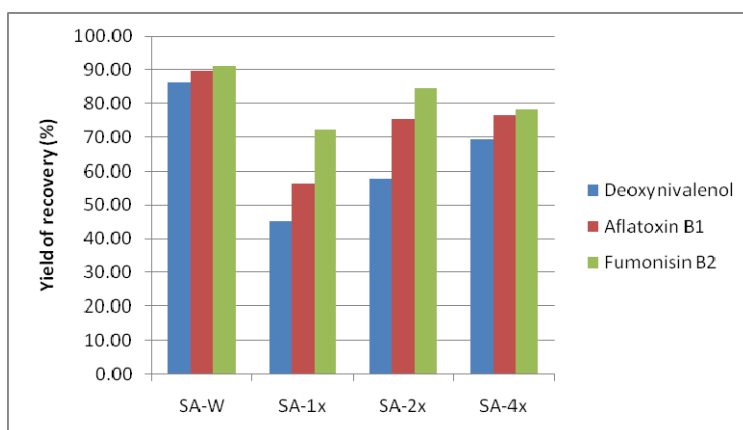
Figure 1. The effect of dilution of the sample on the yield of recovery of the analytes when the method with solvent addition (SA) was used for sample preparation (W – water instead beer, 1x, 2x and 4x – degree of sample dilution
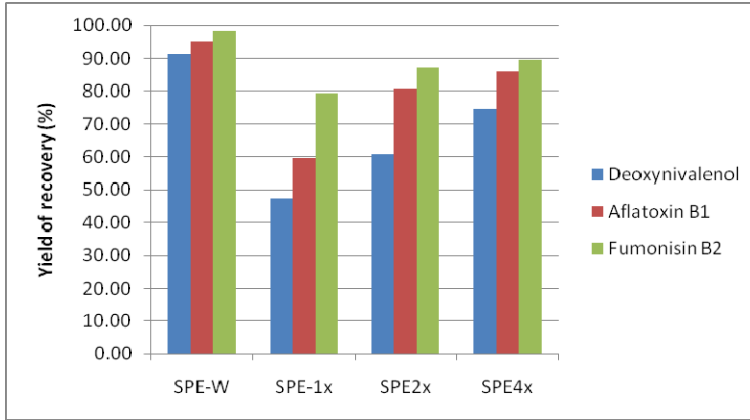
Figure 2. The effect of dilution of the sample on the yield of recovery of the analytes when the SPE method was used for sample preparation (W – water instead beer, 1x, 2x and 4x – degree of sample dilution)

As similar results were obtained when the other two methods of sample preparation were used (i.e. SPE in Figure 2 and SBSE in Figure 3), explicitly when the extraction method is applied to beer fortified to the analytes the degree of recovery is lower in case when the analytes were added to purified water and because the yield of recovery of the analytes increase with the dilution of beer sample, one can conclude that the sample matrix has a major effect on the extraction procedure.
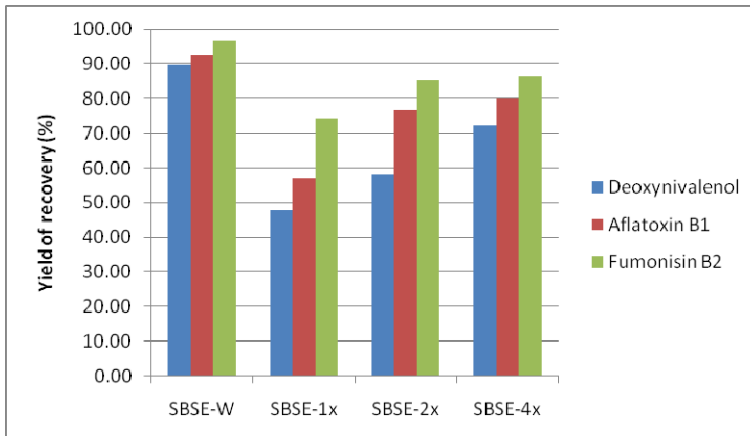
Figure 3. The effect of dilution of the sample on the yield of recovery of the analytes when the SBSE method was used for sample preparation (W – water instead beer, 1x, 2x and 4x – degree of sample dilution

In order to find out which of the three methods of sample preparation is more efficient in the recovery of the analytes, the degree of the recovery of the analytes added to purified water and to beer 4x diluted was graphically presented (Figure 4). Based on the results one may conclude that the method of choice for extraction of the analytes from beer sample is SPE, but a 4x dilution of sample mast be performed before loading the beer in the SPE cartridge.
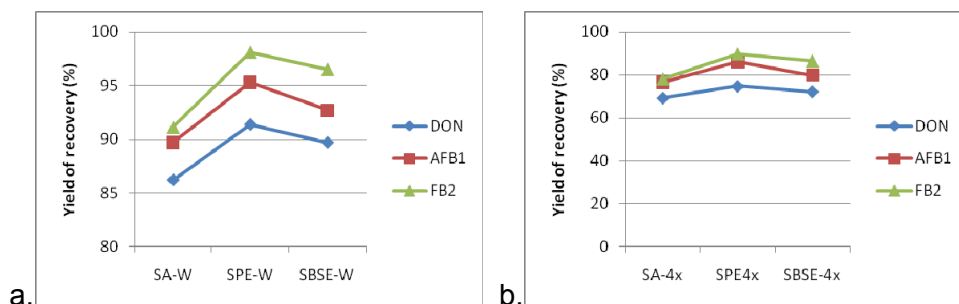
Figure 4. Comparison between the three extraction methods (SA – solvent addition, SPE – solid phase extraction, SBSE – stir bar sorptive extraction). **a**. Extraction methods applied to analytes dissolved in purified water (W) and **b**. Extraction methods applied to beer sample diluted 4x and fortified with known concentration of analytes.

The dilution experiments presented above, although reveal the fact that the beer matrix interfere with the quantization of the mycotoxins, cannot explain if the reduced yield of recovery of the analytes from the fortified samples is due to the interaction of the contaminants from beer during the sample preparation procedure with the analytes or these contaminants influence the analytes ionization process in MS detector. In order to explain which of the two phenomena have a bigger influence, there were realized series of experiments when the samples were fortified with the analytes at the beginning of the sample preparation method and at the end of this procedure. Practically, for each sample preparation method 3 results were obtained: the analytes were added to purified water (w), the analytes were added to beer before the extraction procedure (bex) and after the extraction procedure (aex) was applied to beer. Matrix effect (ME), recovery (RE) and overall process efficiency (PE) were assessed as described by Matuszewski et al. [19]: $ME(\%) = (aex/w)*100$; $RE(\%) = (bex/aex)*100$; $PE(\%) = (bex/w)*100$.

Values of ME(%) around 100% indicate the absence of matrix effects, values lower than 100% point out a suppression of the ionization of the analytes (adsorption of the analytes or a interference with the ionization or detection of the analytes in MS instrument), while values higher than

100% reveal a fake enhancement process (interferences in the ionization interface or other non-normal phenomena leading the artificial increase of the signal in MS detector) [20]. The sample matrix effect was estimated for pale, dark and non-alcoholic beer.

The results presented in Table 1 reveals that in the case of pale beer, the sample matrix interfere with the correct evaluation of the analytes as all the values are lower than 100%. The smallest effect is registered when the sample is prepared by SPE procedure. Similar results were obtained for dark and non-alcoholic beers.

The influence of contaminants from the beer sample on the correct evaluation of the concentration of the analytes, during the sample preparation procedures are revealed by the PE (%) values. Smaller values than 100 indicate the fact that beer contains compounds that contribute to the reduction of the concentration of the analytes in the solution obtained after sample preparation. In this case the best method of extraction was also SPE.

Finally, RE (%) indicates which of the two possible interferences with the signal assigned to the analytes has a greater influence - sample preparation procedure or the ionization and detection in MS instrument. If the obtained values are smaller than 100, the influence upon the sample preparation method prevails (the reduction of the actual concentration of the analytes take place). When the RE value is larger than 100 the chromatographic separation procedure is the one that is influenced by the presence of the contaminants that were not eliminated from the processed sample during sample preparation method. As it can be seen from Table 1 RE do not show a clear tendency of values to be smaller or bigger than 100, to reveals which of the three studied extraction methods is better, as it was the case with the values of ME and PE, when SPE method has presented better results than the other two extraction methods. This means that in the case of some of the studied mycotoxins, depending on their chemical structure, the interactions with the contaminants take place during sample separation procedure and in the case of other analytes this interaction take place during the chromatographic separation process.

From the results (Tables 1 – 3) one may conclude that for extraction of the 11 mycotoxins, the smaller interferences with the quantification of the analytes are obtained when beer samples are prepared by SPE using Oasis HLB cartridges. For all types of beer studied (pale, dark and non-alcoholic) with SPE sample preparation method the percent of recovery of the analytes was better than 85%, which is comparable with other published studies [21-23]. Therefore, this method was used to assess the presence of the 11 micotoxins in real beer samples.

Table 1. Evaluation of the sample matrix effect for pale beer in case of application
for the extraction of the 11 mycotoxins of a sample preparation method
based on solvent addition (SA), solid phase extraction (SPE) and
stir bar sorptive extraction (SBSE) procedure

Analyte	SA			SPE			SBSE		
	ME	RE	PE	ME	RE	PE	ME	RE	PE
DON	86.30	96.42	83.21	93.41	96.95	90.56	76.51	104.59	80.03
AFG2	84.32	93.96	79.23	99.82	91.16	91.00	81.92	87.76	71.89
AFG1	83.64	96.13	80.40	97.35	92.18	89.73	80.84	100.20	81.00
AFB2	84.74	94.47	80.06	87.86	100.86	88.61	84.67	93.30	79.00
AFB1	83.94	93.87	78.79	95.96	89.91	86.28	82.43	93.78	77.30
FB1	83.69	95.55	79.97	96.73	89.15	86.23	84.63	95.69	80.98
T-2	87.99	92.12	81.05	88.94	104.09	92.58	84.78	102.53	86.92
HT-2	85.07	97.48	82.93	93.72	93.38	87.52	86.11	95.03	81.84
ZEA	89.93	94.82	85.27	97.37	95.63	93.12	88.27	94.43	83.36
OTA	81.21	102.30	83.07	94.82	93.26	88.43	90.70	94.94	86.12
FB2	87.56	95.56	83.67	96.61	90.6	87.53	90.47	100.07	90.53

ME – matrix effect (in %), RE – recovery (in %) and PE – process efficiency (in %).

Table 2. Evaluation of the sample matrix effect for dark beer in case of application
for the extraction of the 11 mycotoxins of a sample preparation method
based on solvent addition (SA), solid phase extraction (SPE) and
stir bar sorptive extraction (SBSE) procedure

Analyte	SA			SPE			SBSE		
	ME	RE	PE	ME	RE	PE	ME	RE	PE
DON	81.01	105.84	85.74	99.68	90.68	90.39	64.12	101.84	65.29
AFG2	76.63	90.27	69.17	99.48	84.41	83.97	76.63	101.26	65.20
AFG1	79.97	96.83	77.43	97.00	78.20	75.85	79.97	98.30	81.81
AFB2	86.63	100.53	87.09	110.21	70.32	77.50	86.63	88.66	70.94
AFB1	84.28	91.57	77.18	110.11	71.99	79.26	84.28	99.72	78.50
FB1	78.52	105.79	83.07	91.07	110.37	100.52	78.52	94.10	70.80
T-2	82.33	91.79	75.57	79.62	115.05	91.61	82.33	90.44	69.34
HT-2	81.66	95.36	77.87	88.04	100.71	88.66	81.66	81.34	67.26
ZEA	90.82	116.15	105.48	85.47	104.45	89.27	90.82	78.10	69.68
OTA	85.90	92.32	79.30	82.38	94.77	78.07	85.90	97.90	82.81
FB2	69.06	112.72	77.85	105.46	76.14	80.30	69.06	100.29	83.17

ME – matrix effect (in %), RE – recovery (in %) and PE – process efficiency (in %).
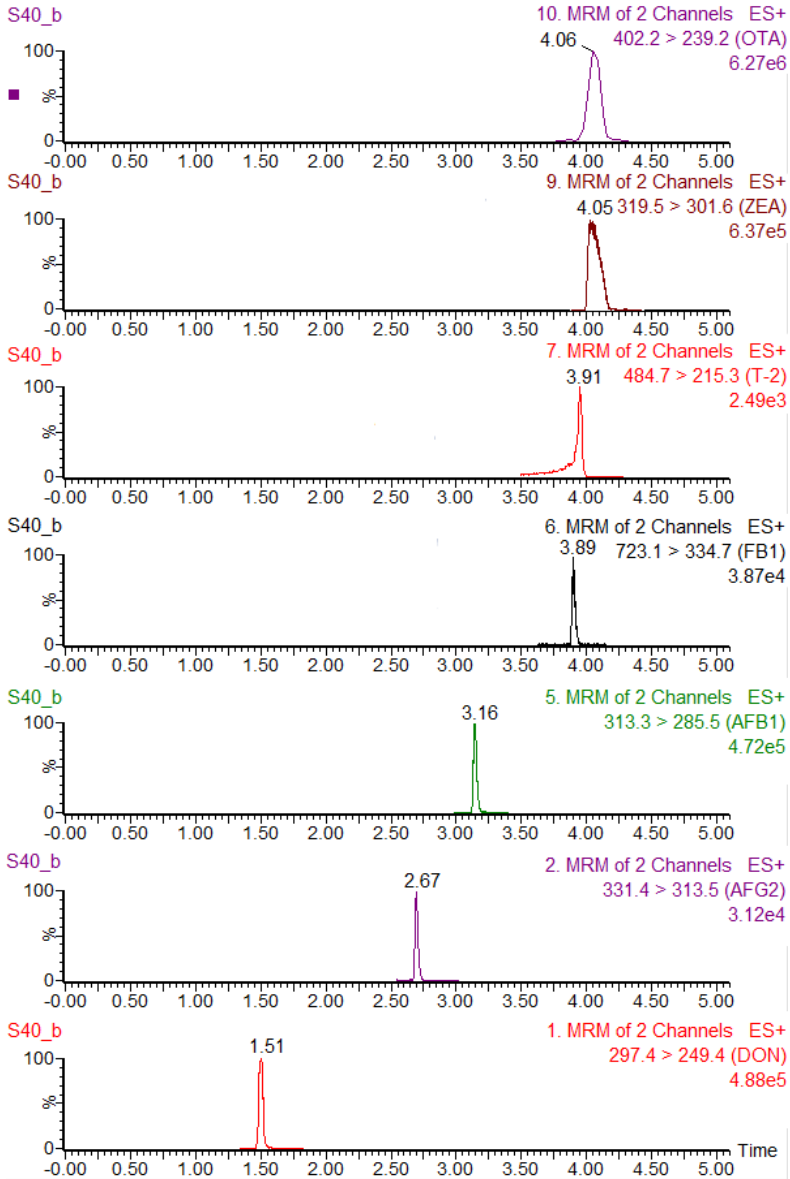
Figure 5. MRM chromatograms of a sample of pale beer (produced in UE and sold in a supermarket from Romania. There are presented only the chromatograms for the transitions used for quantification of the mycotoxins found in concentrations larger than the limit of the quantification.

Table 3. Evaluation of the sample matrix effect for non-alcoholic beer in case of application for the extraction of the 11 mycotoxins of a sample preparation method based on solvent addition (SA), solid phase extraction (SPE) and stir bar sorptive extraction (SBSE) procedure

Analyte	SA			SPE			SBSE		
	ME	RE	PE	ME	RE	PE	ME	RE	PE
DON	95.66	86.92	83.15	102.99	97.90	100.83	86.63	68.81	59.61
AFG2	84.96	96.04	81.60	93.91	99.30	93.25	84.96	77.59	52.52
AFG1	90.57	97.70	88.48	80.43	102.49	82.43	90.57	114.12	73.10
AFB2	100.31	88.51	88.79	87.05	93.54	81.43	100.31	101.50	80.83
AFB1	69.74	121.41	84.67	84.00	89.73	75.37	69.74	107.95	72.98
FB1	92.07	88.16	81.17	84.56	103.28	87.34	92.07	89.46	60.68
T-2	64.79	119.97	77.73	79.05	102.68	81.17	64.79	89.31	81.39
HT-2	72.41	114.60	82.99	97.05	80.70	78.32	72.41	131.74	91.57
ZEA	92.73	94.12	87.27	86.99	101.94	88.67	92.73	98.64	75.51
OTA	84.00	95.29	80.04	91.77	123.90	113.70	84.00	78.51	59.20
FB2	53.43	96.04	51.32	102.37	84.41	86.41	53.43	93.40	77.44

ME – matrix effect (in %), RE – recovery (in %) and PE – process efficiency (in %).

Applications to samples

The optimized extraction procedure (SPE with Oasis HLB cartridges) was applied for the identification and quantification of the 11 mycotoxins in commercial beers sold in Romania. Although the results and discussion of these study are presented elsewhere [15], it is worth to mention that from all the 54 analyzed samples only 2 have contained mycotoxins above the legal limit. In Figure 5 an example of the results obtained in case of a pale beer produced in EU but commercialized in Romania is presented. In this particular sample there were found 7 mycotoxins (with concentration above the quantification limit but below the legal limit).

CONCLUSIONS

Comparing the solvent addition, SPE and SBSE preparation sample methods, the most efficient regarding the relative standard error (under 16%) and yield of recovery of the added analytes (with a median value of 97%) was proved to be the SPE with Oasis HLB cartridges. For this extraction method the best results regarding the matrix effects and process efficiency were also obtained.

With SPE extraction method (with Oasis HLB cartridges), the selected compounds can be determined with acceptable precision and accuracy at lower concentration than the limit established by EU Commission Decision 2002/657/EC guidelines [24].

EXPERIMENTAL SECTION

Chemicals, Reagents and Materials

The mycotoxins used as standards were purchased from Sigma-Aldrich (via Redox, Bucharest): Aflatoxins B1, B2, G1, G2 (#40139-U Supelco; 25 µg/mL each component in acetonitrile), Fumonisins B1 (#34139 Fluka, 50 µg/mL in acetonitrile: water, 50:50) and B2 (#34142 Fluka, 50 µg/mL in acetonitrile: water, 50:50), Ochratoxin A (#34037 Fluka, 10 µg/mL in acetonitrile), HT-2 toxin (#34136 Fluka, 100 µg/mL in acetonitrile), T-2 toxin (#34071 Fluka, 100 µg/mL in acetonitrile), Deoxynivalenol (#34124 Fluka, 100 µg/mL in acetonitrile) and Zearalenone (#34126 Fluka, 100 µg/mL in acetonitrile). All other chemicals were of analytical grade. Ultrapure water was prepared with SG Ultra Clear 2001-B Water Deionization System (Cole-Parmer, via Nitech, Bucharest). Millex-GN nylon filters (0.20 µm, Millipore, Carrightwohill, Ireland) were used for filtration of any solutions before injection in UPLC system. For sample preparation / concentration by solid phase extraction (SPE) Oasis HLB cartridges of 200 mg (Waters, Mildford, USA) and by stir bar sorptive extraction (SBSE) glass bars with magnetic core, coated with silicone film with C18 arms (film thickness 1.0 mm, 10 mm length) (Gerstel, Mülheim an der Ruhr, Germany) were used.

In Table 4 there are presented the analytes used in this study and some related data.

Table 4. List of compounds included in the analyses

Nr.	Name of analytes	Abbreviation	CAS No.	Molecular mass (Da)	logP values
1	Deoxynivalenol	DON	51481-10-8	296,3	-1,41
2	Aflatoxin G2	AFG2	7241-98-7	330,2	-0,25
3	Aflatoxin G1	AFG1	1165-39-5	328,2	-0,17
4	Aflatoxin B2	AFB2	7220-81-7	314,2	0,37
5	Aflatoxin B1	AFB1	1162-65-8	312,2	0,45
6	Fumonisin B1	FB1	116355-83-0	721,8	2,2
7	T-2 toxin	T-2	21259-20-1	466,5	2,25
8	HT-2 toxin	HT-2	26934-87-2	424,2	2,27
9	Zearalenone	ZEA	17924-92-4	318,3	3,83
10	Ochratoxin A	OTA	303-47-9	403,8	4,31
11	Fumonisin B2	FB2	116355-84-1	705,8	4,39

log P predicted values from ACD/Labs' ACD/PhysChem Suite
(http://www.acdlabs.com/products/pc_admet/physchem/physchemsuite/)

A stock solution containing 1000 ppb DON and HT-2, 100 ppb FB1, FB2, ZEA and T2 and 10 ppb OTA, AFB1, AFB2, AFG1 and AFG2 were prepared in a solution of 0.1% ammonium formate in 30% methanol (MeOH). The stock solution was used to make 7 serial dilutions (dilution factor 2) that were injected in the UPLC system to realize the standard curves. Similar standard curves were prepared using as dilution solution pale beer checked to be free of detectable traces of the analytes (matrix-matched calibration curves) [15].

Instrumentation

Chromatographic analyses were performed using an AcquityUPLC™ system (Waters, Milford, MA, USA), and separations were carried out using an AcquityUPLC™ BEH C18 column (100× 2.1 mm, 1.7 μm particle size) from Waters. The C18 column was equilibrated at 30 ˚C. The analytes were separated with a gradient elution profile realized with a mobile phase consisting of 0.1% ammonium formate in 100% methanol (mobile phase A) and an aqueous solution of 0.1% ammonium formate in 10% methanol (mobile phase B). The analysis started with 10% of mobile phase A at a flow rate of 0.35 mL/min, for 0.3 minute. Then the percentage of mobile phase A was increased linearly up to 30% in 1.2 minutes and further to 100% in 2.0 minutes; this composition was hold for 1.0 minute before being returned to 10% of mobile phase A, in 0.1 min, followed by a re-equilibration time of 0.4 minutes (total run time 5 minutes). The injection volume was always 10 μL (full sample loop). The UPLC system was coupled to a XevoTQD triple-quadrupole mass spectrometer with an orthogonal Z-spray–electrospray interface (Micromass, Manchester, UK). For the purpose of optimizing the MS parameters, the selected mycotoxins were dissolved in 0.1 ammonium formate in 30% methanol, at a concentration of 62.5 ppb DON and HT-2, 6.25 ppb FB1, FB2, ZEA and T2 and 0.625 ppb OTA, AFB1, AFB2, AFG1 and AFG2 and infused at 10 μL/min. The MS was operated in the positive electrospray (ESI+) mode with a capillary voltage 3.5 kV. The source and desolvation temperatures used were 140 and 400ºC, respectively. Nitrogen was used as the desolvation and cone gas at the flow rates of 650 and 50 L/h, respectively. Collision-induced dissociation was performed using argon (99.995%, Linde, Timisoara, Romania) as the collision gas at a pressure of 0.3 mbar in the collision cell. The selected precursor ions of the analytes were fragmented to their product ions in the collision cell and the two most intensive product ions per analyte were chosen for quantitative and confirmation purposes (see Table 5). The ions were monitored for a dwell time ranging from 0.01 to 0.04 s [15].

A vortex mixer (model Reax 2000), a rotary agitator (model Reax-2, end-over-end) from Heidolph (Schwabach, Germany), and an analytical AB204-S balance (Mettler Toledo, Greinfesee, Switzerland) were also used. An extraction manifold from Waters connected to a BüchiVac V-500 (Flawil, Switzerland) vacuum system was used for SPE experiments.

Table 5. MS/MS optimized conditions for studied mycotoxins (Rt – retention time; MRM – multiple reaction monitoring, CV – cone voltage, CE – collision energy)

Abbrev.	R$_t$ (min)	Quantification transition			Confirmation transition		
		CV (V)	CE (V)	MRM transition	CE (V)	CV (V)	MRM transition
DON	1,51	25	10	297.4 > 249.4	25	15	297.4 > 231.3
AFG2	2,67	60	25	331.4 > 313.5	60	30	331.4 > 245.3
AFG1	2,83	40	25	329.2 > 243.1	45	25	329.2 > 311.4
AFB2	3,03	50	30	315.2 > 259.2	50	35	315.2 > 243.3
AFB1	3,16	30	25	313.3 > 285.5	30	30	313.3 > 241.3
FB1	3,89	45	40	723.1 > 334.7	40	35	723.1 > 352.8
T-2	3,91	25	20	484.7 > 215.3	25	15	484.7 > 245.4
HT-2	3,92	25	15	442.6 > 263.4	25	15	442.6 > 215.3
ZEA	4,05	30	10	319.5 > 301.6	30	12	319.5 > 283.6
OTA	4,06	25	20	404.2 > 239.2	25	15	404.2 > 358.2
FB2	4,07	55	30	707.1 > 336.7	50	30	707.1 > 354.7

Extraction Methods

The sample matrix effects on quantification of analytes was estimated for three extraction (sample preparation / sample concentration) methods.

Solvent extraction

In 10 mL of degassed beer (tested to be free of analytes) was added 0.4 mL diluted standard solution (62.5 ppb DON and HT-2, 6.25 ppb FB1, FB2, ZEA and T2 and 0.625 ppb OTA, AFB1, AFB2, AFG1 and AFG2 made in 0.1% ammonium formate in 30% MeOH). The most part of the proteins, polysaccharides and other contaminants were precipitated by addition of 40 mL of acetonitrile 100%. After 10 minute of gentle homogenization on rotary agitator, the precipitate was centrifuged at 4000 rpm for 10 minutes. From the supernatant 36 mL solution was recovered and further evaporated to dryness at 35 °C with a gentle stream of nitrogen. The residue was reconstituted to a final volume of 0.4 mL with 0.1% ammonium formate in 30% MeOH, filtered through a 0.20 µm filter and injected to UPLC system.

The extraction procedure was repeated, but 10 mL of purified water was used instead of beer.

To estimate the sample matrix effects on the extraction method another series of experiments was realized but the addition of the standard solution was carried out by adding 0.4 mL of diluted standard solution to the residue resulted after the evaporation of the solvent.

Another way to estimate the effects of the sample matrix was to dilute the sample. In a series of experiments, after the centrifugation step, the recovered supernatant (36 mL) was diluted with purified water in a ratio 1:1 and 1:3, respectively.

Solid phase extraction (SPE)

The Oasis HLB cartridge was conditioned with 5 mL of acetonitrile / methanol (50:50, v/v) and further with 5 mL purified water. To 10 mL degassed beer (tested to be free of analytes), 0.5 mL of diluted standard solution (same as above) was added. The homogenized mixture (10 seconds at 200 rpm on vortex) was percolated at 1 mL/min on a Oasis HLB cartridge. The non-bounded compounds were washed out with 5 mL of 5% acetonitrile. The mycotoxins were eluted by percolating the cartridge with 5 mL of 0.1% formic acid in 100% acetonitrile. The eluate was evaporated to dryness at 35 °C with a gentle stream of nitrogen. The residue was reconstituted to a final volume of 0.5 mL with 0.1% ammonium formate in 30% MeOH. After filtration through a 0.20 µm filter the solution was ready to be injected in UPLC system.

The extraction procedure was repeated, but 10 mL of purified water was used instead of beer.

To assess the influence of the sample matrix, two approaches were considered: addition of standard before chromatographic separation step and dilution of the sample at the earliest possible step. For this, in a series of experiments the extraction procedure was repeated but the diluted standard solution (0.5 mL) was added to the residue obtain after the evaporation of the solvent. Finally, a series of experiments was realized, but the beer sample (10 mL) was diluted 2x and 4x, respectively, before passing the beer through the SPE cartridge.

Stir bar sorptive extraction (SBSE)

Glass bar with magnetic core having C18 coating layer was used as a specific adsorbent and as a magnetic stirrer. Similarly as in SPE procedure, 10 mL of degassed beer were mixed with 0.5 mL of diluted standard solution and homogenized with SBSE for 10 minutes at 200 rpm. The glass bar was introduced for 10 minutes (200 rpm on a magnetic stirrer) in 5 mL of 5% acetonitrile in order to eliminate the non-bonded contaminants. The mycotoxins were eluted from the SBSE mixing the glass bar at 200 rpm, 10 minute in 5 mL 0.1% formic acid in 100% acetonitrile. The glass bar was removed and reconditioned (mixed successively with 10 mL 0.1% formic acid in 100% acetonitrile, 10 mL of dichloromethane, 10 mL 0.1% formic acid in 100% acetonitrile and 10 mL of 0.1% formic acid in 5% acetonitrile). The eluate was evaporated to dryness at 35 °C with a gentle stream of nitrogen. The residue

was reconstituted to a final volume of 0.5 mL with 0.1% ammonium formate in 30% MeOH. Then extraction procedure was repeated, but 10 mL of purified water was used instead of beer.

As in the previous described sample extraction method, two other series of experiments were carried out in order to estimate the sample matrix effects on the quantification of the analytes. In one series of the experiments the diluted standard solution (0.5 mL) was added to re-dissolve the residue obtained after the evaporation of the solvent. In another series of experiments, the beer sample (10 mL) was diluted 2x and 4x, respectively, before the interaction with the SBSE.

MATRIX EFFECTS

As it was described in the previous sub-section, the sample matrix effects were studied in beer samples checked to be free of traces of analytes, realizing several series of experiments. Series 1 represented the neat standard solution in water, series 2 and 3 were prepared similarly, but with beer, adding the standards either pre- or post- application of the entire procedure of the extraction methods described above. All series of experiments were realized in six replicates. Sample matrix effects (ME), recovery (RE) and overall process efficiency (PE) were calculated according to Matuszewski et al. [19]. In all these experiments, the analytes were quantified based of standard curves realized by dilutions of the analytes made in 0.1% ammonium formate in 30% methanol.

The optimized method was applied to assess the 11 mycotoxins in beers commercialized in Romania (Timisoara). Once bought, the beer samples were analyzed in the same day. The open containers were kept at 4 °C until the results were processed (no longer than a week).

ACKNOWLEDGMENTS

REFERENCES

1. M.M. Aguilera-Luiz, P. Plaza-Bolanos, R. Romero-Gonzalez, J.L. Vidal, A.G. Frenich, *Analytical and Bioanalytical Chemistry*, **2011**, *399*, 2863–2875.

2. S. Oueslati, R. Romero-González, S. Lasram, A.G. Frenich, J.L.M. Vidal, *Food and Chemical Toxicology*, **2012**, *50*, 2376–2381.
3. S.K. Mbugua, J.K. Gathumbi, *Journal of the Institute of Brewing*, **2004**, *110*, 227-229.
4. Commission Regulation (EU) 1881/2006, 'Setting maximum levels for certain contaminants in foodstuffs', *Official Journal of the European Union,* **2006**, *58*, 1-24.
5. Commission Regulation (EU) 165/2010, 'Setting maximum levels for certain contaminants in foodstuffs as regards aflatoxins', *Official Journal of the European Union*, **2010**, *L50*, 8-12.
6. IARC: 'Some naturally occuring substances, food and constituents, heterocyclic aromatic amines and mycotoxins', *IARC Monographs on the Evaluation of Carcinogenic risks to Humans,* **1993**, *56*, 489-521.
7. M. Zachariasova, T. Cajka, M. Godula, A. Malachova, Z. Veprikova, J. Hajslova, *Rapid Communications in Mass Spectrometry*, **2010**, *24*, 3357-3367.
8. E. Preda, M.M Mincea, C. Ionascu, A.V. Botez, V. Ostafe, *Studia UBB Chemia*, **2013**, *LVIII*, 167-175.
9. M. Singh, A. Jha, A. Kumar, N. Hettiarachchy, A.K. Rai, D. Sharma, *Journal of Food Science and Technology*, **2014**, *51*, 2070-2077.
10. M. Ventura, D. Guillén, I. Anaya, F. Broto-Puig, J.L. Lliberia, M. Agut, L. Comellas, *Rapid Communications in Mass Spectrometry*, **2006**, *20*, 3199-3204.
11. P.P. Bolaños, R. Romero-González, A.G. Frenich, J.L.M. Vidal, *Journal of Chromatography A*, **2008**, *1208*, 16-24.
12. F. Gao, Y. Hu, X. Ye, J. Li, Z. Chen, G. Fan, *Food Chemistry*, **2013**, *141*, 1962-1971.
13. M. Kawaguchi, A. Takatsu, R. Ito, H. Nakazawa, *TrAC Trends in Analytical Chemistry*, **2013**, *45*, 280-293.
14. E. Beltrán, M. Ibáñez, T. Portolés, C. Ripollés, J.V. Sancho, V. Yusà, S. Marín, F. Hernández, *Analytica Chimica Acta*, **2013**, *783*, 39-48.
15. C. Ionascu, "The Study of Chemical Compounds with Proven Toxicity (Studiul Compușilor Chimici cu Toxicitate Dovedită)", PhD in chemistry thesis, West University of Timisoara, Timisoara, **2014**.
16. C.S.J. Rubert, R. Marin, K.J. James, J. Manes, *Food Control*, **2013**, *30*, 122-128.
17. K. Jorgensen, G. Rasmussen, I. Thorup, *Food Additive Contamination*, **1996**, *13*, 95-104.
18. M. Rodriguez-Aller, R. Gurny, J.-L. Veuthey, D. Guillarme, *Journal of Chromatography A*, **2013**, *1292*, 2-18.

19. B.K. Matuszewski, M.L. Constanzer, C.M. Chavez-Eng, *Analytical Chemistry*, **2003**, *75*, 3019-3030.
20. D. Hampel, E.R. York, L.H. Allen, *Journal of Chromatography A*, **2012**, *903*, 7-13.
21. L. Lucini, G.P. Molinari, *Journal of Chromatographic Science*, **2011**, *49*, 709-714.
22. T.M. Annesley, *Clinical Chemistry*, **2007**, *53*, 1827-1834.
23. Y. Rodriguez-Carrasco, J.C. Molto, J. Manes, H. Berrada, *Talanta*, **2014**, *128*, 125-131.
24. Commission Decision (EU): 'Performance of analytical methods and the interpretation of the results', *Official Journal of the European Union,* **2002**, L221-L232.

SURFACE MODIFICATION OF SILICA GELS FOR SELECTIVE ADSORPTION OF BACTERIAL LIPASES

ZOLTÁN BOROS[a,b], EMESE ABAHÁZIOVÁ[a], DIÁNA WEISER[a], PÉTER KOVÁCS[c], CSABA PAIZS[d], LÁSZLÓ POPPE[a,b,*]

ABSTRACT. Since immobilization of lipases enhances their productivity, stability and selectivity, a series of surface modified silica gel supports was developed and used for hydrophobic adsorption of Lipase AK from *Pseudomonas fluorescens* and Lipase PS from *Burkholderia cepacia.*

Keywords: silica gel, surface modification, adsorption, lipase, immobilization, Pseudomonas fluorescens, Burkholderia cepacia

INTRODUCTION

The use of enzymes as biocatalysts has acquired ever increasing importance in organic chemistry. The native enzymes are, however, expensive, relatively unstable and difficult to handle. Being water soluble, removal of the enzyme or its degradation products from the product may be cumbersome and the recovered enzyme usually cannot be reused. Immobilization of enzymes is an established technique and several of such biocatalysts are commercially available and applied at industrial scale.[1,2,3] The importance of this field is emphasized by a recent exhaustive review on the application of immobilized lipases in reactions conducted in organic solvents[4] as well as an in depth study of the molecular mechanism of acylation with immobilized lipases on derivatized silica gels.[5]

Immobilization of enzymes has many advantages. Being solids, they can be easily recovered and, after the reaction they can often be reused.[6] The

[a] *Budapest University of Technology and Economics, Department of Organic Chemistry and Technology, Műegyetem rkp. 3., H-1111 Budapest, Hungary*
[b] *SynBiocat Ltd., Lázár deák u. 4/1., H-1173 Budapest, Hungary*
[c] *Research Centre for Natural Sciences, Institute of Organic Chemistry, Hungarian Academy of Sciences, Magyar tudósok körútja 2., H-1117 Budapest, Hungary*
[d] *Biocatalysis and Biotransformation Research Group, Babes-Bolyai University of Cluj-Napoca, Arany János str. 11, Ro-400028 Cluj-Napoca, Romania*
[*] *Corresponding author: poppe@mail.bme.hu*

catalytic properties of immobilized enzymes, such as stability, activity and selectivity, can be efficiently influenced by the proper choice of the solid support.

A further advantage of immobilized enzymes is that they can be used in syntheses similar to conventional biocatalysts. A disadvantage of the latter is that, since they operate in homogeneous solutions, the enzyme, or its degradation products, may appear as contaminants in the product the removal of which may be difficult. Immobilization avoids these problems and, as a further advantage, they can be used in continuous-flow reactors.[7]

Lipases (triacylglycerol esterases EC 3.1.1.3) catalyzing the hydrolysis of lipids can be found basically in every living organism and their interfacial activation occurs at specific lipid-water interfaces.[8] Biocatalysts ensure a clean and environmentally friendly way to carry out chemical reactions under mild conditions with high stereoselectivity.[9] Therefore, the use of enzymes, especially in organic solvents, 4has a great potential in the manufacturing of a single enantiomer of chiral drugs.[10] As a result, biotransformations are therefore nowadays a generally accepted method for the synthesis of such drugs.[11]

The objective of the present study was to develop, by surface modifications, silica gel supports which would ensure high efficiency, enantioselectivity and stability of the lipase attached to them.

RESULTS AND DISCUSSION

First, surface modification was carried out by derivatization with mono- and disubstituted alkoxysilanes. The silica gels thus modified were used as carriers in adsorptive immobilization of Lipase AK (from *Pseudomonas fluorescens*) and Lipase PS(from *Burkholderia cepacia*).

Next, the hydrophobic adsorption of Lipase AK was carried out onto 19 surface modified silica gel supports. The modified biocatalysts were tested in a model reaction, in the enantioselective acylation of racemic 1-phenylethanol rac-1 with vinyl acetate (Scheme 1).
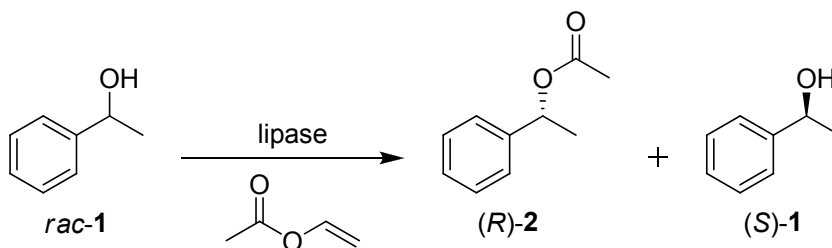
Scheme 1. Kinetic resolution screen for the immobilized bacterial lipases

Table 1. Biocatalytic properties of Lipase AK adsorbed on various surface-modified silica gels tested by kinetic resolution of rac-**1** in n-hexane:MTBE 2:1 at 4 h.

Silicagel derivatization	c [%][a]	$ee_{(R)\text{-}2}$[%][a]	E^{b}	U_{B}^{c} [µmol min^{-1} g^{-1}]
-	1.1	98.6	146	0.4
Methyl	27.5	99.4	467	19.0
Ethyl	19.7	99.4	410	13.6
Propyl	17.0	99.4	426	11.8
Isobutyl	9.0	99.4	367	6.2
Hexyl	12.2	99.4	387	8.4
Octyl	38.3	99.2	440	26.4
Decyl	15.5	99.4	393	10.7
Dodecyl	16.6	99.4	392	11.5
Octadecyl	24.0	99.5	521	16.6
Phenyl	13.4	99.6	553	9.3
Perfluorooctyl	26.9	99.5	528	18.5
Vinyl	22.9	99.3	375	15.8
2-Cyanoethyl	14.3	99.6	600	9.9
3-Chloropropyl	24.9	99.5	506	17.2
3-Mercaptopropyl	24.0	99.5	516	16.6
3-Amino-2-hydroxypropyl	6.2	99.9	1380	4.3
Dimethyl	16.4	99.5	441	11.3
Phenyl/methyl	13.4	99.6	553	9.3
Cyclohexyl/methyl	16.1	99.6	552	11.1

[a] Conversion (c) and enantiomeric excess (ee) were measured by GC.[12]
[b] Enantiomer selectivity (E) was calculated from c and $ee_{(R)\text{-}2}$.
[c] Specific biocatalyst activities (U_B) were calculated by the equation $U_B = n_P / (t \times m_B)$ (where n_P [µmol] is the amount of the product, t [min] the reaction time and m_B [g] the mass of the applied biocatalyst).

Results after 4 hours reaction time are shown in Table 1. Enantioselectivity was high (>99%) for all variants. The highest activity (U_B) was achieved with octyl, methyl, perfluorooctyl and 3-chloropropyl grafted silica supports among which the perfluorooctyl variant was the most selective. Lowest activity was displayed by the enzymes immobilized onto isobutyl- and 3-amino-2-hydroxypropyl grafted silica supports.

After experiments with Lipase AK, the adsorption of Lipase PS was carried out. Results after 4 hours reaction time are shown in Table 2.

As shown above, adsorption of Lipase AK to the perfluorooctyl-grafted silica gave a highly selective biocatalyst (ee=99.5%). Adsorption of Lipase PS on the same support gave even better enantioselectivity (ee=99.6%). With the dodecyl and octadecyl grafted variants, both activity (c=6.5 and6.2%)

and selectivity (*ee*=99.3% and98.5%) were low. Selectivity of the octadecyl grafted support was below 99% i.e. it was of the worst selectivity. The most productive carriers were 3-chloropropyl, 2-cyanoethyl, phenyl and phenyl-methyl grafted supports (*c*=38,8%, 33,9%, 33,6%, and32,9% respectively). These supports showed high enantioselectivity as well. Enantioselectivity was the highest with the hexyl grafted variant (*ee*=99.9%). In general, it was established that the nature of surface modification of the support significantly improved the biocatalytic potential of the adsorbed enzymes. It is of note, that Lipase PS immobilized onto an unmodified support had the lowest activity (*c*=3.2%) and almost all of those attached to a modified carrier proved to be more enantioselective. From Table 2 it can be concluded that the optimal carriers are those grafted with3-chloropropyl, 2-cyanoethyl and phenyl groups.

Table 2. Biocatalytic properties of Lipase PS adsorbed on various surface-modified silica gels tested by kinetic resolution of rac-**1** in n-hexane:MTBE 2:1 at 4 h.

Silica gel derivatization	c [%][a]	$ee_{(R)\text{-}2}$[%][a]	E^{b}	$U_{B}{}^{c}$ [µmol min^{-1} g^{-1}]
-	3.2	99.8	886	2.2
Methyl	31.1	99.6	767	21.6
Ethyl	24.9	99.7	857	17.1
Propyl	27.7	99.7	984	19.1
Isobutyl	8.0	99.3	317	5.5
Hexyl	10.4	99.9	2257	7.2
Octyl	28.2	99.7	970	19.4
Decyl	12.8	99.7	653	8.9
Dodecyl	6.5	99.3	288	4.5
Octadecyl	6.2	98.5	138	4.3
Phenyl	33.6	99.7	1088	23.1
Perfluorooctyl	22.9	99.6	729	15.9
Vinyl	30.9	99.6	855	21.4
2-Cyanoethyl	33.9	99.6	867	23.5
3-Chloropropyl	38.8	99.7	1101	26.9
3-Mercaptopropyl	27.6	99.7	883	19.0
3-Amino-2-hydroxypropyl	16.1	99.7	688	11.2
Dimethyl	29.7	99.7	998	20.6
Phenyl/methyl	32.9	99.7	1178	22.7
Cyclohexyl/methyl	27.8	99.7	1029	19.3

[a] Conversion (*c*) and enantiomeric excess (*ee*) were measured by GC.[12]
[b] Enantiomer selectivity (*E*) was calculated from *c* and *ee*$_{(R)\text{-}2}$.
[c] Specific biocatalyst activities (U_B) were calculated by the equation $U_B = n_P / (t \times m_B)$ (where n_P [µmol] is the amount of the product, t [min] the reaction time and m_B [g] the mass of the applied biocatalyst).

CONCLUSIONS

For the adsorption of Lipase AK, the best carriers were octyl, methyl and perfluorooctyl grafted silica gels, while for the adsorption of Lipase PS, 3-chloropropyl, phenyl and 2-cyanoethyl functionalizations were the most appropriate. Our results demonstrated that among the modified silica gels tested in the present study there cannot be found a support which simultaneously exhibits optimum selectivity and activity. Adsorption is a two-way physical process that depends on the nature of both the enzyme and its support.

EXPERIMENTAL SECTION

Chemicals and enzymes

Racemic 1-phenylethanol, vinyl acetate and all further chemicals and solvents were of analytical grade or higher and were purchased from Sigma-Aldrich (St. Luis, MO, USA) or Merck(Darmstadt, Germany). Lipase PS and AK were the products of AmanoEnzyme (Nagoya, Japan). Surface functionalized silica gels were the products of SynBiocat (Budapest, Hungary).

Analytical methods

GC analyses were carried out on an 4890 instrument, Agilent (Santa Clara, CA, USA) equipped with a FID detector and a Hydrodex β-6TBDM column [25 m × 0.25 mm × 0.25 µm film with heptakis-(2,3-di-*O*-methyl-6-*O*-*t*-butyldimethylsilyl)-β-cyclodextrine; Macherey & Nagel (Düren, Germany)] using H_2 as carrier gas (injector: 250°C, FID detector: 250°C, head pressure: 12 psi, 50:1 split ratio). GC data (oven program), t_r (min): for rac-1 and rac-**2** (120°C, 8 min), 4.0 [(*S*)-**2**], 4.4 [(*R*)-**2**], 5.8 [(*R*)-**1**], 6.0 [(*S*)-**1**].

Adsorption of enzymes on surface modified silica gels

Enzymes were dissolved in Tr is buffer (11.25 mL, 100 mM, pH=7.5, ionic strength controlled with NaCl) then the surface functionalized silica gel (250 mg) was added. The mixture was incubated at 400 rpm and 4°C for 18 h. The immobilized enzymes were filtered off on a glass filter (G4), washed with 2-propanol (2x5 mL), hexane (5 mL), dried at room temperature (2 h) and stored at 4°C.

Enantiomer selective acetylation of racemic 1-phenylethanol *rac*-1 in shake vials

To a solution of racemic 1-phenylethanol *rac*-**1** (101 mg; 0.828 mmol) in a mixture of hexane, *tert*-butyl-methyl-ether and vinyl acetate 6/3/1 (2 mL), the enzyme (50 mg) was added. The mixture was shaken (1000 rpm) in a sealed amber glass vial at 30°C for 4 hours. The products were analyzed by GC and TLC after 1, 2, and 4 hours.

ACKNOWLEDGMENTS

REFERENCES

1. Umemura, S.; Takamatsu, T.; Sato, T.; Tosa, I.; Chibata, I., *Appl. Microbiol. Biotechnol.*, **1984**, *20*, 291-295.
2. Kennedy, J.F.; Melo, E.H.M.; Junel,K., *Chem. Eng. Progress*, **1990**, *7*, 81-89.
3. Parathasarathy, R.V.; Martin, C.R., *Nature*, **1994**, *369*, 298-301.
4. Adlerkreuz, P.; *Chem. Soc. Rev.,* **2013***, 42(15)*, 6406-6436.
5. Jiu, D.; Jia, G.; Zhang, Y.; Yang,Q.; Li, C., *Langmuir*, **2011**, *27*, 12016-12024.
6. Cao L. "*Carrier-bound Immobilized Enzymes: Principles, Application and Design*" Wiley-VCH, Wienheim, **2005**.
7. Itabaiana, I. Jr.; de Mariz e Miranda, L.S.; de Souza, R.O.M.A.,*J. Mol. Catal. B Enzym.*, **2013**, *85-86*, 1-9.
8. Reetz, M.T., *Curr. Opin. Chem. Biol.*, **2002**, *6*, 145-150.
9. Gotor-Fernández, V.; Brieva, R.; Gotor, V., *J. Mol. Catal. B Enzym.*, **2006**, *40*, 111-120.
10. Margolin, A.L., *Enzyme Microb. Technol.*, **2003**,*15*, 266-280.
11. Patel, R.N., *Curr. Opin. Drug Discov. Dev.*, **2003**,*6*, 902-920.
12. Chen, C.S.; Fujimoto, Y.; Girdaukas, G.; Sih, C.J., *J. Am. Chem. Soc.*, **1982**, *104*, 7294-7299.

CORRELATION BETWEEN THE ESTIMATED TOTAL THIOSULFINATES CONTENT AND ANTIPLATELET ACTIVITY OF THREE DIFFERENT VARIETIES *A. CEPA*

ANIELA SAPLONŢAI-POP[a,*], MARIOARA MOLDOVAN[b,*], RADU OPREAN[c], OLGA ORASAN[d], STEFAN SAPLONTAI[e], CORINA IONESCU[f]

ABSTRACT. The present study aims to establish a correlation between the estimated thiosulfinate compound content of *Allium cepa L. (A. cepa)* juices and their antiplatelet activity. The juices were obtained from three different varieties of *A. cepa,* cultivated in three different regions of Romania.

The thiosulfinate compound content was estimated using a spectrophotometric method, based on the reaction with 4-mercapto-pyridine (a chromogenic thiol, with a maximum absorbance coefficient at 324 nm). The constant of the reaction kinetic curve was obtained by overlapping experimental data with an exponential function of first degree.

The antiplatelet activity of the mentioned juices was measured by using *in vitro* tests with platelet rich plasma (PRP) obtained from blood collected from healthy human people, with arachidonic acid as platelet agonist.

A statistically significant direct proportionality between the estimated thiosulfinate compound content and the antiplatelet activity of the tested *A.cepa* juices was established.

Keywords: Allium cepa; natural products; platelet; antiplatelet; thiosulfinate compounds.

---

[a] *Faculty of General Medicine, Department of Cardiology, "Iuliu Haţieganu" University of Medicine and Pharmacy, 8 Victor Babeș str,, RO-400012, Cluj-Napoca, Romania*

[b] *Department of Polymeric Composites, "Raluca Rîpan" Institute of Chemistry, 30 Fântânele str., RO-400294, Cluj-Napoca, Romania*

[c] *Department of Analytical Chemistry, "Iuliu Haţieganu" University of Medicine and Pharmacy, 6 Louis Pasteur str., RO-400349, Cluj-Napoca, Romania*

[d] *4th Medical Clinic, "Iuliu Haţieganu" University of Medicine and Pharmacy, 16-20 Republicii street, Cluj-Napoca, 400015, Romania*

[e] *Faculty of Pharmacy, "Vasile Goldiş" West University, 86 Liviu Rebreanu str., RO-310045, Arad, Romania*

[f] *Department of Biochemistry, "Iuliu Haţieganu" University of Medicine and Pharmacy, 6 Louis Pasteur str., RO-400349, Cluj-Napoca, Romania*

* *Corresponding authors: pop.aniela@umfcluj.ro; mmarioara2004@yahoo.com*

A. SAPLONŢAI-POP, M. MOLDOVAN, R. OPREAN, O. ORASAN, S. SAPLONTAI, C. IONESCU

INTRODUCTION

Allium genus, with over 500 species, belongs to the family *Amaryllidaceae (Alliaceae)*, subfamily *Allioideae. Allium cepa* (*A. cepa*) is a biennial plant that produces a bulb in the first year [1-3].

Water content represents 80-95% from the weight of the fresh onion, the rest of 5-20% being represented by dried substance. From the last one, over 65% was found like non-structural carbohydrates [4]. Other categories of chemical species such as flavonoids and organo-sulfur compounds, with beneficial effects on human health, were identified in the dried substance.

Organosulfur compounds are represented by: non-volatile S-amino acids, derivatives of cysteine, S-alk(en)nyl-L-cysteine sulfoxides (ACSOs) and their degradation products: thiosulfinate compounds and poly-sulfides. The ACSOs are the ones responsible for the characteristic odor, that becomes manifest at the cleavage in the presence of alliinase (alliin alkylsulphenate-lyase). ACSOs generate the characteristic odor and taste. Some of the therapeutic effects of the *A. cepa* are due to the sulfur compounds, formed by cleavage of three types of S-alk(en)nyl-L-cysteine sulfoxides (ACSOs) in the presence of alliinase [5]. In the intact tissue, ACSOs and alliinase are stored in different cellular compartments. Injury of the tissue, that is the destruction of these compartments, takes to ACSO hydrolysis. Consequently, iminopropionic and S-alk(en)yl-cystein-sulphenic acids are formed in the presence of alliinase.

There are many studies focused on the antiplatelet activity of the *A. cepa* juices as well as on their anti-atherosclerotic effects and alteration of the serum lipid profile [6]. Studies on the antiplatelet activity of the aqueous extract of onion suggest the inhibition of the arachidonic acid release from phospholipids, the process that initiates the eicosanoid metabolism leading to the synthesis of prostaglandins, thromboxanes and leucotrienes [7]. Thiosulfinate compounds of *A. cepa* seem to be the active constituents with antiplatelet activity, *via* their inhibition effect on the COX activity, including the arachidonic acid metabolism and the formation of TxA_2 [8].

Because the majority of the studies sustain that the mechanism of the antiplatelet activity of the *A. cepa* juices is based on the COX activity inhibition, one of the platelet agonists chosen to be used in our study is the arachidonic acid.

Many methods have been described for the identification of thiosulfinate compounds from *A. cepa* juices or extracts: fast spectrophotometric determination [9], the use of HPLC (with a chiral stationary phase for the separation of the thiosufinate esters from natural/synthetic extracts of *A. cepa* [10]), H-NMR [11] or GC-MS [12]. Combined analytical methods are also reported. Other

40

determination methods for the alliicin and alliinase activity include the reaction between 2-nitro-5-tiobenzoat (NTB) and alliicin [13] or that of thiosulfinate compounds with chromogenic thiols like mercaptopyridine (2-MP), 4-mercapto-pyridine (4-MP), 1-oxide-2-mercaptopyridine (MPO) and 2-mercaptopyrimidine (MPM), respectively [14].

The aim of this study was to correlate the thiosulfinate compound content from *A. cepa* juices obtained from the three studied varieties with their tested antiplatelet activity by using *in vitro* tests on platelet rich plasma (PRP).

Since most of the studies are focused on examining the effect and the mechanism of platelet aggregation inhibition or on the determination of the relative concentration of the extracts/juices [15-17], this study represents a novelty.

RESULTS AND DISCUSSION

The percentage of the recovered juice from the studied varieties of *A. cepa*, reveals a higher value for the yellow varieties as compared to the white one (figure 1). Some studies are in agreement with our results [18], some on the contrary [19], which shows the existence of multiple variables (such as: raw material, the process used) that can influence the process.
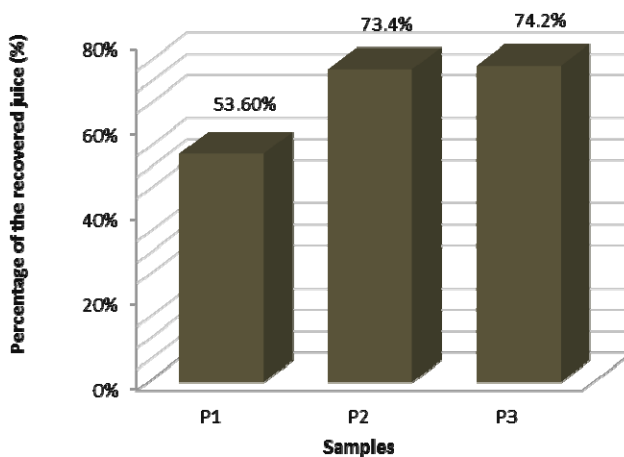
Figure 1. The percentage of the recovered juice *(defined as the ratio between the amount of the juice and the amount of raw material of A. cepa)*
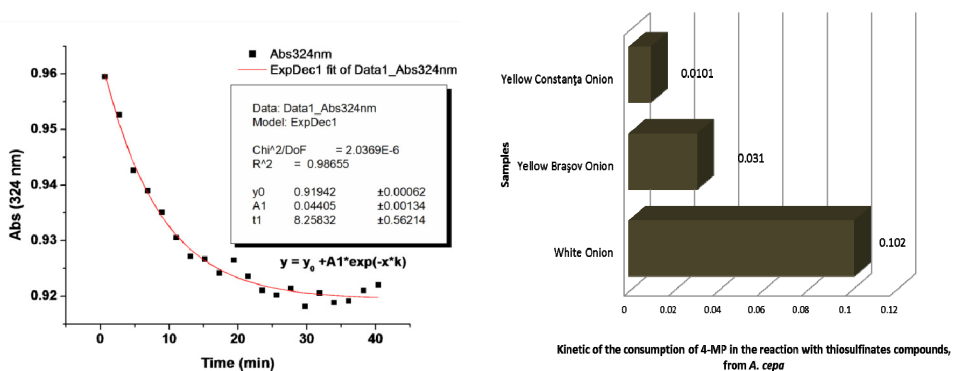
Determination of the total thiosulfinate content

The reaction with 4-mercapto-pyridine (4MP) was used to estimate the thiosulfinate content from *Allium cepa* juice. 4-MP is a chromogenic thiol, commercialized in pure form. It is a stable, inert compound, which reacts with the thiosulfinate compounds from *Allium* juice (alliicin, alliin) [14, 20]. 4-MP presents an absorbance maximum at 324nm wavelength ($\varepsilon = 19,600$ $M^{-1}cm^{-1}$).

The kinetic method for the determination of tiosulfinate content (aliicin, alliin) is temperature and pH dependent [21].

We defined the kinetic curve obtained for sample 1 as a calibration curve in order to estimate the thiosulfinate content from the juices of A. *cepa* (figure 2 left). The highest quantity of 4-MP was used during the reaction with the sample 1. Thiosulfinate compounds from *A. cepa* juices were determined in relation to the reaction kinetic constant of the kinetic curve, an exponential function of first degree [22].

In figure 2left depicts the kinetic curve of the consumption of 4-MP during the reaction with thiosulfinates of juice obtained from sample 1 - the white variety of *A. cepa* (the kinetic constant of the reaction is calculated in function of this). Figure 2 right shows superior estimated amounts of thiosulfinate compounds in the white *A. cepa* than in the other studied yellow varieties.

Figure 2. left) Bleaching of 4-MP by thiosulfinates in sample 1; **right)** Kinetics of the consumption of 4-MP in the reaction with tiosulfinate compounds, (**x-axis** = sample; **y-axis** = coefficient of kinetic consumption (k_1 - min^{-1}))

Determination of antiplatelet activity

We quantified the antiplatelet activity by *in vitro* tests using PRP obtained from blood collected from healthy humans. The principle of the method is based on the increase of the transmittance during the aggregation process. This was recorded by using a spectrophotometer (with magnetic stirrer) at 600 nm wavelenght.

During the antiplatelet effect testing procedure, a significant increase of transmittance was observed for the control sample, in the same time with platelet aggregation. Hence an obvious inhibition of platelet aggregation in the presence of *A. cepa* juice was sensed.

The percentage of the inhibition of platelet aggregation in the presence of *A. cepa* juice was calculated with respect to the maximum transmittance at 7 min (considered the final point of the platelet aggregation inhibition reaction) for the test sample and for the control sample like in figure 3 left, like an extrapolation of our previous researches (in press) [22]. It was observed that sample 1, the white *A. cepa* variety, has the strongest antiplatelet effect, with an inhibition percentage of 87.2% and SD of 2.3% (see figure 3 right).
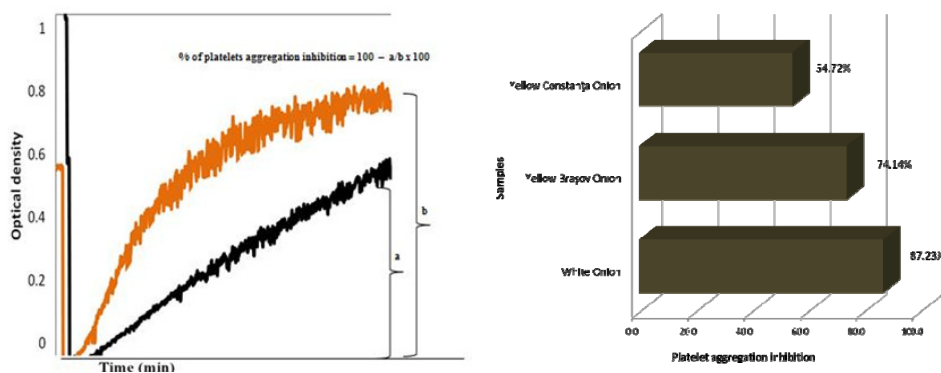
Figure 3. left) Method for calculation of the antiplatelet activity (**a** = maximum transmittance at 7 min for test sample; **b** = maximum transmittance at 7 min for control sample); **right)** The inhibition of the platelet aggregation in the presence of the *A. cepa* juices (**x-axis** = sample; **y-axis** = percentage of the platelet aggregation inhibition).

Thiosulfinate compounds are considered to be responsible for the antiplatelet activity [16, 23]. For this purpose, we have determined the correlation between the estimated thiosulfinate compound content of the studied juices and their effect of platelet aggregation inhibition. (Table 1) This is in agreement with the literature data.

After applying the statistical test described in the „Experimental section" a *Pearson correlation coefficient* of (r) = 0.914 was obtained. It indicates a strong positive correlation between the two sets of values. The *p-value* of 0.0167, obtained by applying the „*T-test*", showed that the correlation is statistically significant.

Table 1. The percentage of the recovered juice, coefficient of kinetic consumption of 4-MP in the reaction with thiosulfinate compounds and percentage of platelet aggregation inhibition for the three different varieties of *A. cepa*

Allium cepa Variety	Recovered juice (%)	Coefficient of kinetic consumption of 4-MP by thiosulfinate compounds (k_1 - min^{-1})	Percentage of platelet aggregation inhibition (%)	Standard Deviation (%)
P1 - White *A. cepa*	53.6	0.1020	87.2	2.3
P2 - Yellow *A. cepa* (Braşov)	73.4	0.0310	74.1	2.4
P3 - Yellow *A. cepa* (Constanţa)	74.2	0.0101	54.7	2.3

Because there is no literature data concerning the comparison of the antiplatelet activity of different varieties of *Allium cepa*, the authors focused their studies on this part as well [22].

CONCLUSIONS

A direct proportionality between the estimated thiosulfinate compound content and the antiplatelet activity of the tested A. cepa juices was observed, but further researches in this direction are needed. The juice of white A. *cepa* has higher antiplatelet activity as well as estimated quantity of thiosulfinate compound than the yellow *A. cepa*.

EXPERIMENTAL SECTION

Obtaining the *Allium cepa* juice

Three varieties of *A. cepa* were used, grown in three different regions of Romania, approximately in the same period of the year, treated similarly against diseases and pests (Table 1). The juice was obtained from portioned *A. cepa* bulbs using an electrical juicer. It was further centrifuged for about 20 minutes at 10000rpm with the recovery of the supernatant.

Determination of the total thiosulfinate compound content

A buffer solution of 4-MP, with a pH=7.2, was prepared in order to estimate the thiosulfinate compound content. The principle of the method is based on the reaction of 4-MP with the activated disulfide bound from the thiosulfide compund -S(O)-S-. It determines the consumption of 4-MP during the chemical reaction with formation of mixed disulfides, 4-allyl-mercapto-pyridine that do not absorbe at 324 nm wavelength [13, 20].

The consumption rate of 4-MP during the reaction was monitored by spectrophotometric means. The continuous measurement of the optical density (OD) during the reaction between 4-MP and the juice of *A. cepa*, permitted the recording of the absorbance decrease during time at the specified wavelength (concomitantly with the consumption of 4-MP).

Determination of the kinetic constant of the reaction is absolutely necessary [20]. This parameter was calculated at 24°C and pH=7.2 for each sample, by using a first order exponential decay function (figure 2left).

After adding a volume of the *A. cepa* juice to the solution of 4-MP, absorbance of the samples was recorded every 2 minutes, during 40 minutes, at room temperature by using a spectrophotometer (UNICAM 4, UV-Vis spectrophotometer).
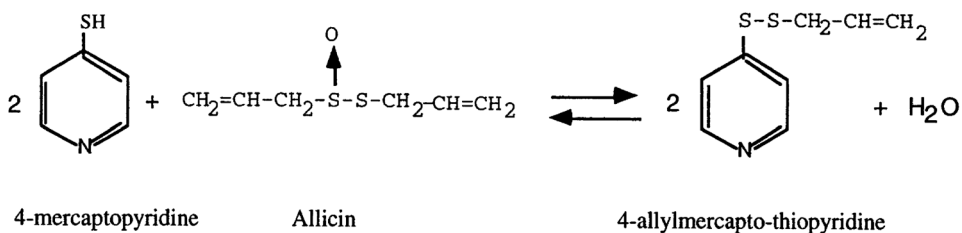
Scheme 1 [20]

Determination of antiplatelet activity

The calibration of the spectrophotometer was done with platelet poor plasma (PPP) and PRP, considered to have transmittance values of 100% and 0%, respectively.

To the PRP sample a well defined antiplatelet agonist (**Arahidonic Acid**, concentration 0.685mM-Sigma-Aldrich, from porcine liver, BioReagent, suitable for cell culture,>99%, USA) was added. For the control and for the test samples first a preset quantity (1:100; v:v) *A. cepa* juice was and then the antiplatelet agonist under continuous recording of transmittance until 7 minutes.

The antiplatelet agonist was added by pipetting it directly into the PRP, not in a part of the cuvette, with the aim to avoid the formation of air bubbles. Two sets of analyses were carried out for the control samples and five sets for the test samples for each variety of *A. cepa*. Presented results are averages of all obtained values.

Statistical test: The "Pearson Correlation" was used for comparison between the means of two quantitative variables. The correlation coefficient r measures the strength and direction of a linear relationship between two variables; the value of r is always between (+1) and (-1). A correlation coefficient of (+1) indicates a perfect positive correlation; (-1) - indicates a perfect negative correlation; near 0 - indicates no correlation.

A "T-test" was used to determine whether the correlation coefficient is "strong" or "significant" or not. It is considered statistically significant when the p value is under 0.05 and statistically highly significant when lower than 0.001.

ACKNOWLEDGMENTS

REFERENCES

1. M.W. Chase, J.L. Reveal, M.F. Fay, *Botanical Journal of the Linnean Society*, **2009,** *161*(*2*), 132.
2. E. Block, "Garlic and other Alliums", The Royal Society of Chemistry, Cambridge, **2010**.
3. J.L. Brewster, "Onions and Other Alliums", Wallingford- CABI Publishing, **2008**.
4. B. Darbyshire, B.T. Steer, "Carbohydrate biochemistry", In: H.D. Rabinowitch, J.L. Brewster, eds. "Onions and allied crops", Vol. III, Botany, physiology and genetics. Boca Raton, CRC Press, Inc., Florida, **1990**, 1–16.
5. H. Tapiero, D. Townsend, K. Tew, *Biomed Pharmacother*, **2004**, *58(3)*, 183.
6. M. Ali, M. Thomson, M. Afzal, *Prost Leuk Essent Fatty Acids*, **2000**, *60*, 43-47.
7. C.H. Moon, Y.S. Jung, M.H. Kim, S.H. Lee, E.J. Baik, S.W. Park, *Prost Leukot Essent Fatty Acids*, **2000**, *62*, 277.
8. W. Breu, W. Dorsch, "Allium cepa L. (Onion): Chemistry, analysis and pharmacology", In: H. Wagner, N.R. Farnsworth, ed. Economic and Medicinal plants Research, Academic Press, London, **1994**, 115-147.
9. G.G. Freeman, F. McBreen. *Biochem Soc Trans*, **1973**, *1*, 1150.
10. R. Bauer, W. Breu, H. Wagner, W. Weigand, *J Chromatogr A*, **1991**, *541*, 464.
11. L.D. Lawson, S.G. Wood, B.G. Hughes, *Planta Med*, **1991**, *57*, 263.
12. E. Block, D. Putman, S.H. Zhao. *J Agric Food Chem*, **1992**, *40*, 2431.
13. T. Miron, A. Rabinkov, D. Mirelman, L. Weiner, M. Wilchek, *Anal Biochem*, **1998**, *265*, 317.
14. O. Zofi, W. Zaborska, *Pol J Food Nutr Sci*, **2012**, *62(1)*, 23.
15. E. Block. *Agnew. Chem. Int. Ed. Engl.*, **1992**, *31*, 1135.
16. K. Osmont, K. Arnt, I. Goldman, *Plant Foods Hum Nutr*, **2003**, *58*, 27.
17. W. Briggs, J. Folts, H. Osman, I. Goldman. *J. Nutr.,* **2001**, *131*, 2619.
18. C. Shenoy, M.B. Patil, R. Kumar, S. Patil, *Int. J Pharm Pharmaceutical Sci*, **2009**, *2(2)*, 167.
19. M. Marotti, R. Piccaglia, *J Food Sci*, **2002**, *67(3)*, 1229.
20. T. Miron, I. Shin, G. Feigenblat, L. Weiner, D. Mirelman, M. Wilchek, A. Rabinkov, *Anal Biochem*, **2002**, *307*, 76.
21. D.R. Grassetti, J.J.F. Murray, *Arch. Biochem. Biophys*., **1967**, *119*, 41.
22. A. Saplonţai-Pop, A. Moţ, M. Moldovan, R. Oprean, R. Silaghi-Dumitrescu, O. Orăşan, M. Pârvu, E. Gal, C. Ionescu, accepted for publication in *Centr Eur. J. Biology*, August **2014** – in press.
23. K.C. Srivastava, *Prostaglandins Leukot Med*, **1986**, *24(1)*, 43.

IMMOBILIZED CYANOBACTERIA ON THE CATHODE AS OXYGEN SOURCE FOR MICROBIAL FUEL CELL

MIRCEA ANTON[a,*], IULIU OVIDIU MARIAN[a], ROBERT SANDULESCU[b] and NICOLAE DRAGOS[c]

ABSTRACT. Oxygen is commonly used as the electron acceptor for the cathode reaction in microbial fuel cells (MFCs). This study demonstrates how to generate oxygen via photosynthesis by means of Synechocystis AICB 51 cyanobacteria immobilized on the cathode. The advantage of using cyano-bacteria immobilized on the cathode was demonstrated using two geome-tries: two-chamber and membrane-less MFCs. The anode chamber was filled with sludge collected from the wastewater treatment plant from Cluj-Napoca, Romania. The oxygen concentration in the cathode space of two-chamber cells rises from about 1mg l^{-1} at 130 lux to 11 mg l^{-1} at 2500 lux of incident illumination. In the case of membrane-less cells, the oxygen concentration varies from 0.2mg l^{-1} to 4.5 mg l^{-1} for the same conditions of illumination. In the case of membrane-less MFCs, the power generated with the immobilized cyanobacteria on the cathode is up to 20 of times greater than the power generated with the standard plain graphite cathode during illumination. In both cases there is a strong correlation between power and dissolved oxygen concentration.

Keywords: immobilized Synechocystis cyanobacteria, microbial fuel cell, photosynthetic oxygen, dissolved oxygen, power density

INTRODUCTION

A microbial fuel cell (MFC) provides direct recovery of the chemical energy stored in organic compounds in wastewater, for example, to electrical energy, *via* the chemical reactions catalyzed by microorganisms [1]. A MFC

* [a] *Babes-Bolyai University, Faculty of Environmental Sciences and Engineering, 30 Fantanele str., RO-400327, Cluj-Napoca, Romania*
[b] *Iuliu Hatieganu University of Medicine and Pharmacy, Faculty of Pharmacy, 8 Victor Babeş str., RO-400012, Cluj-Napoca, Romania*
[c] *Babes-Bolyai University, Faculty of Biology and Geology, 44 Gheorghe Bilaşcu str., RO-400015, Cluj-Napoca, Romania*
* *Corresponding author: mircea.anton@ubbcluj.ro*

consists of an anode and a cathode, separated in most cases by a cation exchange membrane. Microorganisms in the anode chamber oxidize organic materials, generating electrons and protons (anode reaction):

$$n\ CH_2O + n\ H_2O \rightarrow n\ CO_2 + 4n\ e^- + 4n\ H^+$$
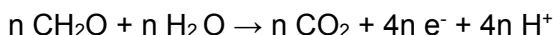
The electrons are transferred to the cathode through the external circuit because of the potential difference developed between the reducing environment in the anaerobic anode chamber and the oxidizing environment in the cathode chamber (supplied with oxygen). The protons are transferred to the cathode through the membrane. Electrons and protons are finally consumed in the cathode chamber, commonly reducing oxygen to water (cathode reaction) [1].

$$n\ O_2 + 4n\ e^- + 4n\ H^+ \rightarrow 2n\ H_2O \quad \text{or}$$
$$n\ O_2 + 2n\ e^- + 2n\ H^+ \rightarrow n\ H_2O_2$$
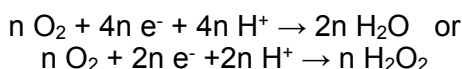
When considering the overall process, the cathodic reaction is, aside from the flux of protons through the membrane, the main bottleneck identified at the moment in increasing the power of MFCs [2].

The cathodic process is determined by the electrode surface, its catalytic properties, the homogeneity in the cathodic compartment and the concentration of the electron acceptor in the bulk liquid [3].

Oxygen is generally used as the electron acceptor for the cathodic reaction in MFCs. The supply with oxygen through sparging is energy demanding, reducing the net energy output of the MFC [4].

The low coulombic efficiency of the MFC is believed to be due to oxygen limitation in the cathode chamber and to oxygen diffusion into the anode chamber through the membrane [5-7].

In order to eliminate the oxygen limitation, the oxygen concentration in the cathode should be kept high, which requires increased power consumption, and results in more oxygen diffusion into the anode [1].

Algae and cyanobacteria have been used as photosynthetic sources of oxygen in the cathode [7-9]. In a two-chamber MFC, algae and/or cyanobacteria could be dispersed in the entire cathode chamber, but when intending to use them in a membraneless (sediment type) MFC, one must immobilize them on the cathode to avoid mixing with the microbes from the anode.

In this paper it has been proposed a method of generating high oxygen concentration near the cathode surface without consuming electrical energy and reducing oxygen diffusion to the anode.

The immobilized cyanobacteria *Synechocystis* sp. AICB 51 on the cathode was investigated as a photosynthetic oxygen supplier in both two-chamber and membraneless MFC.

The *Synechocystis* sp*.* AICB 51 strain is a mesophilic unicellular cyanobacteria able to use the inorganic carbon added in the growth medium as NaHCO3 (Zarrouk medium), described in [10]. The optimal growth temperature is 30° C in fluorescent light, but they also develop a good growth at a lower temperature [11].

RESULTS AND DISCUSSION

Two-Chamber MFC

Any effects of lighting cycles on the microbial flora in the anode chamber were excluded by wrapping the anode chambers in aluminum foil (constant darkness). This also prevents any oxygenic photosynthetic organisms that may be present in the anode sludge from generating oxygen and draining electrons from the outer circuit [12]. Therefore, the evolution of the power density is only influenced by the cathode lighting conditions.

The generated power density (PD) and the dissolved oxygen (DO) at the A1 cell cathode are represented in Figure 1. It is clear that the DO closely follows the light/dark cycles, proving that it is produced via photosynthesis by the immobilized cyanobacteria.
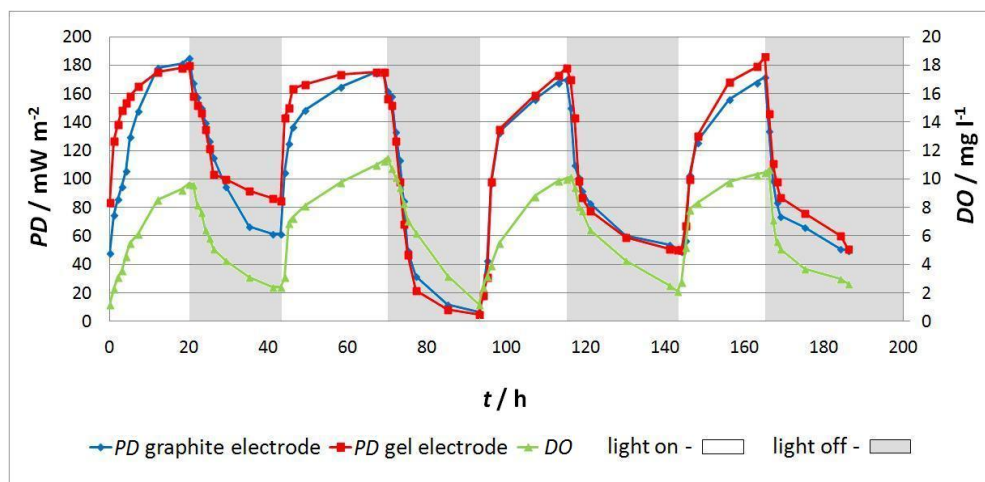
Figure 1. PD and DO during the light/dark cycles: two-chamber MFC (cell A1). Two electrodes were present in the cathode chamber: a graphite electrode and an electrode coated in cyanobacteria immobilized in gel

DO increases from 1 mg l^{-1} when dark to 11 mg l^{-1} when illuminated. The power density, in turn, closely follows the DO concentration. The power densities have comparable values for the immobilized *Synechocystis* cathode and the reference cathode.

In the control experiment represented in Figure 2, the DO reached 7.4 mg l^{-1} and the PD oscillated slightly around 130 mW m^{-2}. In the cell A1 cathode chamber, the DO concentration varied between 0 and 11.5 mg l^{-1}, under the influence of the light cycles. Whenever the DO in A1 reached 7 mg l^{-1} (like in the control experiment), the power output was also similar to that of the control cell (140-160 mW m^{-2} compared to the 130 for the control cell). However, at the end of the light on period, the PD was 30% higher and the DO was 57% higher than the corresponding values in the control experiment.
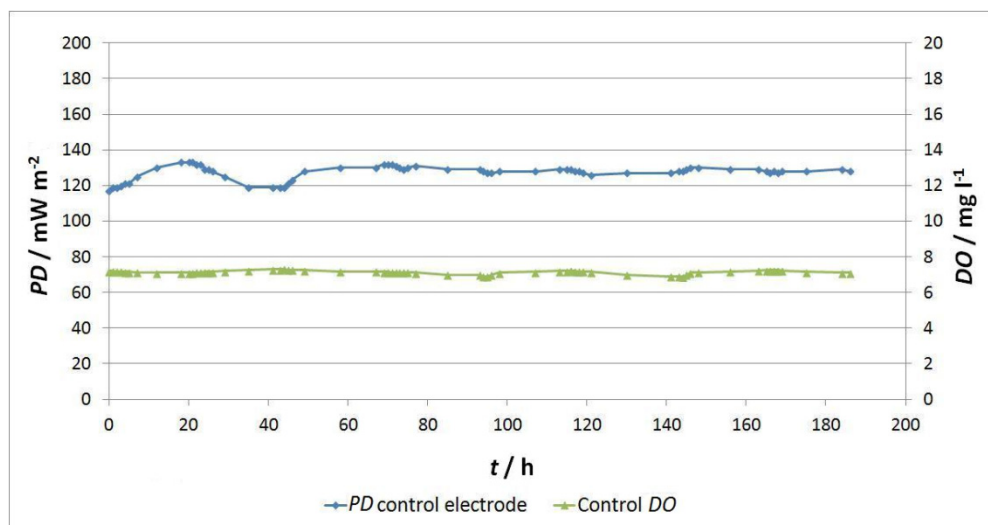
Figure 2. *PD* and *DO* in the control experiment, i.e. oxygen provided by bubbling air at the graphite cathode – two-chamber MFC (cell A0)

Membraneless MFC

It has been observed that the DO and PD dependencies on the light/dark cycles for the membraneless MFC are similar to that of the two-chamber MFC, Figure 3.

The DO produced via photosynthesis varies between 0.2 mg l^{-1} and 4.5 mg l^{-1} and in the control experiment DO reaches 5.5 mg l^{-1}. The PD in the control experiment is 15 mW m^{-2}, greater than that of the graphite electrode at the end of light on period (2 – 8 mW m^{-2}), but far less than the 45 – 60 mW m^{-2} of the immobilized *Synechocystis* cathode, Figure 4.

The immobilized *Synechocystis* had a notable effect on the power density of the gel electrode in the membraneless MFC. During the illumination period, the PD generated by the gel electrode was 8 to 20 times greater than that generated by the graphite electrode.

Figure 3. PD and DO during the light/dark cycles – membraneless MFC (cell M1). There are two cathodes: a graphite and an immobilized *Synechocystis* in gel cathode

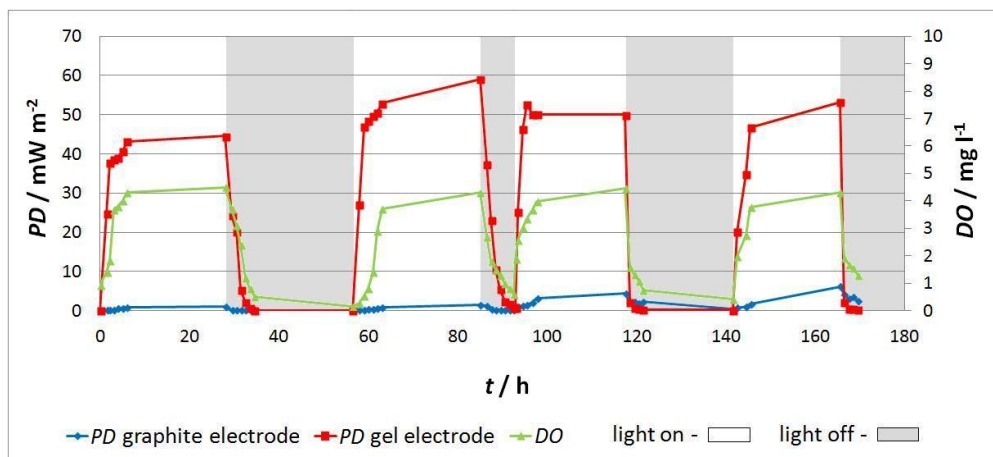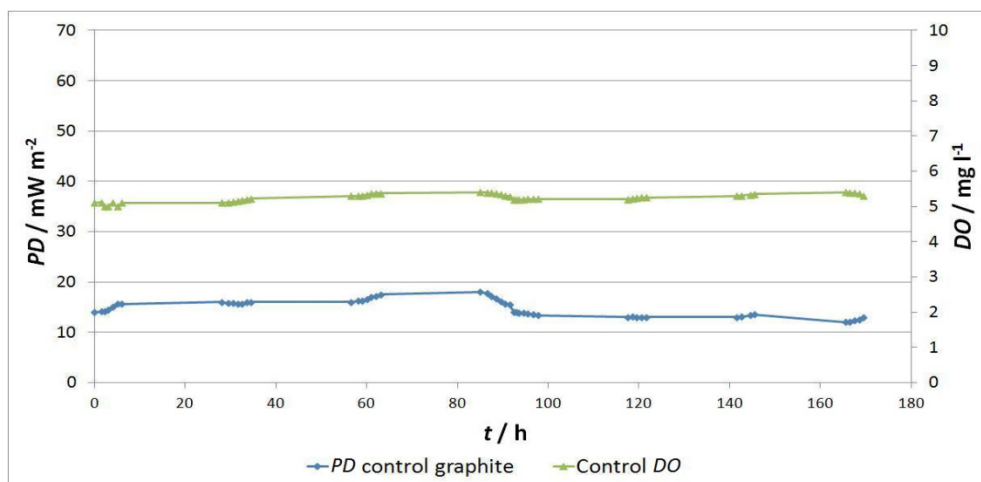**Figure 4.** *PD* and *DO* in the control experiment, i.e. oxygen provided by bubbling air at the graphite cathode – membraneless MFC (cell M0)

Despite the decrease in coulombic efficiency determined by the high concentration of DO at the cathode, because of the increase in diffusion of oxygen to the anode [1] [13] [14], the power density will increase along with the DO. It can thus be inferred that in the case of the membraneless MFC, in the gel containing *Synechocystis*, the DO is considerably higher than in the bulk liquid which surrounds the two cathodes. In what regards the two-

chambered MFC, a difference between the power densities produced by the two cathodes cannot be observed. As a result it can be presumed that for the two-chambered MFC the DO is in equilibrium at the gel zone and at the bulk liquid which surrounds the two cathodes (both cathodes present the same concentration of DO).

The DO for the membraneless MFC is higher in the gel than in the bulk liquid which surrounds the two cathodes due to the consumption of oxygen by the anode bacteria.

CONCLUSION

In two MFCs geometries, bubbling air was successfully replaced by photosynthesizing *Synechocystis* immobilized on the cathode. The gel matrix allowed the photosynthesized oxygen to flow in the catholite: in the case of two-chamber cells, the *DO* is at equilibrium between the gel and the catholite, whereas in the case of membraneless MFCs, the *DO* concentration is higher in the gel than in the catholite.

High *PD* requires high *DO*, even if the coulombic efficiency decreases.

In the case of two-chamber MFCs, the power densities have comparable values for the immobilized *Synechocystis* cathode and the reference cathode because both have access to the same *DO* concentration (in equilibrium between gel and catholyte). The *PD* for the immobilized *Synechocystis* cathode, as well for the graphite cathode for A1 MFC is 30% greater than that generated in the control experiment because the *DO* concentration produced by photosynthesis was higher than that obtained through bubbling.

In the case of membraneless MFCs, the power density increases up to 20 times during illumination in the case of the immobilized *Synechocystis* cathode compared to the reference graphite cathode for the M1 MFC. The *PD* for the immobilized *Synechocystis* cathode is 3 to 4 times greater than that generated in the control experiment.

EXPERIMENTAL SECTION

Two-Chamber Cell Design

Two Plexiglas rectangular bottles (working volume of 200 ml each) were separated by a cation exchange membrane (Nafion, 90 µm thick, AlfaAesar), $3.14 cm^2$ in surface. Spectroscopically pure rod-shaped graphite electrodes (length = 10 cm, diameter = 0.6 cm) were used for both the anode and the reference cathode. A second cathode covered with immobilized Synechocystis was also present in the cathode chamber, Figure 5A). The distance between anode-cathode was 5 cm.

The anode compartment contained sludge collected from the wastewater plant of Cluj-Napoca, Romania. The cathode compartment contained Zarrouk medium.

Membraneless Cell Design

A glass cylinder with a diameter of 10 cm, a height of 15 cm and 1000 ml working volume was used for the membraneless MFC. The 4 cm thick sludge layer at the bottom of the cylinder was separated from the clear water above by a conically shaped porous cloth.

The conical porous cloth, with a hole (0.5 cm^2) in the centre, separates the sludge from the clear water and allows the gas bubbles generated to leave the sludge (Figure 5B).

The electrodes were made of 3 mm thick rectangular graphite plates. The surfaces of the electrodes were: 30 cm^2 for the anode, 8 cm^2 for the reference cathode and 11 cm^2 for the cathode covered with immobilized cyanobacteria. The distance between the anode-cathode was 5 cm. When air (oxygen) was supplied to the cathode, an aquarium pump with a flow rate of 6 l h^{-1} was used.

All the MFCs used in this study (two-chamber and membraneless) were enriched for approximately 500 days by periodically (2 days) feeding with 2 ml 1 M sodium acetate. This rhythm of feeding was found to assure a constant power yield. The MFCs were kept at room temperature and continuously loaded with an external resistance of 1 kΩ.

(A) (B)
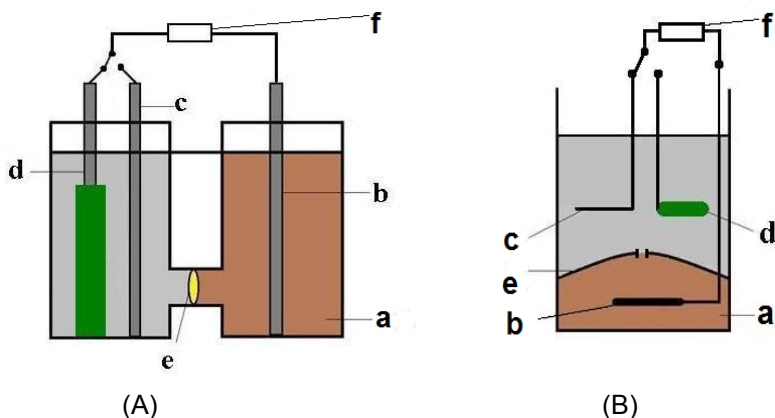
Figure 5. (A) Schematic of two-chamber MFC: a – sludge, b– graphite anode, c – graphite cathode ,d– immobilized cyanobacteria cathode, e – Nafion membrane, f – load; (B) Schematic of the membraneless MFC: a – sludge, b – graphite anode, c – graphite cathode, d – immobilized cyanobacteria cathode, e – porous cloth, f – load

Cyanobacteria immobilization on the cathode

An ideal immobilization matrix would be functional at ambient temperatures, resist in harsh wastewater conditions and allow the flow of nutrients and oxygen, while at the same time effectively immobilizing the cells within [15].

12 ml of *Synechocystis* culture ($\approx 5 \cdot 10^6$ cells ml^{-1}) were mixed with 10 ml nutritive solution containing 1% agar agar dissolved in advance through heating. The cooled mixture was poured into a mould containing the graphite cathode. After curing, the mould was removed (Figure 6). The gel thickness around the cathode was approximately 5 mm.

(A)   (B)

Figure 6. Image of the immobilized *Synechocystis* cathode and the control cathode (A) for two-chamber (B) for membraneless MFC.

The Experiment

We built one type of two-chamber cell and one type of membraneless cell, as follows:

A1 – two-chamber cell containing the reference graphite cathode and the immobilized *Synechocystis* cathode in the nutritive solution. The oxygen is generated by photosynthesis.

A0 – two-chamber cell containing the reference graphite cathode in absence of the immobilized photobiocatalyst, but with air bubbling for oxygen supply.

M1 – the membraneless type cell containing the reference graphite cathode and the immobilized *Synechocystis* cathode. The oxygen is generated by photosynthesis.

M0 – the membraneless type containing the reference graphite cathode in absence of the immobilized photobiocatalyst, but with air bubbling as oxygen supplier.

A control experiment has been developed using the A0 and M0 respectively, in order to compare MFC cells with immobilized photobiocatalyst on the cathode as oxygen supplier with standard cells without immobilized photobiocatalyst on the cathode but with air bubbling. The control cells A0 and M0 were in fact the A1 and M1 respectively, where the original cathodes were switched with the control ones.

Measurements of the power density – normalized to the projected surface of the graphite cathode – and of the dissolved oxygen in the bulk liquid at the cathode for light/dark cycles have been made. The luminous flux varied from 2500 lx (light on) to 130 lx (light off).

During the experiment, only the cathode region was subjected to light/dark cycles, whereas the anode region was wrapped in aluminum foil.

The amperage and voltage were measured with the multimeter PeakTech 3340 DMM (PeakTech Prüf- und Messtechnik GmbH Germany), and the DO was measured with Multi 350i (WTW Germany).

REFERENCES

[1] P.T. Hai, J.K. Jang, I.S. Chang, B.H. Kim, *J. Microbiol. Biotechnol*. **2004**, *14,* 2, 324.
[2] B. Logan, P. Aelterman, B. Hamelers, R. Rozendal, U. Schroder, J. Keller, S. Freguia, W. Verstraete, K. Rabaey, *Environ. Sci. Technol*. **2006**, *40*, 5181.
[3] K. Rabaey, J. Keller, *Water Science & Technology-WST* **2008**, *57*.5, 655.
[4] B.E. Logan, *Nat. Rev.Microbiol*. **2009**, *7*, 5, 375.
[5] G.T.R. Palmore, H. Bertschy, S.H. Bergens, G.M. Whitesides, *J. Electroanal. Chem*. **1998**, *443*, 155.
[6] C.A.Vega, I. Fernandez, *Bioelectrochem.Bioenerg*. **1987**, *17*, 217.
[7] B.H. Kim, I.S. Chang, G.M. Gadd, *Appl Microbiol Biotechnol* **2007**, *76*, 485.
[8] A.K. Yadav, P. Panda, P. Rout, S. Behara, A.K. Patra, S.K. Nayak, B.P. Bag, paper presented at the *XVII th International Conference on Bioencapsulation*, Groningen, Netherlands, **2009**.
[9] Z. He, L.T. Angenent, *Electroanalysis* **2006**, *18*, 19-20, 2009.
[10] N. Dragoş, L.S. Peterfi, L. Momeu, C. Popescu, *An introduction to the algae and the culture collection of algae*, CLUJ UNIV. PRESS, Cluj-Napoca **1997**, pp. 130.
[11] N. Dragoş, A. Mocan, C. Sălăjan, A. Nicoară, A. Bica, B. Drugă, C. Coman, V. Bercea, *Studia UBB. Biologia*, **2010**, *55*, 2, 51.
[12] D. Xing, S. Cheng, J.M. Regan, B.E. Logan, *Biosensors and Bioelectronics* **2009**, *25*, 105.
[13] S. Freguia, K. Rabaey, Z. Yuan, J. Keller, *Water Research* **2008**, *42*, 1387.
[14] D. Xing, S. Cheng, J.M. Regan, B.E. Logan, *Biosensors and Bioelectronics* **2009**, *25*, 105.
[14] G.C. Gil, I.S. Chang, B.H. Kim, M. Kim, J.K. Jang, H.S. Park, H.J. Kim, *J. Biosensors and Bioelectronics* **2003**, *18*, 327.
[15] D.L. Fleming, *PhD Thesis*, Virginia Polytechnic Institute and State University, Blacksburg, Virginia, **2004**.

THERMOCATALYTIC CRACKING OF KAZAKHSTAN'S NATURAL BITUMEN

YERDOS ONGARBAYEV[a,*], ANATOLII GOLOVKO[b], EVGENII KRIVTSOV[b], ERBOL TILEUBERDI[a], YERZHAN IMANBAYEV[a], BERIKKAZY TULEUTAYEV[c], ZULKHAIR MANSUROV[c]

ABSTRACT. The article shows the results of thermal cracking of natural bitumen of Kazakhstan's two deposits. The variation of the chemical and the fractional composition of the cracking products are determined depending on the process conditions. A comparative analysis of the influence of the catalyst is carried out to composition of natural bitumen.

Key words: *Cracking, natural bitumen, microspheres, di-tert-butyl peroxide, molecular weight*

INTRODUCTION

The main trends for the oil refineries is due to the need to increase the depth of oil refining and tightening environmental requirements for refinery processes and products [1]. The worlds refining is currently characterized by destocking light oils, increase the share of mining and processing of heavy oil residues and oil sands. Due to a reduction in production and appreciation of light crude matter of getting raw materials for the production of petroleum products every year becomes more urgent.

One of the growing trends in refinery residues is processing petroleum bitumen rocks. Petroleum bitumen rock should be considered as a source of natural bitumen and hydrocarbon compounds. One of the major problems associated with the processing of natural bitumen, is the high content of high-molecular compounds - resin and asphaltene molecules which concentrates most of the heteroatoms present in the feedstock [2, 3]. Number of resins and asphaltenes determines the properties as a dispersion medium, and the dispersed phase, and natural bitumen aggregate stability under thermolysis

---

[a] *Al-Farabi Kazakh National University, 71, Al-Farabi Pr., Almaty, 050040, Kazakhstan*
[b] *Institute of Petroleum Chemistry SB RAS, 4, Academichesky Av., Tomsk, 634021, Russia*
[c] *Institute of Combustion Problems, 172, Bogenbay Batyr Str., Almaty, 050012, Kazakhstan*
* *Corresponding author: Erdos.Ongarbaev@kaznu.kz*

process [4, 5]. These compounds have a high molecular weight, tend to condense and the formation of coke during the processing, deactivate the catalyst. Creating ways to deep destruction of resin-asphaltene components of heavy oil and natural bitumen will solve the basic problem of conversion of heavy hydrocarbon compounds and hydrocarbon fuels will reduce the deficit in the future [6].

Particularly noteworthy are cracking processes followed by the addition of a catalyst. One of the most perspective catalysts for cracking is microspheres, which can initiate the degradation of macromolecular components. According to the patent it is known that catalysts based on iron oxide, both synthetic and man-made origin or ore to be active in the process steam and hydrocracking of heavy petroleum feedstock [7].

The goal of the work was to conduct catalytic thermal cracking of natural bitumen of Kazakhstan and the establishment of the group and fractional composition of cracking products.

RESULTS AND DISCUSSION

One of the perspective methods for producing synthetic oil is thermocatalytic conversion of heavy hydrocarbons in the presence of catalytic additives such as iron oxides [8-10]. In thermal degradation processes of heavy oil can increase the yield of low-boiling liquid products with the formation of coke.

The object of investigation was selected sample of bitumen Munaily Mola and Beke deposits. Extracting natural bitumen was carried out in the Soxhlet apparatus by chloroform solvent. Content of natural bitumen in the rock was 12 wt. % from Beke deposit and it is as follows: ρ – 1.112 g/cm^3; congelation point is 18 °C; coking content – 30 %; ash content – 0.35 wt. %; sulfur content – 1.5%; elemental composition was C – 84.79 %; H – 11.68 %; N – 0.58 %; O – 2.02-4.04 %. Organic content of the sands from Munaily Mola deposit was 16 wt. %, It is characterized by high densities (0.992 g/cm^3), viscosity (26.0 cSt at 80 °C) and coking (35 %) [11, 12].

As seen from Table 1, the cracking of natural bitumen and liquid products formed amount of coke and gas appeared. Yield of cracking liquid products from Munaily Mola deposits was higher than in the processing of bitumen from Beke deposits for 6 wt. % and coke content was lower 4.7 wt. %. Cracking has led to increased yield of oil components and the amount of high molecular weight components of bitumen decreases: resin content was decreased. Apparently, this is caused by an increase in coke formation and destruction of resinous components to lighter products. The content of oils in the composition of the liquid cracking products from Munaily Mola deposit is more for 22 % than the bitumen of Beke deposits and content of

resin is less for 15 %, asphaltenes content is lower 7 %. These number shows that the bitumen from Munaily Mola deposit more acceptable for cracking than the bitumen from Beke deposit.

In the form of microspheres of the catalyst chosen and for cracking process was given 10 % weight mass of the catalyst. Microspheres are ferrospheres energy ashes with a high content of iron oxides. Selection ferrospheres due to the fact that they contain the iron oxide phase, represented mainly hematite and spinel ferrite, which can initiate the degradation of high molecular weight components. Ferrospheres are one of the most common types of microspheres in volatile ash from pulverized coal combustion in thermal power stations. The formation of a globular structure is a result of the thermochemical transformation of mineral coal forms droplets to form complex high-iron melts (FeO-CaO-MgO-SiO_2-Al_2O_3) macroelement of partial oxidation and crystallization phases separate on cooling.

Table 1. Material balance and composition of cracking products
of natural bitumen

Cracking conditions	S_{total} in oil, wt. %	Yield, wt. %			Composition of liquid products, wt. %		
		Gas	Liquid	Coke	Oil	Resin	Asphaltene
Natural bitumen from Beke deposit							
Natural bitumen	0.30	0.0	100.0	0.0	49.17	44.89	5.94
450 °C, 60 min.	0.43	1.4	67.7	30.9	61.29	28.27	10.44
450 °C, 60 min. with catalysis	0.34	1.3	63	35.7	60.05	32.24	7.71
450 °C, 60 min. with DTBP	0.35	1.1	70.3	28.6	63.27	24.81	11.92
Natural bitumen from Munaily Mola deposit							
Natural bitumen	0.7	0.0	100.0	0.0	47.58	46.37	6.05
450 °C, 60 min.	0.57	0.2	73.6	26.2	83.61	13.39	3.0
450 °C, 60 min with catalysis	0.64	0.5	64.8	34.7	77.53	14.39	8.08
450 °C, 60 min. with DTBP	0.65	1.5	87.6	10.9	77.07	15.23	7.71

Presence of a catalyst in a cracking process had a negative impact on the yield of liquid products and content of oil components: for bitumen both of deposits yield of liquid products decreased, and yield of coke increased for 4-8 %. Oil content decreased, while the total amount of resin-asphaltene components increased for 1 and 6 %, respectively, for the bitumen from Beke and Munaily Mola deposits. Catalyst intensified condensation and consolidation reaction in cracking products.

One of the methods to achieve a more profound transformation of resin-asphaltene components to target products and as a consequence, increase the yield of distillate fractions in the cracking process is a radical-additive component, which are the initiators of radical chain processes of low-temperature cracking. Di-tert-butyl peroxide (DTBP) was added 3 wt. % as the radical-additive addition. This organic peroxide initiates the reaction to the destruction of high-molecular compounds and provides to yield of light products.

The addition of peroxide favorably influenced the cracking process: the yield of liquid products is increased; especially in the case of cracking bitumen increasing was 14 % from Munaily Mola deposit. Yield of coke is reduced; in this case the decrease was 15 %. In part of the liquid cracking products of bitumen from Beke deposits content oil components increased for 2 %, the amount of resin content decreased for 3.4 %. However, the processing of natural bitumen from Munaily Mola deposits despite the significant increase yield of liquid products is showed a decrease the amount of oil and the increase content of resin-asphaltene substances. It appears that the cracking with radical-additive addition involved not only resins and asphaltenes for degradation processes, but also the oil molecules.

After the thermal and catalytic thermal processing of natural bitumen of oil sands from Munaily Mola and Beke deposits were investigated fractional composition of the obtained products. Results of the analysis on the fractional composition of the obtained products are major importance for the study, as the basis of these data we can judge the depth of processing of the bitumen.

Analysis of the fraction composition of the bitumen cracking products (Table 2) showed that a reduction the boiling point fractions under cracking as compared with the initial bitumen. The cracking of bitumen from Beke deposits elevation of boiling point – 360 fractions observed in the case of the catalyst, while the number of fractions of B.p.-200 °C increased for 11 %, the fraction in the range of 200-360 increased for 6.6 %. Cracking bitumen from Munaily Mola deposits in all cases leads to the increase the B.p.-200 fractions, indicating an increase in the proportion of destructive processes in the reaction medium. Here, the maximum increase in the content of light fractions occurred during the cracking of bitumen without addition of catalyst and peroxide: the fraction of B.p.-200 increased for 7.1 %, and the fractions 200-360 increase for 18.6 %. The presence of a catalyst and an initiator additive resulted to higher contents of such light fractions.

Gas composition of cracking products was determined by gas adsorption chromatograph. The main gaseous cracking products include methane, that its content greater than 30 wt. % of Beke deposit and another deposit from

Munaily Mola deposit is more 10 wt. % of methene, in addition has ethane, propane, iso-butane and hydrogen (Table 3). Hydrogen content after cracked gases is 2.5-4.5 wt. %.

Table 2. Fractional composition of cracking products of natural bitumen

Sample	$T_{b.p.}$, °C	Composition, wt. %		
		B.p.-200	200-360	> 360
Natural bitumen of Beke deposit				
Natural bitumen	116.8	5.1	20.2	74.7
After cracking	77.9	2.3	18.9	78.8
With catalysis	73	16.1	26.8	57.1
With DTBP	77.4	4.9	14.6	80.5
Natural bitumen of Munaily Mola deposit				
Natural bitumen	96.5	2.2	15.6	82.2
After cracking	92	9.3	34.2	56.5
With catalysis	75	7.1	23.3	69.6
With DTBP	82.7	6.5	21.4	72.1

Table 3. Gas composition of cracked products

Gas	Composition, wt. %					
	Munaily Mola			Beke		
	After cracking	With catalyst	With DTBP	After cracking	With catalyst	With DTBP
H_2	4.53	4.16	4.1	2.71	2.97	2.53
O_2	3.43	3.59	5.69	3.86	4.84	3.19
N_2	13.43	15.81	24.57	22.78	22.38	15.55
CH_4	24.39	24.93	21.97	30.28	35.87	33.14
C_2H_6	17	13.33	9.16	10.14	11.62	8.12
CO_2	24.79	28.56	19.18	23.77	14.22	16.99
C_3H_8	8.88	7.15	6.8	5.16	6.34	5.26
$i-C_4H_{10}$	2.05	1.41	7.93	0.76	0.97	14.53
$n-C_4H_{10}$	0.08	0.05	0.04	0.03	0.04	0.03
$i-C_5H_{12}$	0.96	0.69	0.32	0.3	0.36	0.4
$n-C_5H_{12}$	0.46	0.32	0.24	0.19	0.32	0.18

Molecular weight of asphaltenes of natural bitumen and cracking products was measured by method cryoscopies in naphthalene in installation "Kryon" that is created in IPC SB RAS. The thermolysis is lead to a deep changing of the structural characteristics of average molecules of asphaltenes

than in subcritical conditions (Table 4). Asphaltene molecules more destroyed by addition of a catalyst to produce lighter products such as: coke, gas and resin compounds.

Table 4. Molecular weight of asphaltenes of natural bitumen (NB) and cracking products

| Sample	Asphaltenes of NB from Munaily Mola deposit	Asphaltenes of NB from Beke deposit
Natural bitumen	1803	2044
After cracking	677	1304
With catalysis	1045	1003
With DTBP	869	1042

CONCLUSIONS

The heat treatment bitumen of Beke deposit leads to deterioration fraction and composition of liquid cracking products, and quality of products from cracking bitumen of Munaily Mola deposits – conversely improved (increasing the amount of oil is increased to three times the amount of gasoline fraction and 10 wt. % diesel fraction). In both cases there was a decrease resin and coke formation.

Microspheres addition, as a catalyst for the cracking of natural bitumen coke formation led to an increase, and decrease in the amount of oil and reduce the start of boiling point of liquid products (compared with the composition of products of thermal cracking). The total content of distillate fractions (B.p.-360) as part of the cracking products of bitumen with the addition of microspheres does not differ from gasoline fraction, with increasing amounts of gasoline fractions of 2-5 wt. %. The amount of oils is increased by 3 to 6 wt. %.

The presence of additives di-tert-butyl peroxide reduces coke formation in the cracking of bitumen (Beke deposits - 2.3 % Munaily Mola - 15.3 wt. %) compared to the thermal cracking products. The content of distillate fractions in products initiated cracking bitumen of Beke deposit minimally probably di-tert-butyl peroxide more initiates the condensation reaction of components of the bitumen. In the composition of liquid purged initiated cracking of bitumen from Munaily Mola deposits dominated oil. The number of fractions of B.p.-360 products initiated cracking bitumen from Munaily Mola deposits larger than the content in the initial bitumen and the cracking products from the microspheres, but less than at thermal cracking of bitumen. It should be noted that the reduction of coke formation has led to an increase of 20 wt. % of residual fractions (>360 °C), which are source for oil distillates.

EXPERIMENTAL SECTION

The scheme of the cracked experiment and analysis of the products is shown in Figure 1.
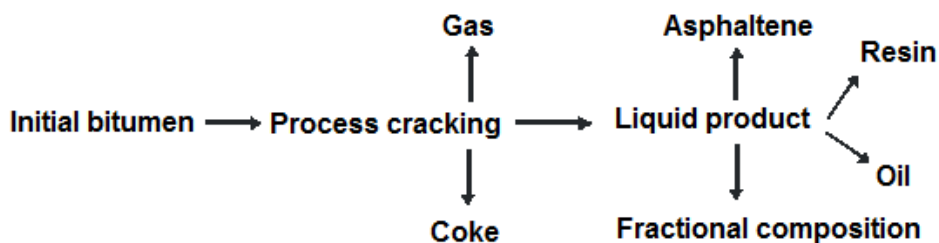
Figure 1. Scheme of the experiment

Both of natural bitumen was extracted from oil sands by chloroform solvent in Soxhlet apparatus. Then cracking process was carried out in bitumen autoclave reactor of 12 cm^3; the bitumen was weighed 7 g cracking duration of 60 minutes at a temperature of 450 °C. After the thermolysis samples from the reactor were quantitatively extracted, then yield of gas, liquid cracking products and content of coke were determined. Group composition of the initial bitumen and liquid cracking products installed on the traditional pattern: determine the content of asphaltenes in the sample by "cold" method Golde. Asphaltene sample solution in hexane settled for 16 hours in the dark at ambient temperature. In a conical funnel expose filter blue ribbon. The pooled sample solution in hexane without stirring carefully filtered through filter paper. For extraction of asphaltene compounds is carried out with filter paper extraction of benzene in a Soxhlet apparatus. The benzene extract was transferred into content of asphaltenes round bottom flask, and benzene is evaporated on a rotary evaporator. Content of asphaltenes with small amount of chloroform solvent transferred into a Petri dish and dried to solidness. Obtained asphaltene compounds should be brittle and shiny and black and brown color.

Maltenes, solution in hexane was placed in a round bottom flask and the hexane was distilled off. The concentrate maltenes small amount of hexane is applied at a Soxhlet apparatus with silica gel ASK marks. Apparatus was placed in a water bath and extracted oil (concentrate hydrocarbons) as long as in the flask of a Soxhlet apparatus will not drain the pure solvent hexane. Then replace the receiver flask with hexane solvent to pure ethanol-benzene mixture, the ratio of mixture was 1:1. Desorption from silica gel resins produced as long as there is no drain of pure ethanol-benzene mixture.

Extract of ethanol-benzene containing resin, solvent removed on a rotary evaporator. Resins with a small amount of the ethanol-benzene mixture was transferred to a Petri dish and dried to solidness (STF technique SZHSHI 1217-2005, IPC SB RAS).

Content of distillate fractions in the initial bitumen and cracking products was estimated by thermogravimetric analysis. Thermogravimetric analysis was performed in air derivatograph MOM (Hungary), which allows to fix the weight loss of the sample with the analytical sample with rising temperature till 350 °C at a heating rate of 10 degree/min.

REFERENCES

1. B. Joshi, A.B. Pandit, *Industrial Engineering & Chemical Research,* **2008**, *47*, 23, 8960.
2. Y. Ma, S. Li, *Fuel Processing Technology*, **2012**, *100*, 11.
3. A.S.M. Junaid, C. Street, W. Wang, M.M. Rahman, W. An, W.C. McCaffrey, S.M. Kuznicki, *Fuel*, **2012**, *94*, 457.
4. P. Murugan, N. Mahinpey, T. Mani, *Fuel Processing Technology*, **2009**, *90*, 1286.
5. S. Hossan Firoozifar, S. Foroutan, S. Foroutan, *Chemical Engineering Research and Design*, **2011**, *89*, 2044.
6. M.A. Kopytov, A.K. Golovko. *Izvestia of Tomsk Technical University*, **2009**, *315*, 3, 83 (in Russian).
7. L.I. Kizilshtein, I.V. Dubov, A.L. Shpiysgluz, S.G. Parada, "Components of ash and slag in TPP", Energoatomizdat, **1995**.
8. Tadashi Murakami, Teruo Suzuka, Yukio Inoue, Shirou Aizawa. USA Patent 4421635. **1983**.
9. E.G. Teliashev, R.R. Vezirov, I.O. Tuktarova, G.G. Teliashev, R.B. Valitov, S.N. Khadzhiev, V.N. Karakuts, U.B. Imashev. USSR Patent 1824422, **1993**.
10. F.R. Sultanov, Ye. Tileuberdi, Ye. K. Ongarbayev, Z.A. Mansurov, K.A. Khaseinov, B.K. Tuleutaev, F. Behrendt, *Eurasian Chemico-Technological Journal*, **2013**, *15*, 1, 77.
11. E.K. Ongarbaev, E. Tileuberdi, B.K. Tuleutaev, Z.A. Mansurov. *Neftepererabotka i neftehimia,* **2013**, *3*, 12.
12. Ye. Tileuberdi, Ye. Ongarbaev, B. Tuleutaev, Z. Mansurov, F. Behrendt. *Applied Mechanics and Materials*, **2014**, *467*, 8.

DESIGN OF ADSORPTIVE DISTILLATION FOR SEPARATION OF ETHANOL-WATER AZEOTROPIC MIXTURE USING BIO-BASED ADSORBENTS

FARIBA TADAYON[a,*], FERESHTEH MOTIEE[a], ATENA ERFANI[a] and BABAK RONAGH BAGHBANI[a]

ABSTRACT. Ethanol is an important and commonly used solvent. Anhydrous ethanol is widely used in painting, medicine, cosmetics, perfume and chemical industries. Use of recyclable and cheaper alternatives such as bio-based adsorbents that are composed of cellulose and starch which exhibit strong affinity to water, is already developed as a part of purification and filtration process. A new design of setup for adsorptive distillation was used in this paper to separate water from ethanol due to its low energy consumption. Six raw materials namely sweet potatoes, sticky rice, corn, corn cobs, crystal sugar and date pits were evaluated for their efficiency of ethanol dehydration. Among the biobased adsorbents examined, sweet potato and sticky rice adsorbents due to higher starch consisted of amylopectin gave the best separation of ethanol-water azeotrope. By means of the selective water adsorption that was carried out in a fixed-bed adsorber packed with sticky rice and sweet potato, 99.9% anhydrous ethanol with high efficiency is obtained.

Keywords: biobased adsorbents, adsorption, adsorptive distillation, azeotrope, ethanol dehydration

INTRODUCTION

Ethanol is considered as one of the most important organic chemicals in the world. Anhydrous ethanol is widely used in industries, such as pharmaceuticals, organic syntheses, painting, cosmetics, perfumes and it can also be used as an additive to the diesel fuels that helps enhancing the octane number and combustibility of gasoline [1, 30]. Ethanol is produced through the anaerobic fermentation of sugars, which can be obtained from

---

[a] *Department of Chemistry, North Tehran Branch, Islamic Azad University, Shariati str., Postal Code: 1913674711, Tehran, Iran*
* Corresponding author: Fariba.tadayon@hotmail.com

a variety of biomass. Production of anhydrous ethanol poses a technological problem, because of the notorious azeotrope formation at 78.15 °C and 1.013 bar, with 4.4% of water that cannot be removed by a normal distillation [2-5].

Various techniques have been developed to break the azeotrope of ethanol and water mixture, such as azeotropic distillation, extractive distillation, pervaporation and adsorptive distillation. In azeotropic and extractive distillation, dehydration is performed in the presence of entrainers such as benzene and ethylene glycol. However benzene, as being a highly carcinogenic substance, is a major health concern.

Furthermore, these distillation methods have a high energy requirement [6-10]. A membrane process known as pervaporation is a separation technology which involves the transition of ethanol through a membrane and it is a cheaper alternative to distillation methods. The disadvantage of pervaporation is low water capacity [11]. However, the energy efficiency can be improved by integrating a common distillation process with a pertinent adsorption system [31]. Among separation methods of azeotrpic mixtures, adsorptive option offers a simple alternative process and due to its energy saving is mainly attractive [12-14]. Low operation costs, high efficiency, as well as a wide variety of selective sorbents make the adsorption method an appealing choice for separation purposes.

The adsorbents used for adsorptive distillation is various, ranging from organic starch [15-18] to inorganic zeolites [19-22]. Dehydration of ethanol using a fixed-bed adsorbents with type A molecular sieves is a well known process [23]. However, molecular sieves are expensive and can only be discarded after being saturated with water, which makes the process uneconomical. Hence, an increasing interest has been focused on the cheaper and recyclable adsorbents. It has been proved that bio-based adsorbents, in particular those composed of cellulose and starch, can adsorb and remove water from alcohol vapors [24-26, 14, 32]. Because of polar attraction between water molecules and the hydroxyl groups on the starch chains, water can adsorb on the adsorbent stronger than ethanol [27, 15, 33].

In addition, The advantages of these starch-based adsorbents in Uptake of water from ethanol-water mixture includes re-use of materials in fermentation, biodegradability, efficiency, relative availability, and cheapness, non-toxic nature and its derivation from renewable sources [34]. Their regeneration also requires less energy [35]. The objective of this work is the development and use of new bio-based desiccants that are able to separate the azeotropic water–ethanol mixture for producing the fuel grade ethanol (>99.9% w/w).

RESULTS AND DISCUSSION

### Characterization and structure of bio-based materials

Starch is the principal polysaccharide produced in plants as a way of storing energy. It exists in two forms: amylose and amylopectin. Both are made from α-glucose. Amylose is an unbranched polymer of α-glucose. The molecules coil into a helical structure. It forms a colloidal suspension in hot water. Amylopectin is a branched polymer of α-glucose. It is completely insoluble in water [28]. A major mechanism for the selective adsorption of water is known to be the interaction of water molecules with the hydroxyl groups of the adsorbent. Both kinds of starch chains, amlylose and amylopectin, interact with water molecules in this way. Based on the mechanism of adsorption of water, different functional groups present in bio-adsorbents were evaluated.

It was found, sweet potato has the high proportion of starch (amylose and amylopectin), sticky rice displays amylopectin and corn represents amylose. Corn cobs have hydroxyl and carboxyl, crystal sugar is a single carbohydrate and content of date pits are hydroxyl, fructose, sucrose and D-glucose.

Design of adsorption system

As shown in Figure 1, a fixed-bed adsorber apparatus was designed. This system consisted of a glass tube (column) with an internal diameter of 25 mm and a height of 20 cm. The different natural adsorbents were packed in this tube. The column was sited on a flask within the water bath. A water pump was sited into another water bath that circulates hot water around the glass tube to avoid condensation. A vacuum tee was placed on the graded u tube and the tube was placed on the column and finally in order to suck the vapors, the whole system was connected to a vacuum pump. As soon as vapor was generated from the flask, ethanol-water vapor enters a column which is packed with adsorbent via vacuum pump. Then water molecules start diffusing through the pores of the adsorbent and were adsorbed by adsorbents. The stream coming from the adsorbed was condensed after coming in contact with the cold pipe wall.

The final purified product was taken from the bed once every two minutes and a volume of about 5 ml was collected. The samples were analyzed by gas chromatography. A column packed with GDX-203 was used in a gas chromatography to analyze the composition. Analysis at 120 °C was monitored by a thermal conductivity detector. At the end of the experiment, the adsorbent was removed from the bed and dried for further use. The adsorbents were efficient after 3 cycles of the process.
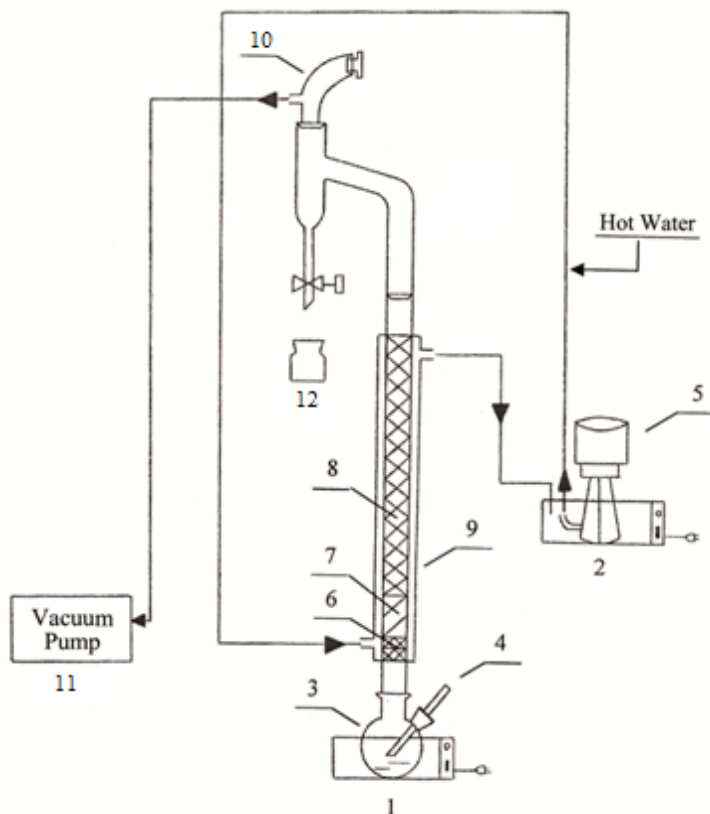
Figure 1. Schematic diagram of fixed-bed adsorption system: (1,2) electric hot plate waterbath; (3) boiling flask; (4) thermocouple; (5) water pump; (6) stainless steel wire guaze; (7) quartz sand; (8) adsorbent; (9) glass tube; (10) vacuum tee; (11) vacuum pump; (12) sample

Initial conditions

The column was filled and packed with 10 g of the different bio-based adsorbents. In this regard, all adsorbents were tested in adsorption experiments under the same condition to select the best materials. The bottom temperature of the tower was 78 °C, fixed-bed temperature 82 °C and feed concentration 96 wt%.

By GC method, the breakthrough curves of six raw materials are illustrated in Figure 2. It can be seen that among the different bio-based adsorbents examined, maximum ethanol concentration was obtained by sweet potato and sticky rice. Thus, sweet potato and sticky rice were chosen as basic materials to achieve the best results.
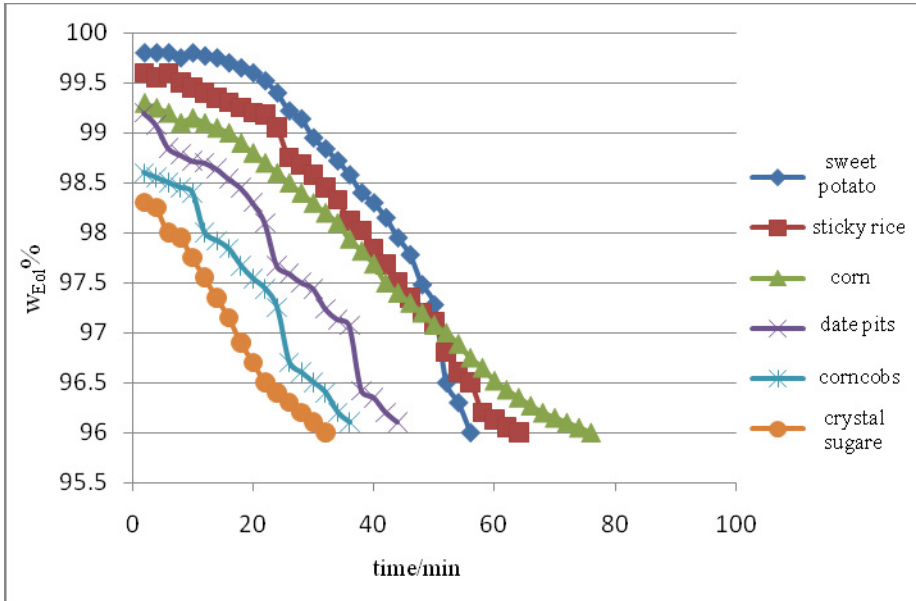
Figure 2. Breakthrough curves of variable natural materials for ethanol/water

      The UV-Vis spectrophotometric determination of water content in alcohol was developed based on the color change in the reaction of cobalt (II) chloride ($CoCl_2$) with water [29]. The calibration curve for standard ethanol solutions of $CoCl_2$ *versus* water content is shown in Figure 3.

$$y = -21.829x + 0.9872$$
$$R^2 = 0.9991$$
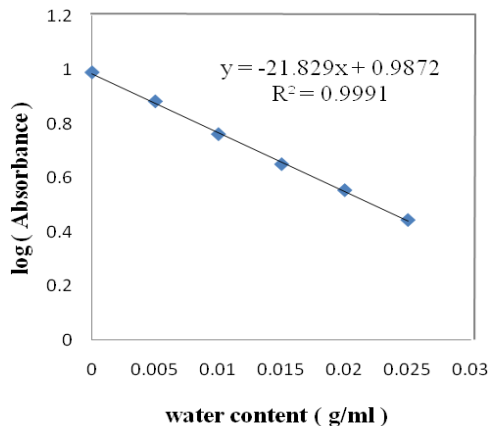
Figure 3. The standard plot of the $log(A_{656})$ versus water content in ethanol solution containing $CoCl_2$ (9.52 $\times$ 10^{-3} mol/L)

As shown in Fig.3, the calibration curve was prepared by dissolving standard solutions of $CoCl_2$ (9.52×10^{-3} mol/L) in ethanol solvent with different amounts of added water. The absorbance at $\lambda_{max} = 656$ nm decreased with water content and good linear relationships were obtained between the logarithm of the absorbance at $\lambda = 656$ nm of $CoCl_2$ and the water concentration in ethanol with 0.999 as good coefficient of correlation. The results are presented in Table 1.

Examining different amounts of sweet potato and sticky rice adsorbents

Experiments in this section include the following steps:

Increasing the amount of adsorbent: Column was packed with increasing the amount 10 g to 20 g of natural adsorbents.

Using discrete columns: The column was filled with 20 g of sweet potato and the sample was passed through the adsorbent. The sample was once again passed through the column which this time was filled with sticky rice. The final sample was collected after this stage.

Mixing the adsorbents: In this part, column was packed with adsorbents via two kinds of mixing status: i) Blending 6 g of sticky rice and 14 g of sweet potato. ii) Blending 8 g of sticky rice and 12 g of sweet potato. The results are indicated in Figure 4 and Figure 5, respectively.
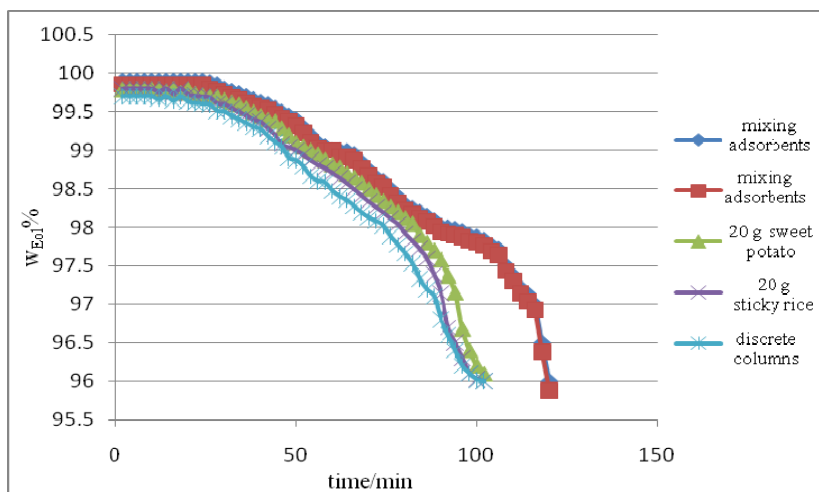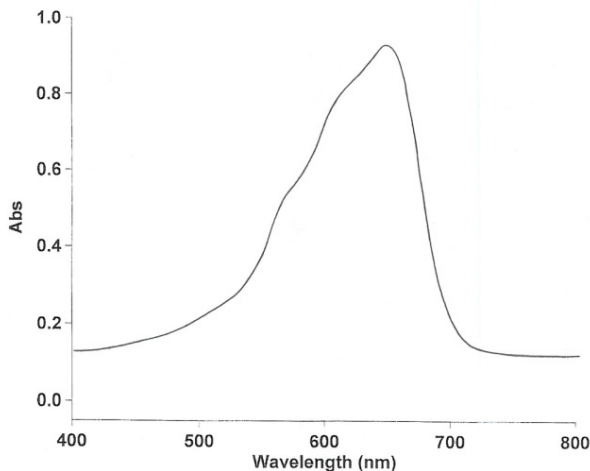

Figure 4. Breakthrough curves of the selective materials for ethanol/water

Figure 5. Vis absorption spectrum of $CoCl_2$ in ethanol solution
in the presence of 0.1% water.

As seen in figure 5, water content in the organic solvent caused the evident presence of peak around 656nm. This $CoCl_2$ solution absorbed red light, while the organic solvent solutions of $CoCl_2$ were blue green.

According to the results, compared to other parts, mixing the adsorbents part due to higher starch and protein content of amylopectin gave the best separation of ethanol-water system and 99.9% anhydrous ethanol was obtained with high efficiency.

Among the reported methods, the UV-VIS spectrophotometric method is a simple, rapid, reproducible and environmentally friendly method. This method had been applied in determination of the water content in some organic solvents with good reproducibility, high sensitivity on 1% as the relative standard deviation and 0.001 g/ml as detection limit. This method has great application in the determination of water content in raw materials, basic chemicals, cosmetics, drugs, foodstuffs, biological samples, petrochemical products, paints, solvents, gaseous samples, etc. In addition, other method for determining water content, such as gas chromatography, is an expensive apparatus, which could determine the water content simply and rapidly.

It can be concluded from data of Table 1 that among the different bio-based adsorbents examined, sweet potato and sticky rice adsorbents gave the desirable separation of ethanol-water system. However, In order to achieve the best results, experiments were tested on two adsorbents.

Table 1. Water content in different biobased adsorbents

Adsorbents	C_{water} (g/ml)	Water content (UV-Vis)
Sweet potato	0.0043	0.43 %
Sticky rice	0.0021	0.21 %
Corn	0.008	0.80 %
Corncobs	0.0140	1.39 %
Crystal sugar	0.0170	1.73 %
Date pits	0.0102	1.02 %

The size of sieved starch-based materials are indicated in below Table 2.

Table 2. Particle size of adsorbents

Adsorbents	Mesh. No	Mean Diameter (mm)
Corn	40 - 80	0.420 – 0.177
Corncobs	70 - 120	0.210 – 0.125
Crystal sugar	40 - 120	0.420 – 0.125
Date pits	70 - 120	0.210 – 0.125
Sticky rice	40 – 120	0.420 – 0.125
Sweet potato	80 – 120	0.177 – 0.125

CONCLUSIONS

A new, simple alternative and, inexpensive process as adsorptive distillation was developed for ethanol drying. The results of water sorption on six starch-based materials showed that sweet potato and sticky rice were found to be more affinitive for water than other biobased adsorbents. The optimum condition was achieved by mixing adsorbents which yielded 99.9% anhydrous ethanol with high efficiency. Furthermore, the proposed technique is more efficiency than other methods and plays a crucial role for separation of ethanol-water system.

EXPERIMENTAL SECTION

Materials and methods

All raw materials used as natural bio-based adsorbents namely sweet potatoes, sticky rice, corn, corn cobs, crystal sugar and date pits were of food quality and purchased in the market. Chemicals such as ethanol 99.9% (absolute), ethanol 96% were purchased from Scharlau Chemie (Spain) and 2-propanol, cobalt(II) chloride ($CoCl_2$) were provided from Merck (Germany). Gas chromatography (Shimadzu GC-17A) and UV-Vis spectrophotometer (Varian, cary 100 Bio, USA) techniques were used in this work.

Preparation of adsorbents

Sweet potatoes, sticky rice, corn, crystal sugar were dried in a vacuum oven at 90 oC for 12 h. Date pits were washed with distilled water and then dried in an oven at 80 oC for 24 h. Corncobs were cut into small pieces and washed with distilled water and then dried in a packed bed using nitrogen at 90 oC for 6 h. This was to ensure that no biological debasement happened to the polysaccharides of corn cobs [16]. All the materials were then milled and sieved into different particle size with shaker. The biobased adsorbents were kept in bottles, which contained with silica gel.

ACKNOWLEDGMENTS

SI Units and Symbols

Symbol	Unit	Deffinition
cm	centimeter	distance
oC	degree Celsius	temprature
g	gram	mass
h	hours	time
mm	millimeter	distance

REFERENCES

1. K.T. Xu, Distillation Processes of Alcohol, China Light Industry Press, **1998**, 356.
2. Y. Morigami, M. Kondo, J. Abe, H. Kita, K. Okamoto, *Separation and Purification Technology*, **2001**, *25* (1-3), 251.
3. D. Shah, K. Kissick, A. Ghorpade, Hannah. R, D. Bhattacharyya, *Journal of Membrane Science*, **2000**, *179* (1-2), 185.
4. M. Nomura, T. Bin, S. Nakao, *Separation and Purification Technology*, **2002**, *27* (1), 59.
5. F.M. Lee, R.H. Pahl, US Patent, 4, 559, 109; **1985**.
6. J. Guan, X. Hu, *Separation and Purification Technology*, **2003**, *31* (1), 31.
7. S. Jain, A.S. Moharir, P. Li, G. Wozny, *Separation and PurificationTechnology*, **2003**, *33* (1), 25- 43.
8. H. Ahn, S. Brandani, *Adsorption*, **2005**, *11* (2), 113.
9. M. Simo, C.J. Brown, V. Hlavacek, *Computers & Chemical Engineering*, **2008**, *32* (7), 1635.

10. J.H. Kim, D.H. Lee, S.K. Hong, S.J. Park, *Chemical Engineering Research*, **2008**, *46* (2), 348.
11. J. Neel, Membrane Separation Technology. Principles and Applications, Elsevier, Amsterdam, **1995**, Chapter 5.
12. R.B. Derr, US Patent, 2,137,605, **1937**.
13. F.A. Banat, F.A. Abu Al-Rub, J. Simandl, *Separation and Purification Technology*, **2000**, *18* (2), 111.
14. A.A. Hassaballah, J.H. Hills, *Biotechnology and Bioengineering*, **1990**, *35* (6), 598.
15. J.Y. Lee, P.J. Westgate, M.R. Ladisch, *American Institute of Chemical Engineers Journal*, **1991**, *37* (8), 1187.
16. P.J. Westgate, M.R. Ladisch, *Industrial & Engineering Chemistry Research*, **1993**, *32* (8), 1676.
17. K.E. Beery, M.R. Ladisch, *Industrial & Engineering Chemistry Research*, **2001**, *40* (9), 2112.
18. M.J. Carmo, M.G. Adeodato, A.M. Moreira, E.J.S. Parente, R.S. Vieira, *Adsorption*, **2004**, *10* (3), 211.
19. J. Weitkamp, S. Ernst, B. Gunzel, W.D. Deckwer, *Zeolites*, **1991**, *11* (4), 314.
20. F.A. Farhadpour, A. Bono*, Chemical Engineering Progress*, **1996**, *35* (2), 141.
21. M. Nomura, T. Yamaguchi, S. Nakao, *Journal of Membrane Science*, **1998**, *144* (1-4), 161.
22. M.J. Carmo, J.C. Gubulin, *Adsorption*, **2002**, *8* (3), 235.
23. B. Sowerby, B.D. Crittenden, *Gas Separation & Purification*, **1988**, *2* (2), 77.
24. M.R. Ladisch, K. Dyck, *Science*, **1979**, *205* (4409), 898.
25. M.R. Ladisch, M. Voloch, J. Hong, P. Bienkowski, G.T. Tsao*, Industrial and Engineering Chemistry Process Design and Development*, **1984**, *23* (3), 437.
26. P.R. Bienkowski, A. Barthe, M. Voloch, R.N. Neuman, M.R. Ladisch, *Biotechnology and Bioengineering*, **1986**, *28* (7), 960.
27. J.Y. Lee, M.R. Ladisch, Polysaccharides as Adsorbents: an Update on Fundamental Properties and Commercial Prospects, Henniker, NH, USA, Acad of Sciences, New York, USA, **1987**, pp. 492–498.
28. D.M. Ruthven, Principles of Adsorption and Adsorption Processes, Wiley, New York, **1984**.
29. H.X. Bai, X.R. Yang, *Journal of the Chinese Chemical Society*, **2007**, *54* (3), 619.
30. J.C. Diaz, I.D. Gil-Chavez, L. Giraldo and J.C. Moreno-Pirajan, *E-journal of Chemistry*, **2010**, *7*(2), 483.
31. Y. Kim, R. Hendrickson, N. Mosier, A. Hilaly and M.R. Ladisch, *Industrial & Engineering Chemistry Research,* **2011**, *50*, 8678.
32. T. Baylak, P. Kumar, C. H. Niu and A. Dalai, *Energy and Fuels*, **2012**, *26*, 5226.
33. A.N. Anozie, E.E. Okuhon, F.N. Osuolale and J.K. Adewole, *Separation Science and Technology*, **2010**, *45*, 1482-1489.
34. A.O. Okewale, B.R. Etuk, P.K. Igbokwe, *International Journal of Engineering & Technology*, **2011**, *11*(*6*), 81-91.
35. Y. Wang, C. Gong, J. Sun, H. Gao, S. Zheng and S. Xu, *Bioresource. Technology*, **2010**, *101*, 6170-6176.

CHEMICAL AND MICROSTRUCTURAL CHARACTERISATION OF CONCRETE MINERAL ADDITIVES

ALEXANDRINA CUIBUS[a], MARIA GOREA[b,*], NICOLAE HAR[b], ZOLTAN KISS[a]

ABSTRACT. This paper summarizes chemical and mineralogical information on concrete mineral additives such as silica fume, fly ash from Mintia and metakaolin, as well as on concrete samples that were obtained by using these additives. The experiments were performed on seven concrete mixtures, with the following composition: S-1=standard concrete, S-2=concrete with 10 % fly ash (FA), S-3=concrete with 10 % metakaolin (MK), S-4=concrete with 10 % FA+10 % MK, S-5=concrete with 10 % silica fume (SF), S-6=concrete with 10 % SF+10 % FA, and S-7=concrete with 10 % SF+10 % MK. The XRD powder diffraction patterns on all these samples indicate the presence of amorphous phases, in particular in the silica fume, besides crystalline phases in metakaolin and the fly ash. The concrete samples consist of calcium silicates, calcium aluminates and calcium ferrites hydrates, calcium hydroxide, sulphated forms of calcium aluminates and respectively phases from the aggregates and the additives used. The particle size is sub-micrometric, with ash particles being the finest. Structurally, concretes are built-up of aggregate, cement matrix with hydration components, pores and "impurities".

Key word: *concrete, pozzolanic additives, by-products, fly ash, metakaolin, silica fume*

INTRODUCTION

One of the major challenges for the modern society is global warming. This represents a consequence of increase amounts of greenhouse gases emitted in the atmosphere. The process of fabrication of the cement clinker takes place at high temperatures (around 1450 ºC); in order to produce this heat, one must use fossil fuels with high caloric capacity (coal, oil fuel or natural

---

[a] *Technical University of Cluj-Napoca, 28 Memorandumului St., Cluj-Napoca, Romania*
[b] *"Babeş-Bolyai" University, 1. M. Kogălniceanu St., Cluj-Napoca, Romania*
[*] *Corresponding author: mgorea@chem.ubbcluj.ro*

gas). As a result, huge amounts of gases are released in the atmosphere – the cement industry being one of the major producer of greenhouse gas [1,2,3].

Researchers all over the world focus their work on obtaining performant concrete types in which cement is partially replaced by various pozzolanic additives (fly ash, metakaolin and silica fume). By using such additives in concrete, less environmental pollution results not only by the decrease of the amount of clinker needed, but also by recycling industrial by-products (wastes) that otherwise require special measures for removal and storage. Moreover, additives used alone or in combination with other components enhance some concrete properties such as density, hydration temperature, mechanical resistance, slump, alkali-silica reactions etc [4-13].

Fly ash is obtained by electrostatic or mechanical separation of solid particles from fired gases in the industrial kilns using coal powder as fuel - as such, or in mixtures. In order to be suitable as concrete raw material, fly ash has to comply with the requirements of Romanian standard SR EN 450-1. Fly ash is a fine powder including sperical glass particles with compositions dominated by SiO_2 and Al_2O_3 showing good pozzolanic properties. Silica powder is a by-product of ferrosilica; it is currently one of the most common concrete mineral additives [14].

Metakaolin is obtained through calcination of clayey raw materials at temperatures between 700 and 800 ºC [15, 16], or as waste in specific technologies [17].

Pozzolanic additives such as fly ash, metakaolin and silica fume react with water in the presence of calcium hydroxide – the latter resulted from hydration reactions of the cement's mineralogical components. The resulting phases are calcium silicates and aluminates hydrates, similar to those forming in Portland cement.

The goal of this paper is to characterize from physical-chemical and mineralogical point of view some hydraulic additives such as fly ash from Mintia steam power plant, metakaolin obtained by kaolin calcination at 780 ºC and commercial silica fume. Additionally, we have investigated concrete samples obtained by partial replacement (10 % and 20 % respectivelly) of cement with such additives.

RESULTS AND DISCUSSION

Characterisation of cement

For obtaining the concrete mixtures, we have used Portland cement CEM I 42,5R (produced by Lafarge Romania) with the main properties summarized in Table 1.

Table 1. Characterisation of Portland cement CEM I 42,5R

Chemical composition (oxides, %)							
SiO_2	Al_2O_3	Fe_2O_3	CaO	MgO	PC	SO_3	Insoluble
18.49	5.01	3.51	62.27	2.44	3.15	3.03	0.80
Physical characteristics							
Surface area (cm^2/g)		Stability (mm)		Hardening time (minutes)			
				initial		final	
3709		0.50		195		247	
Mechanical characteristics							
The compressive strength after 2 days (N/mm^2)				The compressive strength after 28 days (N/mm^2)			
28.30				46.60			

Characterisation of the mineral additives

The fly ash (FA) that we have used for obtaining the experimental concrete samples is produced as waste from coal burning in the Mintia (Deva, Romania) steam power plant. In our experiments we have used the particles with < 3 mm grain size. *Metakaolin* (MK) resulted by calcination of kaolin at constant temperature (780 °C) for 3 h 40 min. S*ilica fume (SF)* is a product of BASF The Chemical Company (commercial name: Elkem Microsilica Grade 940-U-S).

Chemical composition

The chemical compositions obtained by traditional wet chemistry analyses of the fly ash, metakaolin and silica fume are presented in Table 2.

Table 2. Chemical composition (oxides %) of the concrete mineral additives

Oxides (%)/Sample	SiO_2	Al_2O_3	Fe_2O_3	CaO	MgO	SO_4^{2-}	LOI
Fly ash, FA	49.67	26.33	7.66	2.42	3.68	0.13	10.11
Metakaolin, MK	58.77	36.22	1.20	1.16	0.43	0.12	2.10
Silica fume, SF	94.75	1.92	0.50	0.71	0.50	-	1.62

Mineral additives such as fly ash, metakaolin or silica fume are mainly consisting of silica, aluminium and iron oxides that react with $Ca(OH)_2$ resulted from the hydration of the cement components, leading to the generation of new calcium silicates, aluminates and ferrites hydrates respectively. Fly ash is relatively richer in MgO which may further be hydrated, thus negatively influencing the concrete properties. However, our XRD patterns show that MgO is not present as oxide, but chemically bond in magnesium silicates.

Mineralogical composition

The main mineral components of the Portland cement CEM I 42,5R, as calculated by using the Bogue equations based on its oxide composition are presented in Table 3.

Table 3. Mineralogical composition of the cement CEM I 42,5R

Component	C_3S	C_2S	C_3A	C_4AF
(%)	65.59	3.62	7.35	10.67

The mineralogical composition of the pozzolanic additives was investigated by X-ray diffraction on powders. The XRD patterns for the fly ash, metakaolin and silica fume are illustrated in Fig. 1.
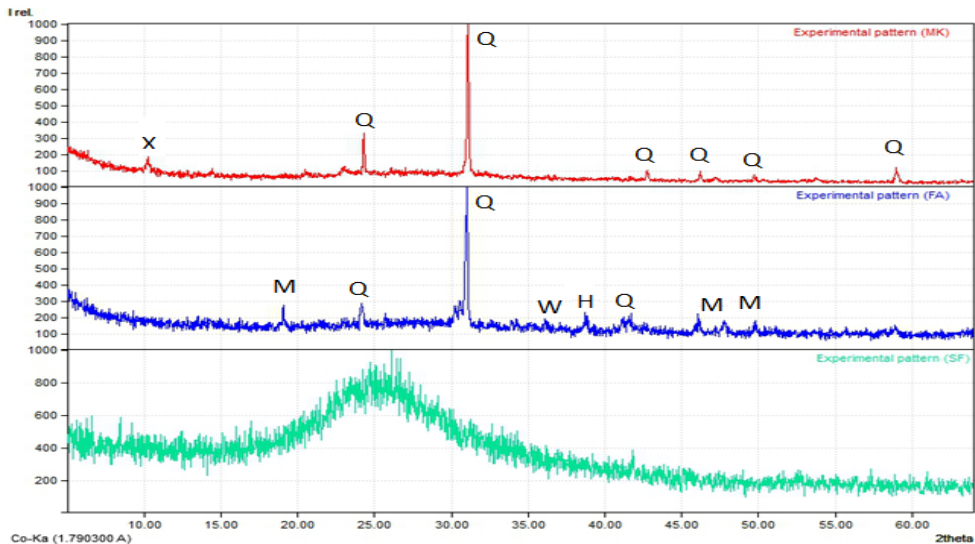
Figure 1. X-ray powder diffraction patterns of metakaolin (MK), fly ash (FA) and silica fume (SF). Q-quartz, M-mullite, H-hematite, W-wollastonite, X-$(K,NH_4,Na)Al_2(Si, Al)O_{10}(OH)_2$)

The metakaolin (MK) XRD pattern shows the peaks of high-temperature quartz (SiO_2) accompanied by less developed peaks of partly-transformed muscovite, $(K, NH_4, Na)Al_2(Si, Al)_4O_{10}(OH)_2$. These components are related to the "impurities" present in kaolin and they were not transformed during the thermal treatment. It is worthy to mention that the transformation products of kaolinite and the free oxides (SiO_2 and Al_2O_3) are mainly amorphous, the characteristic peaks being absent in the XRD pattern. This feature determines metakaolin to be highly reactive.

The fly ash has a complex XRD diffraction pattern that includes the characteristic peaks for quartz (SiO_2), hematite (Fe_2O_3), mullite ($Al_6Si_2O_{13}$), wollastonite ($CaSiO_3$) and a Mg and Fe silicate solid solution, $(Mg,Fe)_2SiO_4$.

The silica fume (SF) diffractogram evidences an amorphous material with no indication of crystalline phases. This explains the high reactivity of SF with the calcium hydroxide in the cement paste, with the formation of calcium silicates hydrates (C-S-H) and the enhancement of some properties of the concrete containing silica fume, such as hardening time and mechanical resistance.

Grain size distribution

Mineral additives are used in concrete compositions due to their reaction with $Ca(OH)_2$ resulting from the hydration of the clinker's mineral components in Portland cements. This reaction leads to the formation of new quantities of calcium aluminates and silicates hydrates that improve the mechanical properties of concretes. The reaction takes place at the contact surfaces between the particles. The smaller the particles, the larger their surface area and thus, the faster and more complete the chemical reaction. Also the fine pozzolanic additives determine the compaction of concrete due to pore filling processes – also leading to an enhanced mechanical resistance. Moreover, the increase in density also results from the crystallization of new phases in the larger pores, the pore surfaces triggering the crystallization of calcium hydrated components. The particle grain size distribution curves for the three studied additives are illustrated in Fig. 2.
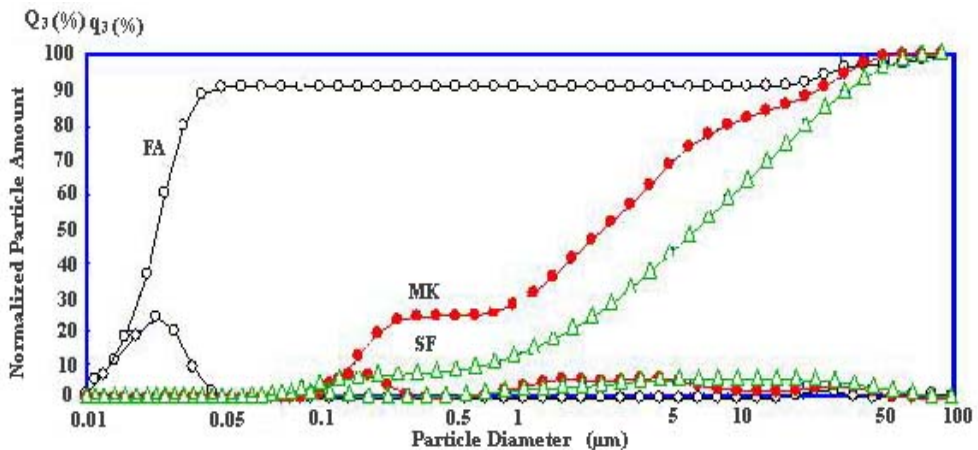
Figure 2. Grain size distribution of additives: FA- fly ash; MK – metakaolin;
SF – silica fume

Fly ash, FA shows the finest grain size, with about 92 % of the grains being 0.041–0.010 µm, the rest of 8 % being 61–21 µm in size. The average grain diameter is 0.021 µm.

Metakaolin shows a wide grain size distribution in the 41–0.123 µm interval. Three sub-intervals can be separated: ~20 % of the grains are in the 41–12 µm range, ~50 % in the 10–1 µm range, while ~30 % in the 1–0.123 µm range. The average grain diameter is 2.5 µm.

Silica fume, SF consists of ~80 % grains with sizes in the 57–1 µm interval, while the rest are in the 1–0.90 µm interval; the average diameter is 6.69 µm.

Based on the particle size distribution and the resulting reactivity, one would expect the highest mechanical resistance values in the concrete samples obtained by using fly ash, FA. Nevertheless, reactivity is also controlled by the crystallinity degree of the pozzolanic material used. In our case, the best combination is present in the silica fume, SF – that is diffractometrically amorphous and shows micrometer-size grains. The expected higher reactivity was experimentally obtained in the concrete samples with silica fume as additive: these concretes show high mechanical resistivity even after short hardening times. In spite of their small particle sizes, the fly ash, FA and the metakaolin, MK show relatively lower reaction speeds with $Ca(OH)_2$ as a result of their higher crystallinity degree. This correlates with longer hardening times for achieving high mechanical resistance [18].

Characterisation of concrete samples

Mineralogical composition of the matrix

X-ray diffraction patterns were collected on mixtures of cement paste with additives, in the absence of coarse aggregate material. S-1 represents the standard composition for the cement paste without additives. S-2, S-3 and S-5 contain 10 % fly ash (FA), metakaolin (MK) and silica fume (SF) respectively. In the S-4, S-6 and S-7 mixtures, the cement was partly substituted as follows: 10 % fly ash and 10 % metakaolin in S-4, 10 % fly ash and 10 % silica fume in S-6, and respectively 10 % silica fume and 10 % metakaolin in S-7.

In all the studied mixtures, the water/cement+additives ratio was 0.4, while the amount of superplastifier (Adium 150) used was 3.15 l/m3 of concrete.

In order to identify the hydration phases formed in the hardened cement paste, the cement mixtures with pozzolanic additives but without SiO_2-containing aggregates were submitted to the same hardening conditions as the aggregate-containing concretes. After 28 days, ground powder samples were submitted to X-ray diffraction.

The XRD powder diffraction patterns for the studied mixt compositions are illustrated in Fig. 3.
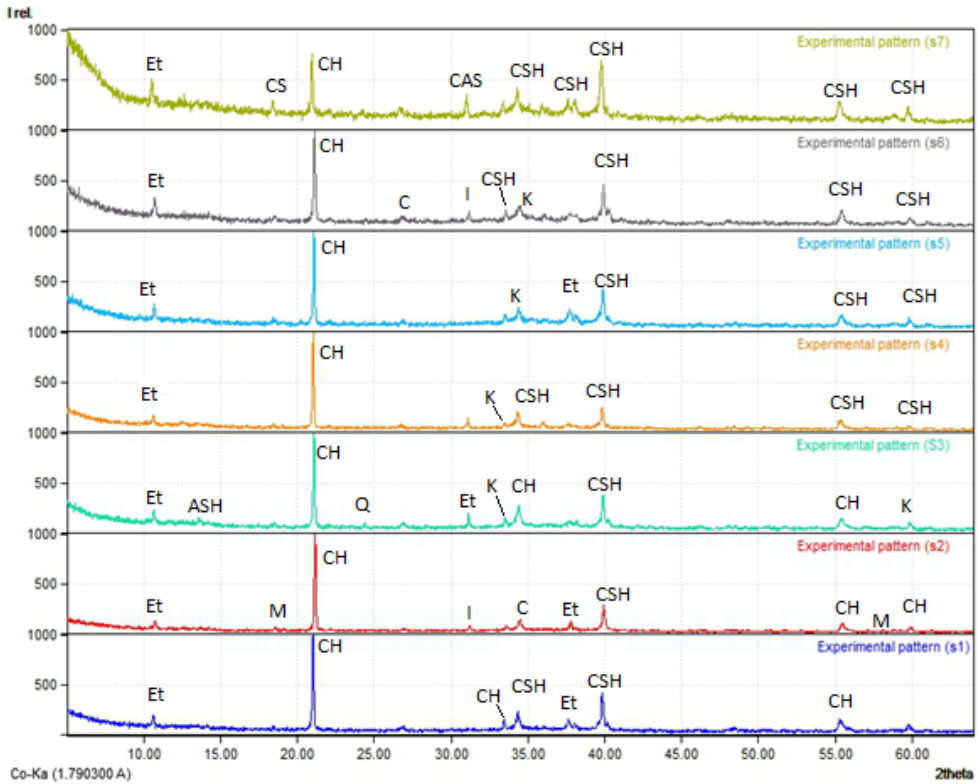
Figure 3. XRD powder diffraction patterns for the studied concrete samples (Et-ettringite, CH-portlandite, CSH-calcium silicate hydrate, CAS-calcium aluminosilicate, I-illite, C-calcite, K-kaolinite, M-mullite)

The XRD patterns reveal the mineral components in each of the studied concrete samples. In the references sample S-1 we have identified hydration products of calcium silicates ($Ca_{1.5}SiO_{3.5} \cdot xH_2O$, $Ca_3Si_2O_7 \cdot H_2O$), calcium aluminates ($Ca_4Al_6O_{13} \cdot 3H_2O$), calcium ferrites ($Ca_3(FeO_3)_2 \cdot 6H_2O$), calcium aluminoferrites ($Ca_{12}Al_{13,86}Fe_{0,14}O_{32}(OH)_2$), sulphated forms of calcium aluminates ($Ca_4Al_2SO_{10} \cdot 12H_2O$) and ettringite $Ca_6Al_2(SO_4)_3(OH)_{12} \cdot 26H_2O$), besides $Ca(OH)_2$ resulted from the hydration of the mineral components.

In sample S-2, besides the cement hydration components we noticed also crystalline components from the fly ash: quartz, mullite and calcite. In sample S-3, the characteristic peaks of quartz are accompanied by those of calcite and clay minerals (kaolinite). The presence of kaolinite can be explained by an incomplete decomposition at the given firing temperature or by a partial

hydration of metakaolin during the preparation of the cement mix. Kaolinite was also identified in sample S-4, which could be the cause for the lowest mechanical resistance at all hardening times for this type of experimental concrete.

In sample S-5, besides the typical hydration compounds we noticed diffraction peaks of calcium orthosilicate (Ca_2SiO_4); this can represent a still unhydrated clinker phase that needs longer time for reacting. Such a composition may explain the relatively higher mechanical resistance in concrete after long hardening times.

Calcium orthosilicate is present also in samples S-6 and S-7, besides crystalline phases from the additives (unhydrated iron phases, gehlenite or even kaolinite, the latter in sample S-7).

Optical microscopy

The optical microscopic study in polarized light performed on thin slices (20-25 micrometer thick) obtained from the concrete samples allowed us to identify and characterize some structural-textural and additional compositional features.

From structural point of view, the studied concrete samples consist of a relatively coarse aggregate (grain sizes between 0-16 mm) embedded in a fine matrix resulted by hydration reactions involving the Portland cement components, or additionally when it is the case, the ones in the mineral additive (FA, MK and SF). The structure is inequigranular, porphyroclastic[1], being characterized by the combination of relatively large aggregate particles and the fine matrix (Fig. 4).
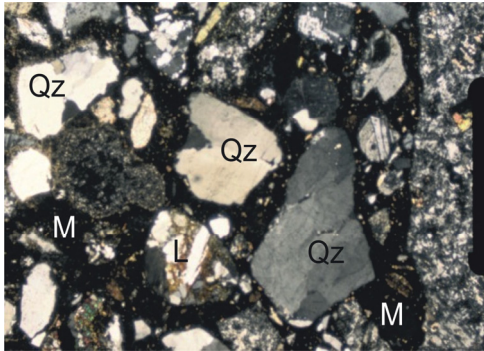
Figure 4. Porphyroclastic structure in sample S-3 with 10 % MK (N+). (Qz- quartz; L- aggregate clast, M – matrix) Scale bar=0.5 mm.
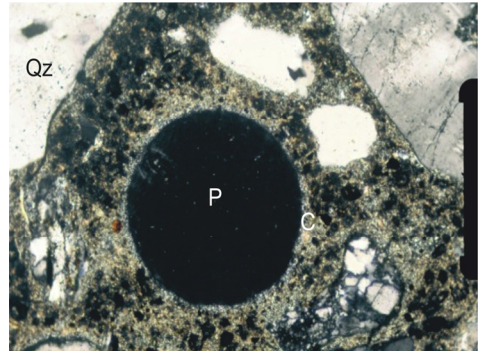
Figure 5. Spherical pore in sample S-1 – standard concrete (N+). (Qz-quartz, C-rim of posthydrating crystals Scale bar=0.5 mm.)

---

[1] The structural term "porphyroclastic" is used here according to its petrographic meaning, concerning natural rocks: the "*porfiro*" prefix points to the presence of clasts (fragments) that are larger than the particles in the matrix, or the fundamental mass of the studied material.

The main textural feature is the presence of pores typically displaying spherical morphologies (Fig. 5). The pores in concrete provide the environment for the crystallization of the hydration products or for secondary alteration processes (carbonation). It is common that calcite is present along the inner pore walls or close to them, as a result of the carbonation process (Fig. 6). In later stages of this process, the matrix may be impregnated with secondary calcite; this may also crystallize on the surface of the aggregate particles (Fig. 7).
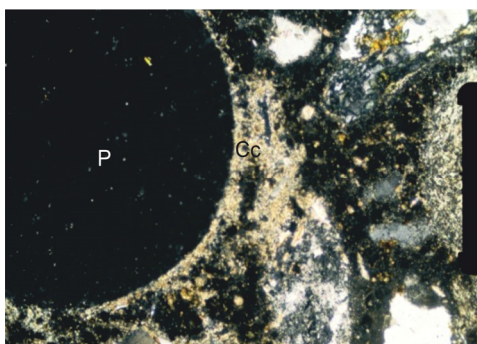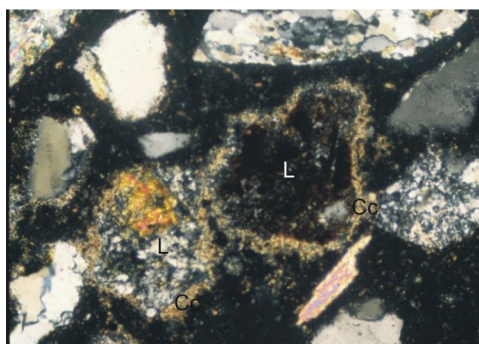

Figure 6. Detailed view of calcium carbonate (calcite-Cc) formed on the pore walls (P) in sample S-3 with 10 % MK, (N+). Scale bar=1.0 mm

Figure 7. Calcite rim (Cc) on aggregate clasts (L) in sample S-5 with 10 % SF, (N+). Scale bar=0.5 mm

From compositional point of view, two main groups of components can be noticed in concrete: the aggregate, and the matrix.

The aggregate consists of fragments of minerals and rocks (the latter are called lithic fragments). The mineral fragments consist of quartz (Fig. 8), plagioclase feldspars, micas (muscovite), pyroxenes (Fig. 9), hornblende etc. The lithic fragments are represented by quartzites (dominating), volcanic rocks (dacites) and crystalline schists (*e.g.*, quartzitic schist; Fig. 9).

The investigated samples show a microcrystalline matrix consisting of calcium silicates, aluminates, ferrites, aluminoferrites hydrates etc accompanied by sulphated forms of calcium aluminates and ettringite, as well as portlandite. The latter phases are related to the mineralogical components of cement. The matrix also contains phases from the mineral additives, as well as products of the reactions between the cement components and water. Because of their very small sizes, the exact composition of the matrix grains cannot be defined by optical microscopy in polarized light; XRD patterns are more relevant in this respect.
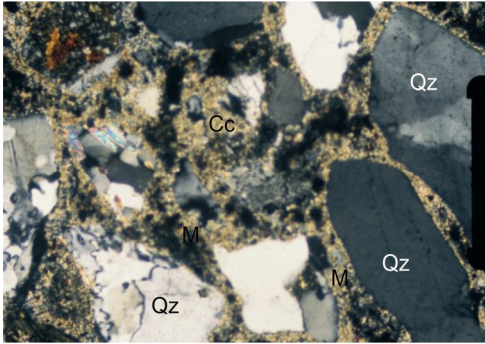
Figure 8. Aggregate components consisting of quartz clasts (Qz) embedded in intensely carbonated microcrystalline matrix (M) in sample S-4 with 10 % FA+10 % MK (N+). Scale bar=0.5 mm
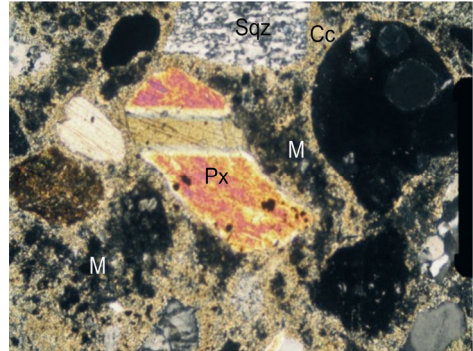
Figure 9. Pyroxene (augite) (Px) and quartzitic schist fragments (Sqz) embedded in intensely carbonated microcrystalline matrix (calcite-Cc) in sample S-4 with 10 % FA+10 % MK (N+). Scale bar=0.5 mm
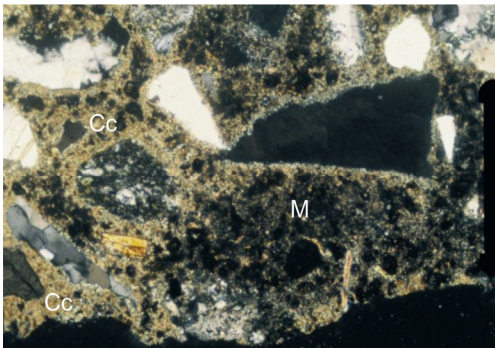
Figure 10. Fine crystalline matrix (M) impregnated with calcite (Cc) in sample S-2 with 10 % FA. (N+). Scale bar=0.5 mm
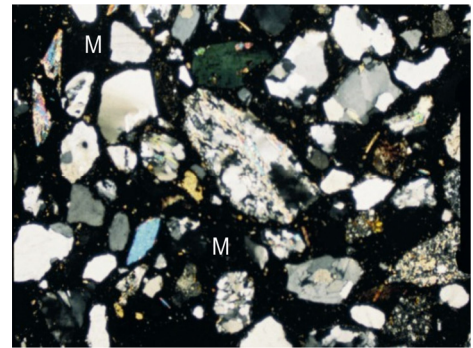
Figure 11. Isotropic matrix (M) with opacitization features in sample S-6 with 10 % SF+10 % FA (N+). Scale bar=0.2 mm

The matrix also contains calcite as secondary phase deposited along the pore walls, as rims on the aggregate clasts, or as impregnations in the matrix (Fig. 10). In some cases, the matrix is optically isotrope (due to the presence of hydration gels), with local opacitization trends (Fig. 11).

CONCLUSIONS

Hydraulically active cementoid additives such as fly ash, silica fume and metakaolin are used in concrete in order to improve its physical-mechanical characteristics, through reactions involving their mineralogical components.

By partial (10 % or 20 %) replacement of cement with such additives, the concrete performs better both fresh, and after hardening. The effect on the concrete properties is closely related to the characteristics of the additives. The studied additives contain high amounts of poorly crystallized, or even amorphous silica and aluminium oxides, which enhance their pozzolanic reaction with the $Ca(OH)_2$ resulting from cement hydration.

The grain size of the studied mineral additives is in the micrometer and nanometer range, thus determining their high reactivity with portlandite in the cement matrix.

The mineral components of the cement matrix are similar to those of a standard cement without additives; nevertheless, the relative content of free $Ca(OH)_2$ is lower, while new hydration phases are also present.

From microstructural point of view, the concrete consists of cement matrix, aggregate and pores. The matrix is dominated by the cement hydration products and by those resulted from the reaction with the pozzolanic additives. The aggregates consist of fragments of minerals and rocks. The mineral clasts are mainly represented by quartz, plagioclase feldspars, micas (muscovite), pyroxenes, and hornblende. The lithic fragments are dominantly quartzites, but also volcanic rocks (dacites) and crystalline (quartzitic) schists.

The pores in concrete provide the environment for the crystallization of hydration or secondary alteration (carbonation) products: on the inner pore walls or close to them calcite forms, as result of the carbonation process.

EXPERIMENTAL

The concrete samples were prepared in a cement mixer. The aggregates were successively added, in decreasing grain size order: 8-16 mm, 4-8 mm and finally 0-4 mm. After ~30 seconds of mixing, half of the water amount is added. Mixing continues for another 90 seconds. The rest of the cement and the mineral additives are then included in the composition and mixed in for 3 minutes. Then the rest of the water, including the additive is mixed together with the rest for 6 minutes. The final mixture is poured into standard moulds for mechanical tests. The moulds are covered with a foil and kept as such for ~24 h, after which the concrete samples are released from the moulds. These samples are then preserved in water at 20±2 ^{0}C for 28 days. Samples from the resulting materials are ground as micrometer-sized powders and submitted to X-ray diffraction for the mineralogical investigation of the hydration products. For this, we have used a Bruker D8 Advance diffractometer with Co anticathode, in the 2 theta interval 5 – 65°.

From the concrete samples S-1, S-2, S-3, S-4, S-5, S-6 and S-7 we have obtained 25-30 micrometers thin sections that we used for the optical study with polarized light under a Nikon Eclipse E 200 microscope.

The grain size distribution for the cementoid additives (fly ash, silica fume and metakaolin) was studied by using a Counter Coulter WING-SALD 7101 granulometer.

REFERENCES

1. R. Reis, A. Camões, Eco-Efficient Ternary Mixtures Incorporating Fly Ash and Metakaolin, International Conference Sustainability of Constructions – Towards a better built environment, **2011**, 71.
2. X. M. Zhou, J. R. Slater, S. E. Wavell, O. Oadiran, *Journal of Advanced Concrete Technology*, **2012**, *10*(2), 74.
3. J. E. Oh, Y. Jun, Y. Jeong, *Cement & Concrete Composites*, **2014**, *50*(3), 16.
4. R. Siddique, J. Klaus*, Applied Clay Science*, **2009**, *43*, 392.
5. L. Soriano, J. Monzo, M. Bonilla, M.M. Tashima, J. Paya, M.V. Borrachero, *Cement & Concrete Composites*, **2013**, *42*, 41.
6. S.M.H. Shafaatian, A. Akhavan, H. Maragheechi, F. Rajabipour, *Cement & Concrete Composites*, **2013**, *37*, 143.
7. Y. Li, A.K.H. Kwan, *Cement & Concrete Composites*, **2014**, *40*, 26.
8. H. K. Venkatanarayanan, P.R. Rangaraju, *Cement & Concrete Composites*, **2013**, *43*, 54.
9. K. Vance, M. Aguayo, T. Oey, G. Sant, N. Neithalath, *Cement & Concrete Composites*, **2013**, *39*, 93.
10. D. p. Bentz, *Cement & Concrete Composites*, **2014**, *53*, 214.
11. E. Belhadj, C. Diliberto, A. Lecomte, *Cement & Concrete Composites*, **2014**, *45*, 15.
12. G. Quercia, A. Lazaro, J. W. Geus, H. J. H. Brouwers, *Cement & Concrete Composites*, **2013**, *44*, 77.
13. J. Moon, S. Bae, K. Celik, S. Yoon, K-H. Kim, K. S. Kim, P. J.M. Monteiro, *Cement & Concrete Composites*, **2014**, *53*, 97.
14. C. Măgureanu, Betoane de înaltă rezistenţă şi performanţă, U.T.PRESS Cluj-Napoca **2010**, 274.
15. H. Paiva, A. Velosa, P.Cachim, V.M. Ferreira, *Cement and Concrete Research*, **2012**, *42*, 607.
16. E. Bodagiannis, S. Tsivilis, *Cement & Concrete Composites*, **2009**, *31*, 128.
17. A. Egersdorfer, M. Schmidt, H. Pöllmann, Increased reactivity. Using a glass-containing metakaolin as an active filler in lime-based binder systems, AT international – mineral processing, Jg:53, Nr. ½, **2012**, 70.
18. A. Cuibus, Z. Kiss, M. Gorea, *Romanian Journal of Materials*, **2014**, *44*(3), 225.

TRANSLUCENCY VARIATION OF LITHIUM DISILICATE CERAMICS WITH CLINICALLY RELEVANT THICKNESSES

ALEXANDRA BOTOŞ[a, *], MÎNDRA BADEA[b], DIANA DUDEA[a]

ABSTRACT. The aim of this study was to investigate the relationship between translucency and thickness of IPS e.max lithium disilicate ceramics (Ivoclar Vivadent). 100 ceramic disks were pressed out in four opacities (high opacity (HO), medium opacity (MO), low translucency (LT) and high translucency (HT) and in five clinically relevant thicknesses (0.3mm, 0.6mm, 0.9mm, 1.2mm, 1.5mm +/-0.1mm) (n=5). The CIE L*a*b* colour parameters against black and white backgrounds were recorded with a dental spectrophotometer (VITA Easyshade®, VITA Bad Säckingen, Germany), in D65 light source (JUST LED Color Viewing Light, JUST Normlicht, Weilheim/Teck, Germany) in a dark room. The translucency parameter (TP) was calculated for each sample. The data were statistically processed with a 2-way ANOVA test, followed by the Tuckey Honestly Significant Difference (HSD). Results showed that TP values recorded for ceramic materials with higher opacity (HO, MO) were lower than those for materials with lower opacity (higher translucency) (LT, HT), with a high statistical significance ($P<.01$). There was an exponential regression curve between thickness and the TP values, with a very good correlation ($R^2=0,981-0,998$). In conclusion, translucency of dental ceramics was significantly influenced by thickness and type of material, with an exponential relationship between TP and thickness.

Keywords: Lithium disilicate, translucency, ceramic thickness

INTRODUCTION

Full ceramic restorations have been preferred to traditional metal ceramic due to their excellent esthetic properties and clinically acceptable mechanical properties. Ceramic materials were extensively investigated and constantly improved in order to provide tooth comparable optical properties [1-4]. Enamel

---

[a] *Dept. of Dental Propaedeutics and Esthetics, Faculty of Dental Medicine, University of Medicine and Pharmacy "Iuliu Haţieganu", Cluj-Napoca, Romania*

[b] *Dept. of Prevention in Dentistry, Faculty of Dental Medicine, University of Medicine and Pharmacy "Iuliu Haţieganu", Cluj-Napoca, Romania*

* *Coresponding author: alexandrabotosch@gmail.com*

and dentin, two functionally and optically different materials, are layered together and interact in a unique way to fulfill their functions [5, 6]. The additional difficulties faced when reconstructing teeth in the anterior area are small dimensions, convex surfaces of teeth, surface texture [7].

Translucency has been found to be one of the main factors influencing the esthetic result of ceramic restorations [8]. Translucency is also closely linked to light transmission through ceramics and to polymerization efficiency of underlying luting agents [9-12].

In order to assess translucency, several methods are used:

Absolute translucency determinations need a dual beam, integrating sphere radiometer or spectrophotometer which is able to record all the intensity of light transmitted through a sample in comparison to the intensity of light from a split beam. A quantitative measurement of absolute translucency was created by calculating the total transmission (T%) of light through the sample, by using a spectroradiometer, according to the formula

$$T\% = (L^*_{sample}/ L^*_{source}) \times 100,$$

where L^*_{sample} stands for luminance recorded with the sample in place, and L^*_{source} stands for luminance reading with no sample in place [13].

Quantitative relative translucency, *contrast ratio* (CR), is registered with any system capable of registering standard radiation intensity and determination according to the formula

$$CR = L_B/L_W,$$

where L_B is the luminance flux (reflectance) with the specimen on a black background and L_W is the luminance flux (reflectance) with the specimen on a white background [13].

The *translucency parameter* (TP) appeared as an extension of the contrast ratio parameter and was introduced in 1995 in order to investigate the translucency of maxillofacial elastomers [13]. The TP formula is based on the color difference of the L*, a*, b* parameters for the samples on black and white backgrounds. The formula is:

$$TP = ((L^*_B-L^*_W)^2+(a^*_B -a^*_W)^2+(b^*_B -b^*_W)^2)^{1/2}.$$

The TP parameter was considered one of the most important visual evaluators [14] and has been one of the most widely used methods to compare relative translucency of dental materials.

In clinical situations when ceramic restorations are recommended, factors such as the available space as well as color and dimensions of the prosthetic appliance should be considered. Therefore, the relationship between translucency and thickness of ceramic restorative materials needs to be thoroughly investigated in order to achieve improved esthetic results.

Lithium disilicate glass ceramics are materials largely used nowadays, due to their mechanical and optical properties that enable the enlargement of the indications in comparison with other ceramic materials. The IPS e.max of the Ivoclar Vivadent Company is a concept designed to adapt to any indication for all-ceramic restorations. One of the processing categories is the IPS e.max Press, pressable ingots of lithium disilicate glass ceramics [15].

The translucency of dental ceramics has been identified within a certain range [16], mostly at material thicknesses recommended by the manufacturers. These values do not totally overlap those of natural enamel and dentin, and therein lays the difficulty to perfectly match the translucency of natural teeth [17-20]. The translucency parameter and CIE L*, a*, b* color parameters of ceramics have previously been investigated [16, 21-23] with either spectroradiometers, spectrophotometers, or dental spectrophotometers. However, the easiest to use and in reach devices for clinicians and dental technicians are dental spectrophotomers [24].

The aim of this study was to investigate the relationship between translucency and ceramic thickness for the IPS e.max Press lithium disilicate ceramics. The null hypothesis was that the translucency of ceramics was not influenced by the type of opacity of the ceramics or its thickness.

RESULTS AND DISCUSSIONS

The mean TP values for the IPS e-max Press ceramics used in this study ranged 5.67 to 12.78 (Table 1). The TP mean values decreased in the following order HT, LT, MO, HO, with the exception of the 0.3mm thickness where the order was LT, HT, MO, HO. The TP mean values ranged less for the more translucent materials (8.74 to 12.47 for HT and 8.34 to 12.78 for LT) and more for the more opaque ones (7.86 to12.01 for MO and 5.67 to 11.49 for HO). Also, the TP decreased with the increase in ceramic thickness for all opacities.

Table 1. TP mean value and standard deviation (SD)
for the lithium disilicate glass ceramics

Ceramic opacity		0.3mm	0.6mm	0.9mm	1.2mm	1.5mm
HO		11.49	9.75	8.31	7.02	5.67
	SD	*0.60*	*0.18*	*0.21*	*0.41*	*0.29*
MO		12.01	11.35	9.64	8.98	7.86
	SD	*0.25*	*0.15*	*0.19*	*0.32*	*0.26*
LT		12.78	11.65	10.48	9.14	8.34
	SD	*0.19*	*0.20*	*0.25*	*0.53*	*0.31*
HT		12.47	11.68	10.67	9.81	8.74
	SD	*0.39*	*0.29*	*0.53*	*0.63*	*0.39*

The results of the 2-way ANOVA showed that both main factors (material and thickness) and their interaction were statistically significant (P<.01) (Table 2). The increase of the TP of the more translucent ceramics due to a decrease in thickness was greater than that of the more opaque ceramics.

Table 2. Results of 2-way ANOVA of TP values
of lithium disilicate glass ceramics

Source	Sum of Squares	df	Mean Square	F
MATERIAL	75.98	3	25.33	17.20
THICKNESS	68.00	4	17.00	11.55
MATERIAL * THICKNESS	94.79	12	7.90	5.37
Error	117.78	80	1.47	
Total	10142.80	100		

The regression analysis of the TP by thickness revealed that the correlation between thickness and the TP value was exponential, according to the resulting equation. The calculations of the regression equations are illustrated in table 3. Very good correlation coefficients with very high statistical significance were found for all four materials tested (R^2=0,981-0,998).

Table 3. Regression analysis results of TP (y) by
thickness (x) of lithium disilicate glass ceramics

Code	Regression equation	R^2	P
HO	$y = 13.822e^{-0.58x}$	0.996	<0.001
MO	$y = 13.63e^{-0.361x}$	0.981	<0.001
LT	$y = 14.38e^{-0.365x}$	0.995	<0.001
HT	$y = 13.816e^{-0.295x}$	0.9912	<0.001
R^2=correlation coefficient			

The null hypothesis, that translucency was not influenced by the type and thickness of ceramics was rejected.

The results of our study are in agreement with literature [21, 25, 26] that translucency of ceramic materials decreases with the increase in thickness. Heffernan et al. [17, 18] stated that the difference in translucency of ceramic materials is mainly influenced by the varied crystalline structure

and specimen thickness. The microstructure of lithium disilicate ceramics is represented by needle like crystals (3 to 6 μm in length), embedded in a glass matrix [15] that resemble the natural structure of enamel, thus facilitating the reproduction of a natural warm aspect of restorations.

The four types of ceramic opacities indicated TP values in agreement with the manufacturer indications. The high opacity ceramics had the smallest TP values and the more translucent materials had higher TP values. Increased opacity of the ceramic material (HO and MO) also meant greater decrease of the TP values with the increase in thickness of the sample. From a clinical point of view, this transfers into better masking capacity of the substrate when in a thinner layer, e.g. a 0.6mm substructure. Higher translucency of LT and HT ceramics translate into a smaller variation of TP in the range between the 0.3mm and 1.5mm samples. Clinically this will allow for a thinner layer of ceramics, hence a more economical tooth preparation in the cases where no masking of the tooth background is needed.

The thickness of the ceramic samples in our study was based on various clinical needs and indications. Veneers can be as thin as 0.3mm, ceramic copings up to 0.7mm [1, 23], and fully anatomical restorations have an average 1.5mm thickness on the labial surface [25] and 2mm thickness [27] in the incisal area [26].

The TP values for 1mm thick human enamel are 18.7 and 16.4 for dentin [28]. Several other studies have investigated the TP factor in dental ceramics [16, 21-23, 29, 30] using different types of materials and different recording devices. Optical parameters of ceramic materials can accurately be registered either by using a spectroradiometer or a spectrophotometer. Some studies compare the two methods and draw the conclusion that their findings correlate [16]. Other studies compared an oral spectrophotometer (Vita Easy Shade, Vita) with a reference spectrophotometer and concluded that the use of the oral spectrophotometer in research will mean different values than those recorded with a reference spectrophotometer, but still highly correlated [31].

Our study used the Vita Easy Shade dental spectrophotometer for the recording of the color parameters. The use of a different measuring device might be responsible for the differences in TP values, in comparison to the ones reported by Wang [21] who used a reference spectrophotometer. Also, the decrease in the window size when recording color parameters resulted in lower CIE L*a*b* measured values [32]. In addition, small-window tooth color recordings may result in edge loss of light due to tooth translucency [33].

The regression analysis used in the present study showed that the more translucent a ceramic material was, a greater change in TP would be expected as a result of thickness variation. This was in agreement with the results of Wang [21] and Antonson [34].

When creating esthetic reconstructions ceramic materials need to reproduce the structure, color, surface texture and translucency of natural teeth, in adequate material thickness and appropriate shade matches [23, 35]. The color of the underlying background and the luting agent also play a role in achieving the desired masking effect of an esthetic reconstruction [36].

Based on the results of the present study and in relation to clinical considerations, the contribution of the discromic substrate to the final perceived color of a restoration should also be considered, along with the input of luting agents available.

CONCLUSIONS

Within the limitations of the present study, the following conclusions were drawn:

1. Translucency of dental ceramics was significantly influenced by both thickness and type of material.
2. There was an exponential relationship between TP and thickness of IPS e.max lithium disilicate ceramics. The more translucent the ceramic material was the higher the TP values were.

EXPERIMENTAL SECTION

Materials

The dental ceramic system evaluated in the present study is IPS e-max Press (Ivoclar Vivadent), in the four basic opacities: high opacity (HO), medium opacity (MO), low translucency (LT) and high translucency (HT). During the fabrication of the specimens, the recommended manufacturers' processing instructions were respected. 100 ceramic disks (10 mm diameter) were pressed out of calibrated wax by the lost wax technique. The disks were divided into four groups of opacity (HO, MO, LT, HT), each having five subgroups of thicknesses (0.3, 0.6, 0.9, 1.2, 1.5mm). The thickness of the ceramic disks was checked with a digital micrometer (0.3, 0.6, 0.9, 1.2, 1.5mm ± 0.1mm). In order to obtain a glossy surface of the ceramics, the surface to be analyzed of the disks was smoothened out and polished by using wet silica paper under finger pressure, in the sequence 400, 600, 800-grit.

Determination of translucency parameter

The CIE L*a*b* colour parameters were recorded using a dental spectrophotometer (VITA Easyshade®, VITA Bad Säckingen, Germany). The colour parameters lightness (L*) and cromacity (a* and b*) were measured

on a black and a white background for all specimens. Saturated sucrose solution was interposed (refractive index n=1,5) between each ceramic disk and the background. The colour measurements were performed in a dark room, with a light source simulating natural daylight (D65) in a special viewing booth (JUST LED Color Viewing Light, JUST Normlicht, Weilheim/Teck, Germany).

The translucency parameter (TP) was obtained by calculating the colour difference between the specimen against the black background and against the white background with the following equation [13]:

$$TP = ((L^*_B - L^*_W)^2 + (a^*_B - a^*_W)^2 + (b^*_B - b^*_W)^2)^{1/2},$$

where *L** refers to the value, *a** to redness to greenness cromatic parameter, and *b** to yellowness to blueness cromatic parameter. The subscripts *B* refers to the colour coordinates on the black background and *W* to those on the white background.

Three measurements were made for each specimen on each background, and the average value was recorded. High TP values indicate high translucency and low opacity and low TP values indicate low translucency and high opacity.

Statistical analysis

The effects of the material and thickness on the TP values of the lithium disilicate ceramics were analyzed with a 2-way analysis of variance (ANOVA), followed by the Tuckey Honestly Significant Difference (HSD) test by using statistical software (SPSS 17.0; SAS, Chicago, Ill). The relationship between the thickness and TP values of each ceramic group was evaluated with a regression analysis.

REFERENCES

1. H.J. Conrad, W-J. Seong, I.J. Pesun. *The Journal of Prosthetic Dentistry*, **2007**, *98(5),* 389.
2. J. McLean. *The Journal of Prosthetic Dentistry*, **2001**, *85*, 61.
3. A. Della Bona, R. Kelly. *Journal of the American Dental Association*, **2008**, *139*(4), 8.
4. J. Grigg. *Dental Clinics of North America*, **2007**, *51*, 713.
5. A. Đozić, C.J. Kleverlaan, I.H. Aartman, A.J. Feilzer. *Dental Materials*, **2004**, *20*(9), 832.
6. A. Đozić, C.J. Kleverlaan, I. Aartman, A.J. Feilzer. *Dental Materials*, **2005**, *21*(3), 187.

7. R.D. Paravina. *Journal of Dentistry*, **2009**, *37*, 5.
8. J.N. Kelly, I. Nishimura, S.D. Campbell. *The Journal of Prosthetic Dentistry,* **1996***, 75*, 18.
9. K.B. Chan, D.B. Boyer. *Journal of Dental Research*, **1989**, *68*, 476.
10. D.C. Watts, A.J. Cash. *Journal of Dentistry*, **1994**, *22*, 112.
11. R.T.Peixoto, V.M. Paulinelli, H.H. Sander, M.D. Lanza, L.A. Cury, L.T. Poletto. *Dental Materials*, **2007**, *23*(11), 1363.
12. N. Ilie, R. Hickel. *Dental Materials*, **2008**, *24*(7), 908.
13. L.S. Spink, P. Rungruanganut, S. Megremis, J.R. Kelly. *Dental Materials*, **2013**, *29*(6), 702.
14. W.M. Johnston, T. Ma, B.H. Kienle. *International Journal of Prosthodontics*, **1995**, *8*, 79.
15. Scientific documentation of IPS e.max Press.
    file:///C:/Users/admin/Downloads/IPS+e-max+Press.pdf, accessed 02.2014.
16. H-N. Lim, B. Yu, Y-K Lee. *The Journal of Prosthetic Dentistry, 2010, 104*, 239.
17. M.J. Heffernan, S.A. Aquilino, A.M. Diaz-Arnold, D.R. Haselton, C.M. Stanford, M.A. Vargas. *The Journal of Prosthetic Dentistry,* **2002**, *88*, 4.
18. M.J. Heffernan, S.A. Aquilino, A.M. Diaz-Arnold, D.R. Haselton, C.M. Stanford, M.A. Vargas. *The Journal of Prosthetic Dentistry,* **2002**, *88*, 10.
19. F. Chu, T.W. Chow, J. Chai. *The Journal of Prosthetic Dentistry*, **2007**, *98*(5), 359.
20. Y.M. Chen, S.J. Smales, K.H. Yip, W.J. Sung. *Dental Materials*, **2008**, *24*(11), 1506.
21. F. Wang, H. Takahashi, N. Iwasaki. *The Journal of Prosthetic Dentistry*, **2013**, *110*(1), 14.
22. Y.K. Lee, B. Yu, H.N. Lim. *The Journal of Prosthetic Dentistry*, **2010**, 104(3), 173.
23. A. Dozić, C.J. Kleverlaan, M. Meegdes, J. van der Zel, A.J. Feilzer. *The Journal of Prosthetic Dentistry*, **2003**, *90*(6), 563.
24. S.J. Chu, R.D. Trushkowsky, R.D. Paravina. *Journal of Dentistry*, **2010**, *38*(2), 2.
25. Y.K. Lee,H.S. Cha, J.S. Ahn. *The Journal of Prosthetic Dentistry*, **2007**, *97*(5), 279.
26. T.E. Shokry,C. Shen, M.M. Elhosary, A.M. Elkhodary. *The Journal of Prosthetic Dentistry*, **2006**, *95*(2), 124.
27. A.F. Vichi, M. Ferrari, C.L. Davidson. *The Journal of Prosthetic Dentistry*, **2000**, *83*, 412.
28. B. Yu, J.S. Ahn, Y.K. Lee. *Acta odontologica Scandinavica*, **2009**, *67*(1), 57.
29. J-S. Ahn, Y-K Lee. *Dental Materials*, **2008**, *24*(11),1539.
30. Q. Li, B.T. Xu, R. Li, Y.N. Wang. *Journal of Dentistry*, **2010**, *38*(2), 117.
31. N. AlGhazali, G. Burnside, R.W. Smith, A.J. Preston, F.D. Jarad. *European Journal of Prosthodontics and Restorative Dentistry*, **2011,** *19*(4), 168.
32. R.A. Bolt, J.J. ten Bosch, J.C. Coops. *Physics in Medicine and Biology*, **1994**, *39*(7), 1133.
33. W.M. Johnston. *Journal of Dentistry*, **2009**, 37(1), 2.
34. S.A. Antonson, K.J. Adusavice. *International Journal of Prosthodontics*, **2001**, *14*, 316.
35. R.D. Douglas, M. Przybylska. *Journal of Prosthetic Dentistry*, **1999**, *82*, 143.
36. C.A. Volpato, S. Monteiro Jr., M.C. de Andrada, M.C. Fredel, C.O. Petter. *Dental Materials*, **2009**, *25*(1), 87.

A TWIST IN THE ANOMERIC EFFECT

RADU SILAGHI-DUMITRESCU[a],
JUAN FRANCISCO CARRASCOZA MAYEN[a,*]

ABSTRACT. Several explanations have been proposed for the anomeric effect – based mainly on sterical interactions, charge separation, and hyperconjugation. Revisiting this topic with computational methods, we find that the pyranoid oxygen is not sp^3-hybridized, and as a result of this situation one of the oxygen lone pairs is found in an *eclipsed* conformation with respect to an equatorial substituent at a neighboring carbon atom. This sterical conflict by itself appears as an important cause of the anomeric effect. The non-sp^3-hybridized nature of the oxygen atom is in fact found not to be limited to carbohydrates, but rather be encountered in basic structural motifs (e.g., water, methanol, formaldehyde). Differences between this situation and those encountered with other heteroatoms (nitrogen, sulfur) are also discussed.

Keywords: Anomeric effect; sugar, pyranoid oxygen.

INTRODUCTION

In the typical 'chair' conformation of saturated cyclohexane-type six-membered rings, substituents prefer equatorial positions over axial ones (Figure 1). However, when one of the six carbon atoms is substituted by a heteroatom (such as in the pyranose form of certain carbohydrates), substitution at the vicinal carbon atom is found experimentally to entail much smaller differences between the axial and equatorial isomers, compared to what is seen in simple hexane-type structures. Several explanations have been proposed based on solid experimental and theoretical data for this so-called anomeric effect; among these were sterical repulsion between the axial/equatorial substituents and the lone pair of the pyranoid oxygen atom, different degrees of charge separation (manifested in different dipole moments), hyperconjugation involving the lone pairs of the pyranoid oxygen atom, and CH---O hydrogen bonding.[1-6]

---

[a] *Babeş-Bolyai University, Faculty of Chemistry and Chemical Engineering, 11 Arany Janos str., RO-400028, Cluj-Napoca, Romania*
* Corresponding author: carrascoza@chem.ubbcluj.ro

Here, we report data highlighting the important role of the pyranoid oxygen atom, via its previously undiscussed tendency to maintain its lone pairs in a *non-sp³-hybridized* orientation, and thus force an *eclipsed* conformer involving the equatorial substituents at the neighboring carbon atom, as opposed to the commonly invoked situation where this oxygen is *sp³-hybridized* and the respective conformer is *staggered*. We further show how the same 'non-sp³-hybridized'-like description of the oxygen in terms of the spatial location of its two lone pairs of electrons, is seen even in some of the most basic organic and inorganic systems.


equatorial   axial
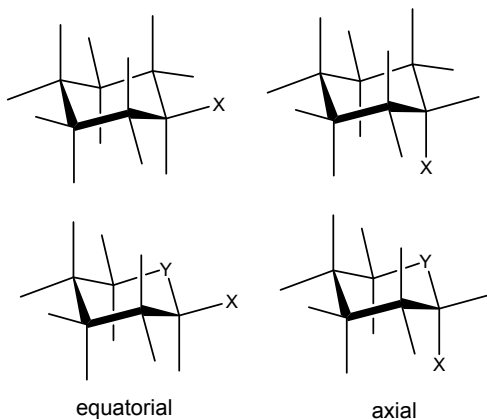
Figure 1. Structures of interest for the present study. X and Y are typically oxygen atoms, in which case the structural motif is relevant for carbohydrate chemistry.

RESULTS AND DISCUSION

Figure 2 illustrates frontier molecular orbitals computed at DFT level for the axial and equatorial isomers of tetrahydropyran-2-ol, one of the simplest compounds expected to present an anomeric effect. It may be seen that one of the pyranoid oxygen lone pairs is perpendicular to the ring's C-O-C plane (in the HOMO), while the other lone pair of the same oxygen atom is contained in this plane (HOMO-2 in the equatorial isomer, HOMO-1 in the axial one). Thus, the pyranoid oxygen atom has two p orbitals essentially perpendicular to each other

This situation is at odds with the sp³ hybridization generally invoked when discussing the anomeric effect and in fact generally expected of oxygen atoms in organic chemistry. Two p orbitals perpendicular with each other, in an atom not involved in multiple bonding would appear to best be explained as a non-hybridized atom. An alternative explanation, involving sp² hybridization, would be at odds with the formal lack of π bonding in the models of Figure 2, as well as in the models further explored in Figure 3. This

situation, with a non-hybridized oxygen atom, then poses a simple conformational problem – substituents found in equatorial positions at the carbon atoms directly bound to the pyranoid oxygen will be found in an eclipsed conformation with one of the lone pairs of the oxygen atom, thus being energetically-disfavored, cf. Figure 2. This finding by itself offers a strong explanation for the anomeric effect. Additionally, the particular conformation of the pyranoid oxygen lone pairs also predicts that in the equatorial conformer of the tetrahydropyran-2-ol the oxygen atoms together with the two carbon atoms vicinal to the pyranoid oxygen will, all four, be found almost in the same plane. Upon our theoretical results, perpendicular to this plane within the equatorial conformer will be the lone pairs from both oxygen atoms and the C-H bonds from the two carbon atoms. All of this makes for an ideal conformation for hyperconjugation in the equatorial isomer – a configuration which would be lost in the axial conformer. Thus, the non-hybridized character of the pyranoid oxygen atom has two effects: creating eclipsed conformers (as opposed to staggered ones) and thus partially destabilizing the equatorial isomer relative to the axial one, and on the other hand favoring hyperconjugation in the equatorial isomer.
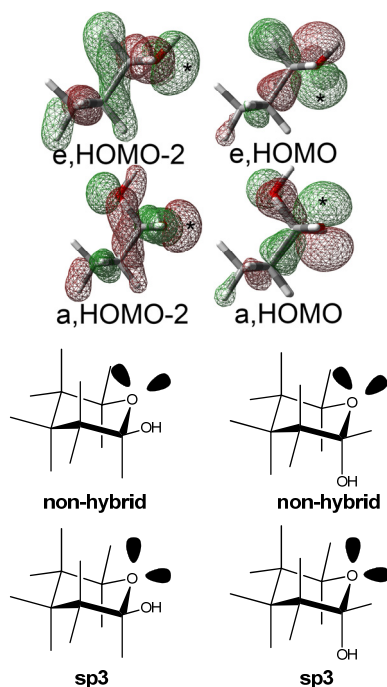

Figure 2. Up: computed frontier orbitals for tetrahydropyran-2-ol, showing the two lone pairs of the pyranoid oxygen atom (each lobe marked with a * symbol), at an angle of 90° to each other. **Down:** comparison of the sterics of a sp^3-hybridized vs a non-hybridized pyranoid oxygen atom in the models examined here; lone pairs are shown as hollow wedges at the oxygen.

Figure 3 illustrates molecular orbitals computed with DFT for a series of simpler molecules, as reference models for the anomeric structures of Figure 1; identical pictures were obtained at the MP2/6-311+G** level (not shown). Water is the simplest molecule where the oxygen is involved in two single bonds, similarly to the anomeric oxygen atom in the tetrahydropyran-2-ol already examined in Figure 2. It can be seen that even in the water molecule there are two perpendicular p orbitals – HOMO and HOMO-1; these two orbitals are the equivalents of those shown in Figure 2 for the anomeric oxygen atom. The water HOMO-2 is also perpendicular to the HOMO, and, although its lobes are elongated towards the hydrogen atoms, they may also be interpreted to be perpendicular to HOMO-1. One may then ask, if the oxygen is non-hybridized, why would the two O-H bonds form a 105º angle, instead of 90º? The answer to this question is in the distance between the two hydrogens in the water molecule – 1.45 Å, which is distinctly shorter that the 2.40 Å representing their sum of van der Waals radii; one may then propose that a distinct repulsion between these two hydrogen atoms is the main reason why the H-O-H angle is not 90º in water.

Examination of the frontier orbitals in methanol (Figure 3) again reveals that the two oxygen lone pairs, as major contributors to the respective HOMO and HOMO-1, are perpendicular to each other and thus irreconcilable with an sp^3 description, all in line with the data shown in Figure 2 for the anomeric oxygen. The relative orientations of the methanol HOMO-2 and HOMO-4, at an apparent 120º, may tempt one to invoke an sp^2 situation, as could have been done for the anomeric oxygen of Figure 2. Such an sp2 description would be somewhat in line with the fact that the C-O-H angle at the oxygen atom is computed to be 109º, as opposed to the 90º expected of an non-hybridized oxygen. However, as in the case of the water molecule, one may identify a sterical reason for this deviation from 90º: the distances between the water-bound proton and the two closest methyl protons are 2.39 Å each, 0.01 Å shorter than the sum of van der Waals radii and suggesting again sterical repulsion as the main factor dictating the bond angles around the oxygen atom. Strongly arguing against a hybridized description is also the HOMO-2 orbital in methanol: in an sp^2 situation this orbital should have been directed along the carbon-oxygen axis – which is not the case.

The frontier molecular orbitals of CH3SH are also instructive to follow (cf. Figure 3): they are almost identical to the ones in CH3OH, even though the bond angle around the sulfur is now only 97º - much closer to 90º and clearly symptomatic of a non-hybridized atom. We then propose that the deviations of orbitals HOMO-1 and HOMO-4 in CH_3SH and CH_3OH from the expected 90º are caused by the need to optimize interaction with the carbon and hydrogen atoms respectively, but that the sulfur and oxygen should equally be described as non-hybridized, rather than sp2 or sp^3.

Figure 3 also shows that an oxygen atom involved in a double bond (as in formaldehyde) is even more clearly describable as non-hybridized, with all its three p orbitals clearly perpendicular to each other. One may then advocate, starting with the example of the anomeric effect, that oxygen atoms in organic chemistry should always be regarded as non-hybridized, and that their lone pairs are always perpendicular to each other.
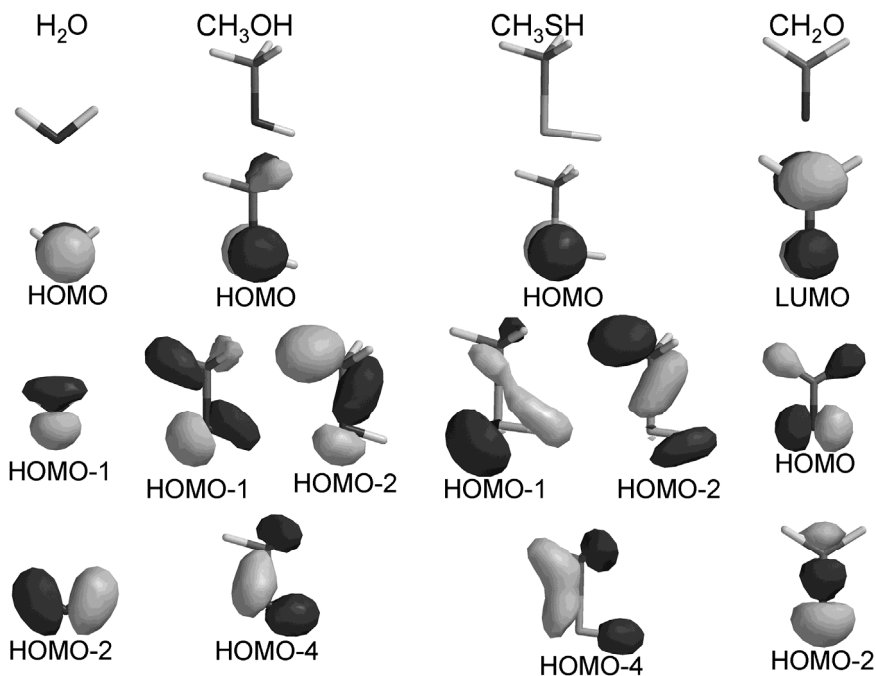
Figure 3. Frontier molecular orbitals for H_2O, CH_3OH, CH_3SH and CH_2O.

To our knowledge when the pyranoid oxygen in the tetrahydropyran-2-ol is replaced with an NH group the anomeric effect is essentially lost.[4] In fact, unlike the pyranoid oxygen in the tetrahydropyran-2-ol, the NH atom has largely a tetrahedral sp^3-like geometry, inevitably since it has three substituents in addition to the lone pair. In such a true-sp^3 situation, the sterical argument, in its form traditionally invoked when explaining the anomeric effect, does not seem to provide enough repulsive energy to generate an anomeric effect – further strengthening our argument that the *eclipsed* conformation induced by the lack of hybridization at the anomeric oxygen atom is the main reason for the anomeric effect. It is important to note that the same computational methods that predict a 'non-hybrid' nature in the oxygen atom, do in fact predict an sp^3-like

orientation of the nitrogen-based molecular orbitals in systems as simple as ammonia. A final comment is that we are merely concerned with the spatial location of the lone pairs of the respective heteroatoms, and labels such as 'sp^3' should be viewed merely as such, and not as attempts to endorse an otherwise debated bonding theory.

Information extracted from Natural Bonding Orbital (NBO) analysis (cf. Table 1) for the models shown in Figure 1 indicates that in the equatorial conformer one of the oxygen's lone pairs is 56.4% s and 43.6% p character, while the other lone pair orbital is 0.3% s and 99.7% p, meaning that only one of the lone pairs is not hybrid. Likewise, in the axial conformer the percentages are 54% s and 46% p while the other lone pair is 1.4% s and 98.6% p. These data then may be taken to support an sp^2 description of the pyranoid oxygen. Such a description is in line with observations made on the spatial orientation of the oxygen models in most of the models in Figure 3 – and the spatial orientation of the pyranoid oxygen orbitals as well – in that they are not *all* perpendicular to each other. It remains to be debated whether the argument discussed above for the Figure 3 models, of repulsion between the atoms bound to the oxygen, is acceptable here as well, and whether the NBO data is a manifestation of that effect, or a cause.

Table 1. NBO Analysis for pyranoid oxygen in the equatorial conformer.
Only lone pair and Rydberg orbitals are shown.

OT	Equatorial Conformer		Axial Conformer	
	Occ	% Hybridation	Occ	Coefficients/ Hybrids
LP(1)	-1.97	s 56.42% p 43.58%	-1.96	s 49.61% p 50.39%
LP(2)	-1.93	s 0.36% p 99.64%	-1.90	s 0.87% p 99.13%
RY*1	-5.97e-3	s 16.75% p 83.25%	-5.12e^{-3}	s 1.26% p 98.74%
RY*2	-2.40e-3	s 22.45% p 77.55%	-2.23e^{-3}	s 6.57% p 93.43%
RY*3	-6.80e-3	s 11.55% p 88.45%	-16.0e-3	s 44.75% p 55.25%
RY*4	- 4.70e-3	s 12.73% p 87.27%	- 1.0e-3	s 10.76% p 89.24%

Abbreviations. OT: Orbital type; Occ: Occupancy. LP: Lonely pair orbital; RY*: Rydberg orbital.

CONCLUSIONS

In conclusion, the results shown here support the concept that the ability of the pyranoid oxygen to remain in a 'non-sp^3-hybridized'-like conformation, i.e. at 90º from each other, leads to an eclipsed position of an equatorial substituent at the carbon atom bound directly to this oxygen in a

tetrahydropyranoid structure, and this factor has an important role in the anomeric effect. This 'non-sp³-hybrid'-like (or even 'non-hybrid-like') situation of the oxygen atom is proposed to be relatively common in (bio)organic molecules.

METHODS

Geometries for all models were optimized using the BP86 functional, which uses the gradient-corrected exchange functional proposed by Becke,[7] the correlation functional by Perdew,[8] 6-31G** were used as implemented in Spartan.[9] For the SCF calculations, a fine grid was used, and the convergence criteria were set to 10^{-6} (for the root mean square of electron density) and 10^{-8} (energy), respectively. For geometry optimization, convergence criteria were set to 0.001 a.u. (maximum gradient criterion) and 0.0003 (maximum displacement criterion).

NBO analysis were obtained optimizing using density functional theory also with BVP86 functional and 6-31(d,p) basis set, at vacuum as implemented in Gaussian 09[10] using default SCF convergence criteria for geometry optimization.

ACKNOWLEDGMENTS

REFERENCES

1. Box V.G.S. *Heterocycles*, **1998**, *48*, 2389.
2. Takahashia O., Yamasakia K., Kohnob Y., Ohtakib R., Uedab R., Suezawac H., Umezawad Y., Nishioe M. *Carbohydr. Res*., **2007**, *342*, 1202.
3. Vila A., Mosquera R.A. *J Comput Chem*, **2007**, *28*, 1516.
4. Szarek W.A., Derek Horton D.; American Chemical Society: Washington, D.C., **1979**, pp 115.
5. Grein F., Deslongchamps P. *Can. J. Chem*., **1992**, *70*, 1562.
6. Woodcock H.L., Moran D., Pastor R.W., MacKerell A.D.J., Brooks B.R. *Biophys J*, **2007**, *93*, 1.
7. Becke A.D. *Phys. Rev*., **1988**, 3098.
8. Perdew J.P. *Phys. Rev*., **1986**, B33, 8822.
9. Spartan 5.0, Wavefunction, Inc., 18401 Von Karman Avenue Suite 370, Irvine, CA 92612 U.S.A.
10. Gaussian 09 (Revision A.02). Gaussian Inc. Wallingford, CT, C009.

THEORETICAL STUDY ON NITROGEN TRIFLUORIDE AND ITS ADDUCT WITH BF$_3$

HONGCHEN DU[a,*], PING YANG[a], LIJUN ZHANG[a], YU WANG[b,*]

ABSTRACT. The molecular and crystal structure of the adduct NF$_3$·BF$_3$ has been studied using complete basis set method (CBS-4M). It shows that the adduct exists in the form of complex but not ionic, the heat of formation of the gas and condensed phase of the adduct are -1266.09 and -1276.37 kJ·mol-1 respectively, which denotes it is stable under atmospheric conditions. The crystal form tends to crystalline in P21/c space group. The large calculated band gap (ΔEg) of the crystal proves it is stable, which is consistent with the conclusion from gas phase. The conduction band (LUCO) is mainly contributed from the p state of N atom and valence band (HOCO) from the p state of F atom.

Keywords: molecular, crystal, structure, property, theoretical study

INTRODUCTION

Molecular complexes containing boron trifluoride as a Lewis acid have been known for many years [1]. Nitrogen trifluoride (NF3) is a colorless, toxic, odourless, nonflammable gas, it was first prepared in 1928 by Ruff, Fischer, and Luft [2] by electrolyzing molten anhydrous ammonium bifluoride in an electrically heated copper cell. Nitrogen trifluoride can also be formed by the direct fluorination of ammonia. It is a stable gas with strong oxidizing properties, can be used as a potential oxidant for space-craft propulsion. Decades ago, the studies on the compound had been performed: the infrared spectrum of NF$_3$ has been reported by Bailey, Hale, and Thompson [3]. In 1950, NF$_3$ had been shown to have the C_{3v} symmetry [4,5].

Today nitrogen trifluoride is predominantly employed in the cleaning of the PECVD chambers in the high volume production of liquid crystal displays and silicon-based thin film solar cells. NF3 has been considered as an environmentally preferable substitute for sulfur hexafluoride or perfluorocarbons

---

[a] *School of Science, Zhejiang A & F university, Linan, 311300, China*
[b] *Zhejiang Provincial Key Laboratory of Chemical Utilization of Forestry Biomass, Zhejiang A & F University, Linan, 311300, China*
* *Corresponding authors: duhongc@zafu.edu.cn, yuwang79@gmail.com*

such as hexafluoroethane [6]. It proved to be far less reactive than the other nitrogen trihalides such as nitrogen trichloride, nitrogen tribromide and nitrogen triiodide, all of which are explosive. But explosion will occur when mixtures of nitrogen trifluoride with ammonia, hydrogen, methane, ethylene, carbon monoxide.

Understanding the nature of the structure-property relationship is of the fundamental importance for further investigation. However, the investigation on structure property relationship especially the crystal structure of NF_3 with BF_3 are limited, in 1996, Ford et al. performed a theoretical study on the adduct using *ab initio* method mainly about its binding energies [7].

As the adduct has similar properties with high energy density materials (HEDMs) which we are interested in, i.e., it is reactive and highly energetic but still stable enough under certain conditions, but the available information about it is limited, so we performed this study to predict its molecular and crystal structures and corresponding properties with the complete basis set method.

COMPUTATIONAL METHODS

The title compound was optimized at CBS-4M level, and vibrational analysis was performed thereafter for the most stable conformer with the Gaussian 03 program package [8].

The gas phase heat of formation ($\Delta_f H^\circ_{gas}$) was obtained using the following reaction:

$$NF_3 + BF_3 = NF_3 \cdot BF_3$$
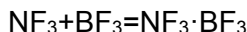
The changes in enthalpy (ΔH°_{298}) of the above reactions were evaluated using the following equation:

$$\Delta H^\circ_{298} = \sum \Delta_f H^\circ_{298,P} - \sum \Delta_f H^\circ_{298,R} = \Delta E_0 + \Delta E_{ZPE} + \Delta H^\circ_T + \Delta nRT$$

where $\sum \Delta_f H^\circ_{298,P}$ and $\sum \Delta_f H^\circ_{298,R}$ are the sum of the heats of formation of the products and reactants, respectively; ΔE_0 is the difference between the total energies of the products and the reactants at 0 K; ΔE_{ZPE} is the difference between the zero-point vibrational energy of the products and the reactants; ΔH^0_T is the difference between the thermal correction from 0 K to 298 K of the products and the reactants, Δn is the change in the quantity of gaseous substances, which is -1 here. In the reactions above, the experimental heats of formation of all reactants (BF_3, NF_3) are known [9], the heats of formation of the adduct can then be obtained with the calculated ΔH°_{298}.

Interaction energies were estimated from the energy differences between NF3 and BF3. The basis sets commonly used to calculate energies are far from being saturated. As a result, each sub-system in any complex will tend to lower its energy depending on the use of basis set functions of the other sub-system. The energies obtained at equilibrium geometry of complex for each sub-system are lower than those calculated at the same geometry with basis set functions of respective sub-system alone. This energy difference is so-called basis set superposition error (BSSE). The binding energies of the supermolecules are equal to the differences between the supermolecules and the monomers after correcting for the BSSE energies.

On the basis of the principle of statistical thermodynamics [10], standard molar heat capacity ($C^0_{p,m}$), entropy (S^0_m), and enthalpy (H^0_m) from 200 to 800 K were evaluated using the scaled frequencies.

To find the possible molecular packings in crystal phase, empirical Dreiding force field and polymorph module in MS [11] were used. Since most crystals belong to 7 space groups (P21/c, P-1, P212121, P21, Pbca, *C2/c*, and Pna21) on the basis of statistical data [12-15], the global search was confined in these groups only. By analyzing the simulation trajectory of molecular packing within 7 space groups, the structures were arranged in their ascending energies for each group and the one having the lowest energy was selected as the most possible packing with the corresponding space group. These possible crystal structures were then refined with the DFT GGA-RPBE method and CASTEP module [16].

RESULTS AND DISCUSSION

Molecular Structure

Figure 1 (left) lists the molecular structure of adduct under CBS-4M level, it can be seen that in unit of NF$_3$, the bond length of N-F are all similar but N1-F3 is slightly larger, which denotes N1-F3 is weaker. The bond length of B5-F3 is 2.33 Å, thus the bond is very weak. In addition, the negative charges on F(3) (-0.195e) is also similar with F(2) and F(4), implying the same properties between F(3) and other F atoms. The total charges of NF3 and BF$_3$ are nearly zero (0.075e and -0.075e), therefore, adduct exists in basically the complex form NF$_3 \cdot$BF$_3$ but not ionic form.

Sorescu et al. performed theoretical predictions for several energetic molecular crystals, and claimed that the dispersion-corrected density functional theory (DFT-D) method as parametrized by Grimme provides significant improvements for the description of intermolecular interactions in molecular crystals at both ambient and high pressures relative to conventional DFT [17]. Thus, DFT-D calculations are also included. DFT-D method was used in this article, Binding energy of the complex is only about -10 kJ·mol^{-1}.

Figure 1 (right) lists the molecular structure of the adduct under DFT-D level, we can see that the molecular structures are similar with each other.
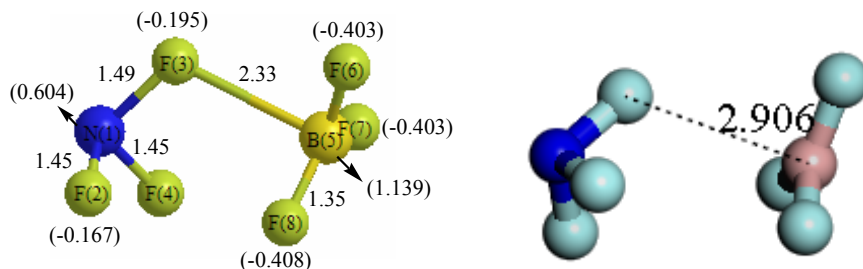
Figure 1. Structural parameters of the adduct obtained at CBS-4M (left) and DFT-D levels (bond lengths are in Å, Mulliken charges (in brackets) in e)

The molecular electrostatic potential (MEP) is used commonly in analyzing molecular reactivity and is very useful since it provides information about local polarity due to the charge density distribution. After having chosen some sort of region to be visualized, a color-coding convention is chosen to depict the MEP. Figure 2 illustrates the MEP for the 0.001 electron/bohr^3 isosurface of electron density at the CBS-4M level for the $NF_3 \cdot BF_3$, The color with red denoting the most negative potential and blue denoting the most positive potential. Inspection of the MEP for the title compound, the negative potentials appear to be distributed mostly on the fluoride atoms, and the positive ranges characterize at the center of the skeleton mainly on the nitrogen and boron atom. After taking into account of the basis set superposition error (BSSE), we found that the binding energy of the complex is only about -10 kJ·mol^{-1}.
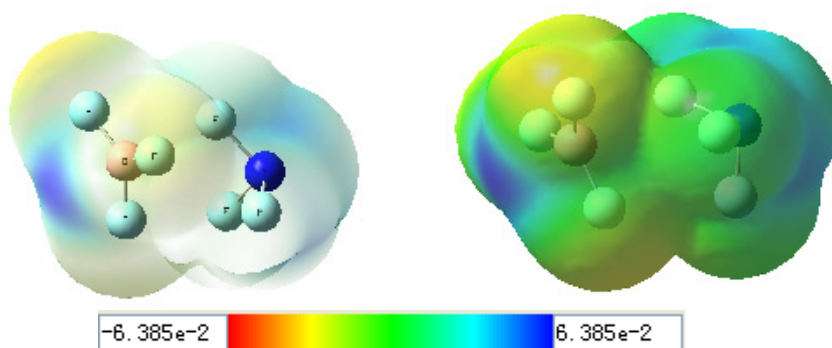
Figure 2. Molecular electrostatic potential (MEP) surface mapped onto 0.001 electron/bohr^3 contour of the electronic density for the title compound calculated at the CBS-4M level

Thermodynamic Properties

Based on the scaled vibrational frequencies and the principle of statistic thermodynamics, the standard thermodynamic properties are evaluated and shown in Figure 3. Obviously, with the increasing temperature, all the thermodynamic properties increase, which is mainly because the vibrational movement is intensified at the higher temperature and therefore makes more contributions to the thermodynamic properties. The relationships between the thermodynamic functions and temperature are found and shown as follows (the units of $C^{\circ}_{p,m}$, S°_{m}, H°_{m} are J·K^{-1}·mol^{-1}, J·K^{-1}·mol^{-1}, kJ·mol^{-1}, respectively, and the correlation coefficients are 0.9940, 0.9996, and 0.9999 respectively):
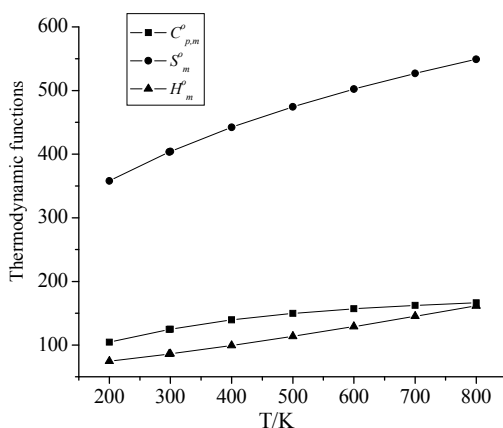
Figure 3. Relationships between the thermodynamic functions and temperature

$$C^{\circ}_{p,m} = 60.29 + 0.25\,T - (1.60\times10^{-4})T^2$$

$$S^{\circ}_{m} = 259.62 + 0.54\,T - (2.35\times10^{-4})T^2$$

$$H^{\circ}_{m} = 52.49 + 0.09\,T + (4.77\times10^{-5})T^2$$

From these equations, we have

$$\frac{dC^{o}_{p,m}}{dT} = 0.25 - (3.20\times10^{-4})T$$

$$\frac{dS^{o}_{m}}{dT} = 0.54 - (4.70\times10^{-4})T$$

$$\frac{dH^{o}_{m}}{dT} = 0.09 + (9.54\times10^{-5})T$$

Obviously, with the increase of temperature, the increasements of $C^0_{p,m}$ and S^0_m decrease, while that of H^0_m increases.

Gas-Phase Heats of Formation

Heat of formation is usually taken as the indicator of the "energy content" of a compound, it is very important to predict the heat of formation accurately. The gas-phase heat of formation ($\Delta_f H^\circ_{gas}$) has been estimated using the above reaction. The experimental ($\Delta_f H^\circ_{gas}{}^{exp}$) and predicted ($\Delta_f H^\circ_{gas}{}^{pre}$) $\Delta_f H^\circ_{gas}$ using the reaction of $NF_3 \cdot BF_3$ are shown in Table 1, we can see that the $\Delta_f H^\circ_{gas}$ of the adduct is large and negative (-1266.09 kJ·mol^{-1}), which indicates the adduct is stable under atmospheric condition.

Table 1. Total energies (E_0) at the CBS-4M level and the gas-phase heats of formation

Compounds	E_0 (a.u.)	$\Delta_f H^\circ_{gas}{}^{exp}$ (kJ·mol^{-1})	$\Delta_f H^\circ_{gas}{}^{pre}$ (kJ·mol^{-1})
BF$_3$	-324.6964	-1135.60	
-NF$_3$	-354.2227	-132.09	
NF$_3$·BF$_3$	-678.9213		-1266.09

Condensed–Phase Heats of Formation

For a crystal, the lattice energy (E_{latt}) is important for predicting its structural and physicochemical properties such as polymorphism and growth morphology. E_{latt} can be calculated from the energy difference between the crystal ($E_{crystal}$) and the isolated molecules ($E_{molcule}$), i.e.,

$$E_{latt} = E_{crystal} - Z\, E_{molecule}$$

where Z is the number of molecules in unit cell and equals to 4 here. E_{latt} is therefore the energy required for vaporizing a crystal and represents the strength of cohesion or interaction between molecules in the solid state. A negative value of E_{latt} indicates an attractive intermolecular interaction in a crystal. The lattice energies of $NF_3 \cdot BF_3$ obtained at DFT GGA/RPBE level is -20.19 kJ·mol^{-1}.

E_{latt} was further used to evaluate the enthalpy of sublimation (ΔH_{sub}) using the following relationship [18]:

$$-\Delta H_{sub} = E_{latt} + E_{ZPE} + ZRT$$

A rough estimation of the ΔH_{sub} is obtained by neglecting the E_{ZPE} term, and the solid phase heat of formation ($\Delta_f H^\circ_{solid}$) is then predicted from $\Delta_f H^\circ_{gas}$:

$$\Delta_f H°_{solid}=\Delta_f H°_{gas}-\Delta H_{sub}$$

The calculated $\Delta_f H°_{solid}$ of $NF_3 \cdot BF_3$ is -1276.37 kJ·mol^{-1}.

Crystal Structure

As is known, among the 230 space groups, over 80% organic crystals belong to 7 typical space groups based on the statistical data, which are $P2_1/c$, $P2_12_12_1$, P-1, $Pbca$, $C2/c$, $Pna2_1$ and $P2_1$ [19-22]. The chosen force field methods (Universal and Dreiding) are commnly used to do a global search in the above 7 space groups, and finally 7 most stable polymorphs are obtained, the polymorph with the lowest energy will be recommended as the reasonable crystal from (Table 2).

According to the principle the most possible polymorph usually possesses lower energy, it can be concluded from Table 2 that $NF_3 \cdot BF_3$ tends to crystalline in $P2_1/c$ from both Universal and Dreiding force field.

The density functional theory method DFT-GGA-RPBE was then performed to optimize the predicted packing $P2_1/c$, the corresponding cell parameters are a=6.93 Å, b=13.44 Å, c=5.79 Å, α=90.00º, β=116.60º, γ=90.00º, ρ=1.72 g·cm^{-3} (Figure 4).

Table 2a. Possible molecular packing for $NF_3 \cdot BF_3$ in 7 most possible space groups obtained from the universal force field

Space groups	$P2_1/c$	$P2_12_12_1$	P-1	$Pbca$	$C2/c$	$Pna2_1$	$P2_1$
Z	**4**	4	2	8	8	4	2
E/ kcal/mol/asym cell	**-7.92**	-7.73	-7.84	-7.85	-7.82	-7.86	-7.91
a/ Å	**4.49**	12.11	5.91	12.01	12.93	12.40	4.82
b/ Å	**14.22**	4.81	7.52	5.01	4.42	4.79	7.09
c/ Å	**6.59**	7.27	4.85	13.94	16.79	7.05	6.14
α/ °	**90.00**	90.00	86.84	90.00	90.00	90.00	90.00
β/ °	**82.57**	90.00	101.08	90.00	118.73	90.00	97.21
γ/ °	**90.00**	90.00	86.38	90.00	90.00	90.00	90.00
ρ/ g·cm^{-3}	**2.21**	2.18	2.18	2.20	2.19	2.20	2.21

Table 2b. Possible molecular packing for $NF_3 \cdot BF_3$ in 7 most possible space groups obtained from the Dreiding force field

Space groups	$P2_1/c$	$P2_12_12_1$	P-1	$Pbca$	$C2/c$	$Pna2_1$	$P2_1$
Z	**4**	4	2	8	8	4	2
E/ kcal/mol/asym cell	**-6.07**	-5.80	-5.98	-5.69	-5.95	-5.89	-5.93
a/ Å	**4.66**	6.24	4.76	8.823	17.71	12.70	6.35
b/ Å	**14.56**	8.82	11.35	15.61	4.79	4.94	7.30
c/ Å	**10.62**	8.36	6.82	6.75	13.06	7.29	4.97
α/ °	**90.00**	90.00	128.56	90.00	90.00	90.00	90.00
β/ °	**141.21**	90.00	73.23	90.00	124.40	90.00	98.01
γ/ °	**90.00**	90.00	126.98	90.00	90.00	90.00	90.00
ρ/ g·cm^{-3}	**2.04**	2.01	2.02	1.98	2.02	2.02	2.02
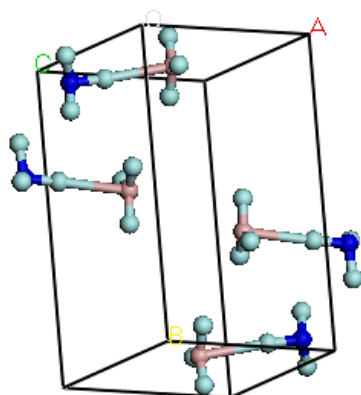
Figure 4. The optimized cell using DFT-GGA-RPBE method

Band Structure and Density of States

In principle, band gap (ΔE_g) between the highest occupied crystal orbital (HOCO) and the lowest unoccupied crystal orbital (LUCO) can be used as a criterion to predict the sensitivity of energetic materials with similar structure, and the smaller the ΔE_g, the easier the electron transits, and the larger the sensitivity will be. This principle has been illustrated by many experimental results and is useful both for the ionic crystals [23–27], and molecular crystals [28]. Figure 5 presents the band of the predicted most probable packing using the GGA-RPBE method, it can be seen that the ΔE_g of the title compound is large (6.06 eV) which denotes that the crystal form of the adduct is also stable.
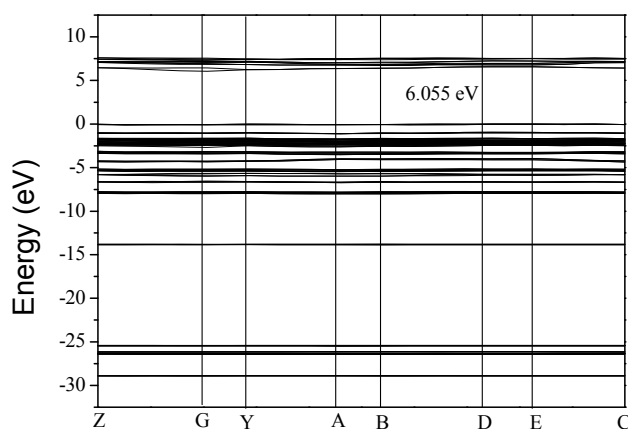
Figure 5. Banding structure of the title compound

Density of state is a presentation of the band structure of a crystal. A better understanding of the band structure is its PDOS, in which DOS is projected on atom-centered orbital, and PDOS can be used to investigate the constitution of energy bands. Figure 6 gives the DOS and PDOS of the predicted crystal structure using the GGA-RPBE method, and the origin of the energy is taken to be the Fermi level (the vertical dotted line). It is noted that the conduction band (LUCO) is mainly contributed from the *p* state of N atom and valence band (HOCO) from the *p* state of F atom.
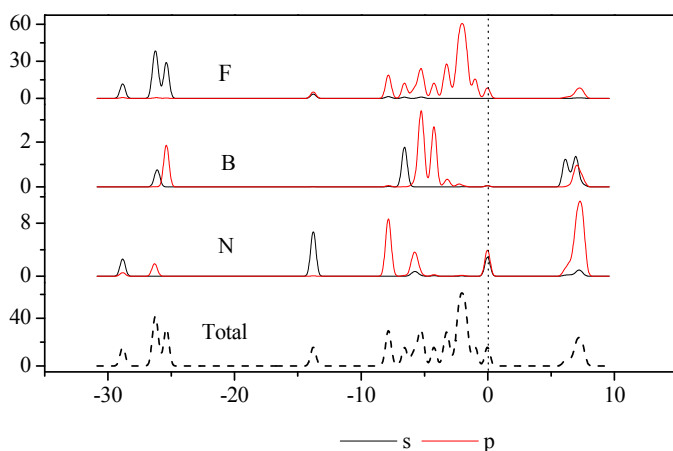
Figure 6. DOS and partial DOS of the adduct

CONCLUSIONS

The molecular and crystal structure of adduct $NF_3 \cdot BF_3$ has been investigated computationally using density functional theory. The adduct exists in complex form but not ionic. The heat of formation of the gas and condensed phase of the adduct are -1266.09 and -1276.37 kJ·mol^{-1}, respectively. Its crystal tends to crystalline in *P*2$_1$/*c* space group, the optimized cell parameters are *a*=6.93 Å, *b*=13.44 Å, *c*=5.79 Å, α=90.00º, *β*=116.60º, *γ*=90.00º, *ρ*=1.72 g·cm^{-3} under DFT-GGA-RPBE level. The calculated large band gap (6.06eV) proves the crystal is also stable, the conduction band (LUCO) is mainly contributed from the *p* state of N atom and valence band (HOCO) from the *p* state of F atom.

ACKNOWLEDGMENTS

REFERENCES

1. N.N. Greenwood, R. L. Martin, *Quart. Rev.,* **1954**, *8*, 1.
2. O. Ruff, J. Fischer, F. Luft, *Z. Anorg. Chem.,* **1928**, *172*, 417.
3. C.R. Bailey, J.B. Hale, J.W. Thompson, *J. Chem. Phys.,* **1937**, *5*, 274.
4. S. John, W. Gordy, *Phys. Rev.,* **1950**, *79*, 513.
5. V. Schomaker, Chia-Si Lu, *J. Am. Chem. Soc.,* **1950**, *72*, 1182.
6. H. Reichardt, A. Frenzel, K. Schober, *Microelectron. Eng.,* **2001**, *56*, 73.
7. T.A. Ford, D. Steele, *J. Phy. Chem.,* **1996**, *100*, 19336.
8. M.J. Frisch, G.W. Trucks, J.A. Pople, Gaussian-98, Revision A.7, Gaussian, Inc., Pittsburgh PA, **2003**.
9. M.W. Chase, C.A. Davies, J.R. Downey, D.J. Frurip, R.A. McDonald, A.N. Syverud, JANAF Thermochemical Tables, 3rd ed. *J. Phys. Chem. Ref. Data*, **1985**, 14, Suppl. 1.
10. T.L. Hill, Introduction to Statistic Thermodynamics, Addison-Wesley, New York, **1960**.
11. Materials Studio, Version 4.4, Accelrys Software, San Diego, **2008**.
12. A.J.C. Wilson, *Acta Crystallogr Sect A: Found Crystallogr.,* **1988**, *44*, 715.
13. A.D. Mighell, V.L. Himes, J.R. Rodgers, *Acta Crystallogr Sect A: Found Crystallogr.,* **1983**, *39*, 737.
14. R. Srinivasan, *Acta Crystallogr. Sect A: Found Crystallogr.,* **1992**, *48*, 917.
15. W.H. Bau, D. Kassner, *Acta Crystallogr. Sect B: Struct. Sci.,* **1992**, *48*, 356.
16. M.D. Segall, P.J.D. Lindan, M.J. Probert, C.J. Pickard, P.J. Hasnip, S.J. Clark, M.C.J. Payne, *J. Phys-Condens. Mat.,* **2002**, *14*, 2717.
17. S. Grimme, *Journal of Computational Chemistry,* **2006**, *27*, 1787.
18. C. Giacovazzo, Fundamentals of Crystallography, Oxford University Press: New York, **1992**.
19. A.J.C. Wilson, Space groups rare for organic structures. I. Triclinic, *Acta Crystallogr. Sect A: Found Crystallogr.,* **1988**, *44*, 715.
20. A.D. Mighell, V.L. Himes, J.R. Rodgers*, Acta Crystallogr. Sect A: Found Crystallogr.,* **1983**, *39*, 737.
21. R. Srinivasan, *Acta Crystallogr. Sect A: Found Crystallogr.,* **1992**, *48*, 917.
22. W.H. Baur, D. Kassner, *Acta Crystallogr. Sect B: Struct. Sci.,* **1992**, *48*, 356.
23. G. Wang, C. Shi, X. Gong, *J. Hazard. Mater.,* **2009**, *169*, 813.
24. H. Xiao, Y. Li, Banding and electronic structures of metal azides, Science Press, Beijing, **1996** (in Chinese).
25. W. Zhu, J. Xiao, H. Xiao, *J. Phy. Chem. B,* **2006**, *110*, 9856.
26. W. Zhu, J. Xiao, H. Xiao, *Chem. Phy. Lett.,* **2006**, *422*, 117.
27. X. Xu, H. Xiao, J. Xiao, *J. Phy. Chem. B,* **2006**, *110*, 7203.
28. W. Zhu, J. Xiao, G. Ji, *J. Phy. Chem. B,* **2007**, *11*, 12715.

ON TOPOLOGICAL PROPERTIES
OF NANOCONES CNC$_k$[n]

SAKANDER HAYAT[a], MUHAMMAD IMRAN[a,*]

ABSTRACT. In this paper, we compute fourth atom-bond connectivity indices and fifth geometric-arithmetic indices for conical graphite. We also compute atom-bond conncetivity (ABC) and geometric-arithmetic (GA) indices for these conical graphite.

2010 Mathematics Subject Classification: *05C12, 05C90*

Keywords: *Atom-bond connectivity (ABC) index, Geometric-arithmetic (GA) index, ABC$_4$ index, GA$_5$ index, CNC$_k$[n] nanocones*

INTRODUCTION

Mathematical calculations are of much importance to investigate essential concepts in chemistry. There is a substantial use of graph theory in chemistry. *Chemical graph theory* is the subject in which we model chemical structures and then study these structures by using graph theoretical properties/invariants. In the last few decades there is a lot of research which has been done in this field. A *moleculer/chemical* graph is a simple finite hydrogen depleted graph in which vertices denote the atoms and edges denote the chemical bonds in underlying chemical structure.

A *topological index* is a function "Top" from $\sum$ to the set of real numbers, where $\sum$ is the set of finite simple graphs with the property that $Top(G) = Top(H)$ if both G and H are isomorphic. Obviously, the number of edges and vertices of a graph are topological indices also. A graph can be recognized by a numeric number, a polynomial, a sequence of numbers or a matrix which represents the whole graph, and these representations are aimed to be uniquely defined for that graph. Topological indices are graph invariants and are used for Quantitative Structure - Activity Relationship (QSAR) and Quantitative Structure-Property Relationship (QSPR) studies [1]. Many

[a] *Department of Mathematics, School of Natural Sciences (SNS), National University of Sciences and Technology (NUST), Sector H-12, Islamabad, Pakistan*
* Corresponding author: imrandhab@gmail.com

topological indices have been defined and several of them have found applications as means to model physical, chemical, pharmaceutical and other properties of molecules.

A *nanostructure* is an object of intermediate size between microscopic and molecular structures. It is a product derived through engineering at molecular scale. *Carbon nanocones* are conical structures which are allotropes of carbon having at least one dimension of the order one micrometer or smaller. Carbon cones have also been observed, since 1968 or even earlier, on the surface of naturally occurring graphite. Their bases are attached to the graphite and their height varies between less than 1 and 40 micrometers. The analytical applications of carbon nanocones are still quite limited, however, and fall in the field of solid-phase extraction, in which surpassed carbon nanotubes thanks to their lower aggregation tendency.

Throughout this article, G is considered to be a connected graph with the vertex set $V(G)$ and edge set $E(G)$, d_u is the degree of vertex $u \in V(G)$ and $S_u = \sum_{v \in N_G(u)} d_G(v)$ where $N_G(u) = \{v \in V(G) \mid uv \in E(G)\}$.
The notations used in this paper are mainly taken from books [2,3].

The first degree-based connectivity index for the graphs, constructed on the ground of vertex degrees is *Randić* index [4]. The Randić index of graph G is defined as

$$R_{-\frac{1}{2}}(G) = \sum_{uv \in E(G)} \frac{1}{\sqrt{d_u d_v}}$$

The general *Randić* connectivity index $R_\alpha(G)$ is the sum of $(d_u d_v)^\alpha$ over all edges $e = uv \in E(G)$ defined as

$$R_\alpha(G) = \sum_{uv \in E(G)} (d_u d_v)^\alpha$$

Obviously $R_{-\frac{1}{2}}(G)$ is the particular case of $R_\alpha(G)$ when $\alpha = -\frac{1}{2}$.

One of the well-known connectivity topological index is *atom-bond connectivity* (ABC) index, introduced by *Estrada* et al. in [5]. The ABC index of graph G is defined as

$$ABC(G) = \sum_{uv \in E(G)} \sqrt{\frac{d_u + d_v - 2}{d_u d_v}}$$

Another well-known connectivity topological descriptor is *geometric-arithmetic* (GA) index, introduced by *Vukičević* et al. in [6]. The GA index for graph G is defined by

$$GA(G) = \sum_{uv \in E(G)} \frac{2\sqrt{d_u d_v}}{d_u + d_v}$$

The fourth version of ABC index was introduced by *Ghorbani* et al. [7] in 2010. For graph G, the ABC_4 index is defined as

$$ABC_4(G) = \sum_{uv \in E(G)} \sqrt{\frac{S_u + S_v - 2}{S_u S_v}}$$

Recently, the fifth version of GA index was proposed by *Graovac* et al. [8] in 2011. The GA_5 index for graph G is defined as follows

$$GA_5(G) = \sum_{uv \in E(G)} \frac{2\sqrt{S_u S_v}}{(S_u + S_v)}$$

In this paper, we discuss two topological descriptors, namely ABC_4 and GA_5 indices for $CNC_k[n]$, $3 \le k \le 6$ nanocones. We also present the two important types of partitions of $CNC_k[n]$ nanocones in two parameters k and n, and then apply them on nanocones $CNC_k[n]$ to compute certain topological indices.

RESULTS AND DISCUSSON

In this paper, we find general partitions of the edge set of $CNC_k[n]$ nanocones for $n \ge 1, k \ge 3$, based on the degrees sum of neighbors of each edge and degrees of end vertices for each. We used these partitions to computed ABC_4, GA_5, *ABC* and *GA* indices of these nanocones.

Results for *CNC₃[n]* Nanocones

In this section, we compute exact formulas of ABC_4 and GA_5 indices of $CNC_3[n]$ nanocones. A $CNC_3[n]$ nanocone consists of a triangle as its core and encompassing the layers of hexagons on its conical surface. If there are n layers of hexagons on the conical surface around triangle, then we denote the graph of that nanocones as $CNC_3[n]$ in which n denotes the number of layers of hexagons while the subscript number shows the

sides of polygon which acts as the core of nanocones. The $CNC_3[2]$ nanocone is shown in Figure 1. We have $|V(CNC_3[n])| = 3(n+1)^2$ and $|E(CNC_3[n])| = \frac{9}{2}n^2 + \frac{15}{2}n + 3$. In the next theorem, we compute the ABC_4 index of $CNC_3[n]$ nanocones.

Theorem 1. *Consider the graph of $CNC_3[n]$ nanocones, for $n \geq 1$, then their ABC_4 index is equal to*

$$ABC_4(CNC_3[n]) = 2n^2 + (\frac{\sqrt{462}}{7} + \frac{3\sqrt{2}-2}{3})n + \frac{6\sqrt{2}}{5} + \frac{6\sqrt{14}}{17} - \frac{\sqrt{462}}{7}$$

Proof. Let G be the graph of $CNC_3[n]$ nanocones. We find the edge partition of $CNC_3[n]$ nanocones based on the degree sum of vertices lying at the unit distance from end vertices of each edge, as in Table 1.

Table 1. The edge partition of $CNC_3[n]$

(S_u, S_v) where $uv \in E(G)$	(5,5)	(5,7)	(6,7)	(7,9)	(9,9)
Number of edges	3	6	$6(n-1)$	$3n$	$\frac{9}{2}n^2 - \frac{3}{2}n$

Now we can apply the formula of ABC_4 index to compute it for G. Since

$$ABC_4(G) = \sum_{uv \in E(G)} \sqrt{\frac{S_u + S_v - 2}{S_u S_v}}, \text{ then}$$

$$ABC_4(G) = (3)\sqrt{\frac{5+5-2}{5\times 5}} + (6)\sqrt{\frac{5+7-2}{5\times 7}} + 6(n-1)\sqrt{\frac{6+7-2}{6\times 7}} +$$

$$(3n)\sqrt{\frac{7+9-2}{7\times 9}} + (\frac{9}{2}n^2 - \frac{3}{2}n)\sqrt{\frac{9+9-2}{9\times 9}}$$

After simplification, we get

$$ABC_4(G) = 2n^2 + (\frac{\sqrt{462}}{7} + \frac{3\sqrt{2}-2}{3})n + \frac{6\sqrt{2}}{5} + \frac{6\sqrt{14}}{17} - \frac{\sqrt{462}}{7} \qquad \square$$
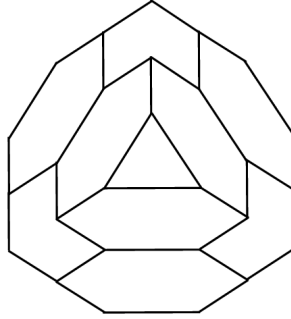
Figure 1. Graph of $CNC_3[2]$ nanocone.

The GA_5 index for $CNC_3[n]$ nanocones is computed in the following theorem.

Theorem 2. *Consider the graph of $CNC_3[n]$ nanocones, for $n \geq 1$, then their GA_5 index is equal to*

$$GA_5(CNC_3[n]) = \frac{9}{2}n^2 + \left(\frac{12\sqrt{42}}{13} + \frac{9\sqrt{7}}{8} - \frac{3}{2}\right)n + \sqrt{35} - \frac{12\sqrt{42}}{13} + 3$$

Proof. Let G be the graph of $CNC_3[n]$ nanocones. The edge partition of $CNC_3[n]$ nanocones based on the degree sum of vertices lying at the unit distance from end vertices of each edge is given in Table 1.

Now we apply the formula of GA_5 index to compute this index for G. Since

$$GA_5(G) = \sum_{uv \in E(G)} \frac{2\sqrt{S_u S_v}}{S_u + S_v}, \text{ then}$$

$$GA_5(G) = (3)\frac{2\sqrt{5 \times 5}}{5 + 5} + (6)\frac{2\sqrt{5 \times 7}}{5 + 7} + 6(n-1)\frac{2\sqrt{6 \times 7}}{6 + 7} + (3n)\frac{2\sqrt{7 \times 9}}{7 + 9} +$$

$$\left(\frac{9}{2}n^2 - \frac{3}{2}n\right)\frac{2\sqrt{9 \times 9}}{9 + 9}$$

After simplification, we get

$$GA_5(G) = \frac{9}{2}n^2 + \left(\frac{12\sqrt{42}}{13} + \frac{9\sqrt{7}}{8} - \frac{3}{2}\right)n + \sqrt{35} - \frac{12\sqrt{42}}{13} + 3 \qquad \square$$

Results for *CNC₄[n]* Nanocones

In this section, we compute the ABC_4 and GA_5 indices of $CNC_4[n]$ nanocones. These $CNC_4[n]$ nanocones consist of a square as the core and tiling of hexagonal layers on its conical surface. A $CNC_4[2]$ nanocone is shown in Figure 2. The vertex and edge cardinalities are $|V(CNC_4[n])| = 4(n+1)^2$ and respectively $|E(CNC_4[n])| = 6n^2 + 10n + 4$.

Now we compute the closed formula for ABC_4 index of $CNC_4[n]$ nanocones in the following theorem.

Theorem 3. *Consider the graph of $CNC_4[n]$ nanocones, for $n \geq 1$, then their ABC_4 index is equal to*

$$ABC_4(CNC_4[n]) = \frac{8}{3}n^2 + (\frac{4\sqrt{462}}{21} + \frac{4\sqrt{2}}{3} - \frac{8}{9})n + \frac{8\sqrt{2}}{5} + \frac{8\sqrt{14}}{7} - \frac{4\sqrt{462}}{21}$$

Proof. Let G be the graph of $CNC_4[n]$ nanocones. We determine the edge partition of $CNC_4[n]$ based on the degree sum of neighbors of end vertices of each edge.

Table 2. The edge partition of $CNC_4[n]$

(S_u, S_v) where $uv \in E(G)$	(5,5)	(5,7)	(6,7)	(7,9)	(9,9)
Number of edges	4	8	$8(n-1)$	$4n$	$6n^2 - 2n$

Now we use this partition to compute ABC_4 index of $CNC_4[n]$ nanocones. Since

$$ABC_4(G) = \sum_{uv \in E(G)} \sqrt{\frac{S_u + S_v - 2}{S_u S_v}} \text{ , then}$$

$$ABC_4(G) = (4)\sqrt{\frac{5+5-2}{5 \times 5}} + (8)\sqrt{\frac{5+7-2}{5 \times 7}} + 8(n-1)\sqrt{\frac{6+7-2}{6 \times 7}} +$$

$$(4n)\sqrt{\frac{7+9-2}{7 \times 9}} + (6n^2 - 2n)\sqrt{\frac{9+9-2}{9 \times 9}}$$

After an easy simplification, we get

$$ABC_4(G) = \frac{8}{3}n^2 + (\frac{4\sqrt{462}}{21} + \frac{4\sqrt{2}}{3} - \frac{8}{9})n + \frac{8\sqrt{2}}{5} + \frac{8\sqrt{14}}{7} - \frac{4\sqrt{462}}{21} \qquad \square$$

Theorem 4. *Consider the graph of $CNC_4[n]$ nanocones, for $n \geq 1$, then their GA_5 index is equal to*

$$GA_5(CNC_4[n]) = 6n^2 + (\frac{16\sqrt{42}}{13} + \frac{3\sqrt{2}-4}{2})n + \frac{4\sqrt{35}}{3} - \frac{16\sqrt{42}}{13} + 4$$

Proof. Let G be the graph of $CNC_4[n]$ nanocones. The edge partition of $CNC_3[n]$ nanocones based on the degree sum of vertices lying at the unit distance from end vertices of each edge is given in Table 2.

Now we apply the formula of GA_5 index to compute this index for G.

Since

$$GA_5(G) = \sum_{uv \in E(G)} \frac{2\sqrt{S_u S_v}}{S_u + S_v},$$

then

$$GA_5(G) = (4)\frac{2\sqrt{5 \times 5}}{5+5} + (8)\frac{2\sqrt{5 \times 7}}{5+7} + 8(n-1)\frac{2\sqrt{6 \times 7}}{6+7} + (4n)\frac{2\sqrt{7 \times 9}}{7+9} +$$

$$(6n^2 - 2n)\frac{2\sqrt{9 \times 9}}{9+9}$$

After simplification, we get

$$GA_5(G) = 6n^2 + (\frac{16\sqrt{42}}{13} + \frac{3\sqrt{2}-4}{2})n + \frac{4\sqrt{35}}{3} - \frac{16\sqrt{42}}{13} + 4 \qquad \square$$
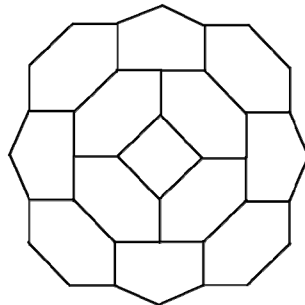
Figure 2. Graph of $CNC_4[n]$ nanocone with $n = 2$.

Results for *CNC₅[n]* Nanocones

In this section, we determine ABC_4 and GA_5 indices of $CNC_5[n]$ nanocones. The vertex and edge cardinalities are $|V(CNC_5[n])| = 5(n+1)^2$ and $|E(CNC_5[n])| = \dfrac{15}{2}n^2 + \dfrac{25}{2}n + 5$. This family of nanocones are often called *one pentagonal* nanocones, is depicted in Figure 3. In the following theorem, the ABC_4 index of $CNC_5[n]$ nanocones is computed.

Theorem 5. *Consider the graph of $CNC_5[n]$ nanocones, for $n \geq 1$, then their ABC_4 index is equal to*

$$ABC_4(CNC_5[n]) = \frac{10}{3}n^2 + (\frac{5\sqrt{462}}{21} + \frac{5\sqrt{2}}{3} - \frac{10}{9})n + \frac{10\sqrt{4}}{7} - \frac{5\sqrt{462}}{21} + 2\sqrt{2}$$

Proof. Consider G be the graph of $CNC_5[n]$ nanocones. We find the partition of edge set of $CNC_5[n]$ nanocones based on the degree sum of vertices lying at the unit distance from end vertices of each edge. Table 3 shows the data for theabove discussed edge partition of $CNC_5[n]$ nanocones.

Table 3. The edge partition of the graph of $CNC_5[n]$ nanocones

(S_u, S_v) where $uv \in E(G)$	(5,5)	(5,7)	(6,7)	(7,9)	(9,9)
Number of edges	5	10	$10(n-1)$	$5n$	$\dfrac{15}{2}n^2 - \dfrac{5}{2}n$

Now we use this partition to compute ABC_4 index of $CNC_4[n]$ nanocones. Since

$$ABC_4(G) = \sum_{uv \in E(G)} \sqrt{\frac{S_u + S_v - 2}{S_u S_v}} \text{ then,}$$

$$ABC_4(G) = (5)\sqrt{\frac{5+5-2}{5 \times 5}} + (10)\sqrt{\frac{5+7-2}{5 \times 7}} + 10(n-1)\sqrt{\frac{6+7-2}{6 \times 7}} +$$

$$(5n)\sqrt{\frac{7+9-2}{7 \times 9}} + (\frac{15}{2}n^2 - \frac{5}{2}n)\sqrt{\frac{9+9-2}{9 \times 9}}$$

After an easy simplification, we get

$$ABC_4(G) = \frac{10}{3}n^2 + (\frac{5\sqrt{462}}{21} + \frac{5\sqrt{2}}{3} - \frac{10}{9})n + \frac{10\sqrt{4}}{7} - \frac{5\sqrt{462}}{21} + 2\sqrt{2}$$ □

In the following theorem, the GA_5 index of $CNC_5[n]$ nanocones is computed.

Theorem 6. *Consider the graph of* $CNC_5[n]$ *nanocones, for* $n \geq 1$, *then their* GA_5 *index is equal to*

$$GA_5(CNC_5[n]) = \frac{15}{2}n^2 + (\frac{20\sqrt{42}}{13} + \frac{15\sqrt{7}}{8} - \frac{5}{2})n + \frac{5\sqrt{35}}{3} - \frac{20\sqrt{42}}{13} + 5$$

Proof. Let G be the graph of $CNC_5[n]$ nanocones. The edge partition of $CNC_5[n]$ based on the degree sum of neighbors of end vertices of each edge is given in Table 3. Since

$$GA_5(G) = \sum_{uv \in E(G)} \frac{2\sqrt{S_u S_v}}{S_u + S_v} \quad \text{then,}$$

$$GA_5(G) = (5)\frac{2\sqrt{5 \times 5}}{5+5} + (10)\frac{2\sqrt{5 \times 7}}{5+7} + 10(n-1)\frac{2\sqrt{6 \times 7}}{6+7} + (5n)\frac{2\sqrt{7 \times 9}}{7+9}$$
$$+ (\frac{15}{2}n^2 - \frac{5}{2}n)\frac{2\sqrt{9 \times 9}}{9+9}$$

After simplification, we get

$$GA_5(G) = \frac{15}{2}n^2 + (\frac{20\sqrt{42}}{13} + \frac{15\sqrt{7}}{8} - \frac{5}{2})n + \frac{5\sqrt{35}}{3} - \frac{20\sqrt{42}}{13} + 5$$ □
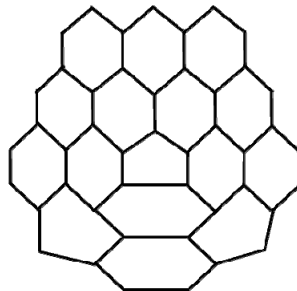
Figure 3. Graph of one pentagonal nanocone $CNC_5[n]$ with $n = 2$.

Results for *CNC₆[n]* Nanocones

Now we compute ABC_4 and GA_5 indices of $CNC_6[n]$ nanocones. In this family of nanocones the hexagon acts as the core for the surrounding hexagonal layers; in fact, it is a coronene family. For such a plane graph we have $|V(CNC_6[n])| = 6(n+1)^2$ and $|E(CNC_6[n])| = 9n^2 + 15n + 6$. A graph of $CNC_6[3]$ nanocone is depicted in Figure 4. In the following theorem, ABC_4 index of $CNC_6[n]$ nanocones is exhibited.

Theorem 7. *Consider the graph of $CNC_6[n]$ nanocones, for $n \geq 1$ then their ABC_4 index is equal to*

$$ABC_4(CNC_6[n]) = 4n^2 + \left(\frac{2\sqrt{462}}{7} + 2\sqrt{2} - \frac{4}{3}\right)n + \frac{12\sqrt{2}}{5} + \frac{12\sqrt{14}}{17} - \frac{2\sqrt{462}}{7}$$

Proof. Let G be the graph of $CNC_6[n]$ nanocones. We first compute the edge partition of $CNC_6[n]$ nanocones based on the degree sum of neighbors of end vertices of each edge (Table 4).

Table 4. The edge partition of $CNC_6[n]$

(S_u, S_v) where $uv \in E(G)$	(5,5)	(5,7)	(6,7)	(7,9)	(9,9)
Number of edges	6	12	$12(n-1)$	$6n$	$9n^2 - 3n$

Now we use this partition to compute ABC_4 index of $CNC_4[n]$ nanocones. Since

$$ABC_4(G) = \sum_{uv \in E(G)} \sqrt{\frac{S_u + S_v - 2}{S_u S_v}} \text{ then,}$$

$$ABC_4(G) = (6)\sqrt{\frac{5+5-2}{5 \times 5}} + (12)\sqrt{\frac{5+7-2}{5 \times 7}} + 12(n-1)\sqrt{\frac{6+7-2}{6 \times 7}} +$$

$$(6n)\sqrt{\frac{7+9-2}{7 \times 9}} + (9n^2 - 3n)\sqrt{\frac{9+9-2}{9 \times 9}}$$

After an easy simplification, we get

$$ABC_4(G) = 4n^2 + (\frac{2\sqrt{462}}{7} + 2\sqrt{2} - \frac{4}{3})n + \frac{12\sqrt{2}}{5} + \frac{12\sqrt{14}}{17} - \frac{2\sqrt{462}}{7} \qquad \square$$

In the following theorem, we compute GA_5 index of $CNC_6[n]$ nanocones.

Theorem 8. *Consider the graph of $CNC_6[n]$ nanocones, for $n \geq 1$ then their GA_5 index is equal to*

$$GA_5(CNC_6[n]) = 9n^2 + (\frac{24\sqrt{42}}{13} + \frac{9\sqrt{7}}{4} - 3)n + 2\sqrt{35} - \frac{24\sqrt{42}}{13} + 6$$

Proof. Let G be the graph of $CNC_6[n]$ nanocones. The required edge partition to compute GA_5 index is in Table 4. Since

$$GA_5(G) = \sum_{uv \in E(G)} \frac{2\sqrt{S_u S_v}}{S_u + S_v} \text{ then,}$$

$$GA_5(G) = (6)\frac{2\sqrt{5 \times 5}}{5+5} + (12)\frac{2\sqrt{5 \times 7}}{5+7} + 12(n-1)\frac{2\sqrt{6 \times 7}}{6+7} + (6n)\frac{2\sqrt{7 \times 9}}{7+9} +$$

$$(9n^2 - 3n)\frac{2\sqrt{9 \times 9}}{9+9}$$

After simplification, we get

$$GA_5(CNC_6[n]) = 9n^2 + (\frac{24\sqrt{42}}{13} + \frac{9\sqrt{7}}{4} - 3)n + 2\sqrt{35} - \frac{24\sqrt{42}}{13} + 6$$

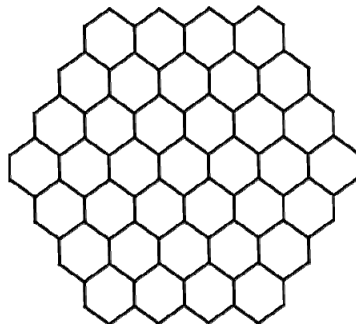**Figure 4.** Graph of $CNC_6[n]$ nanocone with $n = 3$.

Results for *CNC$_k$[n]* Nanocones

Now we determine the ABC_4 and GA_5 indices of $CNC_k[n], k \geq 3, n \geq 1$ nanocones. A general representation of $CNC_k[n]$ nanocones is shown in Figure 5 in which parameters k and n are shown. We have $|V(CNC_k[n])| = k(n+1)^2$ and $|E(CNC_k[n])| = \frac{3}{2}(kn^2) + \frac{5}{2}(kn) + k$. For further study of nanocones, see [9,10,11,12,13,14,15].

Table 5. The edge partition of $CNC_k[n]$ based on the degree sum of neighbors of end vertices of each edge

(S_u, S_v) where $uv \in E(G)$	(5,5)	(5,7)	(6,7)	(7,9)	(9,9)
Number of edges	k	$2k$	$2k(n-1)$	kn	$\frac{3}{2}kn^2 - \frac{1}{2}kn$

In the following theorem, we present exact formula to calculate ABC_4 index of $CNC_k[n], k \geq 3, n \geq 1$ nanocones.

Theorem 9. *Consider the graph of* $CNC_k[n], k \geq 3, n \geq 1$ *nanocones, then their* ABC_4 *index is equal to*

$$ABC_4(CNC_k[n]) = \frac{2\sqrt{2}}{5}(k) + \frac{\sqrt{14}}{7}(2k) + \frac{\sqrt{462}}{42}(2k(n-1)) +$$
$$\frac{\sqrt{2}}{3}(kn) + \frac{4}{9}(\frac{3}{2}(kn^2) - \frac{1}{2}(kn))$$

Proof. Consider the graph of $CNC_k[n], k \geq 3, n \geq 1$ nanocones. In order to compute the ABC_4 index of $CNC_k[n]$ nanocones, we find the general partition of $CNC_k[n]$ nanocones in two parameters k and n based on the degree sum of vertices lying at unit distance from end vertices of each edge. Table 5 shows such partition.

Now by using the edge partition given in Table 5, we compute the ABC_4 index of $CNC_k[n]$ nanocones. Since

$$ABC_4(G) = \sum_{uv \in E(G)} \sqrt{\frac{S_u + S_v - 2}{S_u S_v}} \text{ then,}$$

$$ABC_4(CNC_k[n]) = (k)\sqrt{\frac{5+5-2}{5\times 5}} + (2k)\sqrt{\frac{5+7-2}{5\times 7}} + 2k(n-1)\sqrt{\frac{6+7-2}{6\times 7}} +$$

$$(kn)\sqrt{\frac{7+9-2}{7\times 9}} + (\frac{3}{2}kn^2 - \frac{1}{2}kn)\sqrt{\frac{9+9-2}{9\times 9}}$$

After an easy simplification, we get

$$ABC_4(CNC_k[n]) = \frac{2\sqrt{2}}{5}(k) + \frac{\sqrt{14}}{7}(2k) + \frac{\sqrt{462}}{42}(2k(n-1)) +$$

$$\frac{\sqrt{2}}{3}(kn) + \frac{4}{9}(\frac{3}{2}(kn^2) - \frac{1}{2}(kn))$$

Following theorem exhibits the GA_5 index of $CNC_k[n]$ nanocones.

Theorem 10. *Consider the graph of* $CNC_k[n], k \geq 3, n \geq 1$ *nanocones, then their* GA_5 *index is equal to*

$$GA_5(CNC_k[n]) = k + \frac{\sqrt{35}}{6}(2k) + \frac{2\sqrt{42}}{13}(2k(n-1)) + \frac{3\sqrt{7}}{8}(kn) +$$

$$(\frac{3}{2}(kn^2) - \frac{1}{2}(kn))$$

Proof. Consider G be the graph of $CNC_k[n], k \geq 3, n \geq 1$ nanocones. We have $|V(CNC_k[n])| = k(n+1)^2$ and $|E(CNC_k[n])| = \frac{3}{2}(kn^2) + \frac{5}{2}(kn) + k$. By using the edge partition given in Table 5, we compute the ABC_4 index of $CNC_k[n]$ nanocones. Since

$$GA_5(G) = \sum_{uv \in E(G)} \frac{2\sqrt{S_u S_v}}{S_u + S_v} \text{ then,}$$

$$GA_5(G) = (k)\frac{2\sqrt{5\times 5}}{5+5} + (2k)\frac{2\sqrt{5\times 7}}{5+7} + 2k(n-1)\frac{2\sqrt{6\times 7}}{6+7} + (kn)\frac{2\sqrt{7\times 9}}{7+9} +$$

$$(\frac{3}{2}kn^2 - \frac{1}{2}kn)\frac{2\sqrt{9\times 9}}{9+9}$$

After simplification, we get

$$GA_5(CNC_k[n]) = k + \frac{\sqrt{35}}{6}(2k) + \frac{2\sqrt{42}}{13}(2k(n-1)) + \frac{3\sqrt{7}}{8}(kn) + (\frac{3}{2}(kn^2) - \frac{1}{2}(kn))$$

Now we compute the edge partition of $CNC_k[n]$ nanocones with respect to degree of end vertices of edges. Table 6 shows such a partition of $CNC_k[n]$ nanocones.

Table 6. The edge partition of $CNC_k[n]$ based on the degrees of end vertices of each edge.

(d_u, d_v) where $uv \in E(G)$	(2,2)	(2,3)	(3,3)
Number of edges	k	$2kn$	$\frac{3}{2}kn^2 + \frac{1}{2}kn$

In the following theorem, ABC index of $CNC_k[n]$ nanocones is presented.

Theorem 11. *Consider the graph of $CNC_k[n], k \geq 3, n \geq 1$ nanocones, then their ABC index is equal to*

$$ABC(CNC_k[n]) = \frac{\sqrt{2}}{2}(k(1+2n)) + \frac{2}{3}(\frac{3}{2}kn^2 + \frac{1}{2}kn)$$

Proof. By using the edge partition based on the degrees of end vertices of each edge of $CNC_k[n]$ nanocones given in Table 6 we compute the ABC index of $CNC_k[n]$ nanocones. Since

$$ABC(G) = \sum_{uv \in E(G)} \sqrt{\frac{d_u + d_v - 2}{d_u d_v}} \text{ then,}$$

$$ABC(CNC_k[n]) = (k)\sqrt{\frac{2+2-2}{2 \times 2}} + (2kn)\sqrt{\frac{2+3-2}{2 \times 3}} + (\frac{3}{2}kn^2 + \frac{1}{2}kn)\sqrt{\frac{3+3-2}{3 \times 3}}$$

After an easy simplification, we get

$$ABC(CNC_k[n]) = \frac{\sqrt{2}}{2}(k(1+2n)) + \frac{2}{3}(\frac{3}{2}kn^2 + \frac{1}{2}kn)$$

The GA index of $CNC_k[n]$ nanocones is computed in the following theorem.

Theorem 12. *Consider the graph of $CNC_k[n], k \geq 3, n \geq 1$ nanocones, then their GA index is equal to*

$$GA(CNC_k[n]) = k + \frac{2\sqrt{6}}{5}(2kn) + \frac{k}{2}(3n^2 + n)$$

Proof. By using the edge partition based on the degrees of end vertices of each edge of $CNC_k[n]$ nanocones given in Table 6 we compute the GA index of $CNC_k[n]$ nanocones. Since

$$GA(G) = \sum_{uv \in E(G)} \frac{2\sqrt{d_u d_v}}{d_u + d_v} \quad \text{then,}$$

$$GA(CNC_k[n]) = (k)\frac{2\sqrt{2 \times 2}}{2+2} + (2kn)\frac{2\sqrt{2 \times 3}}{2+3} + (\frac{3}{2}kn^2 + \frac{1}{2}kn)\frac{2\sqrt{3 \times 3}}{3+3}$$

After simplification, we get

$$GA(CNC_k[n]) = k + \frac{2\sqrt{6}}{5}(2kn) + \frac{k}{2}(3n^2 + n)$$
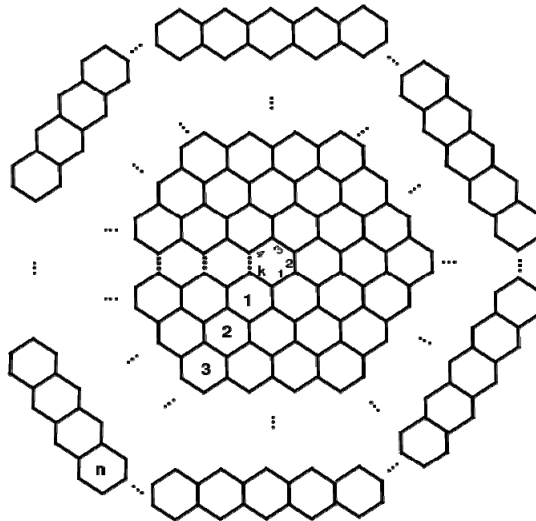
Figure 5. A general representation of graph of $CNC_k[n]$ nanocones.

CONCLUSIONS

In this paper, two new connectivity topological indices ABC_4 and GA_5 of $CNC_k[n], k \geq 3, n \geq 1$ nanocones were studied. We derived closed formulae of these topological indices for them. We found general partitions of the edge set of $CNC_k[n]$ nanocones based on the degrees sum of neighbors of each edge and degrees of end vertices for each. We used these partitions to computed ABC_4, GA_5, ABC and GA indices of $CNC_k[n], n \geq 1, k \geq 3$ nanocones.

ACKNOWLEDGMENTS

REFERENCES

1. M. Saheli, H. Saati, A.R. Ashrafi, *Optoelectron. Adv. Mater. Rapid Commun.*, **2010**, *4*, 896.
2. N. Trinajstić, *CRC Press, Boca Raton, FL,* **1992**.
3. I. Gutman, O.E. Polansky, *Springer-Verlag, New York*, **1986**.
4. M. Randić, *J. Amer. Chem. Soc.,* **1975**, *97*, 6609.
5. E. Estrada, L. Torres, L. Rodríguez, I. Gutman, *Indian J. Chem.*, **1998**, *37*, 849.
6. D. Vukičević, B. Furtula, *J. Math. Chem.,* **2009**, *46*, 1369.
7. M. Ghorbani, M.A. Hosseinzadeh, *Optoelectron. Adv. Mater. Rapid Commun.*, **2010**, *4*, 1419.
8. A. Graovac, M. Ghorbani, M.A. Hosseinzadeh, *J. Math. Nanosciences*, **2011**, *1*, 33.
9. A.E. Vizitiu and M.V. Diudea, *MATCH Commun. Math. Comput. Chem.*, **2008**, *60*, 927.
10. A. Ilić, M.V. Diudea, F. Gholami-Nezhaad, A.R. Ashrafi, Topological indices in nanocones in: I. Gutman, B. Furtula (Eds.), New Molecular Structure Descriptors - Theory and Applications I, *Univ. Kragujevac*, **2010**, 217.
11. Y. Alizadeh, S. Klavzar, M.A. Hosseinzadeh, *MATCH Commun. Math. Comput. Chem.*, **2013**, *69*, 523.
12. A. Khaksar, M. Ghorbani, H.R. Maimani, *Optoelectron. Adv. Mater. Rapid Commun.*, **2007**, *4*, 1868.
13. M.A. Alipour, A.R. Ashrafi, *J. Comput. Theor. Nanosci.,* **2009**, *4*, 1.
14. M. Ghorbani, M. Jalali, *MATCH Commun. Math. Comput. Chem.*, **2009**, *62*, 353.
15. M.H. Khalifeh, M.R. Darafsheh, Hassan Jolany, *J. Cur. Nanosci.*, **2013**, *9*, 557.

COMPUTING MODIFIED ECCENTRIC CONNECTIVITY INDEX AND CONNECTIVE ECCENTRIC INDEX OF V-PHENYLENIC NANOTORUS

NILANJAN DE[a,*], SK. MD. ABU NAYEEM[b] and ANITA PAL[c]

ABSTRACT. The modified eccentric connectivity index of a molecular graph is defined as the sum, of the products of eccentricity with the total degree of neighbouring vertices, over all vertices of the graph. On the other hand, the connective eccentric index of a graph is defined as the sum of the ratio of degree and eccentricity of the vertices. In this paper the exact expressions for the modified eccentric connectivity index and connective eccentric index of V-phenylenic nanotorus are computed.

Keywords: Eccentricity, V-phenylenic nanotorus, modified eccentric connectivity index, connective eccentric index.

INTRODUCTION

Topological indices are numeric quantities of a molecular graph G, which are invariants under the symmetry properties of G. In recent years a number of graph invariants related to vertex eccentricity have been derived and studied. Let G be a simple connected molecular graph with vertex set $V(G)$ and edge set $E(G)$. For any vertex $v \in V(G)$, let $\deg(v)$ denotes the number of first neighbor of v. The distance between the vertices u and v of G is equal to the length, that is the number of edges, of the shortest path connecting u and v and we denote it by $d(u,v)$. For a given vertex v, its eccentricity $\varepsilon(v)$ is the largest distance from v to any other vertices of G. If $N(v) = \{u \in V(G) : uv = e \in E(G)\}$, then the modified eccentric connectivity index of any graph is defined as

$$\xi_c(G) = \sum_{v \in V(G)} \delta(v)\varepsilon(v) \tag{1}$$

---

[a] *Department of Basic Sciences and Humanities (Mathematics), Calcutta Institute of Engineering and Management, Kolkata, India.*
[b] *Department of Mathematics, Aliah University. Kolkata, India.*
[c] *Department of Mathematics, National Institute of Technology, Durgapur, India.*
* *Corresponding author: de.nilanjan@rediffmail.com*

where, $\delta(v) = \sum_{u \in N(v)} \deg(u)$. There are several chemical as well as mathematical studies of this modified eccentric connectivity index and polynomial. In [1], the modified eccentric connectivity polynomial for three infinite classes of fullerenes was computed. In [2], a numerical method for computing modified eccentric connectivity polynomial and modified eccentric connectivity index of one-pentagonal carbon nanocones was presented. In [3], some exact formulas for the modified eccentric connectivity polynomial of Cartesian product, symmetric difference, disjunction and join of graphs were presented. Some upper and lower bounds for this modified eccentric connectivity index was recently studied by the present authors in [4]. Also in [5] modified eccentric connectivity index of generalized thorn graphs was presented.

Another vertex eccentricity based topological index, named the connective eccentricity index, was introduced by Gupta, Singh and Madan [6] and is defined as

$$C^{\xi}(G) = \sum_{v \in V(G)} \deg(v) \varepsilon(v)^{-1} \qquad (2)$$

In [7], M. Ghorbani gave some bounds of connective eccentricity index and also computed this index for two infinite classes of dendrimers. The eccentric connectivity index and the connective eccentric index of an infinite family of fullerenes was computed in [9] by Ghorbani and Malekjani. Yu and Feng, in [10] derived some upper or lower bounds for the connective eccentric index and investigated the maximal and the minimal values of connective eccentricity index among all n-vertex graphs with fixed number of pendent vertices. De [8] reported some bounds for this index in terms of some graph invariants. In [11] different graph operations of connective eccentric index were reported.

Carbon nanotubes are rolled-up sheets of graphite and if its ends meet, a nanotorus is produced. In this paper, we consider V–phenylenic nanotorus where the phenylenic lattice can be constructed from a square net embedded on the toroidal surface [17]. In figure 1, the molecular graph of V–phenylenic nanotorus is constructed from 4-, 6-, 8- gons. Studies of different topological indices of this nanotorus were reported in [12-16]. Let, in the two-dimensional lattice of V–phenylenic nanotorus, p denotes the number of hexagons in a fixed row and q denotes the number of hexagons in a fixed column, so that V–phenylenic nanotorus (TO) can be represented as TO(p,q). The molecular graph of this nanotorus TO(4,5) is given in Figure 1. For V–phenylenic nanotorus it is clear that, $|V(TO)| = 6pq$ and $|E(TO)| = 9pq$. Let u, v be two different vertices of TO. Then, we notice that $\varepsilon(u) = \varepsilon(v)$ and V–phenylenic nanotorus is cubic and thus for all $v \in V(TO)$, $\deg(v) = 3$. In this paper we derive some exact expressions for the modified eccentric connectivity index and the connective eccentric index of V-phenylenic nanotorus is computed.
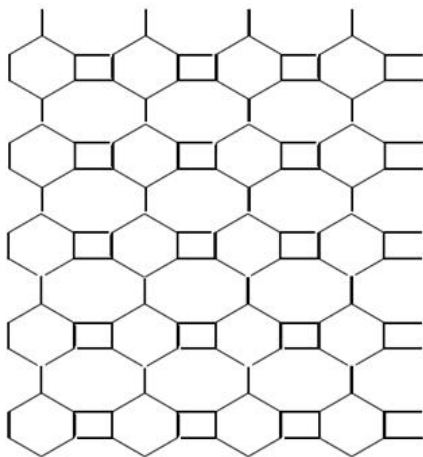
Figure 1. V-Phenylenic Nanotorus, TO[4,5].

MAIN RESULTS

The main aim of this section is to compute the modified eccentric connectivity index and connective eccentric index of the molecular graph of a V–phenylenic nanotorus for different values of p and q. Let us first consider the modified eccentric connectivity index of V–phenylenic nanotorus.

Proposition 1

Let p and q be even integers. Then the modified eccentric connectivity index of V-phenylenic nanotorus is computed as follows

$$\xi_c(TO) = \begin{cases} 27pq(p+4q) \text{ if } q \geq p \\ 27pq(3p+2q) \text{ if } q \leq p . \end{cases}$$

Proof: Since, a V–phenylenic nanotorus is cubic, so for all $v \in V(TO)$, $\delta(v) = 9$. We first assume that $q \geq p$. Then for all $v \in V(TO)$,

$$\varepsilon(v) = 2q + \frac{p}{2} = \frac{1}{2}(4q + p).$$

Thus, from (1)

$$\xi_c(TO) = \sum_{v \in V(TO)} \delta(v)\varepsilon(v) = \sum_{v \in V(TO)} \frac{9}{2}(4q + p) = \frac{9}{2}(p + 4q) \times |V(TO)|.$$

131

Again, if $q \leq p$ then for all $v \in V(TO)$, $\varepsilon(v) = q + \dfrac{3p}{2} = \dfrac{1}{2}(3p + 2q)$.

Hence, from (1)

$$\xi_c(TO) = \sum_{v \in V(TO)} \delta(v)\varepsilon(v) = \sum_{v \in V(TO)} \frac{9}{2}(3p + 2q) = \frac{9}{2}(3p + 4q) \times |V(TO)|.$$

which completes the proof. $\qquad\qquad\qquad\qquad\qquad\qquad\qquad\qquad\qquad\qquad$ $\square$

Proposition 2

Let p and q be odd integers. Then the modified eccentric connectivity index of V -phenylenic nanotorus is computed as follows

$$\xi_c(TO) = \begin{cases} 27pq(p + 4q - 1) \text{ if } q \geq p \\ 27pq(3p + 2q - 1) \text{ if } q \leq p \,. \end{cases}$$

Proof: Suppose, $q \geq p$, then for all $v \in V(TO)$,

$$\varepsilon(v) = 2q + \frac{p-1}{2} = \frac{1}{2}(4q + p - 1).$$

Also if $q \leq p$ then for all $v \in V(TO)$,

$$\varepsilon(v) = q + \frac{3p-1}{2} = \frac{1}{2}(3p + 2q - 1).$$

Since, for a V–phenylenic nanotorus $\delta(v) = 9$, for all $v \in V(TO)$, therefore the desired result follows similarly.

Proposition 3

Let p be even and q be odd integers. Then the modified eccentric connectivity index of V-phenylenic nanotorus is computed as follows

$$\xi_c(TO) = \begin{cases} 27pq(p + 4q) \text{ if } q \geq p \\ 27pq(3p + 2q) \text{ if } q \leq p \,. \end{cases}$$

Proof: Let us assume that $q \geq p$. Then for all $v \in V(TO)$,

$$\varepsilon(v) = 2q + \frac{p}{2} = \frac{1}{2}(4q + p).$$

Thus, from (1)

$$\xi_c(TO) = \sum_{v \in V(TO)} \delta(v)\varepsilon(v) = \sum_{v \in V(TO)} \frac{9}{2}(4q + p) = \frac{9}{2}(p + 4q) \times |V(TO)|.$$

Again, if $q \le p$ then for all $v \in V(TO)$, $\varepsilon(v) = q + \dfrac{3p}{2} = \dfrac{1}{2}(3p + 2q)$.

Therefore, from (1) we get

$$\xi_c(TO) = \sum_{v \in V(TO)} \delta(v)\varepsilon(v) = \sum_{v \in V(TO)} \frac{9}{2}(3p + 2q) = \frac{9}{2}(3p + 4q) \times |V(TO)|$$

from where the desired result follows.   □

Proposition 4

Let p be odd and q be even integers. Then the modified eccentric connectivity index of V-phenylenic nanotorus is computed as follows

$$\xi_c(TO) = \begin{cases} 27pq(p + 4q - 1) \text{ if } q \ge p \\ 27pq(3p + 2q - 1) \text{ if } q \le p \,. \end{cases}$$

Proof: Let, $q \ge p$, then all the vertices of TO are of eccentricity $2q + \dfrac{p - 1}{2} = \dfrac{1}{2}(4q + p - 1)$.

Similarly, if $q \le p$, then the eccentricity of all the vertices of TO is equal to $q + \dfrac{3p - 1}{2} = \dfrac{1}{2}(3p + 2q - 1)$.

Since, for a V–phenylenic nanotorus all the vertices are of degree 3, therefore the desired result follows similarly.   □

The above results can be summarized as follows:

Theorem 1

Let p be even, then the modified eccentric connectivity index of V-phenylenic nanotorus is given by

$$\xi_c(TO) = \begin{cases} 27pq(p + 4q) \text{ if } q \ge p \\ 27pq(3p + 2q) \text{ if } q \le p \end{cases}$$

and if p be odd, then the modified eccentric connectivity index of V-phenylenic nanotorus is given by

$$\xi_c(TO) = \begin{cases} 27pq(p + 4q - 1) \text{ if } q \ge p \\ 27pq(3p + 2q - 1) \text{ if } q \le p. \end{cases}$$

Now we compute connective eccentric index of the molecular graph of a V–phenylenic nanotorus for different values of p and q.

Proposition 5

Let p and q be even integers. Then the connective eccentric index of V-phenylenic nanotorus is computed as follows

$$C^{\xi}(TO) = \begin{cases} \dfrac{36pq}{(p+4q)} & \text{if } q \geq p \\ \dfrac{36pq}{(3p+2q)} & \text{if } q \leq p. \end{cases}$$

Proof: First, assume that $q \geq p$. Then for all $v \in V(TO)$,

$$\varepsilon(v) = 2q + \frac{p}{2} = \frac{1}{2}(4q + p).$$

Therefore, from (2) we have

$$C^{\xi}(TO) = \sum_{v \in V(TO)} \frac{d(v)}{\varepsilon(v)} = \sum_{v \in V(TO)} \frac{6}{(p+4q)} = |V(TO)| \times \frac{6}{(p+4q)}.$$

Again if $q \leq p$ then for all $v \in V(TO)$, $\varepsilon(v) = q + \dfrac{3p}{2} = \dfrac{1}{2}(3p + 2q)$.

Thus, using (2) we have

$$C^{\xi}(TO) = \sum_{v \in V(TO)} \frac{d(v)}{\varepsilon(v)} = \sum_{v \in V(TO)} \frac{6}{(3p+4q)} = |V(TO)| \times \frac{6}{(3p+2q)}$$

which completes the proof. □

Proposition 6

Let p and q be odd integers. Then the connective eccentric index of V - phenylenic nanotorus is computed as follows

$$C^{\xi}(TO) = \begin{cases} \dfrac{36pq}{(p+4q-1)} & \text{if } q \geq p \\ \dfrac{36pq}{(3p+2q-1)} & \text{if } q \leq p. \end{cases}$$

Proof: Let, $q \geq p$. Then for all $v \in V(TO)$,

$$\varepsilon(v) = 2q + \frac{p-1}{2} = \frac{1}{2}(4q + p - 1).$$

Again if $q \leq p$ then for all $v \in V(TO)$,

$$\varepsilon(v) = q + \frac{3p-1}{2} = \frac{1}{2}(3p + 2q - 1).$$

Since, for a V–phenylenic nanotorus all the vertices are of degree 3, therefore applying a similar argument as Proposition 5, we get the result. □

Proposition 7

Let p be even and q be odd integers. Then the connective eccentric index of V-phenylenic nanotorus is computed as follows

$$C^{\xi}(TO) = \begin{cases} \dfrac{36pq}{(p+4q)} & \text{if } q \geq p \\ \dfrac{36pq}{(3p+2q)} & \text{if } q \leq p. \end{cases}$$

Proof: We first assume that $q \geq p$. Then for all $v \in V(TO)$,

$$\varepsilon(v) = 2q + \frac{p}{2} = \frac{1}{2}(4q + p).$$

Thus, from (2) $C^{\xi}(TO) = \displaystyle\sum_{v \in V(TO)} \frac{d(v)}{\varepsilon(v)} = \sum_{v \in V(TO)} \frac{6}{(p+4q)} = |V(TO)| \times \frac{6}{(p+4q)}$.

Again if, $q \leq p$ then for all $v \in V(TO)$, $\varepsilon(v) = q + \frac{3p}{2} = \frac{1}{2}(3p + 2q)$.

Therefore, from (2),

$$C^{\xi}(TO) = \sum_{v \in V(TO)} \frac{d(v)}{\varepsilon(v)} = \sum_{v \in V(TO)} \frac{6}{(3p+2q)} = |V(TO)| \times \frac{6}{(3p+2q)},$$

which completes the proof. □

Proposition 8

Let p be odd and q be even integers. Then the connective eccentric index of V-phenylenic nanotorus is computed as follows

$$C^{\xi}(TO) = \begin{cases} \dfrac{36pq}{(p+4q-1)} & \text{if } q \geq p \\ \dfrac{36pq}{(3p+2q-1)} & \text{if } q \leq p. \end{cases}$$

Proof: Let us first assume that, $q \geq p$. Then for all $v \in V(TO)$,

$$\varepsilon(v) = 2q + \frac{p-1}{2} = \frac{1}{2}(4q + p - 1).$$

Again if $q \leq p$ then for all $v \in V(TO)$, $\varepsilon(v) = q + \frac{3p-1}{2} = \frac{1}{2}(3p + 2q - 1)$.

Since, for a V–phenylenic nanotorus all the vertices are of degree 3, therefore following a similar argument as Proposition 7, we get the result. □

The propositions 5, 6, 7 and 8 can be summarized as follows:

Theorem 2

Let p be even, then the connective eccentric index of V-phenylenic nanotorus is given by

$$C^\xi(TO) = \begin{cases} \dfrac{36pq}{(p+4q)} & \text{if } q \geq p \\[3mm] \dfrac{36pq}{(3p+2q)} & \text{if } q \leq p. \end{cases}$$

and if p be odd, then the connective eccentric index of V-phenylenic nanotorus is given by

$$C^\xi(TO) = \begin{cases} \dfrac{36pq}{(p+4q-1)} & \text{if } q \geq p \\[3mm] \dfrac{36pq}{(3p+2q-1)} & \text{if } q \leq p. \end{cases}$$

CONCLUSIONS

In this paper, we studied the V-phenylenic nanotorus. As our main result, we have derived exact formulas for the modified eccentric connectivity index and connective eccentric index of V-phenylenic nanotorus. For further study, lower and an upper bound for these topological indices of V-phenylenic nanotorus can be computed.

REFERENCES

1. A.R. Ashrafi, M. Ghorbani, *Electronic Materials Letters*, **2010**, *6(2)*, 87.
2. M. Alaeiyan, J. Asadpour, R. Mojarad, *Fullerenes, Nanotubes and Carbon Nanostructures*, **2013**, *21(10)*, 825.
3. A.R. Ashrafi, M. Ghorbani, M.A. Hossein-Zadeh, *Serdica Journal of Computing*, **2011**, *5*, 101.
4. N. De, S.M.A. Nayeem, A. Pal, *Advanced Modeling and Optimization*, **2014**, *16(1)*, 133.

5. N. De, A. Pal, S.M.A. Nayeem, Modified eccentric connectivity of generalized thorn graphs, *International Journal of Computational Mathematics* (To appear).
6. S. Gupta, M. Singh, A.K. Madan, *Journal of Molecular Graphics and Modelling*, **2000**, *18*, 18.
7. M. Ghorbani, *Journal of Mathematical Nanoscience*, **2011**, *1*, 43.
8. N. De, *International Journal of Contemporary Mathematical Sciences*, **2012**, *7(44),* 2161.
9. M. Ghorbani, K. Malekjani, *Serdica Journal of Computing*, **2012**, *6*, 299.
10. G. Yu, L. Feng, *MATCH communications in mathematical and in computer chemistry*, **2013**, *69*, 611.
11. N. De, A. Pal, S.M.A. Nayeem, On some bounds and exact formulae for connective eccentric indices of graphs under some graph operations, *International Journal of Combinatorics* (To appear).
12. A.R. Ashrafi, M Ghorbani, M. Jalali, *Indian Journal of Chemistry*, **2008**, *47A*, 535.
13. H. Yousefi–Azari, J. Yazdani, A. Bahrami, A.R. Ashrafi, *Journal of Serbian Chemical Society*, **2007**, *72(11)* 1063.
14. V. Alamian, A. Bahrami, B. Edalatzadeh, *International Journal of Molecular Sciences*, **2008**, *9(3),* 229.
15. M. Ghorbani, H. Mesgarani, S. Shakeraneh, *Optoelectronics and advanced materials*, **2011**, *5(3),* 324.
16. Z. Yarahmadi, A.R. Ashrafi, S. Moradi, *Journal of Applied Mathematics and Computing*, **2014**, *45(1-2),* 35.
17. M.V. Diudea, *Fullerenes, Nanotubes and Carbon Nanostructures*, **2002**, *10*, 273.

THEORETICAL STUDY OF NANOSTRUCTURES USING TOPOLOGICAL INDICES

NAJMEH SOLEIMANI[a], MOHAMMAD JAVAD NIKMEHR[a,*], HAMID AGHA TAVALLAEE[a]

ABSTRACT. In this research, we give some theoretical results for linear $[n]$-Pentacene, V-Pentacenic nanotube, H-Pentacenic nanotube and V-Pentacenic nanotori by using topological indices. The main result of this paper is represented by the formulas for calculating values of Zagreb indices, Zagreb coindices and connectivity indices. These formulas make it possible to correlate the chemical structure of Nanostructures with a large amount of information about their physical features.

Keywords: *Nanostructures, Vertex-degree, Zagreb indices, Zagreb coindices, Connectivity indices.*

INTRODUCTION

The chemical graph theory is an important branch of mathematical chemistry. A chemical graph is a model of a chemical system, used to characterize the interactions among its components: atoms, bonds, groups of atoms or molecules. A structural formula of a chemical compound can be represented by a molecular graph, its vertices being atoms while edges correspond to covalent bonds; hydrogen atoms are often omitted. A single number, representing a chemical structure, in graph-theoretical terms, is called a topological index. Topological indices were successfully employed in developing a suitable correlation between chemical structure and biological activity by translating chemical structures into numerical descriptors. In the past years, nanostructures involving carbon have been the focus of an intense research activity which is driven to a large extent by the quest for new materials with specific applications. Carbon nanotubes are nano-objects that have raised great expectations in a number of different applications, including field emission, energy storage, molecular electronics, atomic force microscopy, and many others. The use of topological indices as structural

---

[a] *Department of Mathematics, Karaj Branch, Islamic Azad University, Karaj, Iran*
* Corresponding author: nikmehr@kntu.ac.ir

descriptors is important in the proper and optimal nanostructure design. The present authors, [1-6], derived some exact formulae for topological indices of some graphs.

The main purpose of this paper is to compute some topological indices for families of linear [n]-Pentacene, lattice of V-Pentacenic nanotube, H-Pentacenic nanotube and V-Pentacenic nanotori. The paper is organized as follows: In the next sections we give the necessary definitions. Section 3 contains the results; the paper is completed with the list of references.

DEFINITIONS

In this section, we gathered some notations as well as preliminary notions which will be needed for the rest of the paper. Let $G = (V, E)$ be a simple molecular graph without directed and multiple edges and without loops, the vertex and edge sets of it being represented by $V = V(G)$ and $E = E(G)$, respectively. The vertices in G are connected by an edge if there exists an edge $uv \in E(G)$ connecting the vertices u and v in G such that $u, v \in V(G)$. The complement of G, denoted by $\overline{G}$, is a simple graph on the same set of vertices $V(G)$ in which two vertices u and v are adjacent, i.e., connected by an edge uv, if and only if they are not adjacent in G. Hence, $uv \in E(\overline{G}) \Longleftrightarrow uv \notin E(G)$. The degree of $u \in V(G)$, denoted by d_u, is the number of vertices in G adjacent to u. There are several topological indices defined in the literature.

The Zagreb indices have been introduced more than thirty years ago by Gutman and Trinajstić [7]. For a (molecular) graph G, the *first Zagreb index* is equal to the sum of the squares of the vertex degrees; the *second Zagreb index* equals to the sum of the products of pair adjacent vertex degrees. They are defined as:

$$M_1(G) = \sum_{u \in V(G)} d_u^2, \qquad M_2(G) = \sum_{uv \in E(G)} (d_u \times d_v),$$

respectively. In fact, one can rewrite the first Zagreb index as:

$$M_1(G) = \sum_{uv \in E(G)} (d_u + d_v).$$

The *first and second Zagreb polynomials* of a graph G are defined as:

$$M_1(G, x) = \sum_{uv \in E(G)} x^{(d_u + d_v)}, \qquad M_2(G, x) = \sum_{uv \in E(G)} x^{(d_u \times d_v)},$$

where x is a dummy variable. For more studies about polynomials in graph theory you can see [8-12].

On the other hand, for a graph G, the *modified second Zagreb index* is defined as [13]:

$$M_2^*(G) = \sum_{uv \in E(G)} \frac{1}{d_u \times d_v}$$

The *third Zagreb index* was first introduced by Fath-Tabar [14]. This index is defined as follows:

$$M_3(G) = \sum_{uv \in E(G)} |d_u - d_v|.$$

Recently, Ashrafi et al. [15] have defined, respectively, the *first Zagreb coindex* and the *second Zagreb coindex* as follows:

$$\overline{M_1}(G) = \sum_{uv \notin E(G)} (d_u + d_v), \quad \overline{M_2}(G) = \sum_{uv \notin E(G)} (d_u \times d_v).$$

Zagreb coindices are dependent on the degrees of non-adjacent vertices and thereby quantifying a possible influence of remote vertex pairs to the molecular properties. The reader should note that Zagreb coindices of G are not Zagreb indices of $\bar{G}$; the defining sums run over $E(\bar{G})$, but the degrees are with respect to G.

Among molecular descriptors, topological connectivity indices are very important and many of them have found applications in modeling chemical, pharmaceutical and other properties of the molecules. The *product-connectivity index*, also called Randić index of a graph G and is defined as:

$$\chi(G) = \sum_{uv \in E(G)} \frac{1}{\sqrt{d_u d_v}}.$$

This topological index was first proposed by Randić [16]. Zhou and Trinajstić [17] proposed another connectivity index, named the *Sum-connectivity index*. This index is defined as:

$$X(G) = \sum_{uv \in E(G)} \frac{1}{\sqrt{d_u + d_v}}.$$

Estrada et al. [18] introduced *atom-bond connectivity index*, which it has been applied in studies on the stability of alkanes and the strain energy of cycloalkanes. This index is defined as follows:

$$ABC(G) = \sum_{uv \in E(G)} \sqrt{\frac{d_u + d_v - 2}{d_u d_v}}.$$

Vukičević and Furtula [19] proposed a topological index named the *geometric-arithmetic index*. This index is defined as:

$$GA(G) = \sum_{uv \in E(G)} \frac{2\sqrt{d_u d_v}}{d_u + d_v}.$$

RESULTS AND DISCUSSION

The use of topological and connectivity indices as structural descriptors is important in proper and optimal nanostructure design. Pentacene is a polycyclic aromatic hydrocarbon consisting of five linearly-fused benzene rings. This highly conjugated compound is an organic semiconductor. The compound generates excitons upon absorption of ultra-violet (UV) or visible light; this makes it very sensitive to oxidation. For this reason, this compound, which is a purple powder, slowly degrades upon exposure to air and light. In Figure1, one can see the linear [n]-Pentacene.
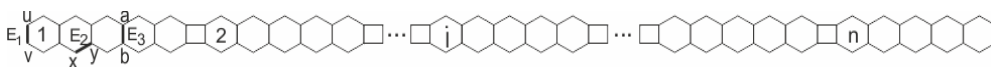
Figure 1. The molecular graph of a linear [n]-Pentacene.

Before we proceed to our main results, we will express the lemma which will be useful later.

Lemma 1. *Topological indices of [n]-Pentacene (Figure 1), hereafter denoted T=T[n], are calculated from the molecular graph, considering the vertex degree and the number of edges. Obviously, for $n = 1, |V| = 22$ and $|E| = 26$. There exist 3 type of edges, namely $[E_1] = uv$, $[E_2] = xy$ and $[E_3] = ab$. On the other hand $d_u = d_v = 2$, $d_a = d_b = 3$ and $d_x = 2$, $d_y = 3$. By enumerating these edges there are $6, 16$ and 4 edges of types $1, 2$ and 3, respectively. Now, it is easy to see that $T = T[n]$ has $22n$ vertices and $28n - 2$ edges. Similar to the above argument, the edge set of graph can be dividing into three partitions: $E_1(T), E_2(T)$ and $E_3(T)$. There are three type of edges, e. g. edges with endpoints $2[E_1]$, edges with endpoints $2,3[E_2]$ and edges with endpoints $3[E_3]$. By using an algebraic method we obtain $|E_1| = 6$, $|E_2| = 20n - 4$ and $|E_3| = 8n - 4$.*

Table 1. Type and number of edges in the molecular graph T

(d_u, d_v) where $uv \in E(T)$	Total Number of Edges
$E_1 = [2,2]$	6
$E_2 = [2,3]$	$20n - 4$
$E_3 = [3,3]$	$8n - 4$

Theorem 2. *Let T be a linear [n]-Pentacene; the Zagreb polynomials are:*

i. $M_1(T, x) = (8n - 4)x^6 + (20n - 4)x^5 + 6x^4$.
ii. $M_2(T, x) = (8n - 4)x^9 + (20n - 4)x^6 + 6x^4$.

Proof. By definition of the first and second Zagreb polynomials and partition of edges described in Lemma 1, we can see that:

i. $M_1(T, x) = \sum_{uv \in E(T)} x^{(d_u + d_v)} = \sum_{uv \in [E_1]} x^4 + \sum_{uv \in [E_2]} x^5 + \sum_{uv \in [E_3]} x^6 = 6x^4 + (20n - 4)x^5 + (8n - 4)x^6$.

ii. $M_2(T, x) = \sum_{uv \in E(T)} x^{(d_u \times d_v)} = \sum_{uv \in [E_1]} x^4 + \sum_{uv \in [E_2]} x^6 + \sum_{uv \in [E_3]} x^9 = 6x^4 + (20n - 4)x^6 + (8n - 4)x^9$.

Theorem 3. *Let T be a linear [n]-Pentacene; the topological indices are calculated from the corresponding polynomials as the first derivative, in $x = 1$:*

$$M_1(T) = 148n - 20.$$

$$M_2(T) = 192n - 36.$$

Proof.
The first Zagreb index will be the first derivative of $M_1(T, x)$ evaluated at $x = 1$:

$$M_1(T) = \left. \frac{\partial M_1(T, x)}{\partial x} \right|_{x=1} = 6 \times (8n - 4) + 5 \times (20n - 4) + 4 \times (6) = 148n - 20.$$

Also, the second Zagreb index will be the first derivative of $M_2(T, x)$ evaluated at $x = 1$:

$$M_2(T) = \left. \frac{\partial M_2(T, x)}{\partial x} \right|_{x=1} = 9 \times (8n - 4) + 6 \times (20n - 4) + 4 \times (6) = 192n - 36.$$

Given the edge partitions in the linear [n]-Pentacene (Lemma 1) we can prove the following theorem:

Theorem 4. *Consider the graph T of a linear $[n]$-Pentacene. The following topological indices can be calculated:*

i. $M_2^*(T) = \sum_{uv \in E(T)} \frac{1}{d_u \times d_v} = \sum_{uv \in [E_1]} \frac{1}{4} + \sum_{uv \in [E_2]} \frac{1}{6} + \sum_{uv \in [E_3]} \frac{1}{9} = \frac{1}{4} \times 6 + \frac{1}{6} \times (20n - 4) + \frac{1}{9} \times (8n - 4) = \frac{38}{9}n + \frac{7}{18}$.

ii. $M_3(T) = \sum_{uv \in E(T)} |d_u - d_v| = \sum_{uv \in [E_2]} |2 - 3| = 20n - 4$.

iii. $\chi(T) = \sum_{uv \in E(T)} \frac{1}{\sqrt{d_u d_v}} = \sum_{uv \in [E_1]} \frac{1}{\sqrt{4}} + \sum_{uv \in [E_2]} \frac{1}{\sqrt{6}} + \sum_{uv \in [E_3]} \frac{1}{\sqrt{9}} = \frac{1}{\sqrt{4}} \times 6 + \frac{1}{\sqrt{6}} \times (20n - 4) + \frac{1}{\sqrt{9}} \times (8n - 4) = \left(\frac{10\sqrt{6} + 8}{3} \right) n + \left(\frac{5 - 2\sqrt{6}}{3} \right)$.

iv. $X(T) = \sum_{uv \in E(T)} \frac{1}{\sqrt{d_u + d_v}} = \sum_{uv \in [E_1]} \frac{1}{\sqrt{4}} + \sum_{uv \in [E_2]} \frac{1}{\sqrt{5}} + \sum_{uv \in [E_3]} \frac{1}{\sqrt{6}} = \frac{1}{\sqrt{4}} \times 6 + \frac{1}{\sqrt{5}} \times (20n - 4) + \frac{1}{\sqrt{6}} \times (8n - 4) = \left(4\sqrt{5} + \frac{4\sqrt{6}}{3} \right) n + \left(3 - \frac{4\sqrt{5}}{5} - \frac{2\sqrt{6}}{3} \right)$.

v. $ABC(T) = \sum_{uv \in E(T)} \sqrt{\frac{d_u + d_v - 2}{d_u d_v}} = \sum_{uv \in [E_1]} \sqrt{\frac{2}{4}} + \sum_{uv \in [E_2]} \sqrt{\frac{3}{6}} + \sum_{uv \in [E_3]} \sqrt{\frac{4}{9}} = \sqrt{\frac{2}{4}} \times 6 + \sqrt{\frac{3}{6}} \times (20n - 4) + \sqrt{\frac{4}{9}} \times (8n - 4) = \left(\frac{16 + 30\sqrt{2}}{3} \right) n + \left(\frac{3\sqrt{2} - 8}{3} \right)$.

vi. $GA(T) = \sum_{uv \in E(T)} \frac{2\sqrt{d_u d_v}}{d_u + d_v} = \sum_{uv \in [E_1]} \frac{2\sqrt{4}}{4} + \sum_{uv \in [E_2]} \frac{2\sqrt{6}}{5} + \sum_{uv \in [E_3]} \frac{2\sqrt{9}}{6} = \frac{2\sqrt{4}}{4} \times 6 + \frac{2\sqrt{6}}{5} \times (20n - 4) + \frac{2\sqrt{9}}{6} \times (8n - 4) = (8 + 8\sqrt{6})n + \left(2 - \frac{8\sqrt{6}}{5} \right)$.

Lemma 5. [15] Let G be a simple graph with n vertices. Then

i. $\overline{M_1}(G) = 2|E(G)|(n - 1) - M_1(G)$.

ii. $\overline{M_2}(G) = 2|E(G)|^2 - M_2(G) - \frac{1}{2} M_1(G)$.

Theorem 6. *The first and second Zagreb coindices of a linear $[n]$-Pentacene are computed as:*

i. $\overline{M_1}(T) = 1232n^2 - 292n + 24$.

ii. $\overline{M_2}(T) = 1568n^2 - 490n + 54$.

Proof. By applying Lemma 1 and Lemma 5 we have the proof.

The 2-dimensional lattices of V-Pentacenic nanotube (denoted by $F = F[p, q]$), H-Pentacenic nanotube (denoted by $K = K[p, q]$) and V-Pentacenic nanotori (denoted by $L = L[p, q]$) the readers can see in Figures 2, 3 and 4, respectability.
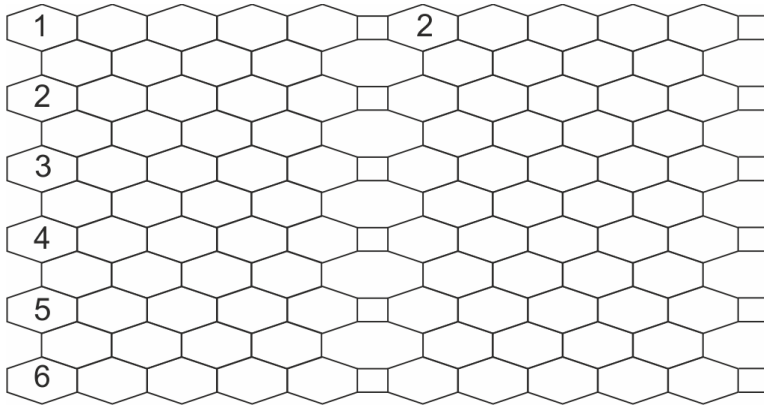
Figure 2. The 2-D graph lattice of $F = F[p, q]$ with $p = 2$ and $q = 6$.
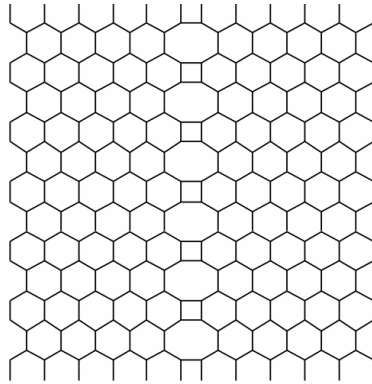
Figure 3. The 2-D graph lattice of $K = K[p, q]$ with $p = 2$ and $q = 6$.
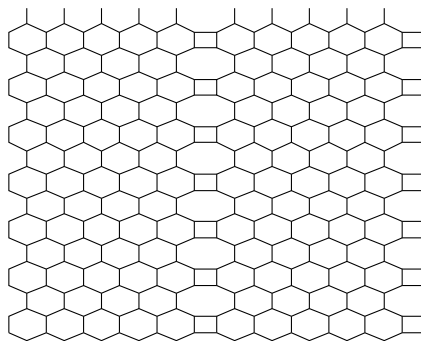
Figure 4. The 2-D graph lattice of $L = L[p, q]$ with $p = 2$ and $q = 7$.

In order to provide a unified approach to the results discussed in this paper, we express the following lemma.

Lemma 7. It holds that:

Table 2. Type and number of vertices and edges
in the molecular graphs *F*, *K* and *L*.

Nanostructure	$|V|$	$|E|$	$|E_1|$	$|E_2|$	$|E_3|$
F	$22pq$	$33pq - 5p$	0	$20p$	$33pq - 25p$
K	$22pq$	$33pq - 2q$	$2q$	$4q$	$33pq - 8q$
L	$22pq$	$33pq$	0	0	$33pq$

Proof. We apply similar reasoning as in Lemma 1 to calculate the quantities of $|V|, |E_1|, |E_2|$ and $|E_3|$ of Nanostructures F, K and L.

Theorem 8. *The first, second, modified second and third Zagreb indices of Nanostructures are computed as:*

Nanostructure	M_1	M_2	M_2^*	M_3
F	$198pq - 50p$	$297pq - 105p$	$\frac{11}{3}pq + \frac{5}{9}p$	$20p$
K	$198pq - 20q$	$297pq - 40q$	$\frac{11}{3}pq + \frac{5}{18}p$	$4q$
L	$198pq$	$297pq$	$\frac{11}{3}pq$	0

Proof. We just apply Lemma 7 and the proof of Theorem 4.

Theorem 9. *The first and second Zagreb coindices of Nanostructures are calculated as:*

Nanostructure	$\overline{M_1}$	$\overline{M_2}$
F	$1452p^2q^2 - 220p^2q - 264pq + 60p$	$2178p^2q^2 - 660p^2q + 50p^2 - 396pq + 130p$
K	$1452p^2q^2 - 88pq^2 - 264pq + 24q$	$2178p^2q^2 - 264pq^2 - 396pq + 58q$
L	$1452p^2q^2 - 264pq$	$2178p^2q^2 - 396pq$

Proof. The proof is obtained exactly from Lemma 5, Lemma 7 and Theorem 8.

Finally, we calculate the Randić index, Sum-connectivity index, atom-bond connectivity index and geometric-arithmetic index of Nanostructures by use an algebraic method. The next results are proven like Theorem 4 therefore, we omit the proofs.

Theorem 10. *The Product and Sum-connectivity indices are computed as:*

Nanostructure	χ	X
F	$11pq + \left(\dfrac{10\sqrt{6}-25}{3}\right)p$	$\dfrac{11\sqrt{6}}{2}pq + \left(\dfrac{120\sqrt{5}-125\sqrt{6}}{30}\right)p$
K	$11pq + \left(\dfrac{2\sqrt{6}-5}{3}\right)q$	$\dfrac{11\sqrt{6}}{2}pq + \left(\dfrac{30+24\sqrt{5}-40\sqrt{6}}{30}\right)q$
L	$11pq$	$\dfrac{11\sqrt{6}}{2}pq$

Theorem 11. *The* atom-bond connectivity index and geometric-arithmetic index *are computed as:*

Nanostructure	ABC	GA
F	$22pq + \left(10\sqrt{2}-\dfrac{50}{3}\right)p$	$33pq + (8\sqrt{6}-25)p$
K	$22pq + \left(3\sqrt{2}-\dfrac{16}{3}\right)q$	$33pq + \left(\dfrac{8\sqrt{6}}{5}-6\right)q$
L	$22pq$	$33pq$

We end this section with some examples.

Example 12. *Let $F = F[2,7]$ be a lattice with* 308 *atoms and* 452 *chemical bonds. Then one can see that*

$$M_1(F) = 2672, \ M_2(F) = 3948, \ M_2^*(F) = 52.44 \ and \ M_3(F) = 40.$$

Example 13. *Let $L = L[2,7]$ be a nanotube with* 308 *atoms and* 462 *chemical bonds. Then one can see that* $\chi(L) = 154$ *and* $X(L) = 188.611$.

Example 14. *Let $F = F[2,6]$ be a nanotube with* 330 *atoms and* 480 *chemical bonds. Then one can see that* $ABC(F) = 258.951$.

Example 15. *Let $K = K[2,6]$ be a nanotube with 264 atoms and 384 chemical bonds. Then one can see that $GA(K) = 257.456$.*

CONCLUSIONS

Among topological descriptors, topological indices are very important and they have a prominent role in chemistry. We have mentioned here some theoretical results about the Zagreb and conectivity indices of linear $[n]$-Pentacene, vertical and horizontal Pentacenic nanotube and nanotori.

REFERENCES

1. M.V. Diudea, Fullerenes, *Nanotubes Carbon Nanostruct.*, **2002**, *10*, 273.
2. M. Eliasi, B. Taeri, *J. Comput. Theor. Nanosci.*, **2007**, *4*, 1174.
3. A. Heydari, B. Taeri, *MATCH Commun. Math. Comput. Chem.*, **2007**, *57*, 665.
4. A. Mahmiani, A. Iranmanesh, Y. Pakravesh, *Ars Comb.*, **2008**, *89*, 309.
5. M.J. Nikmehr, L. Heidarzadeh, N. Soleimani, *Studia Scientiarum Mathematicarum Hungarica*, **2014**, *51*, 133.
6. M.J. Nikmehr, N. Soleimani, M. Veylaki, *Proceedings of the Institute of Applied Mathematics*, **2014**, *3*, 89.
7. I. Gutman, N. Trinajstić, *Chem. Phys.Lett.*, **1972**, *17*, 535.
8. A.R. Ashrafi, B. Manoochehrian, H.Yousefi- Azari, *Bull. Iranian Math. Soc.*, **2007**, *33*, 37.
9. M.V. Diudea, *Iranian J. Math. Chem.*, **2010**, *1*, 69.
10. G.H. Fath-Tabar, *Dig. J. Nanomater. Bios.*, **2009**, *4*, 189.
11. G.H. Fath-Tabar, A.R. Ashrafi, *Iranian J. Math. Sci. Inf.*, **2011**, *6*, 67.
12. H. Mohamadinezhad-Rashti, H. Yousefi-Azari, *Iranian J. Math. Chem.*, **2010**, *1*, 37.
13. S. Nikolić, G. Kovačević, A. Miličević, N. Trinajstić, *Croatica Chemical Acta*, **2003**, *76,* 113.
14. G.H. Fath-Tabar, *MATCH Commun. Math. Comput. Chem.*, **2011**, *65*, 79.
15. A.R. Ashrafi, T. Doslić, A. Hamzeh, *Discrete Applied Mathematics*, **2010**, *58*, 1571.
16. M. Randić, *J. Am. Chem. Soc.*, **1975**, *97*, 6609.
17. B. Zhou, N. Trinajstić, *J. Math. Chem.*, **2009**, *46*, 1252.
18. E. Estrada, L. Torres, L. Rodriguez, I. Gutman, *Indian J. Chem.*, **1998**, *37*, 849.
19. D. Vukičević, B. Furtula, *Journal of Mathematical Chemistry*, **2009**, *46*, 1369.

FORTH ATOM-BOND CONNECTIVITY INDEX OF SOME FAMOUS NANOTUBES

MARYAM VEYLAKI[a], MOHAMAD J. NIKMEHR[a,*],
HAMID AGHA TAVALLAEE[a]

ABSTRACT. Let $G = (V, E)$ be a simple connected graph. The sets of vertices and edges of G are denoted by $V = V(G)$ and $E = E(G)$, respectively. In such a simple molecular graph, vertices represent atoms and edges represent bonds. The goal of this paper is to compute the ABC_4 index for some nanotubes designed by Diudea.

Keywords: Molecular graph, Atom-bond connectivity index, ABC_4 index.

INTRODUCTION

Chemical graph theory is a branch of graph theory whose focus of interest is to find topological indices of chemical graphs (i.e. graphs that represent chemical molecules) which correlate well with chemical properties of the corresponding molecules. A molecular graph is a collection of points representing the atoms in the molecule and a set of lines representing the covalent bonds. These points are named vertices and the lines are named edges in the graph theory language.

Many topological indices are closely correlated with some physico-chemical characteristics of the underlying compounds. All graphs considered in this study are finite, simple and connected graphs (without loops and multiple edges). For a connected graph G, $V(G)$ and $E(G)$ denote the set of vertices and edges, and $|V(G)|$ and $|E(G)|$ the number of vertices and edges, respectively. The degree d_u of a vertex $u \in V(G)$ is the number of vertices of G adjacent to u.

A connected graph is a graph such that there is a path between all pairs of vertices. Among topological descriptors, connectivity indices are very important and they have a prominent role in chemistry. First connectivity index has been introduced in 1975 by Milan Randić [1]; it reflects the molecular

---
[a] *Department of Mathematics, Karaj Branch, Islamic Azad University, Karaj, Iran*
* Corresponding author: nikmehr@kntu.ac.ir

branching and by this reason was called the branching index, later becaming the well-known Randić connectivity index. It is defined as:

$$\chi(G) = \sum_{e=uv\in E(G)} \frac{1}{\sqrt{d_u d_v}}.$$

In 2009, Furtula et al. [2] introduced the Atom-Bond Connectivity (ABC) index, which found applications in the study of stability of alkanes and cycloalkanes. This index is defined as follows:

$$ABC_1(G) = \sum_{uv\in E(G)} \sqrt{\frac{d_u + d_v - 2}{d_u d_v}}.$$

Recently, M. Ghorbani et al. [3] introduced a new version of atom-bond connectivity index, named ABC_4:

$$ABC_4(G) = \sum_{uv\in E(G)} \sqrt{\frac{S_u + S_v - 2}{S_u S_v}}.$$

where S_v is the sum of degrees of all vertices adjacent to vertex v. In other words, $S_u = \sum_{v\in N_G(u)} d_v$ and $N_G(u) = \{v \in V(G) | uv \in E(G)\}$.

The goal of this paper is to compute a close formula of ABC_4 index of a famous family of nanotubes such as HC_5C_7, VC_5C_7 and VAC_5C_7 designed by Diudea [4]. Our notation is standard and for more information and background biography, refers to paper series [5-12].

RESULTS AND DISCUSSION

The structure of HC_5C_7, VC_5C_7 and VAC_5C_7 nanotubes consists of cycles with the length five and seven (or C_5C_7 net). A C_5C_7 net is a trivalent decoration made by alternating C5 and C7. It can cover either a cylinder or a torus. For a review, historical details and further bibliography see refs. [4] and the 3-dimensional lattice of HC_5C_7, VC_5C_7 and VAC_5C_7 nanotubes in Figures 1, 4 and 7.

Theorem 1. *Let* G *be the nanotube* $VC_5C_7[p,q]$. *Then the fourth atom bond connectivity index of* G *is*

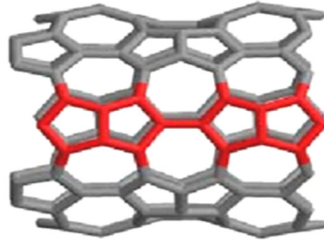$$ABC_4(VC_5C_7[p,q]) = 10pq\sqrt{\frac{11}{42}} + 11pq\left(\frac{3\sqrt{2}+4}{9}\right).$$
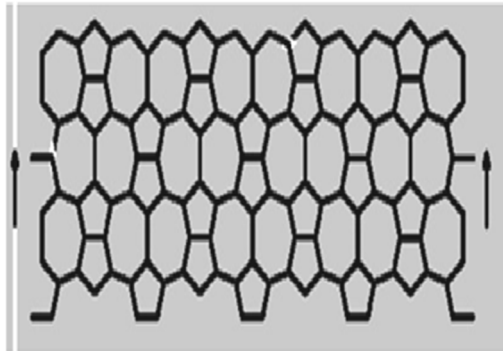
Figure 1. The 3D lattice of VC_5C_7 nanotube

Figure 2. The 2D lattice of $VC_5C_7[16, 8] = VC_5C_7[4p, 4q]$ nanotube

Proof. We denoted the number of paired pentagons in the first row by p. In this nanotube the two first rows of vertices and edges are repeated alternatively and we denoted the number of this repetition by q. Consider the nanotube $G = VC_5C_7[p, q]$. The number of vertices in this nanotube is equal to $|V(VC_5C_7[p, q])| = 16pq$ and obviously the number of edges is equal to $|E(VC_5C_7[p, q])| = 24pq - 3p$. There are two partitions $V_2 = \{v \in V(G)|d_v = 2\}$ and $V_3 = \{v \in V(G)|d_v = 3\}$ of $(VC_5C_7[p, q])$, and $E(VC_5C_7[p, q])$ can be divided in three partitions,

$$E_4 = \{u, v \in V(VC_5C_7[p, q]) \mid d_u = d_v = 2\}, \; E_5 = \{u, v \in V(VC_5C_7[p, q])|d_u = 3 \,\&\, d_v = 2\}$$
$$\text{and} \; E_6 = \{u, v \in V(VC_5C_7[p, q])|d_u = d_v = 3\}.$$

From Figure 2, it is easy to see that the size of edge partitions E_4, E_5 and E_6 are equal to $p, 10p$ and $24pq - 14p$, respectively. We assume u, v, u_1, u_2, u_3 and b are some of the vertices of this graph. From Figure 3, one can see that for every atoms

$$u \in V_2, S_u = 3 + 3 = 6, S_v = 2 + 2 + 3 = 7, S_{u_2} = S_{u_3} = 2 + 3 = 5 \text{ and}$$
$$S_{u_1} = 3 + 3 + 3 = 9.$$

Also for all other vertices b (which belong to V_a), $S_b = 3 \times 3 = 9$.
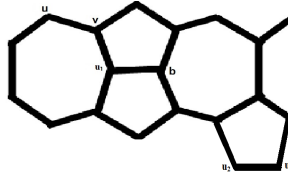
Figure 3. A particular of 2D lattice of $VC_5C_7[p,q]$ nanotube

$ABC_4\left(VC_5C_7[p,q]\right)$

$$= \sum_{uv\in E_5}\sqrt{\frac{S_u+S_v-2}{S_u\times S_v}} + \sum_{vu_1\in E_6}\sqrt{\frac{S_v+S_{u_1}-2}{S_v\times S_{u_1}}} + \sum_{bu_1\in E_6}\sqrt{\frac{S_{u_1}+S_b-2}{S_{u_1}\times S_b}}$$

$$+ \sum_{u_2u_3\in E_4}\sqrt{\frac{S_{u_2}+S_{u_3}-2}{S_{u_2}\times S_{u_3}}}$$

$$= 10p\sqrt{\frac{6+7-2}{6\times 7}} + (24pq-14p)\sqrt{\frac{7+9-2}{7\times 9}} + (24pq-14p)\sqrt{\frac{9+9-2}{9\times 9}}$$

$$+ p\sqrt{\frac{5+5-2}{5\times 5}} = 10p\sqrt{\frac{11}{42}} + (24pq-14p)\sqrt{\frac{14}{63}} + (24pq-14p)\sqrt{\frac{16}{81}} + p\sqrt{\frac{8}{25}}$$

$$= \frac{\left(4+3\sqrt{2}\right)(24pq-14p)}{9} + 2p\left(5\frac{\sqrt{11}}{42}+\frac{\sqrt{2}}{5}\right).$$

Theorem 2. *Let G be the nanotube $HC_5C_7[p,q]$. Then the fourth atom bond connectivity index of G is*

$$ABC_4(HC_5C_7[p,q]) = 4p + (12pq-5p)\left(\frac{9\sqrt{14}+6\sqrt{30}+32}{36}\right).$$
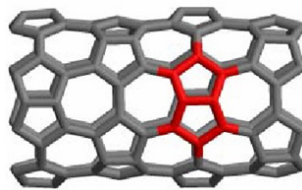
Figure 4. The 3D lattice of HC_5C_7 nanotube
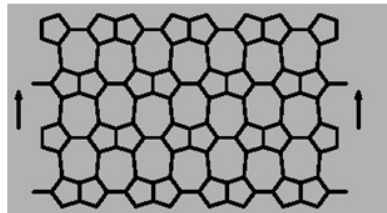
Figure 5. The 2D lattice of $HC_5C_7[16,8]$ nanotube

Proof. In this nanotube we denoted the number of heptagons in one row by p, and the three first rows of vertices and edges are repeated alternatively, we denoted the number of this repetition by q. Consider the nanotube $G = HC_5C_7[p, q]$. The number of vertices in this nanotube is equal to $|V(HC_5C_7[p, q])| = 16\,pq$ and the number of edges is equal to $|E(HC_5C_7[p, q])| = 24pq - 2p$. There are two partitions V_2 and V_3 of $V(HC_5C_7[p, q])$ and $E(HC_5C_7[p, q])$ can be divided in two partitions E_5 and E_6. From Figure 5, it is easy to see that, the size of edge partitions E_5 and E_6 are equal to $8p$ and $24pq - 10p$, respectively. From Figure 6, one can see that for every atom $u \in V_2$, S_u=3+3=6, S_v=2+3×2=8, S_w=2+3×2=8, S_{u_1}=3+3+3=9, and $\forall b \in V_3, S_b$=3×3=9.
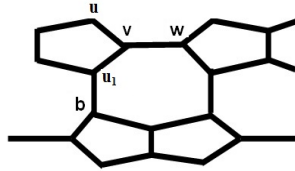
**Figure 6.** A particular of 2D lattice of $HC_5C_7[p, q]$ nanotube

$ABC_4\,(HC_5C_7[p, q])$

$$= \sum_{uv \in E_5} \sqrt{\frac{S_u + S_v - 2}{S_u \times S_v}} + \sum_{vw \in E_6} \sqrt{\frac{S_v + S_w - 2}{S_v \times S_w}} + \sum_{vu_1 \in E_6} \sqrt{\frac{S_v + S_{u_1} - 2}{S_v \times S_{u_1}}}$$

$$+ \sum_{bu_1 \in E_6} \sqrt{\frac{S_{u_1} + S_b - 2}{S_{u_1} \times S_b}}$$

$$= 8p\sqrt{\frac{6 + 8 - 2}{6 \times 8}} + (24pq - 10p)\sqrt{\frac{8 + 8 - 2}{8 \times 8}} + (24pq - 10p)\sqrt{\frac{8 + 9 - 2}{8 \times 9}}$$

$$+ (24pq - 10p)\sqrt{\frac{9 + 9 - 2}{9 \times 9}}$$

$$= 8p\sqrt{\frac{12}{48}} + (24pq - 10p)\sqrt{\frac{14}{64}} + (24pq - 10p)\sqrt{\frac{15}{72}} + (24pq - 10p)\sqrt{\frac{16}{81}}$$

$$= 4p + (12pq - 5p)\left(\frac{9\sqrt{14} + 6\sqrt{30} + 32}{36}\right).$$

Theorem 3. *Let G be the nanotube $VAC_5C_7[p, q]$. Then the fourth atom bond connectivity index of G is:*

$$ABC_4(VAC_5C_7[p,q]) = p\left(\frac{4\sqrt{2} + 2\sqrt{110} + 20}{5}\right) +$$
$$(24pq - 13p + 3)\left(\frac{9\sqrt{14} + 6\sqrt{30} + 32}{72}\right)$$
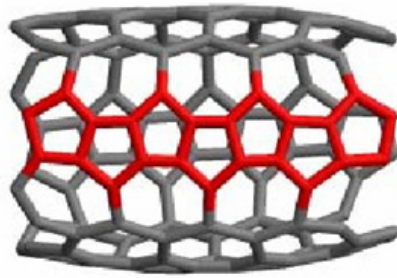
Figure 7. The 3D lattice of VAC_5C_7 nanotube
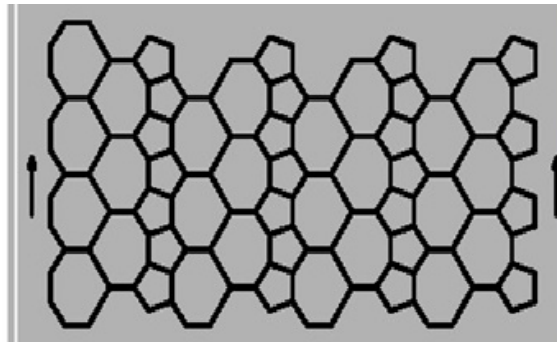
Figure 8. The 2D lattice of $VAC_5C_7[16,8]$ nanotube

Proof. Consider the nanotube $= VAC_5C_7[p,q]$. The number of vertices in this nanotube is equal to $|V(VAC_5C_7[p,q])| = 16pq + 2$ and the number of edges is equal to $|E(VAC_5C_7[p,q])| = 24pq - 3p + 3$. There are two partitions V_2 and V_3 of $V(VAC_5C_7[p,q])$, and $E(VAC_5C_7[p,q])$ can be divided in three partitions E_4, E_5 and E_6. From Figure 8, it is easy to see that the size of edge partitions E_4, E_5 and E_6 are equal to $2p$, $8p$ and $24pq - 13p + 3$, respectively. From Figure 9, one can see that for every atoms u and

$$v \in V_2, S_u = S_v = 2 + 3 = 5, S_w = 2 + 3 \times 2 = 8, S_{u_1} = 2 + 3 \times 2 = 8,$$

$$S_{u_2} = 3 + 3 = 6, S_{u_3} = 3 + 3 + 3 = 9$$

and for all other vertices b (which belong to V_a), $S_b = 3 \times 3 = 9$.
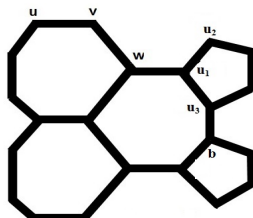
Figure 9. A particular of 2D lattice of $VAC_5C_7[p, q]$ nanotubes

It follows that:
$ABC_4\ (G)$

$$= \sum_{uv\in E_4} \sqrt{\frac{S_u + S_v - 2}{S_u \times S_v}} + \sum_{vw\in E_5} \sqrt{\frac{S_v + S_w - 2}{S_v \times S_w}} + \sum_{u_1 w\in E_6} \sqrt{\frac{S_w + S_{u_1} - 2}{S_w \times S_{u_1}}}$$

$$+ \sum_{u_1 u_2\in E_5} \sqrt{\frac{S_{u_1} + S_{u_2} - 2}{S_{u_1} \times S_{u_2}}}$$

$$+ \sum_{u_1 u_3\in E_6} \sqrt{\frac{S_{u_1} + S_{u_3} - 2}{S_{u_1} \times S_{u_3}}} + \sum_{bu_3\in E_6} \sqrt{\frac{S_{u_3} + S_b - 2}{S_{u_3} \times S_b}}$$

$$= 2p\sqrt{\frac{8}{25}} + 8p\sqrt{\frac{11}{40}} + (24pq - 13p + 3)\sqrt{\frac{14}{64}} + 8p\sqrt{\frac{12}{48}} + 24pq - 13p$$

$$+ 3)\sqrt{\frac{15}{72}} + (24pq - 13p + 3)\sqrt{\frac{16}{81}}$$

$$= p\left(\frac{4\sqrt{2} + 2\sqrt{110} + 20}{5}\right) + (24pq - 13p + 3)\left(\frac{9\sqrt{14} + 6\sqrt{30} + 32}{72}\right).$$

REFERENCES

1. M. Randić. *J. Am. Chem. Soc.* **1975**, *97*, 6609.
2. B. Furtula, A. Graovać and D. Vukičević. *Disc. Appl. Math.* **2009**, *157*, 2828.
3. M. Ghorbaniand, M. A. Hosseinzadeh. *Optoelectron. Adv. Mater-Rapid Comm.* **2010**, *4*(9), 1419.
4. M.V. Diudea. *Studia UBB. Chemia.* **2003**, *48* (2), 17.
5. K.C. Das. *Disc. Appl. Math.* **2010**, *158*, 181.
6. Z. Du and B. Zhou. B. *Bull. Malays. Math. Sci. Soc.* **2012**, *35* (1), 101.
7. Z. Du, B. Zhouand, N. Trinajstić. *Appl. Math. Lett.* **2010**, *24*, 402.

8. R. Xing, B. Zhou and N. Trinajstić. *J. Math. Chem.* **2001**, *48*, 583.
9. B. Zhou and N. Trinajstić. *J. Math. Chem*. **2009**, *46*, 1252.
10. B. Zhou and N. Trinajstić. *J. Math. Chem*. **2010**, *47*, 210.
11. A.R. Ashrafi, M. Ghorbani and M. Jalali. *J. Theor. Comput. Chem.* **2008**, *7* (2), 221.
12. M.R. Farahani and M.P. Vlad, *Studia UBB. Chemia.* **2014**, *59* (2), 71.

COMPUTATION OF ECCENTERIC CONNECTIVITY AND RANDIĆ INDICES OF SOME BENZENOID GRAPHS

JAFAR ASADPOUR[a,*], RASOUL MOJARAD[b] and BEHROUZ DANESHIAN[c]

ABSTRACT. Chemical compounds are often modeled as polygonal shapes, where a vertex represents an atom and an edge symbolizes a bond. A topological index is a number related to a molecular graph invariant. In this paper, exact formulas for the eccentricic connectivity and Randić indices of hexagonal parallelogram of benzenoids are given.

Keywords: *Eccentric connectivity, Randić index, hexagonal parallelogram Benzenod, Nanotorus.*

INTRODUCTION

The molecular graph of a molecule *M* is a graph which has atoms of *M* as vertices and two atoms are adjacent if there is a bond between them. Let G be a simple molecular graph without directed and multiple edges and without loops, the vertex and edge sets of which being represented by *V(G)* and *E(G)*, respectively.

A topological index is a real number related to a molecular graph, which is a graph invariant. Topological indices have been used extensively for the prediction of physical properties of specific classes of molecules. The oldest topological index is the Wiener index, introduced by Harold Wiener [11].

For vertices $u, v \in V(G)$ the edge connecting *u* and *v* is denoted by *uv* and the distance $d_G(u,v)$ is defined as the length of a shortest path connecting *u* and *v* in *G*. The eccentricity $ecc_G(u)$ is the largest distance between *u* and any other vertex *v* of *G*. We will omit the subscript *G* when the graph is clear from the context. The eccentric connectivity index of the molecular graph G, $\xi^c(G)$, was proposed by Sharma, Goswami and Madan [10].

---

[a] *Department of Mathematics, Miyaneh Branch, Islamic Azad University, Miyaneh, Iran*
[b] *Department of Science, Bushehr Branch, Islamic Azad University, Bushehr, Iran*
[c] *Department of Mathematics, Tabriz Branch, Islamic Azad University, Tabriz, Iran*
* *Corresponding author*: *asadpour@m-iau.ac.ir*

It is defined as: $\xi^c(G) = \sum_{u \in V} d(u)ecc(u)$, where $d(u)$ denotes the degree of the vertex u in G. We encourage the reader to consult papers [1, 2, 6] for some applications and papers [3-5] for the mathematical properties of this topological index.

In studying branching properties of alkanes, several numbering schemes for the edges of the associated hydrogen-suppressed graph were proposed based on the degrees of the end vertices of an edge [9]. To preserve rankings of certain molecules, some inequalities involving the weights of edges is needed to be satisfied. Randić [9] stated that weighting all edges *uv* of the associated graph *G* by $(d(u)d(v))^{-1/2}$ preserved these inequalities, where *d(u)* and *d(v)* are the degrees of *u* and *v*. The sum of weights over all edges of *G*, which is called the Randić index, *R(G)*

$$R(G) = \sum_{uv \in E} \frac{1}{\sqrt{d(u)d(v)}}.$$

This index has been closely correlated with many chemical properties [7] and found to parallel the boiling point, Kovats constants, and a calculated surface. In addition, the Randić index appears to predict the boiling points of alkanes more closely, and only it takes into account the bonding or adjacency degree among carbons in alkanes (see [8]).

RESULTS AND DISCUSSION

A graph formed by a row of n hexagonal cells is called an n-hexagonal chain. A hexagonal parallelogram *Lₙ[G]*, is a graph containing n n-hexagonal chains in every row, see Figure 1. It is clear that *Lₙ[G]* has *|V|=2n(n+2)* and *|E|=3n²+4n-1*.

In this section, we compute the eccentric connectivity and Randić indices of hexagonal parallelogram *Lₙ[G]*.
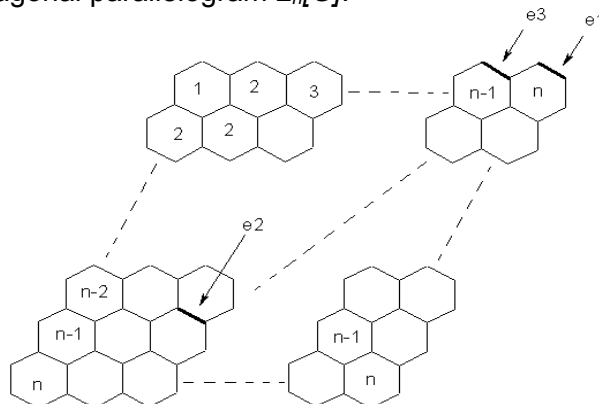
Figure 1. 2-Dimensional graph of a hexagonal parallelogram *Lₙ[G]*

Theorem 1. The eccentric connectivity index of $L_n[G]$ is

$$\xi^c(L_n[G]) = 24n^3 - 31n^2 + 18n - 28 - \sum_{k=0}^{n-2}(24k^2 + k) + \sum_{k=0}^{2n-2} 4k \ .$$

Proof. We have for $u \in V(L_n[G])$, *Max ecc(u)=4n-1* and *Min ecc(u)= 2n*.
In Fig. 2, one can see the eccentricity for every $u \in V(L_n[G])$ while in Fig. 3, one can see several deictic lines for computing the eccentric connectivity index: first line starts with Max *ecc(u)=4n-2* and finishes with *ecc(u)=2n+1*. The second line starts with *ecc(u)=4n-2* and finally it has *ecc(u)=2n*. Similarly for another lines we can compute the eccentric connectivity index. Vertices with eccentric connectivity index *4n-1, 4n-2, 4n-4, 4n-6,…, 2n+2, 2n+1*, have *deg(u)= 2* while the other vertices have *deg(u)=3*, where $u \in V(L_n(G))$. Then by using Figs. 2 and 3, we can fill the Table 1, for eccentric connectivity index of the graph.
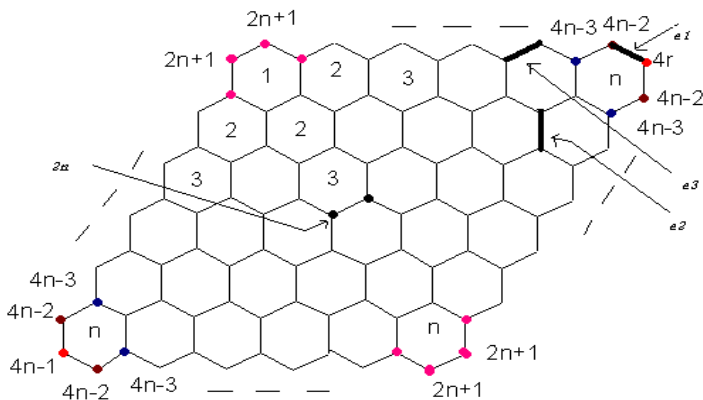
Figure 2. Eccentricity of some vertices $L_n[G]$
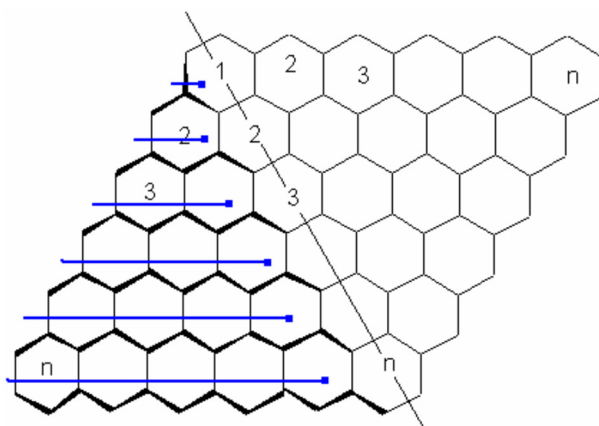
Figure 3. Lines for computing the eccentric connectivity $L_n[G]$

Table 1. Eccentricity of all vertices of $L_n[G]$

Line1	Line2	Line3	Line4	Line5	….	Line(n-1)	Line(n)	ecc
4n-1								max ecc
4n-2	4n-2							
4n-3	4n-3							
4n-4	4n-4	4n-4						
4n-5	4n-5	4n-5	4n-5					
4n-6	4n-6	4n-6	4n-6	4n-6				
4n-7	4n-7	4n-7	4n-7	4n-7				
…..	…..	…..	…..	…..	….			
2n+2	2n+2	2n+2	2n+2	2n+2	….	2n+2		
2n+1	2n+1	2n+1	2n+1	2n+1	….	2n+1	2n+1	
2n+1	2n	2n	2n	2n	….	2n		min ecc

Thus the eccentric connectivity index of hexagonal parallelogram $L_n[G]$ is calculated as follows:

$\xi^c(L_n[G])$ =2[(4n-1)+2(4n-2)+(4n-3)+(4n-6)+…+(2n+3)+(2n+2)+2(2n+1)]
+6[(n-1)2n+n(2n+1)+5(n-1)+9(n-2)+13(n-3)+…+3(4n-11)+2(4n-7)].

By arranging the above formula, we have:

$$\xi^c(L_n[G]) = \sum_{k=0}^{n-2} 24(n^2 - k^2) + \sum_{k=0}^{n-2}(n-k) + \sum_{k=0}^{2n-2} 4(2n+k) + 20n-12$$

and next

$$\xi^c(L_n[G]) = 24n^3 - 31n^2 + 18n - 28 - \sum_{k=0}^{n-2}(24k^2 + k) + \sum_{k=0}^{2n-2} 4k$$

As it was to be demonstrated.

Theorem 2. The Randić index of $L_n[G]$ is

$$R(L_n[G]) = n^2 - n + 3 - \frac{(n-1)(4\sqrt{6}-1)}{3}.$$

Proof. For computing the Randić index for $L_n[G]$ we consider three type edges, (see fig. 4): (a) edge e_1 with ended vertices of degree 2 and 2, (b) edge e_2 with ended vertices of degree 3 and 3, (c) edge e_3 with ended vertices of degree 2 and 3.
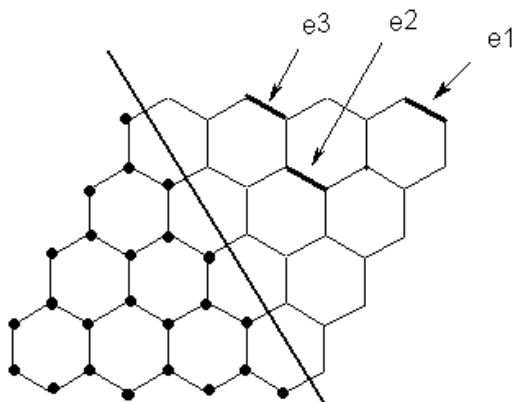
Figure 4. Three type edges e_1, e_2 and e_3 of $L_4[G]$

It is easy to see that

$$|e_1| = 6, \quad |e_3| = 8(n-1), \qquad |e_2| = (3n-1)(n-1),$$

Thus

$$R(L_n[G]) = \frac{6}{\sqrt{2 \times 2}} + \frac{8(n-1)}{\sqrt{2 \times 3}} + \frac{(3n-1)(n-1)}{\sqrt{3 \times 3}}$$

$$= 3 + \frac{(3n-1)(n-1)}{3} + \frac{4\sqrt{6}(n-1)}{3}.$$

REFERENCES

1. A.R. Ashrafi, T. Doslic, M. Saheli, *MATCH Commun. Math. Comput. Chem*. **2011**, *65* (1), 221.
2. H. Dureja, A.K. Madan, *Med. Chem. Res*. **2007**, *16,* 331.
3. T. Doslic, M. Saheli, D. Vukicevic, *MATCH Commun. Math. Comput. Chem,* **2010**, *1* (2), 45.
4. M. Fischermann, A. Homann, D. Rautenbach, L.A. Szekely, L. Volkmann, *Discrete Appl. Math*., **2002**, *122*, 127.
5. S. Gupta, M. Singh, A.K. Madan, *J. Math. Anal. Appl.* **2002**, *266*, 259.
6. V. Kumar, S. Sardana, A.K. Madan, *J. Mol. Model.* **2004**, *10*, 399.
7. L.B. Kier and L.H. Hall, Molecular Connectivity in Chemistry and Drug Research, Academic Press, San Francisco, **1976**.

8. L.B. Kier and L.H. Hall, Molecular Connectivity in Structure-Activity Analysis, Wiley, **1986**.
9. M. Randić, *J. Amer. Chem. Soc*., **1975**, *97*, 6609.
10. V. Sharma, R. Goswami, A. K. Madan, *J. Chem. Inf. Comput. Sci*., **1997**, *37*, 273.
11. H. Wiener, *J. Am. Chem. Soc*. **1947**, *69*, 17.

THE HYPER-WIENER AND MODIFIED HYPER-WIENER INDICES OF GRAPHS WITH AN APPLICATION ON FULLERENES

SIAMAK FIROUZIAN[a,*], MORTEZA FAGHANI[a], FATEMEH KOOREPAZAN-MOFTAKHAR[b] AND ALI REZA ASHRAFI[b,c]

ABSTRACT. Graovac and Pisanski have proposed an algebraic approach for generalizing the Wiener index by automorphism group of the graph under consideration. In this paper we introduce a new modification of the hyper-Wiener index. The hyper-Wiener and modified hyper-Wiener indices of two infinite classes of fullerenes are presented.

Keywords: *Wiener index, hyper-Wiener index, modified hyper-Wiener index, fullerene*.

INTRODUCTION

Throughout this paper, graph means connected graphs without loops and multiple edges. Suppose G is such a graph, with the vertex set $V(G)$. The distance between the vertices $u, v \in V(G)$ is denoted by $d(u,v)$ and it is defined as the number of edges in a shortest path connecting them. The Wiener index, $W(G)$, equals the sum of distances between all pairs of vertices in G [1]. This graph invariant found remarkable applications in chemistry [1,2]. The hyper-Wiener index of acyclic graphs was introduced by Milan Randić in 1993. Then Klein, Lukovits and Gutman [3], generalized Randić's definition for all connected graphs, as a generalization of the Wiener index. It is defined as

$$WW(G) = 1/2\,W(G) + 1/2\sum\nolimits_{\{x,y\}} d(x,y)^2.$$

We refer to [4,5] for mathematical properties and chemical meaning of this topological index. It merits to mention the matrix-based version of some distance-based topological indices, introduced by Diudea [6-9]. To explain,

---

[a] *Department of Mathematics, Payame Noor University, PO Box 19395-3697, Tehran, Iran*
[b] *Department of Mathematics, Faculty of Mathematical Sciences, University of Kashan, Kashan 87317-51167, I. R. Iran*
[c] *Department of Nanocomputing, Institute of Nanoscience and Nanotechnology, University of Kashan, Kashan 87317-51167, I. R. Iran*
* *Corresponding author: siamfirouzian@pnu.ac.ir*

we assume that D and W are Distance and Wiener matrices of a given graph G of order n. The distance matrix is an $n \times n$ matrix in which the ij^{th} entry is the length of a shortest path connecting the ith and j^{th} vertices of the graph under consideration. The Wiener matrix is another $n \times n$ matrix such that its ij^{th} entry is defined as the number of paths containing the (i, j)-path. These matrices can be taken as the basis for calculating W (as the half-sum of matrix entries), whereas Distance-Path D_p and Wiener-Path W_p can be used to calculate the hyper-Wiener index. D_p counts the internal paths of the path ij while W_p the external paths containing the path ij. In a tree graph, the sum of all internal paths equals the sum of external paths (as established in [3]) while, in cyclic graphs, W_p is not defined, thus D_p being the only matrix enabling the calculation of hyper-Wiener index. We encourage the interested readers to consult the mentioned papers by Diudea and references therein for more information on this topic.

Graovac and Pisanski [10] in a pioneering work proposed an algebraic approach for generalizing the Wiener index by automorphism group of the graph under consideration. To explain, we assume that G is a graph with automorphism group $\Gamma = Aut(G)$. The modified Wiener index of G is defined as:

$$\hat{W}(G) = \frac{|V(G)|}{2|\Gamma|} \sum_{x \in V(G)} \sum_{\alpha \in \Gamma} d(x, \alpha(x)).$$

They introduced this generalization of the classical Wiener index to consider the symmetry structure of the graph G. Define in a similar way the modified hyper-Wiener index of G as follows:

$$\overset{\wedge}{WW}(G) = \frac{1}{2} \hat{W}(G) + \frac{|V(G)|}{4|\Gamma|} \sum_{u \in V(G), \alpha \in \Gamma} d(u, \alpha(u))^2.$$

Throughout this paper we use standard notations of graph theory. The path, cycle, star and complete graphs with n vertices are denoted by P_n, C_n, S_n and K_n, respectively.

MODIFIED HYPER-WIENER INDICES OF PATH, CYCLE, STAR AND COMPLETE GRAPHS

It is easy to see that the modified Wiener index of a graph G is equal to zero if and only if $Aut(G)$ is a trivial group. The same is true for the modified hyper-Wiener index of G. On the other hand, it is well-known that most of the finite graphs have trivial automorphism groups. In an exact phrase, suppose α_n and β_n denote the number of n-vertex graphs and n-vertex graphs with trivial automorphism group, respectively. Then,

$$\lim_{n\to\infty} \frac{\alpha_n}{\beta_n} = 1.$$

This means that the modified Wiener and hyper-Wiener indices of most of graphs are zero.

From now on, we consider some well-known graphs like path, cycle, star and complete graph on n vertices. On the other hand, the hyper-Wiener index of n-vertex path P_n, the n-vertex cycle C_n and the n-vertex star S_n can be computed by the following formula:

$$WW(P_n) = \frac{1}{24}(n^4 + 2n^3 - n^2 - 2n); \ WW(S_n) = \frac{1}{2}(n-1)(3n-4),$$

$$WW(C_n) = \begin{cases} \dfrac{n^2(n+1)(n+2)}{48} & 2|n \\[4mm] \dfrac{n(n^2-1)(n+3)}{48} & 2\nmid n \end{cases}.$$

We recall that the symmetry group of a path P_n is a cyclic group of order two and its non-identity element g is as follows:

$$g = \begin{cases} (1 \ n)(2 \ n-1) \dots \left(\dfrac{n+3}{2}\right)\left(\dfrac{n-1}{2} \ \dfrac{n+3}{2}\right) & n \text{ is odd} \\[4mm] (1 \ n)(2 \ n-1) \dots \left(\dfrac{n}{2} \ \dfrac{n+2}{2}\right) & n \text{ is even} \end{cases}.$$

On the other hand the group of all symmetries of a regular polygon, including both rotations and reflections is called the dihedral group. This group has the order $2n$ and is denoted by D_{2n}.

Assume that n is odd. Then we have:

$$\begin{aligned} \widehat{W}(P_n) &= \frac{|V(G)|}{2|Aut(G)|} \sum_{u\in V(G),g\in Aut(G)} d(u,g(u)) \\ &= \frac{n}{4} \times 2 \times \left[d(1,n) + d(2,n-1) + \cdots + d\left(\frac{n-1}{2}, \frac{n+3}{2}\right) \right] \\ &= \frac{n}{2} \times [(n-1) + (n-3) + \cdots + 2] \\ &= \frac{n^3 - n}{8}; \text{ when } n \text{ is odd.} \end{aligned}$$

$$
\begin{aligned}
\widehat{W}(P_n) &= \frac{|V(G)|}{2|Aut(G)|} \sum_{u \in V(G), g \in Aut(G)} d(u, g(u)) \\
&= \frac{n}{4} \times 2 \times \left[d(1, n) + d(2, n-1) + \cdots + d\left(\frac{n}{2}, \frac{n+2}{2}\right) \right] \\
&= \frac{n}{2} \times \left[(n-1) + (n-3) + \cdots + 1 \right] \\
&= \frac{n^3}{8}; \text{ when } n \text{ is even.}
\end{aligned}
$$

This corrects the calculation of modified Wiener index given [10]. If n is odd then the modified hyper-Wiener index can be calculated in the following form:

$$
\begin{aligned}
\widehat{WW}(P_n) &= \frac{1}{2} \times \frac{n^3 - n}{8} + \frac{n}{8} \times 2 \times (2^2 + 4^2 + \cdots + (n-1)^2) \\
&= \frac{n^3 - n}{16} + \frac{n^4 - n^2}{24} \\
&= \frac{n^4}{24} + \frac{n^3}{16} - \frac{n^2}{24} - \frac{n}{16},
\end{aligned}
$$

and if n is even then we have,

$$
\begin{aligned}
\widehat{WW}(P_n) &= \frac{1}{2} \times \frac{n^3}{8} + \frac{n}{8} \times 2 \times (1^2 + 3^2 + \cdots + (n-1)^2) \\
&= \frac{n^3}{16} + \frac{n^2}{24}(n^2 - 1).
\end{aligned}
$$

To compute the modified hyper-Wiener index of cycle graph C_n, we apply calculation of the modified Wiener index of C_n given [Example 5.7, 10] as follows:

$$
\widehat{W}(C_n) = \begin{cases} \dfrac{n^3}{8} & n \text{ is even} \\ \dfrac{n^3 - n}{8} & n \text{ is odd} \end{cases}.
$$

By a method similar to the case of P_n, we have:

$$
\widehat{WW}(C_n) = \begin{cases} \dfrac{1}{48}n^4 + \dfrac{1}{16}n^3 + \dfrac{1}{24}n^2 & n \text{ is even} \\[3mm] \dfrac{1}{48}n^4 + \dfrac{1}{16}n^3 - \dfrac{1}{48}n^2 - \dfrac{1}{16}n & n \text{ is odd} \end{cases}.
$$

It is clear that if $u,v \in K_n$ then $d(u,v) = 1$ and so between graphs with exactly n vertices, the complete graph K_n has the minimum hyper–Wiener index. Hence for every n–vertex graph G,

$$WW(G) \geq WW(K_n) = \binom{n}{2}.$$

On the other hand, it is easy to see that the symmetry group of K_n is isomorphic to the symmetric group S_n and so

$$\widehat{W}(K_n) \;=\; \widehat{WW}(K_n) = \frac{n^2}{2} - \frac{n}{2}.$$

Since graphs with trivial automorphism group have zero hyper-Wiener index, the complete group K_n does not have the minimum value of hyper-Wiener index in the set of all n-vertex graphs.

We end this section by calculation of the modified hyper-Wiener index of S_n. Suppose $X = \{1, \dots, k\}$. We denote by Sym_k the set of all permutations of X. Sym_k forms a group under composition of functions. It is well-known that the symmetry group of the star graph is isomorphic to Sym_{n-1}. So,

$$\widehat{W}(S_n) = \frac{|V(S_n)|}{2|Aut(S_n)|} \sum_{u \in V(S_n), g \in Aut(S_n)} d\big(u, g(u)\big) = \frac{n}{2(n-1)!} \sum_i i \times n_i.$$

Define $A = \{\big(u, g(u)\big) | u \in \{1, \dots, n-1\}, g \in Aut(S_n) = Sym_{n-1}, \; g(u) \neq u\}$ and note that in the star graph all pairs of vertices are in distance 0, 1 or 2. By the structure of star graph, we have $d(u, g(u)) = 2$ and so $|A| = (n-1)! - (n-2)! = (n-2)(n-2)!$. Therefore,

$$\widehat{W}(S_n) = (n-1) \times \frac{n}{2(n-1)!} \times 2 \times (n-2)(n-2)! = n(n-2),$$

$$\widehat{WW}(S_n) = \frac{1}{2}\widehat{W}(S_n) + \frac{|V(S_n)|}{4|Aut(S_n)|} \sum_{u \in V(S_n), g \in Aut(S_n)} d(u, g(u))^2$$

$$= \frac{n(n-2)}{2} + \frac{n}{4(n-1)!} \times 4 \times (n-1) \times |A|$$

$$= \frac{n(n-2)}{2} + n(n-2) = \frac{3}{2}n(n-2).$$

FULLERENE GRAPHS

A graph G is called 3-regular or cubic, if the degree of each vertex is three. G is said to be 3-connected, if there does not exist a set of two vertices whose removal disconnects the graph. A planar, cubic and 3-connected graph is called a fullerene graph if all faces are pentagons and hexagons. The importance of fullerene graphs is for applications in fullerene chemistry. This new topic has been developed after pioneering work of Kroto and his team [11]. The mathematical properties of fullerene graphs are a new branch of nanoscience started by pioneering work of Fowler *et al.* [12,13]. We encourage the reader to consult the papers [14-16] and references therein for more information on this topic.

In [17-20], the symmetry and topology of some infinite classes of fullerenes are investigated. The aim of this section is to continue our last works on two fullerene series C_{50+10n} and C_{60+12n} (Figures 1 and 2, respectively) by computing the modified Wiener and hyper-Wiener indices. We first notice that the symmetry group of the fullerene C_{50+10n} has D_{5h} point group symmetry and so it is isomorphic to the dihedral group D_{20}. The fullerene graphs C_{60+12n} have D_{6d} point group symmetry that is isomorphic to the dihedral group D_{24}, when n is odd. If n is even, these fullerenes have the point group symmetry D_{6h} isomorphic to $Z_2 \times Z_2 \times Sym_3$, the symmetry group on three symbols. By this information, we apply HyperChem [21] and TopoCluj [22] to calculate

$$WW(C_{72}) = 47178, WW(C_{84}) = 75564, \widehat{WW}(C_{72}) = 52056, \widehat{WW}(C_{84}) = 84042.$$

On the other hand, some of the present authors [23], proved a matrix method for calculation of the Wiener index of some classes of fullerenes. By applying this method, one can see that:

$$WW\left(C_{50+10n}\right) = \begin{cases} \dfrac{25}{6}n^4 + \dfrac{400}{3}n^3 + \dfrac{9635}{6}n^2 + \dfrac{31625}{3}n + 14515 & n \text{ is odd} \\[3mm] \dfrac{25}{6}n^4 + \dfrac{400}{3}n^3 + \dfrac{9635}{6}n^2 + \dfrac{31715}{3}n + 14710 & n \text{ is even} \end{cases},$$

$$WW\left(C_{60+12n}\right) = \begin{cases} 6n^4 + 204n^3 + 2628n^2 + 20076n + 21924 & n \text{ is odd} \\ 6n^4 + 204n^3 + 2628n^2 + 20136n + 22362 & n \text{ is even} \end{cases}.$$
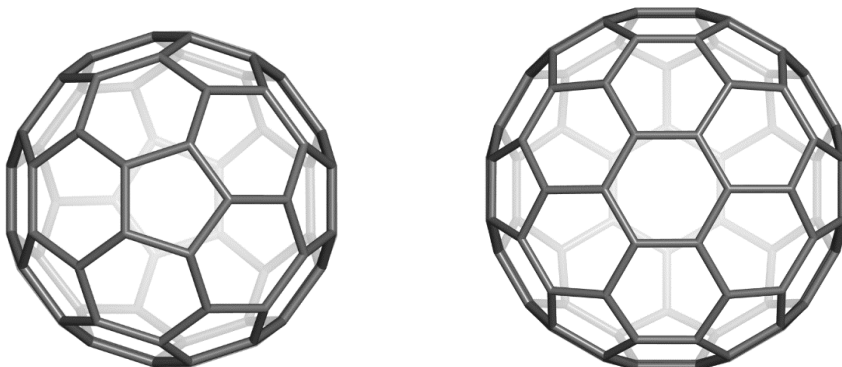
Figure 1. The Case of $n = 9$ in C_{50+10n}.   **Figure 2**. The Case of $n = 9$ in C_{60+12n}.

We now use the automorphism group of these fullerenes to compute their modified hyper-Wiener indices. A simple case by case calculation for pairs of vertices at distance i can provide the following formulas for the modified hyper-Wiener indices of C_{50+10n} and C_{60+12n} fullerenes:

$$\widehat{WW}\left(C_{50+10n}\right) = \begin{cases} \dfrac{25}{6}n^4 + \dfrac{725}{6}n^3 + \dfrac{5320}{3}n^2 + \dfrac{60745}{6}n + \dfrac{37575}{2} & n \text{ is odd} \\[3mm] \dfrac{25}{6}n^4 + \dfrac{725}{6}n^3 + \dfrac{5350}{3}n^2 + \dfrac{30335}{3}n + 18475 & n \text{ is even} \end{cases},$$

$$\widehat{WW}\left(C_{60+12n}\right) = \begin{cases} 6n^4 + 183n^3 + 3069n^2 + 18075n + 32775 & n \text{ is odd} \\ 6n^4 + 183n^3 + 3093n^2 + 18606n + 34830 & n \text{ is even} \end{cases}.$$

Our calculation, on fullerene graphs of small order suggests the following conjecture:

CONJECTURE

If F is a fullerene graph then $\dfrac{WW(F)}{\widehat{WW}(F)} \leq 3$.

ACKNOWLEDGMENTS

169

REFERENCES

1. H. J. Wiener, *J. Am. Chem. Soc.*, **1947**, *69*, 17.
2. I. Gutman, L. Šoltés, *Z. Naturforsch.*, **1991**, *46a*, 865.
3. D. J. Klein, I. Lukovits, I. Gutman, *J. Chem. Inf. Comput. Sci.*, **1995**, *35,* 50.
4. M. H. Khalifeh, H. Yousefi–Azari, A. R. Ashrafi, *Comput. Math. Appl.,* **2008**, *56,* 1402.
5. I. Gutman, W. Linert, I. Lukovits, A. A. Dobrynin, *J. Chem. Inf. Comput. Sci.,* **1997**, *37,* 349.
6. M. V. Diudea, *J. Chem. Inf. Comput. Sci.*, **1996**, *36,* 535.
7. M. V. Diudea, G. Katona, B. Pârv, *Croat. Chem. Acta*, **1997**, *70,* 509.
8. M. V. Diudea, *J. Chem. Inf. Comput. Sci.,* **1996**, *36,* 833.
9. M. V. Diudea, *J. Chem. Inf. Comput. Sci.,* **1997**, *37,* 300.
10. A. Graovac, T. Pisanski, *J. Math. Chem.*, **1991**, *8*, 53.
11. H. W. Kroto, J. R. Heath, S. C. O'Brien, R. F. Curl, R. E. Smalley, *Nature*, **1985**, *318*, 162.
12. P. W. Fowler, D. E. Manolopoulos, "An Atlas of Fullerenes", Oxford Univ. Press, Oxford, **1995**.
13. W. Myrvold, B. Bultena, S. Daugherty, B. Debroni, S. Girn, M. Minchenko, J. Woodcock, P. W. Fowler, *MATCH Commun. Math. Comput. Chem.*, **2007**, *58,* 403.
14. P. Schwerdtfeger, L. Wirz, J. Avery, *J. Comput. Chem.*, **2013**, *34*, 1508.
15. O. Ori, F. Cataldo, S. Iglesias-Groth, A. Graovac, Topological modeling of $C_{60}H_{36}$ hydrides, In "Fulleranes: The Hydrogenated Fullerenes", F. Cataldo, S. Iglesias-Groth (Eds.), Springer-Varlag, **2010**, p. 251.
16. J. E. Graver, Catalog of all fullerenes with ten or more symmetries, Graphs and discovery, DIMACS Ser. Discrete Math. Theoret. Comput. Sci., **2005**, 69, 167, Amer. Math. Soc., Providence, RI.
17. S. Djafari, F. Koorepazan-Moftakhar, A. R. Ashrafi, *J. Comput. Theor. Nanosci.,* **2013**, *10*, 2636.
18. F. Koorepazan-Moftakhar, A. R. Ashrafi, *J. Comput. Theor. Nanosci.*, **2013**, *10*, 2484.
19. F. Koorepazan-Moftakhar, A. R. Ashrafi, Fullerenes: Topology and Symmetry, In: I. Gutman (Ed.), "Topics in Chemical Graph Theory", University of Kragujevac, Faculty of Science Kragujevac, **2014**, p. 163.
20. F. Koorepazan-Moftakhar, A. R. Ashrafi, Z. Mehranian, *MATCH Commun. Math. Comput. Chem.*, **2014**, *71*, 425.
21. HyperChem package, Release 7.5 for Windows, Hypercube Inc., Florida, USA, **2002**.
22. M. D. Diudea, O. Ursu, L. Cs. Nagy, TOPOCLUJ software program, Babes-Bolyai University, Cluj, **2002**.
23. H. Hua, M. Faghani, A. R. Ashrafi, *MATCH Commun. Math. Comput. Chem.*, **2014**, *71,* 361.

QSAR STUDIES ON DERIVATIVES OF RESVERATROL

ALEXANDRA M. HARSA[a], TEODORA E. HARSA[a] AND MIRCEA V. DIUDEA[a,*]

ABSTRACT. A set of 40 resveratrol derivatives, downloaded from the PubChem database, was submitted to a QSAR study, following Diudea's algorithm, involving the hypermolecule concept, in a procedure similar to that of the „alignment" of drug molecules to the biological receptors. The best models describing log P of this set of resveratrols were validated by the leave-one-out procedure, in the external test set and in a new version of prediction by using clusters of similar molecules. The structures have been optimized at HF 6-31G(d,p) level of theory. Topological indices have been computed by TOPOCLUJ software.

Keywords: resveratrol, QSAR, hypermolecules, log P.

INTRODUCTION

Resveratrol is a plant polyphenolic derivative, highly abundant in grapes, peanuts, and other plants [1,2]. Numerous studies have reported interesting properties of trans-resveratrol as a preventive agent of several important pathologies: vascular diseases, cancers, viral infection, neurodegenerative processes such as Alzheimer's [3-6].

The octanol–water partition coefficient (log P) is a key parameter in the passive transport of drug molecules to the biological receptors [7].

Quantitative structure-activity relationships (QSAR) are widely used to relate biological activity with chemical structure, by means of topological indices [8]. Among thousands of topological indices [9], the Cluj indices (proposed by Diudea [10, 11]) are used for molecular graph description.

In testing the predictive ability of QSAR models, among many other tests, the leave one out LOO is a simple and useful method. [12].

---

[a] *Babeş-Bolyai University, Faculty of Chemstry and Chemical Engineering, 11 Arany Janos str., RO-400028, Cluj-Napoca, Romania*
* Corresponding author: diudea@gmail.com

STRUCTURAL MOLECULAR DATA

A set of 40 resveratrol derivatives, taken from PubChem Database [13] (Table 1), were divided into a training set (25 molecules) and a test set (15 molecules), taken randomly; the modelled property was log P (Table 1).

Table 1. Resveratrol derivatives molecular structures (in SMILES code) and their log P (taken from PubChem).

Mol.	Canonical SMILES	log P	CID
1	C1=CC(=CC=C1CCC2=CC(=CC(=C2)O)O)O	3.1	185914
2	CC(=CC1=CC=C(C=C1)O)C2=CC(=CC(=C2)O)O	3.7	75071272
3	C1=CC(=CC(=C1)O)CCC2=CC(=CC(=C2)O)O	3.1	21574990
4	C1=CC=C(C=C1)CCC2=CC(=CC(=C2)O)O	3.4	442700
5	CC(CC1=CC(=CC(=C1)O)O)C2=CC=C(C=C2)O	3.4	58892268
6	COC1=C(C=CC(=C1)C=CC2=CC(=CC(=C2)O)O)O	3.2	5318650
7	COC1=C(C=C(C=C1)CC(C2=CC(=C(C(=C2)OC)OC)OC)O)O	2.6	335929
8	C1=CC(=CC=C1C=CC2=CC(=CC(=C2)O)O)O	3.1	445154
9	C1=CC(=CC(=C1)O)CCC2=CC=C(C=C2)O	3.5	181511
10	C1=CC=C(C=C1)COC2=CC=C(C=C2)O	3.4	7638
11	C1=CC=C(C=C1)C2C(O2)C3=CC=CC=C3	2.9	5742860
12	CCC(C1=CC=C(C=C1)O)C(CC)C2=CC=C(C=C2)O	5.2	3606
13	O(C1=CC(=CC(=C1)OC)\C(=C(\C2=CC=C(OC)C=C2)[H])[H])C	4.1	5388063
14	COC1=CC=C(C=C1)C=CC2=CC(=C(C(=C2)OC)OC)OC	4.1	125922
15	COC1=C(C=C(C=C1)C(C(C2=CC(=C(C(=C2)OC)OC)OC)O)O)O	1.4	10247286
16	COC1=CC(=CC(=C1O)OC)C(CC2=CC=C(C=C2)O)OC)OC	2.8	75149948
17	COC1=CC(=CC(=C1O)O)C(CC2=CC=C(C=C2)O)OC	2.5	74429419
18	CCOC(CC1=CC=C(C=C1)O)C2=CC(=C(C(=C2)OC)O)O	2.8	74429420
19	CC(C(=CC1=CC(=C(C=C1)OC)O)C2=CC(=C(C(=C2)OC)OC)OC)O	3.5	54586166
20	COC1=CC=C(C=C1)CC(C2=C(C(=C(C=C2)OC)OC)O)O	3.1	44429048
21	COC1=CC=C(C=C1)C(C(C2=CC(=C(C(=C2)OC)OC)OC)O)O	1.8	10592816
22	COC1=C(C=C(C=C1)CC(C2=CC(=CC(=C2)OC)OC)O)OC	2.5	66673695
23	COC1=CC=C(C=C1)CC(C2=CC(=C(C(=C2)OC)OC)OC)O	2.9	57423765
24	COC1=C(C=C(C=C1)C(C(C2=CC=C(C(=C2)OC)OC)OC)O)O)O	1.6	54129628
25	COC1=C(C=C(C=C1)C=C(CO)C2=CC(=C(C(=C2)OC)OC)OC)O	3.1	11078510
26	COC1=C(C=C(C=C1)C(CC2=CC(=C(C(=C2)OC)OC)O)OC	2.9	356755
27	COC1=CC(=CC(=C1OC)OC)C(CC2=CC=CC=C2)O	2.9	353079
28	CC(=CC1=CC(=CC(=C1)OC)OC)C2=CC=C(C=C2)OC	4.7	75071221
29	COC1=CC=CC(=C1)C=CC2=CC(=CC(=C2)OC)OC	4.1	69452320
30	COC1=CC(=O)OC(C1)C=CC2=CC=CC=C2	2.5	5369129
31	COC1=CC(=CC(=C1)C=CC2=CC=CC=C2)OC	4.1	13556468
32	CC(=CC1=CC(=CC(=C1)OC)OC)C2=CC=CC=C2	4.8	68796507
33	O(C1=CC(=CC(=C1)OC)C=CC2=CC(=CC(=C2)OC)OC)C	4.1	67145168

Mol.	Canonical SMILES	log P	CID
34	COC1=CC(=CC(=C1)C=CC2=CC=C(C=C2)C=C)OC	4.9	70184295
35	CCOC1=CC=C(C=C1)C=CC2=CC(=CC(=C2)OC)OC	4.5	69899106
36	CC1=CC=C(C=C1)C=CC2=CC(=CC(=C2)OC)OC	4.5	58240360
37	CCOC1=CC=C(C=C1)C=CC2=CC(=CC(=C2)OCC)OCC	5.2	67435273
38	O(C2=C(C=CC1=CC(=CC(=C1)OC)OC)C=CC(=C2)OC)C	4.1	5491
39	COC1=CC(=CC(=C1)CC(=C)C2=CC=CC=C2)OC	4.8	69940018
40	CC(C)OC1=CC=C(C=C1)C=CC2=CC(=CC(=C2)OC)OC	4.9	66674282

On the set of 40 resveratrols, a Hypermolecule [14] was built up, as a reunion of their substructures (Figure 1).

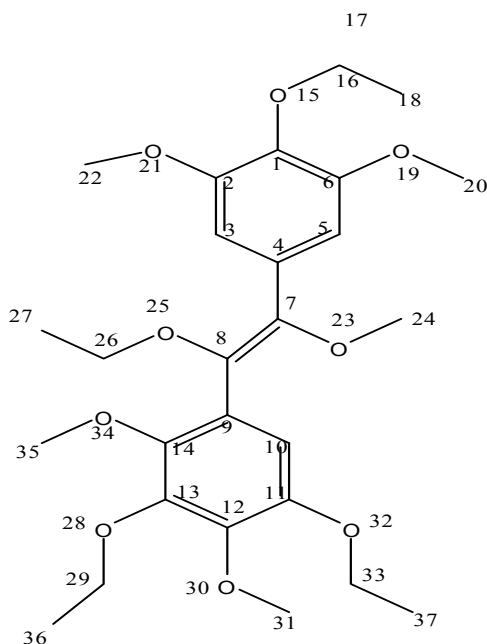**Figure 1**. The hypermolecule built on 40 resveratrols of the dataset

COMPUTATIONAL DETAILS

The structures have been optimized at Hartree-Fock HF (3-21g(,p)) level of theory, in gas phase, by Gaussian 09 [15]. Topological indices have beed computed by TOPOCLUJ software [16]; some of them (Conectivity =C, Total adjacency = Adj, Charges=Ch, Detour = De, Distance = Di, D3D, SD), HOMO (in au) and log P are listed in Table 2.

RESULTS AND DISCUSSION

Two cases are discussed in the Hypermolecule description: (1) mass fragments and (2) partial charges (HF level of theory).

1. Mass fragments description (case 1)

1.1.Data reduction

The local correlation-weighted descriptors are summed to give SD1 global descriptor, over the following significant positions in the hypermolecule: H1, H5, H6, H7, H8, H13, H15, H17, H22, H23, H25, H26, H28. SD_1 correlation with log P: $\log P = 116.302 + 1.00001 \times SD_1$, $R^2=0.934$, n=40, s=0.253, F=536.085, and the best results are listed below and in Table 3.

1.2. QSAR models

The models were performed on the training set (25 structures in Table 1) and the best results are listed below and in Table 3. The number of descriptors was limited to four, to fulfil the considerations of Topliss and Costello [17].

Table 2. Log P, correlating descriptors SD_k, and topological indices for the set of 40 Resveratrols in Table 1.

Mol.	log P	SD_1	SD_2	HOMO	Ch	C	Di	D3D	De
1	3.1	-113.037	-1.181	-8.971	0.12	24	582	564.13	956
2	3.7	-112.731	-0.690	-8.764	0.074	26	650	629.21	1052
3	3.1	-113.538	-1.513	-8.981	0.22	24	572	550.25	966
4	3.4	-113.053	-0.872	-9.005	0.11	23	485	472.69	831
5	3.4	-112.656	-0.583	-8.990	0.089	25	651	625.47	1053
6	3.2	-112.661	-0.992	-8.813	0.25	27	780	718.72	1258
7	2.6	-113.882	-2.115	-9.092	0.37	31	1417	1269.69	2095
8	3.1	-112.689	-1.089	-8.558	0.11	25	582	622.57	956
9	3.5	-113.037	-1.144	-8.989	0.051	23	499	488.45	829
10	3.4	-112.944	-0.960	-8.712	0.015	22	420	462.68	708
11	2.9	-112.914	-1.742	-9.733	0.11	23	387	438.72	738
12	5.2	-111.713	0.345	-8.919	-0.054	27	814	815.42	1222
13	4.1	-112.126	-0.135	-8.712	0.15	28	926	877.77	1422
14	4.1	-112.093	-0.212	-8.669	0.2	30	1175	1090.57	1751
15	1.4	-114.860	-3.114	-9.105	0.46	32	1530	1344.92	2242

174

Mol.	log P	SD_1	SD_2	HOMO	Ch	C	Di	D3D	De
16	2.8	-113.547	-1.801	-8.991	0.41	31	1372	1234.4	2072
17	2.5	-113.564	-1.649	-8.929	0.3	28	960	930.04	1474
18	2.8	-113.587	-1.640	-8.926	0.27	29	1081	1055.79	1625
19	3.5	-112.301	-0.938	-8.965	0.31	34	1681	1603.94	2427
20	3.1	-113.345	-1.043	-9.033	0.34	29	1132	1063.14	1704
21	1.8	-114.322	-2.474	-8.975	0.38	31	1384	1274.14	2024
22	2.5	-113.830	-1.470	-9.004	0.35	30	1276	1138.86	1936
23	2.9	-113.345	-1.519	-8.981	0.29	30	1276	1177.67	1884
24	1.6	-114.921	-2.893	-8.951	0.54	33	1665	1533.68	2481
25	3.1	-113.486	-1.527	-8.528	0.26	32	1417	1325.27	2095
26	2.9	-113.410	-1.784	-9.019	0.36	32	1584	1425.58	2332
27	2.9	-113.394	-1.519	-9.229	0.27	28	956	918.89	1500
28	4.7	-111.745	0.041	-8.940	0.12	28	1016	1005.11	1544
29	4.1	-112.100	-0.164	-8.983	0.19	28	902	825.24	1446
30	2.5	-113.801	-1.871	-9.406	0.25	24	574	579.89	962
31	4.1	-112.176	-0.109	-8.920	0.14	26	669	645.06	1101
32	4.8	-111.795	0.486	-8.988	0.1	27	746	724.84	1210
33	4.1	-112.241	-0.553	-8.908	0.29	30	1155	1086.77	1819
34	4.9	-111.601	0.193	-8.769	0.051	29	926	880.89	1422
35	4.5	-111.435	0.352	-8.700	0.12	29	1084	1027.89	1612
36	4.5	-111.601	-0.438	-8.755	0.14	27	788	750.88	1252
37	5.2	-111.435	0.336	-8.669	0.041	31	1396	1331.03	2026
38	4.1	-112.142	-0.177	-8.821	0.37	30	1155	1058.79	1819
39	4.8	-111.757	0.266	-8.961	0.1	27	746	747.63	1210
40	4.9	-111.435	0.568	-8.668	0.082	30	1244	1173.82	1804

(i) Monovariate regression

$$\log P = 111.136 + 0.954 \times SD_1$$

(ii) Bivariate regression

$$\log P = 108.915 + 0.933 \times SD_1 - 0.0002 \times D3D$$

(iii) Three-variate regression

$$\log P = 109.175 + 0.939 \times SD_1 - 0.003 \times Di + 0.002 \times De$$

(iv) Four-variate regression

$$\log P = 111.411 + 0.927 \times SD_1 + 0.433 \times HOMO + 0.004 \times De - 0.005 \times CjDi$$

Table 3. Best models in describing log P in the training set
of resveratrol derivates in Table 1.

	Descriptors	R^2	Adjust. R^2	St. Error	F
1	SD1	0.951	0.949	0.205	448.907
2	HOMO	0.150	0.113	0.857	4.072
3	Di	0.149	0.112	0.858	4.029
4	De	0.149	0.112	0.858	4.036
5	SD1, D3D	0.956	0.952	0.200	237.196
6	SD1, Di	0.955	0.951	0.201	235.945
7	SD1, CjDe	0.955	0.951	0.202	233.911
8	SD1, De	0.955	0.951	0.202	232.918
9	SD1, HOMO	0.952	0.948	0.209	217.899
10	SD1, Di, De	0.961	0.955	0.193	171.693
11	SD1, De, CjDi	0.960	0.954	0.196	165.871
12	SD1, HOMO, D3D	0.958	0.952	0.199	160.408
13	SD1, HOMO, Di	0.958	0.952	0.200	159.512
14	SD1, D3D, De	0.958	0.952	0.199	159.893
15	SD1, HOMO, Ch	0.957	0.951	0.201	156.987
16	SD1, D3D, Di	0.956	0.950	0.204	152.179
17	SD1, HOMO, De, CjDi	0.964	0.957	0.189	133.954
18	SD1, HOMO, D3D, De	0.961	0.953	0.198	122.206
19	SD1, De, D3D, Di	0.961	0.953	0.197	122.716
20	SD1, C, Di, D3D	0.958	0.950	0.204	115.137

1.3. Model Validation

(a) Leave-one-out
The performances in leave-one-out analysis related to the models listed as the best in Table 3 are presented in Table 4 [18,19].

Table 4. Leave-one-out analysis for best log P models (Table 3).

	Descriptors	Q^2	R^2-Q^2	St. Error$_{loo}$	F_{loo}
1	SD_1	**0.941**	0.1	0.225	368.511
5	SD_1, D3D	**0.938**	0.018	0.231	349.079
11	SD_1, Di, De	**0.944**	0.017	0.219	389.566
19	SD_1, HOMO, De, CjDi	**0.944**	0.02	0.219	389.113

(b) External Validation

The values log P for the test set of resveratrols (Table 1) were calculated by using the best equation (with three variables) in Table 3, entry 10. Data are listed in Table 5 and the monovariate correlation: $\log P = 0.763 \times \log P_{calc.} + 0.876$; n=15; R^2=0.859; s=0.411; F=79.105 is plotted in Figure 2.

Table 5. Calculated values of log P for the molecules in the test set (Table 1)

Mol.	log P	log P$_{calc.}$
5	3.4	3.67
6	3.2	3.72
7	2.6	2.40
8	3.1	3.65
9	3.5	3.30
10	3.4	3.36
11	2.9	3.58
12	5.2	4.40
13	4.1	4.11
14	4.1	4.08
15	1.4	1.45
37	5.2	4.60
38	4.1	4.28
39	4.8	4.57
40	4.9	4.59
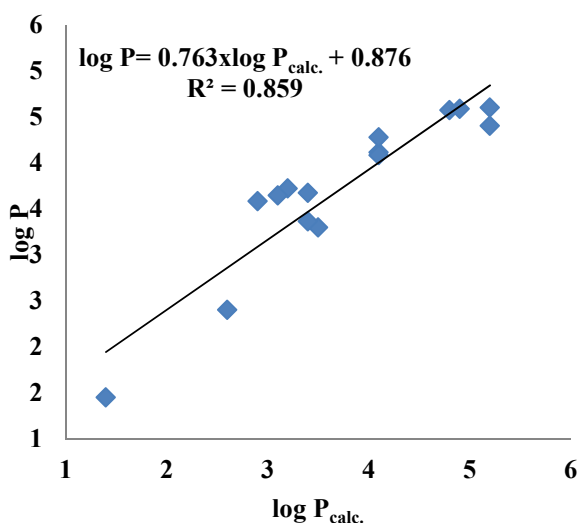
Figure 2. The plot log P vs. log P$_{calc.}$ for the test set (external validation)

(c) Similarity Cluster Validation

Validation can be performed by calculating log P for the molecules in the test set with equations learned on clusters of similarity: each of the 15 molecules is the leader in its own cluster, selected by (2D) similarity among the 25 structures of the initial learning set. The values log P$_{calc.}$ for each of the 15 molecules in the test set were computed by 15 new equations (the leader being left out) with the same descriptors as in eq. 10, Table 3. Data are listed in Table 6 and the monovariate correlation: $\log P = 0.923 \times \log P_{calc.} + 0.288$; n=15; R^2=0.979; s=0.157; F=622.623 is plotted in Figure 3 [20].

177

Table 6. Calculated values of log P by similarity clusters, for the molecules in the test set (Table1)

Mol.	log P	log $P_{calc.}$
5	3.4	3.31
6	3.2	3.31
7	2.6	2.57
8	3.1	3.28
9	3.5	3.32
10	3.4	3.39
11	2.9	3.15
12	5.2	4.88
13	4.1	4.12
14	4.1	4.08
15	1.4	1.52
37	5.2	5.08
38	4.1	4.27
39	4.8	4.60
40	4.9	5.03

$$\log P = 0.923 \times \log Pcalc. + 0.288$$
$$R^2 = 0.979$$
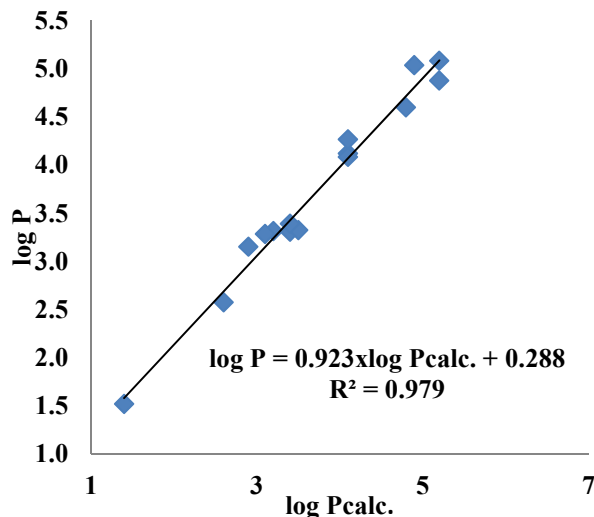
Figure 3. The plot log P vs. log $P_{calc.}$ for the test set (similarity clusters)

2. Partial charges description (case 2)

2.1. Data reduction (for log P)

This new descriptor SD_2, that is a linear combination of the local correlating descriptors for the significant positions in the hypermolecule H1, H3, H4, H7, H8, H9, H13, H14, H16, H17, H18, H20, H23, H29, H30, H31, eq., $\log P = 4.428 + 0.999 \times SD_2$ $R^2=0.940$, s=0.240, F=600.419.

2.2. QSAR models (for log P)

QSAR models using different combinations of descriptors were tried, but the models which provided best correlation coefficient for training set are described below and in Table 7 [21].

(i) Monovariate regression
$$\log P = 4.458 + 1.025 \times SD_2$$

(ii) Bivariate regression
$$\log P = 7.993 + 0.994 \times SD_2 + 0.399 \times HOMO$$

(iii) Three-variate regression

$$\log P = 3.377 + 0.872 \times SD_2 - 1.706 \times Ch. + 0.046 \times C$$

(iv) Four-variate regression

$$\log P = 3.878 + 1.039 \times SD_2 - 0.004 \times Di + 0.003 \times D3D. + 0001 \times De$$

Table 7. Best models in describing log P in the training set
of resveratrol derivatives in Table1.

	Descriptors	R^2	Adjust. R^2	St. Error	F
1	SD$_2$	0.949	0.947	0.243	430.049
2	HOMO	0.232	0.199	0.945	6.967
3	De	0.158	0.121	0.990	4.309
4	Di	0.146	0.108	0.997	3.918
5	SD$_2$, HOMO	0.953	0.949	0.239	222.847
6	SD$_2$, C	0.952	0.947	0.243	216.235
7	SD$_2$, D3D	0.952	0.947	0.242	216.767
8	SD$_2$, Di	0.951	0.947	0.244	214.565
9	SD$_2$, CjDe	0.951	0.947	0.244	214.150
10	SD$_2$, De	0.951	0.947	0.244	214.662
11	SD$_2$, Ch, C	**0.961**	0.956	0.223	172.920
12	SD$_2$, Di, Ch	0.960	0.954	0.226	168.094
13	SD$_2$, D3D, Di	0.954	0.947	0.243	144.189
14	SD$_2$, HOMO, D3D	0.953	0.947	0.244	142.881
15	SD$_2$, HOMO, Di	0.953	0.946	0.245	142.271
16	SD$_2$, Di, C	0.952	0.945	0.248	138.131
17	SD$_2$, CjDi, CjDe	0.952	0.945	0.247	139.068
18	SD$_2$, D3D, De	0.952	0.945	0.247	139.724
19	SD$_2$, Di, D3D, De	0.955	0.946	0.246	105.304
20	SD$_2$, HOMO, D3D, De	0.954	0.945	0.249	103.317
21	SD$_2$, C, D3D, Di	0.954	0.945	0.248	104.166

2.3. Model Validation (for log P)

(a) Leave-one-out

The performances in leave-one-out analysis related to the models listed as the best in Table 7 are presented in Table 8 [22].

**Table 8.** Leave-one-out analysis for best log P models in Table 7.

	Descriptors	Q^2	R^2-Q^2	St. Error$_{loo}$	F_{loo}
1	SD_1	0.941	0.008	0.262	367.752
5	SD_1, HOMO	0.943	0.01	0.258	377.825
11	SD_1, Ch, C	0.949	0.012	0.244	426.74
19	SD_1, Di, D3D, De	0.933	0.022	0.279	321.249

(b) External Validation

The values log P for the test set of resveratrols (Table 1),were calculated by using the best equation in Table 7, entry 11. Data are listed in Table 9 and the monovariate correlation: $\log P = 1.031 \times \log P_{calc.} - 0.051$; n=15; R^2=0.938; s=0.213; F=195.279 is plotted in Figure 4 [23].

Table 9. Calculated values of log P for the molecules in the test set (Table 1)

| Mol.	log P	log P$_{calc.}$
1	3.1	3.26
2	3.7	3.86
3	3.1	2.80
4	3.4	3.50
5	3.4	3.88
6	3.2	3.34
7	2.6	2.34
8	3.1	3.40
9	3.5	3.36
10	3.4	3.54
11	2.9	2.74
12	5.2	5.03
13	4.1	4.31
14	4.1	4.25
15	1.4	1.37
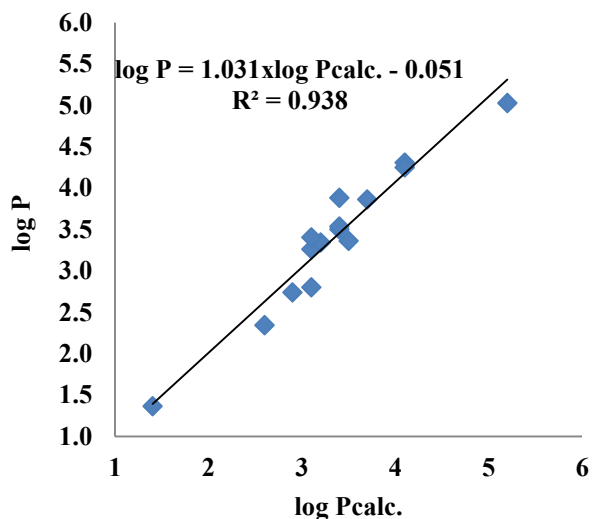
Figure 4. The plot log P vs. log P$_{calc.}$ for the test set (external validation)

(c) Similarity Cluster Validation

The values log P calc. for each of the 15 molecules in the test set were computed with the same descriptors as in eq. 11, Table 7. Data are listed in Table 10 and the monovariate correlation: $\log P = 1.020 \times \log P_{calc.} + 0.002$; n=15; R^2=0.981; s=0.119; F=659.369 plotted in Figure 5 [22].

Table 10. Calculated values of log P by similarity clusters, for the molecules in the test set (Table 1)

Mol.	log P	log $P_{calc.}$
1	3.1	3.29
2	3.7	3.84
3	3.1	2.90
4	3.4	3.53
5	3.4	3.58
6	3.2	3.34
7	2.6	2.69
8	3.1	3.13
9	3.5	3.42
10	3.4	3.55
11	2.9	2.97
12	5.2	5.14
13	4.1	4.31
14	4.1	4.23
15	1.4	1.34
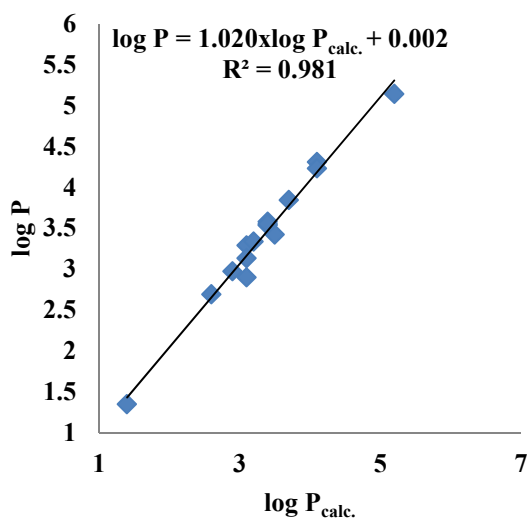
Figure 5. The plot log P vs. log P calc. for the test set (similarity clusters)

CONCLUSIONS

A set of 40 resveratrol derivatives, downloaded from the PubChem database, was submitted to a QSAR study. The best models have been validated in the external test set and in a new version of validation/prediction by using clusters of similarity, that favorise apparition of „quasi-congeneric" state, mandatory for a best correlation.

ACKNOWLEDGMENTS

REFERENCES

1. S.K. Goswami, D.K. Das*, Cancer Lett*, **2009**, *284*, 1.
2. L. Fremont, *Life Sci*., **2000**, *66*, 8, 663.
3. S. Larifa, C.B. Salem, H. Hmouda, K. Bouraoui, *Journal of Molecular Graphics and Modelling,* **2014**, *53*, 1.
4. P.M. Kris-Etherton, and C.L. Keen, *Curr. Opin. Lipidol*., **2002**, *13*, 1, 41-49.
5. A. Russo, M. Palumbo, C. Aliano, L. Lempereur, G. Scoto, and M. Renis, *Life Sci.,* **2003**, *72*, 21, 2369.
6. Y. Surh, *Mutat Res*., **1999**, *428*, 1-2, 305.
7. M.M. Wiliam, H.H. Philip, *Perspectives in Drug Discovery and Design*, **2000**, *19*, 67.
8. H. Zhu, Z. Shen, Q. Tang, W. Ji, L. Jia, *Chemical Engineering Journal*, **2014,** *255*, 431.
9. M Randić, *J. Chem. Inf. Comput. Sci.,* **1995**, *35*, 373.
10. M.V. Diudea, *MATCH Commun. Math. Comput. Chem.,* **1997**, *35*, 169.
11. M.V. Diudea, *J. Chem. Inf. Compu. Sci.,* **1997**, *37*, 300.
12. A. Zollanvari, U. Braga-Neto, E.R. Dougherty, *Pattern Recognition,* **2012**, *45*, 908.
13. PubChem database, accessed 20.08. 2014.
14. A.T. Balaban, A. Chiriac, I. Motoc, Z. Simon, Steric Fit in QSAR (*Lectures Notes in Chemistry*, Vol. 15), Springer Berlin, **1980**.
15. **Gaussian 09**, M.J. Frisch, G.W. Trucks et al., Gaussian Inc Wallingford CT, **2009**.
16. O. Ursu, M.V. Diudea, "TOPOCLUJ software program", Babes-Bolyai University, Cluj, **2005**.
17. J.G. Topliss and R. J. Costello, *J. Med*. *Chem*., **1972**, *15*, 1066.
18. D.M. Hawkins, S.C. Basak and D. Mills, Assessing model fit by cross-validation, *J. Chem. Inf. Comput. Sci.,* **2003**, *43*, 579.
19. L. Jäntschi, LOO Analysis (LOO: leave one out), Academic Direct Library of software, **2005**, Available at:
    http://l.academicdirect.org/Chemistry/SARs/SARs/loo/
20. A.M. Harsa, T.E. Harsa, S.D. Bolboacă, M.V. Diudea, Current Computer-Aided Drug Design, *BEntham Science*, **2014**, *2*, 10, 115.
21. S.D. Bolboacă, L. Jäntschi and M.V. Diudea, Molecular Design and QSARs with Molecular Descriptors Family, *Current Computer-Aided Drug Design*, **2013**, *9*(2), 195.
22. T.E. Harsa, A.M. Harsa, B. Szefler, *Cent. Eur. J. Chem*., **2014**, *12*, 365.

THE FAST FORMATION OF AN INTERMEDIATE IN THE CHROMIUM (VI) REDUCTION BY THIOLACTIC ACID – A KINETIC APPROACH BY MEANS OF THE STOPPED-FLOW TECHNIQUE

DANA-MARIA SABOU[a,*]

ABSTRACT. The reaction between thiolactic acid and Cr(VI) in aqueous acidic solution at 295 K is a quite fast multi-step process, beginning with the formation of a condensation species, in an equilibrium that involves both the main reactants and H$^+$ ions. The kinetics of this first step was studied by means of the stopped-flow and spectrophotometrical techniques. Reaction orders of one were found for both the thiolactic acid (RSH) and Cr(VI), showing a 1:1 combination ratio of the two in the intermediate. A fractional order was found in the case of the hydrogen ion, consistent with two parallel pathways: one assisted and one not assisted by H$^+$.

Keywords: kinetics, thiolactic acid, chromium(VI), redox, stopped-flow

INTRODUCTION

There has always been an interest in the mechanism of Cr(VI)-thiol reactions, recently mostly under physiological conditions (pH in and near the neutral region), since biological thiols (glutathione, cysteine etc.) play a role in the detoxification from heavy metal ions [1] and because chromium(VI) is a known occupational and environmental hazard, due to its allergenic, carcinogenic and mutagenic properties [2-4].

Contamination with Cr(VI) can happen by inhalation of dusts of chromate salts or by prolonged skin contact with either solid or solution, (mainly in some industry workers) making lung cancers and skin ulcerations the most common harmful effects. Accidental intake cannot be excluded, for instance by repeated consumption of dietary chromium(III) food supplements - widely used for their effects in helping weight loss - that may be contaminated with low levels of Cr(VI).

[a] *Babeş-Bolyai University, Faculty of Chemistry and Chemical Engineering, 11 Arany Janos str., RO-400028, Cluj-Napoca, Romania*
* *Corresponding author: dsabou@chem.ubbcluj.ro*

The toxicity of Cr(VI) is attributed mainly to the Cr(V) and Cr(IV) species formed during its reduction to Cr(III) inside the cell [5-7]. Besides the aggressive oxidizing properties of these intermediate valence states, their lability to ligand substitution allows them to bind to DNA protein sites, where the further reduction to stable Cr(III) complexes ultimately results in DNA cleavage and alteration of the genetic information [5-10]. The biological thiols, along with ascorbic acid, are known to readily reduce Cr(VI) [7-12], *in vivo*, thus likely getting involved in the mechanism of cellular damaging.

Thiolactic acid comes to the proximity of the human body by being used in cleaning and cosmetic products (such as permanent cold hair waving creams). Also, in small amounts (up to 50 ppm in the finished product), it has been approved as a food flavouring agent [13], but there is still a call for more genotoxicity data. Since acidic medium has usually been found to enhance the rate of the Cr(VI) reduction, besides the flavouring properties, thiolactic acid could potentially help reduce the trace amounts of freshly ingested Cr(VI) already in the acidic environment of the stomach, diminishing its transfer to the cells.

The oxidations of thiols by Cr(VI) are known to take place *via* complex multi-step mechanisms which allow for a quite large variety of path choices for a particular pair of reactants to follow, often ending up in disulfides as the oxidation product [14-17]. An established feature of these mechanisms is their debut by an equilibrium process in which a condensation intermediate is formed, with the replacement of an oxygen ligand by the thiolic sulphur [18,19]. Its formation may also benefit from a catalytic assistance of hydrogen ions. The composition of such a complex may vary, based on the chemical and steric properties of the reactants.

This study reports on the kinetic aspects of the fast build-up of such a condensation intermediate in the reaction between thiolactic acid and Cr(VI) in aqueous solutions of perchloric acid ($HClO_4$), under controlled temperature and ionic strength ($\mu = 0.5$ M ($NaClO_4$)).

RESULTS AND DISCUSSION

The oxidation of thiolactic acid (denoted RSH) by chromium(VI) in aqueous acidic ($HClO_4$) environment is overall a fairly fast process, that also consists of more than one stage, as tests at room temperature and the employment of solutions of the two reactants at concentrations in the range of $10^{-4} - 10^{-3}$ M have shown. This was observable by the changes in the colour of the reaction mixture, which very quickly turned from yellow to reddish-brown, and then somewhat slower, but still within seconds, to colourless. Given these features, flow methods and the spectrophotometrical detection technique were considered suitable for following the reaction progress, in particular the stage in which the formation of the intermediate takes place.

It is well known that Cr(VI) is subject to a number of equilibria in aqueous solutions, depending on both its own total concentration and the acidity of the solution [20,21]. In diluted solutions, mainly CrO_4^{2-}, $HCrO_4^-$ or $Cr_2O_7^{2-}$ species are encountered. In this work, the conditions were chosen so that the $HCrO_4^-$ form was dominant [20-22]. To limit the formation of the dimer, the total concentration of Cr(VI) could not be higher than $6 \cdot 10^{-4}$ M.

The UV-VIS region of the $HCrO_4^-$ electronic spectrum has its highest peak centred at 350 nm (molar absorptivity of 1560 M^{-1} cm^{-1} [23]), and a second, lower one, around 420 nm. The 350 nm wavelength was chosen to monitor the reaction progress, for two reasons.

First, the molar absorptivity, together with the path length of the mixing chamber of the stopped-flow apparatus ($\ell = 0.336$ cm), were the factors deciding the lowest Cr(VI) concentration still detectable with a good signal to noise ratio. In this case, it was 10^{-4} M.

Second, some spectral data have shown that the reddish-brown intermediate displays a significant interfering absorbance around 420 nm, consistent with the expected batochromic shift in the charge-transfer maximum when a sulphur replaces an oxygen. The same spectra were inconclusive for 350 nm, so it was hoped that at this wavelength the intermediate does not absorb. However, this was proved to not be the case.

A curve describing the entire reaction progress at 350 nm is shown in figure 1. The obvious biphasic behaviour undoubtedly establishes both the formation of the intermediate, and the fact that it also absorbs at 350 nm. Its composition can be assessed based on the reaction orders of the participants in the elementary step of its formation, since for an elementary process the reaction orders accurately describe its molecularity.
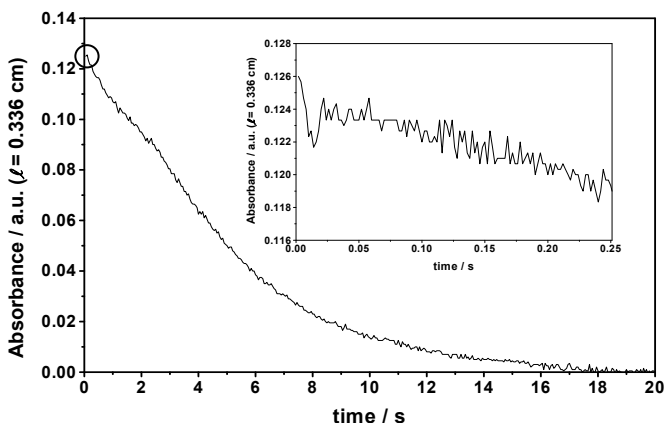
Figure 1. Experimental curve at 350 nm - long and short run (inset). Conditions: [Cr(VI)] = $4 \cdot 10^{-4}$ M, [RSH] = $8 \cdot 10^{-3}$ M, [H$^+$] = 0.1 M, T = 295 K, μ = 0.5 M (NaClO$_4$).

To determine these reaction orders, the initial rates method has been employed, in conjunction with the isolation method.

Under the range of conditions employed, the whole process takes 15 to 45 seconds. In order to obtain the initial rates, only the beginning (about the circled region in figure 1) is of interest, thus the measurements targeted this region (inset in figure 1). The points accounting for 1.5% or less of the total reaction served to determine the initial slopes of the time resolved absorbance curves by linear regression. In all cases, this corresponded to at least 150 data points.

Although the formation of the intermediate is considered to be an equilibrium process, in its initial stages it can reasonably be assumed that the amount of intermediate formed is so small that its decay by either the reverse step or the further decomposition to products is insignificant, and the build-up rate is dominant. Therefore, the rate law at zero reaction time can be expressed as in equation (1):

$$r_0 \approx r_1 = \left| \frac{d[HCrO_4^-]}{dt} \right|_{t \to 0} = k_1 \cdot [RSH]_0^a [H^+]_0^b [HCrO_4^-]_0^c \qquad (1)$$

where r_0 is the initial rate, r_1 and k_1 are the reaction rate and the rate coefficient for the forward step, and a, b and c are the reaction orders for the three possible reactants: RSH, H^+ and $HCrO_4^-$ respectively.

The initial rate can further be expressed in terms of absorbance. If the respective molar absorptivities of the reactant and the intermediate (denoted I) are $\varepsilon_{350,HCrO4^-}$ and $\varepsilon_{350,I}$, and ℓ is the path length of the mixing chamber (0.336 cm), the total absorbance at 350 nm (A_{350}) is:

$$A_{350} = [HCrO_4^-] \cdot \varepsilon_{350,HCrO_4^-} \cdot \ell + [I] \cdot \varepsilon_{350,I} \cdot \ell \qquad (2)$$

Under the assumptions made, the concentration of the intermediate can be expressed as:

$$[I] = [HCrO_4^-]_0 - [HCrO_4^-] \qquad (3)$$

Combining equations 2 and 3 to obtain the expression of the concentration of $HCrO_4^-$, and substituting into equation 1, the following form for the reaction rate results (equation 4):

$$\frac{1}{(\varepsilon_{350,HCrO_4^-} - \varepsilon_{350,I}) \cdot \ell} \left| \frac{dA_{350}}{dt} \right|_{t \to 0} = k_1 \cdot [RSH]_0^a [H^+]_0^b [HCrO_4^-]_0^c \qquad (4)$$

Equation 5 (in which $\alpha = (\varepsilon_{350,HCrO4-} - \varepsilon_{350,I}) \cdot \ell \cdot k_1$) is the logarithmic form of equation 4, and permits the determination of the reaction order (i.e. a, b or c) of a certain reactant, if all the terms of the sum are constant, except for the term involving that reactant (the isolation method).

$$\log \left| \frac{dA_{350}}{dt} \right| = \log(\alpha) + a \cdot \log([RSH]_0) + b \cdot \log([H^+]_0) + c \cdot \log([HCrO_4^-]_0) \quad (5)$$

As needed, three series of measurements were made. In each of them the concentration of one species (Cr(VI), RSH or H$^+$) was varied, with the other two kept constant. Always, Cr(VI) was the limiting reactant. Also, the excess of thiolactic acid and hydrogen ion were ensured to be large enough in each case, so that they could be considered invariable. The reaction order with respect to the species of which the concentration varied in each series of measurements can be determined as the slope of the appropriate double-logarithmic plot. Since the initial slopes (dA_{350}/dt) of the absorbance-time curves are directly proportional to the rates, they were used in their stead.

Details about the actual concentrations of the reactants in the three series of measurements, as well as the dA_{350}/dt values, are listed in table 1.

In a parallel approach, similar data were collected at 435 nm. The dA_{435}/dt values obtained are also presented in table 1, and will be discussed later in the paper.

Table 1. Initial slopes $\left| dA_{350}/dt \right|$ (directly proportional to the initial rates) computed from the experimental curves of absorbance *vs.* time, for the three series of measurements used to determine de reaction orders (T = 295 K, μ = 0.5 M).

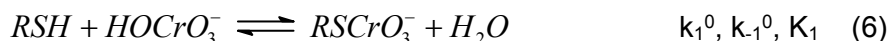| $[H^+]_0$ $(10^{-2}$ M)	$[RSH]_0$ $(10^{-3}$ M)	$[HCrO_4^-]_0$ $(10^{-3}$ M)	$\left| dA_{350}/dt \right|$ $(10^{-3}$ s$^{-1})$	$\left| dA_{435}/dt \right|$ $(10^{-3}$ s$^{-1})$
2.6	8.0	0.40	10.3 ± 0.2	54.5 ± 0.9
	14		17.6 ± 0.4	71 ± 2
	20		27.7 ± 0.7	140 ± 6
	24		32.9 ± 0.9	171 ± 7
2.6	8.0	0.10	24.0 ± 0.5	11.1 ± 0.7
		0.30	8.6 ± 0.2	32.4 ± 0.7
		0.40	12.0 ± 0.7	50.3 ± 0.7
		0.50	16.2 ± 0.3	56.2 ± 0.7
		0.60	14.6 ± 0.8	63.5 ± 0.8
10	8.0	0.40	23.6 ± 0.3	144 ± 7
8.0			21.9 ± 0.5	106 ± 5
6.3			15.8 ± 0.4	93 ± 2
5.0			20.0 ± 0.5	95 ± 2
4.0			13.9 ± 0.6	56 ± 1
2.6			9.9 ± 0.6	43 ± 1
1.6			6.3 ± 0.2	27.8 ± 0.7
1.0			5.5 ± 0.4	21.3 ± 0.6

The errors mentioned in the table and in the rest of the paper, are the standard errors of the parameter, as determined from the linear regression.

The corresponding double-logarithmic plots for the data at 350 nm and their results are presented in figure 2, for all three participants in the reaction process. The slopes of the plots, with their respective errors, are given on the figure 2 and represent the values of the three reaction orders (a, b and c).
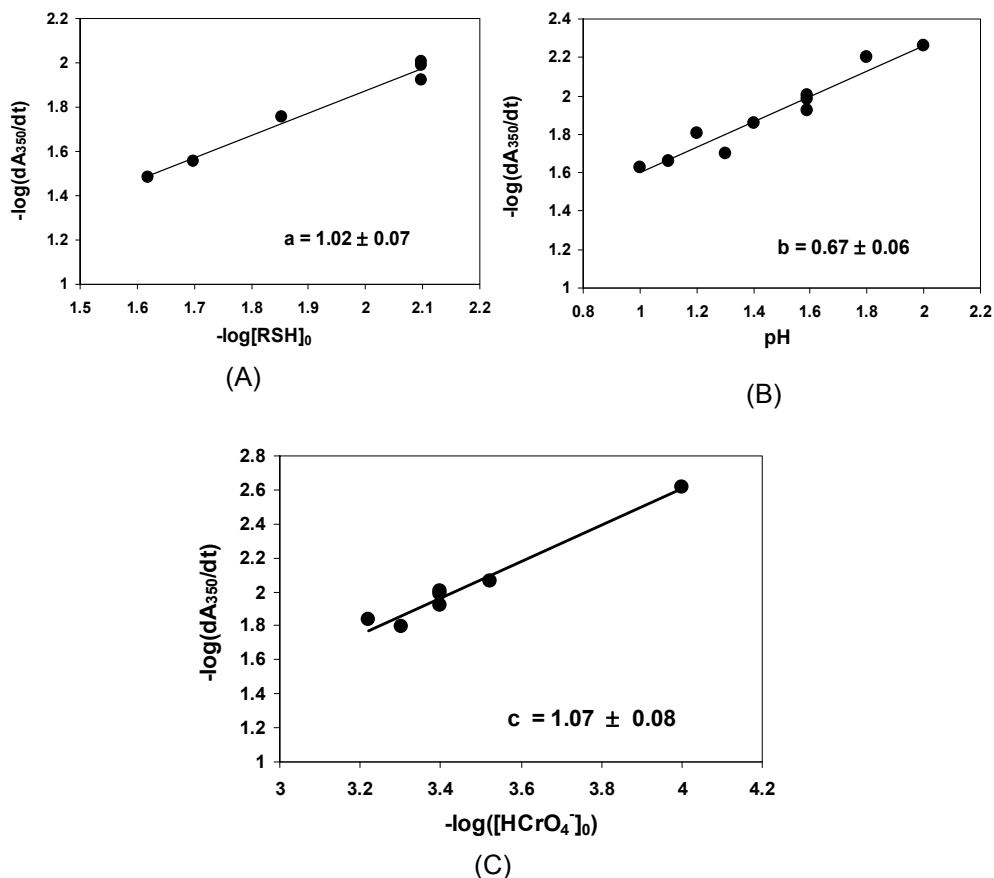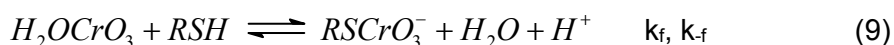

Figure 2. Double-logarithmic plots for determining the reaction orders with respect to the RSH (A), H$^+$ (B) and Cr(VI) (C), for the formation of the intermediate (at 350 nm). Conditions like in table 1.

First order with each RSH and Cr(VI) (figure 2A and 2C) and a fractional order between zero and one with H^+ (figure 2B) were found. In mechanistic terms, this means that the intermediate has a 1:1 ratio RSH:Cr(VI) - namely that one oxygen ligand in $HOCrO_3^-$ is substituted by one thiolactic acid molecule - and its formation can happen either catalyzed by one proton or not. Therefore, the reaction can be described by one of the equations 6 or 7, respectively:

$$RSH + HOCrO_3^- \rightleftharpoons RSCrO_3^- + H_2O \qquad\qquad k_1^0,\ k_{-1}^0,\ K_1 \quad (6)$$

$$RSH + HOCrO_3^- + H^+ \rightleftharpoons RSCrO_3^- + H_2O + H^+ \quad k_1^H,\ k_{-1}^H,\ K_1 \quad (7)$$

where k_1^0 and k_{-1}^0 stand for the reaction coefficients of the forward and reverse reactions of the non-catalysed path respectively, k_1^H and k_{-1}^H are their analogues for the H^+ assisted path and K_1 denotes the equilibrium constant (which is the same, regardless the path).

Beforehand and kinetically indistinguishable from each other, in the presence of H^+, either RSH or $HOCrO_3^-$ is involved in a protolytic equilibrium. If $HOCrO_3^-$ is the one that protonates, the species so formed is not the chromic acid (H_2CrO_4), but rather H_2OCrO_3. Indeed, by protonating the –OH ligand in the tetrahedral complex $HCrO_4^-$, the leaving group would become H_2O, much easier to be substituted by the thiolic sulphur. Therefore, this seems the likelier choice. The H^+ assisted path (equation 7) would in this case consist of two consecutive equilibria (equations 8 and 9):

$$HOCrO_3^- + H^+ \rightleftharpoons H_2OCrO_3 \qquad\qquad K_p \qquad (8)$$

$$H_2OCrO_3 + RSH \rightleftharpoons RSCrO_3^- + H_2O + H^+ \qquad k_f,\ k_{-f} \qquad (9)$$

where K_p is the equilibrium constant for the protonation of $HCrO_4^-$ and k_f, k_{-f} are the reaction constants for the forward and reverse elementary steps of the intermediate formation, with $K_p \cdot k_f = k_1^H$.

If the parallel reactions 6 and 7 are considered, the overall rate law that can be written for the build-up of the intermediate consists of two terms, as described in equation 10:

$$r_1 = k_1^H [RSH][H^+][HCrO_4^-] + k_1^0 [RSH][HCrO_4^-] \qquad\qquad (10)$$

The values of the two rate constants (k_1^H and k_1^0) are not accessible, since they can only be computed if $\varepsilon_{350,HCrO4^-}$ and $\varepsilon_{350,I}$ are both known, and the value for $\varepsilon_{350,I}$ could not be determined. Instead, it was possible to estimate

the importance of the two terms in the sum, in relation to the H$^+$ concentration. For this purpose, the quantities (dA$_{350}$/dt)/(ℓ·[RSH]·[HCrO$_4^-$]) were computed and plotted against the concentration of the hydrogen ion (figure 3).

The slope and the intercept of the plot presented in figure 3 correspond to the quantities ($\varepsilon_{350,HCrO4-}$ - $\varepsilon_{350,I}$)·k_1^H and ($\varepsilon_{350,HCrO4-}$ - $\varepsilon_{350,I}$)·k_1^0. Their values, obtained by linear regression, are given on the figure. The errors of the two parameters (as computed from the plot only) were of 15% and 9.7% respectively. From the ratio between the intercept and the slope, (2.8 $\pm$ 0.7)·10^{-2} M, it can be estimated that for a concentration of H$^+$ corresponding to a pH of approximately 1.56, the H$^+$ catalysed and non-catalysed paths (the two terms in equation 10) contribute equally to the total rate. For higher H$^+$ concentration, the catalysed path becomes dominant, while for concentrations 10 times lower or less (pH 2.6 or higher), it will already become negligible.
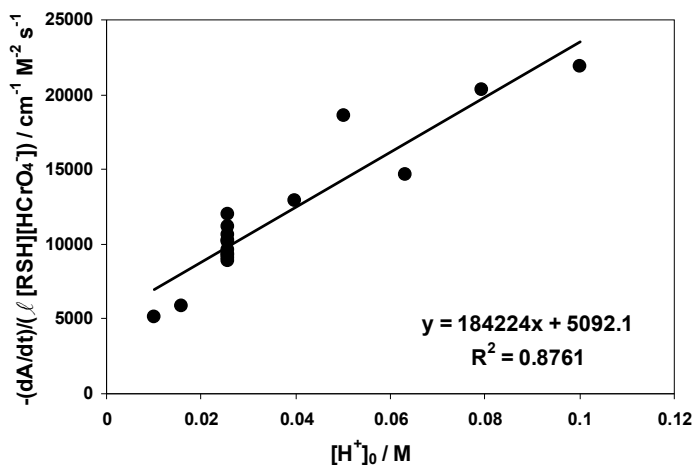
Figure 3. Global plot for determining the ratio of the rate constants
(T = 293 K, μ = 0.5 M).

Some final considerations are worth mentioning.

First, it was established that both HCrO$_4^-$ and the Cr(VI)-RSH intermediate absorb at all wavelengths, meaning that there is no simpler spectrophotometrical approach for this reaction. It should be added that all the measurements were repeated at the wavelength of 435 nm (the exact wavelength of 420 nm could not be applied due to the lamp configuration of the experimental setup). At this wavelength, the experimental curves showed in the beginning a steep increase (consistent with the intermediate having here a higher absorbance than the reactant), reached a maximum and later decreased. The obtained

values of $\left|dA_{435}/dt\right|_{t\to0}$ have been included in table 1. The big differences in the numbers, as compared to those for 350 nm, are likely due to a much higher difference between the absorption coefficients $\varepsilon_{435,HCrO4^-}$ and $\varepsilon_{435,I}$ at 435 nm. However the outcome was very similar, as far as the kinetic parameters are concerned. The obtained orders were 1.1 ± 0.1; 1.01 ± 0.05 and 0.81 ± 0.05 for the thiolactic acid, $HCrO_4^-$ and H^+ respectively, with a notable difference found only in the intercept to slope ratio $((1.5 \pm 0.5)\cdot10^{-2}$ at 435 nm). The results obtained at 350 nm are considered more reliable. Any decay of the intermediate that may happen within the time frame used to determine the slopes would affect more the slopes at 435 nm, where the absorption of the intermediate dominates.

Second, the whole reaction process is quite fast. The stopped-flow approach is aimed at gathering as accurate data as possible for the beginning of the reaction, but in this case it drastically limited the range of concentrations that could be spanned, partly due to the small dimensions of the mixing chamber. On one hand, concentrations of Cr(VI) lower than 10^{-4} M gave too noisy experimental curves. On the other hand, they needed to be lower than $6\cdot10^{-4}$ M, in order to: 1) have the Cr(VI) solely in the form of $HCrO_4^-$, and 2) allow the use of the thiolactic acid and the mineral acid in high enough excess to ensure their constancy without the reaction becoming too fast to follow, even by the stopped-flow technique. In turn, this also limited the concentration range of these two other reactants.

CONCLUSIONS

In the reaction between thiolactic acid and Cr(VI) in aqueous acidic solution, a reaction intermediate is first built, in a fast step. First orders were found for each of the two reactants, meaning a 1:1 composition of the intermediate. The fractional reaction order (0.67 or 0.81) found with respect to H^+ shows that the formation of the intermediate happens both in the presence or the absence of protons. The $(k_1^H\cdot[H^+])$ term becomes more and more dominant for pH's lower than 1.56.

For a better kinetic description of the overall process and in particular of the second stage, dealing with the decay of the intermediate, the reaction conditions need to be changed, so that larger ranges of concentrations of the reactants can be spanned. This requires lower concentrations of Cr(VI), which would make the reaction slower, but also would require a longer path length for the spectrophotometrical cell. Hence, batch measurements could be considered for studying this system in greater detail.

EXPERIMENTAL SECTION

A custom-built multi-channel stopped-flow apparatus with spectrophoto-metrical detection and oscillographic recording has been utilized to collect the data. The mixing chamber of the apparatus has a path length of 0.336 cm. The working wavelength was 350 nm or 435 nm and the temperature 295 K. For each set of conditions, the experiments were repeated four times, using the same batches of solutions. To minimize the noise, the obtained curves were first mediated and the averaged curve was further processed to obtain the kinetic data.

The solutions of the two main reactants were prepared in identical environments (the same concentrations of $HClO_4$ and $NaClO_4$). The total ionic strength was 0.5 M.

Initial Cr(VI) concentrations between 10^{-4} and $6 \cdot 10^{-4}$ M were used. Due to the small path of the mixing chamber, an appropriate signal could not be obtained for lower concentrations. The concentrations for the thiolactic acid ($8 \cdot 10^{-3}$ to $2.4 \cdot 10^{-2}$ M) and hydrogen ion (0.01 to 0.1 M) were chosen accordingly, to ensure a significant excess over the Cr(VI).

ACKNOWLEDGMENTS

REFERENCES

1. G.N. Babu, R. Ranjani, G. Fareeda, S.D.S. Murthy, *Journal of Phytological Research*, **2007**, *20*, 1.
2. V. Bianchi, A.G. Lewis, *Toxicological and Environmental Chemistry*, **1987**, *15*, 1.
3. M. Cieślac-Golonka, *Polyhedron*, **1996**, *15,* 3667.
4. N. McCarroll, N. Keshava, J. Chen, G. Akerman, A. Kligerman, E. Rinde, *Environmental and Molecular Mutagenesis,* **2010**, *51*, 89.
5. S. Veritt, L.S. Levy, *Nature*, **1974**, *250*, 493.
6. R. Codd, C.T. Dillon, A. Levina, P.A. Lay, *Coordination Chemistry Reviews* **2001**, *216-217*, 537 and references therein.
7. P.H. Connett, K.E. Wetterhahn, *Structure and Bonding (Berlin)*, **1983**, *54*, 93.
8. A.S. Standeven, K.E. Wetterhahn, *Journal of the American College of Toxicology*, **1989**, *8*, 1275.
9. A.L. Holmes, S.S. Wise, J.P. Wise Sr., *Indian Journal of Medical Research*, **2008**, *128*, 353.

10. A. Levina, G. Barr-David, R. Codd, P.A. Lay, N.E. Dixon, A. Hammershoi, P. Hendry, *Chemical Research in Toxicology*, **1999**, *12*, 371.
11. A. Levina, H.H. Harris, P.A. Lay, *Journal of the American Chemical Society*, **2007**, *129*, 1065.
12. G.B. Borthiry, W.E. Antoline, J.M. Meyers, C.R. Meyers, *Journal of Inorganic Biochemistry*, **2008**, *102*, 1449.
13. EFSA Panel on Food Contact Materials, Enzymes, Flavourings and Processing Aids, *European Food Safety Agency Journal*, **2012**, *10(2)*, 2455.
14. A. Levina, P.A. Lay, *Inorganic Chemistry*, **2004**, *43*, 324.
15. V.P. Roldán, V.A. Daier, B. Goodman, M.I. Santoro, J.C. González, N. Calisto, S.R. Signorella, L.F. Sala, *Helvetica Chimica Acta,* **2000**, *83*, 3211.
16. P.H. Connett, K.E. Wetterhahn, *Journal of the American Chemical Society,* **1985**, *107*, 4282.
17. J.P. McCann, A. McAuley, *Journal of the Chemical Society, Dalton Transactions*, **1975**, 783.
18. M. Mitewa, P. Bontchev, *Coordination Chemistry Reviews,* **1985,** *61*, 241.
19. I. Bâldea, D.-M. Sabou, *Studia UBB Chemia,* **2001**, *46(1-2)*, 17.
20. N.N. Greenwood, A. Earnshaw, "Chemistry of the Elements", 2. Edition Butterworth-Heinemann, Oxford, **1997**, chapter 23.
21. J.Y. Tong, E.L. King, *Journal of the American Chemical Society*, **1953**, *75*, 6180.
22. J.D. Ramsey, L. Xia, M.W. Kendig, R.L. McCreery, *Corrosion Science*, **2001**, *43*, 1557.
23. R.W. Burke, R. Mavrodineanu, *Journal of Research of the National Bureau of Standards – A. Physics and Chemistry*, **1976**, *80(A)*, 631.

VALIDATED HPLC METHOD FOR DETERMINATION OF NEBIVOLOL IN PHARMACEUTICAL DOSAGE FORM AND IN VITRO DISSOLUTION STUDIES

ZOLTÁN-ISTVÁN SZABÓ[a,*], TÍMEA SZABÓ[a], RÉDAI EMŐKE[b], EMESE SIPOS[a]

ABSTRACT. A rapid and simple liquid chromatographic method was developed and validated according to current ICH guidelines for the quantitative assessment of nebivolol from tablet dosage forms and dissolution medium. Chromatography was carried out on a BDS Hypersil C18 column (150 x 4.0 mm, particle size 5 µm), employing a Merck 7000 series HPLC system with UV detection at 281 nm. The mobile phase consisted of 0.1 % (v/v) trifluoroacetic acid in water: acetonitrile (60:40, v/v) and was delivered at a flow rate of 1.25 mL min^{-1}. Injection volume was 100 µL and the analysis was performed at ambient temperature. The developed method was validated taking into consideration current international guidelines for specificity, linearity, accuracy, precision (system precision and both intra- and interday precision). The validated analytical method proved to be suitable for quantitative analysis of nebivolol from commercially available tablets and also performed well in determination of active substance during dissolution studies.

Keywords: nebivolol, dissolution, HPLC

INTRODUCTION

Nebivolol (NEB), 2,2'-Azanediylbis(1-(6-fluorochroman-2-yl)ethanol) (Fig. 1) is third-generation, highly cardioselective beta$_1$-receptor blocker with a unique haemodynamic profile. It combines beta-adrenoreceptor blocking activity with endothelial L-arginine nitric oxide (NO) pathway mediated vasodilation [1,2]. Apart from its antihypertensive properties, NEB also improves arterial compliance and left ventricular function in heart failure. Owning to its unique

[a] *University of Medicine and Pharmacy Tîrgu Mureș, Faculty of Pharmacy, Department of Drugs Industry and Pharmaceutical Management, Gh. Marinescu 38, RO-540139, Tîrgu Mureș, Romania*

[b] *University of Medicine and Pharmacy Tîrgu Mureș, Faculty of Pharmacy, Department of Pharmaceutical Technology, Gh. Marinescu 38, RO-540139, Tîrgu Mureș, Romania*

* *Corresponding author: szabo.zoltan@umftgm.ro*

pharmacodynamic properties, it provides higher response rates and presents lower frequency and severity of adverse event compared with other agents from its class [3,4].
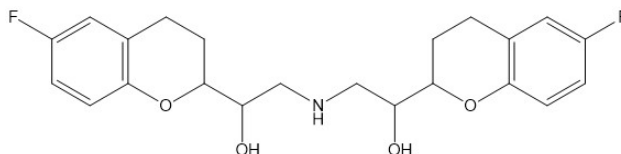
Figure 1. Chemical structure of NEB

Chemically, it differs from other beta-receptor blocker agents, displaying a symmetrical configuration [5]. According to the Biopharmaceutical Drug Classification System, NEB is a class II compound, characterized by low, pH dependent aqueous solubility and high membrane permeability. It is a weakly basic compound, with a pKa of 8.22 [6,7].

Given the therapeutic importance of this beta-blocker and also its intensive use in combination antihypertensive therapy, there are several methods describing the quantitative assessment of NEB from dosage forms, including spectrophotometric[8-10], thin-layer chromatographic [10-12] and liquid chromatographic [9,10,13-16] methods. However, there are no analytical methods described for the chromatographic analysis of NEB from dissolution samples. Moreover, according to the authors' knowledge, full dissolution profiles of NEB and subsequent dissolution behaviour analysis has not been published yet.

Our aim was to develop a simple, rapid and efficient high-performance liquid chromatographic (HPLC) method suitable for the quantitative assessment of NEB from both pharmaceutical dosage forms and dissolution media, which could be applied in routine quality control. In order to meet regulatory requirements, validation of the method, according to current ICH Guidelines was prime ordinary. Investigation of dissolution behaviour for NEB was also targeted, employing three different dissolution media and applying different experimental conditions.

RESULTS AND DISCUSSION

Method development and validation

Among the methods used for quality control of pharmaceuticals, liquid chromatographic methods excel with higher specificity and selectivity. In order to accurately quantify NEB, reverse-phase high-performance liquid chromatography was chosen as the method of choice. Our aim was to

196

establish a high-throughput method, suitable for rapid quantification of the active substance from a large number of dissolution samples occurring during dissolution profile assessment. The method should also be selective, in order to unequivocally determine the analyte in the presence of possible interfering species (*i.e.* excipients in the case of dosage form).

Several mobile phase compositions were employed, using methanol or acetonitrile as organic modifiers and aqueous solutions of acetic acid and trifluoroacetic acid. In order to achieve adequate retention of NEB, but also maintain a short analysis time, a mobile phase consisting of 0.1 % (v/v) trifluoroacetic acid in water and acetonitrile in a proportion of 60:40 (v/v) was chosen. Using base-deactivated silica stationary phase (BDS Hypersil C18) over "classical" C18 column, an improvement of peak shape was observed for the basic analyte. Using the abovementioned conditions and employing a flowrate of 1.25 mL min^{-1}, we succeeded in eluting NEB in under 4 minutes at ambient temperature.

Validation was carried out in accordance to current ICH Validation Guideline [17], in terms of specificity, linearity, accuracy and precision (system precision, repeatability and intermediate precision).

In order to test the specificity of the method, chromatograms of standard and sample solutions were recorded and dissolution media were also injected (Fig. 2). No interference was observed at the retention time of NEB, moreover both standard and sample solutions showed comparably high peak purity results (>0.98); results indicating that the method could determine the analyte in the presence of potentially interfering species.
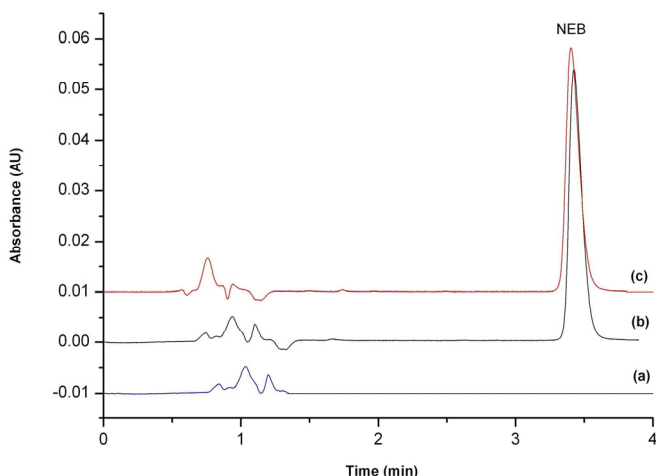
Figure 2. Representative chromatograms of: (a) dissolution medium/solvent (HCl 0.1 N), (b) tablet sample solution, (c) standard solution.

The method performed well during validation, with all results being within the acceptance limits (Table 1), thus demonstrating its suitability for its intended purpose.

Table 1. Summary of method validation results

Studied parameter	Results	
Linearity (N=15, n=5)	Range (µg mL^{-1})	1-12
	Slope (a)	28433
	Intercept (b)	10885
	r^2	0.997
Accuracy and repeatability (N=9, n=3)	Mean recovery (%)	99.57
	SD	1.575
	RSD (%)	1.582
	CI (95 %)	98.36-100.78
System precision (n=10)	Mean (ASC)	181173.8
	SD	791.3
	RSD (%)	0.437
	CI (95 %)	180606.9-181739.1
Inter-day precision (N=18, n=3)	Mean (%)	99.91
	SD	0.616
	RSD (%)	0.617
	CI (95 %)	99.52-100.30
Analyst variation (N=18, n=3)	Mean (%)	100.26
	SD	0.826
	RSD	0.824
	CI (95 %)	99.74-100.78

N – total number of experiments; n – number of concentration levels;
r^2 – coefficient of correlation; SD – standard deviation; RSD – relative standard deviation

Quantitative determination of NEB from tablets

The validated method was applied for determination of NEB from tablet dosage form. Two separate commercially available products were analyzed, one batch with a valid expiration date and another batch with expired shelf-life. Although, the formulation with expired validity date had a lower NEB content, results indicated that the active substance content of both formulations were between acceptable limits *i.e.* ±5% of the nominal concentration (Table 2).

Table 2. Quantitative determination of NEB from tablets

Sample number	NEB content (mg/tablet)	
	Valid Batch	Expired Batch
1	4.77	4.54
2	4.68	4.63
3	4.75	4.58
Mean	**4.73**	**4.58**
SD	0.047	0.045
RSD (%)	0.998	0.984

In vitro dissolution studies

Proper dissolution testing methodology is essential for evaluating quality of solid pharmaceutical dosage forms. In the case of BCS Class II compounds, such as NEB, presenting low, pH dependent aqueous solubility, the assessment of dissolution profiles at different pH values is not only a regulatory requirement, but also a necessity.

Determination of *in vitro* release profiles of NEB were performed employing three different dissolution media, varying the volume of the medium (500 and 900 mL) and stirring speed (50 and 75 rpm).

NEB, having a weakly basic character, presented high dissolution rates in HCl 0.1 N (Fig. 3a). Under the acidic conditions employed, the secondary amino group from the structure of NEB is fully protonated, thus possessing higher solubility. Using higher dissolution medium, the release profiles of NEB were almost identical, regardless of the rotation speed employed. Whereas, in the case of lower dissolution medium volume, there was a noticeable difference between the first timepoint (67.32 % dissolved at 50 rpm rotation speed versus 91.60 % dissolved at 75 rpm). At later timepoints, these differences started decreasing and at the end of the dissolution test, the full quantity of NEB was dissolved in all cases.

At pH 4.5, dissolution rate of NEB decreased (Fig. 3b). Still, employing high dissolution medium volume and high rotation speeds, almost 80 % of NEB was dissolved at 10 min. However, when the dissolution volume of 500 mL was utilized, along with mild agitation conditions (50 rpm) the slowest dissolution rate was recorded. Nonetheless, at the final sampling point, all dissolution efficacies were above 90 %, in all cases.

Dissolution kinetics of NEB was the slowest at pH 6.8: with an increase of pH, as ionization decreased, solubility also decreased, resulting in poor dissolution efficacy (Fig. 3c). In order to achieve a final cumulative dissolution of above 80 %, 900 mL of dissolution volume needed to be

used, along with a higher rotation speed (75 rpm). Whereas, employing the "harshest" conditions (500 mL, 50 rpm), at the end of the test only 52.12 % of NEB was dissolved.
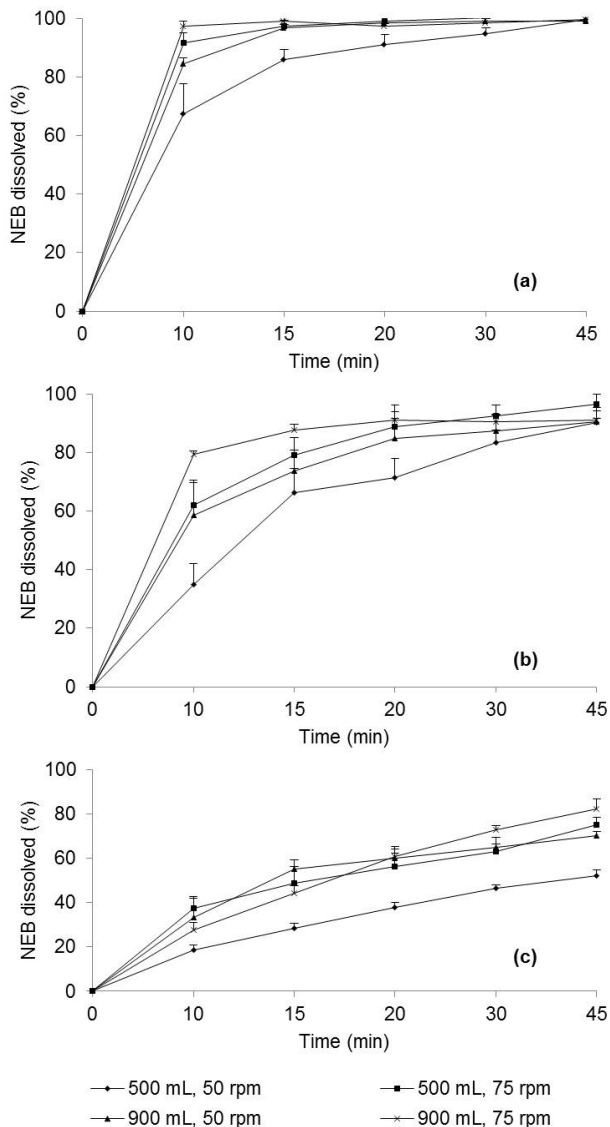
Figure 3. Dissolution profiles of NEB in (a) HCl 0.1 N, (b) acetate buffer pH 4.5, (c) phosphate buffer pH 6.8, employing different conditions. (error bars represent standard deviation values)

CONCLUSIONS

An efficient reverse-phase HPLC method was developed for the determination of NEB from tablet dosage form and dissolution samples. Use of a simple, easy to prepare mobile phase, combined with short analysis time, make the method a good contender for routine quality control testing. The method performed well during validation studies and was subsequently applied for comparative quantification of NEB from valid and expired tablets. Dissolution profiles of NEB were also constructed, employing three different dissolution media and various experimental conditions (different volume of dissolution medium and rotation speed). As expected, results revealed the pH dependent dissolution of NEB and a great influence of the instrumental variables upon dissolution efficacy.

EXPERIMENTAL SECTION

Reagents

Nebivolol clorhidrate working standard was obtained as a free sample from Nivika Chemo Pharma PvT, India. Supergradient grade acetonitrile, acetic acid (glacial), hydrochloric acid (solution, 35 %) were from Merck KGaA (Germany). Sodium acetate trihydrate, sodium hydroxide and methanol were from Lach Ner (Czech Republic), while trifluoroacetic acid and potassium dihydrogen phosphate were from Chemical (Romania). All reagents were of analytical grade, purchased through a local vendor and used without further purification.

Ultrapure, deionized water was prepared with a Millipore Direct Q5 water purification system (Merck Millipore, Germany) and was utilized for chromatographic purposes.

Apparatus

The HPLC system was a Merck Hitachi LaChrom Series 7000, equipped with a quaternary L-7100 pump, L-7200 autosampler, L-7360 column thermostate, L-7455 diode-array detector and L-7612 degasser. Data acquisition was performed using D-700 HSM Manager software. Chromatographic separation was carried out on a Hypersil™ BDS C18 column, with dimensions of 150 x 4.6 mm, particle size 5 µm (Thermo Scientific, USA) at ambient temperatures. Final mobile phase consisted of 0.1 % (v/v) trifluoroacetic acid in water: acetonitril 60:40 (v/v), delivered at a flowrate of 1.25 mL min^{-1}. Injection volume was 100 µL and detection was performed at 281 nm.

Dissolution studies were performed using Apparatus 2 (paddle) setting on an Erweka DT 80 dissolution tester, coupled with an ET 1500I heater/circulator, maintaining the temperature of the dissolution medium at

37.0 ± 0.5 °C. Three different dissolution media (HCl 0.1 N, acetate buffer pH 4.5 and phosphate buffer pH 6.8) were tested at two different volumes (500 mL and 900 mL) and two different rotation speeds (50 and 75 rpm). Samples of 3 mL were withdrawn at 10, 15, 20, 30 and 45 min and filtered through a 0.45 μm polyamide filter. The withdrawn volume of sample was replaced with an equal volume of preheated medium.

Preparation of solutions

NEB stock solution (concentration: 0.2 mg mL^{-1}) was prepared by dissolving 21.8 mg NEB hydrochloride (equivalent to 20 mg NEB) in methanol and diluting it to 100 mL. Appropriate dilutions were made from this solution with HCl 0.1 N for validation studies.

Standard solution for tablet assay: 1 mL NEB stock solution was diluted to 50 mL with HCl 0.1 N (concentration: 4 μg mL^{-1}).

Standard solution for dissolution studies were prepared the same way as for tablet assay, weighting appropiate ammount of NEB hydrochloride to match 100 % of dissolution concentrations (aprox. 5.56 μg mL^{-1} for 900 mL dissolution medium and 10 μg mL^{-1} for 500 mL, respectively).

Tablet sample solution: appropiate quantity of tablet powder was weighted, ultrasonicated in 50 mL methanol for 20 minutes and diluted to 100 mL with the same solvent. 1 mL of the obtained solution was diluted to 50 mL with HCl 0.1 N.

Validation of the method

In order to test specificity, the chromatograms of standard, sample solutions and dissolution samples were recorded and compared.

Linearity was assessed over a concentration range of 1-12 μg mL^{-1}, at five concentration levels with three replicates each.

Accuracy and repeatability was assessed at three different concentrations (1, 5.56 and 12 μg mL^{-1}), each concentration being prepared in triplicate. The same concentration levels were also used in order to assess intermediate precision: solutions were prepared on different days by the same analyst (inter-day precision) or were prepared by a different analyst, on the same day (analyst variation). System precision was evaluated by injecting the same solution (5.56 μg mL^{-1}) 10 times.

ACKNOWLEDGMENTS

REFERENCES

1. J. Cockcroft, *Expert Opin. Pharmacother.*, **2004**, *5*, 893.
2. W. Gielen, T.J. Cleophas, R. Agrawal, *Int. J. Clin. Pharmacol. Ther.*, **2006**, *44*, 344.
3. J. Cockcroft, *Vasc. Health Risk Manag.*, **2007**, *3*, 909.
4. O. Hilas and D. Ezzo, *P T*, **2009**, *34*, 188.
5. L.J. Ignarro, *Cardiovasc. Ther.*, **2008**, *26*, 115.
6. E.G.C. Clarke, *Clarke's Analysis of Drugs and Poisons: In Pharmaceuticals, Body Fluids and Postmortem Material*, Pharmaceutical Press, **2004**.
7. S. Limbachiya, H. Nagar, H. Dodiya, D. Mehta, *Int. J. Pharma Sci.*, **2013**, *3*, 136.
8. M.M. Kamila, N. Mondal, L.K. Ghosh, B.K. Gupta, *Pharmazie*, **2007**, *62*, 486.
9. D.A. Shah, K.K. Bhatt, R.S. Mehta, S.L. Baldania, *J. AOAC Int.*, **2008**, *91*, 1075.
10. B. Dhandapani, N. Thirumoorthy and D.J. Prakash, *J. Chem.*, **2010**, *7*, 341.
11. T.S. Reddy, P.S. Devi, *JPC-Journal Planar Chromatogr. TLC*, **2007**, *20*, 149.
12. A.A. Shirkhedkar, P.M. Bugdane, S.J. Surana, *J. Chromatogr. Sci.*, **2010**, *48*, 109.
13. S.J. Joshi, P.A. Karbhari, S.I. Bhoir, *Chromatographia*, **2009**, *70*, 557.
14. N. Gowda, S. Panghal, K. Vipul, M. Rajshree, *J. AOAC Int.*, **2009**, *92*, 1356.
15. M.K. Sahoo, R.K. Giri, C.S. Barik, S.K. Kanungo, B.V.V. Kumar, *J. Chem.*, **2009**, *6*, 915.
16. P.K. Kachhadia, A.S. Doshi, H.S. Joshi, *J. AOAC Int.*, 2008, **91**, 557.
17. ICH Tripartite Guideline*, Q2 (R1): Validation of Analytical Procedures: Text and Methodology*, Step 4 version, **2005**.

TECHNO-ECONOMIC EVALUATION OF CALCIUM LOOPING CYCLE FOR CO$_2$ CAPTURE FROM SUPER-CRITICAL POWER PLANTS

DORNEANU BIANCA[a], CALIN-CRISTIAN CORMOS[a,*]

ABSTRACT. Calcium looping is an innovative CO$_2$ capture process using solid CaO as sorbent to remove CO$_2$ from flue gases. In the work presented in this paper, the calcium looping cycle was applied to a super-critical power plant to capture CO$_2$ (purity >95%). This capture technology is based on calcium looping process which uses CaO for CO$_2$ capture. Calcium looping process has very good techno-economic results compared to other CO$_2$ capture options (e.g. gas-liquid absorption) and has many advantages, one of those being: the raw material used for CO$_2$ capture (limestone) is abundant and cheap, the high carbon capture rate (>90%) and the relatively small efficiency penalty that it imposes on the power/ industrial process. The energy penalty for carbon capture is about 9 net electricity percentage points. Compared to the design without carbon capture, the specific capital investment is increasing with about 48%, the operational & maintenance (O&M) costs are increasing with 60% and the levelised cost of electricity is increasing with 54%.

Keywords: Carbon Capture and Storage (CCS), Calcium looping process, Super-critical power plant, Techno-economic assessments.

INTRODUCTION

In the last years, scientific studies on climate change have progressed considerably offering a new vision over the current problem of warming of the Earth. According to basic physics of heat trapping gases, exponential rise in population and energy consumption, humans have become, trough all the industries developed, the main problem leading to Earth's degradation [1]. Clearly, this is a complex topic with enormous political, socio-economic and emotional dimensions, but the scientific results show quite clear that human activities [2], in particular the wide usage of fossil fuels – e.g. coal is the

---

[a] *Babes-Bolyai University, Faculty of Chemistry and Chemical Engineering, 11 Arany Janos, RO-400028, Cluj-Napoca, Romania*
* *Corresponding author: cormos@chem.ubbcluj.ro*

most abundant fossil fuel used for the electric power generation as well as the largest world-wide source of CO_2 emissions [3], then human - driven changes in land use and land cover such as deforestation, urbanization and shifts in vegetation patterns [4], bring serious damages to the climate [5].

Because the primary cause of global climate change is human, the solutions are also within the human domain [6]; the scientists tried in the last years to find the best solution for reducing CO_2 emissions (e.g. improving energy efficiency), but also by developing and deployment of CO_2 capture and storage technologies [7]. One of the solutions found is the Calcium looping, (CaL), process which stands for absorption of CO_2 by means of CaO; in this case the objective is to obtain a pure stream of CO_2 suitable for storage. In this process the solids circulate between two interconnected fluidized bed reactors, the carbonator and the calciner, as shown in Figure 1. Flue gas coming from an existing power plant enters into a carbonator working at 600-650°C and atmospheric pressure where CO_2 reacts with CaO and converts into $CaCO_3$ [8]. Solids from carbonator are composed mainly of CaO and $CaCO_3$ and are separated at the end of the reaction from the clean flue gas which is released to the atmosphere. The solids are sent to the second reactor (calciner in Fig. 1) where the temperature is kept at around 900°C so that CO_2 is released from $CaCO_3$ and the CaO is recirculated into the carbonator.
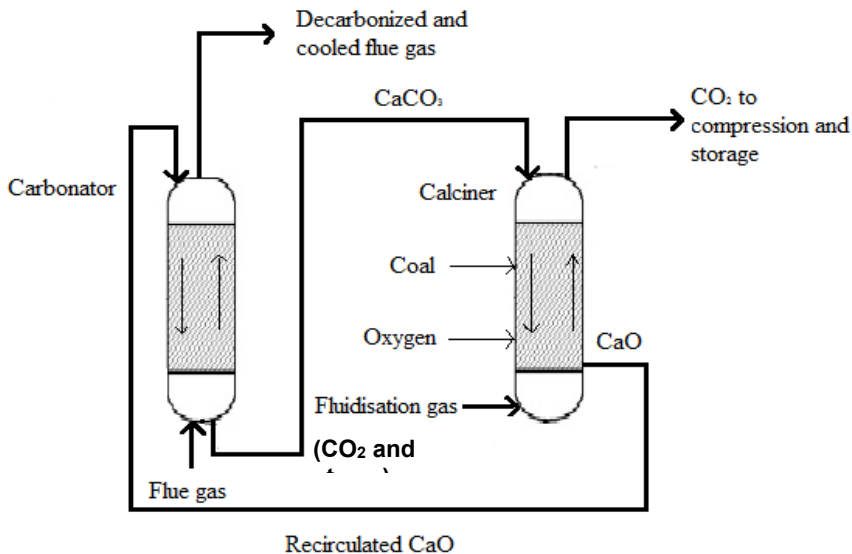
Fig. 1. Calcium looping (CaL) process

Calcium looping process has many advantages, one of those being the fact that CO$_2$ sorption and sorbent regeneration are carried out at high temperatures, (600 – 650°C and 900 – 1000°C for carbonation and calcination, respectively) therefore, the heat from reactions can be recovered very easily by steam generation. Among other advantages it can be said that with this process it can be obtained a concentrated steam of CO$_2$, more than 90%, suitable for storage and the materials used are widely available and cheap, (derived mostly from limestone).

Process reactions:

$$CaO + CO_2 \longrightarrow CaCO_3 \qquad \text{- carbonator reaction} \qquad (1)$$
$$CaCO_3 \longrightarrow CaO + CO_2 \qquad \text{- calciner reaction} \qquad (2)$$

RESULTS AND DISCUSSION

Process Model

Calcium looping model has been developed using commercial process flow modeling software, CHEMCAD 6.1.3. The process diagram of super-critical power plant with CaL unit including all the important components is shown in Fig. 2.
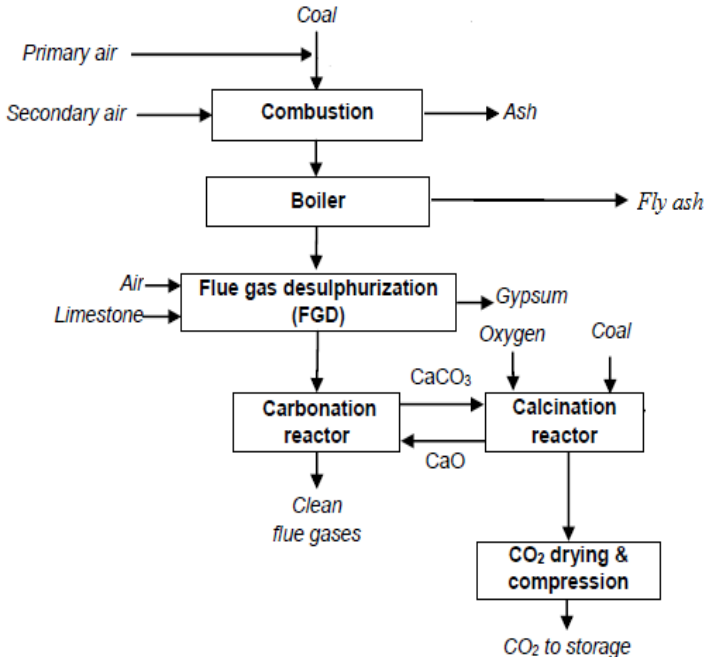

Fig. 2. Process diagram of power plant with CaL

The whole plant is structured in two important parts – the first part of the installation it is represented by coal-based combustion power plant with super-critical steam conditions, and the second part, the calcium looping process, where CO_2 is captured from the flue gases [9]. The main interest of the article is concentrated on the second part of the process – calcium looping unit but also on the techno-economic evaluation of the whole plant. Common aspects such as CO_2 capture rate, energy efficiency, economic aspects were observed in order to establish which is the most convenient approach to have a profitable process [10].

In the first part of the installation, the coal is burned with combustion air in boiler, (modeled as a Gibbs reactor), at atmospheric pressure, then the flue gases are desulphurised by reacting with limestone slurry and oxidation air resulting flue gases and gypsum. The desulphurised flue gas is used in the second part of the process, meaning the capture of CO_2 - the flue gas, (composition from Table 1), and CaO enters into the carbonator where a temperature of 620°C favors the formation of $CaCO_3$.

Table 1. Composition of the desulphurised flue gas from the power plant

Component	Composition (% vol.)
Carbon dioxide	18.12
Carbon monoxide	0.10
Water	4.37
Nitrogen	69.85
Oxygen	6.55
Argon	1.01
Total	100.00

After heat recovery units, who generate steam from available hot streams, the super-critical steam is then expanded in a steam turbine to produce energy. Decarbonized and cooled flue gas is released into the atmosphere, while formed calcium carbonate is converted back into CaO and gaseous CO_2 in a calciner, at 950°C, where thermal power for the endothermic reverse reaction, (calcination), is given by oxy-combustion of coal, oxy-combustion is necessary in order to maintain a high concentration of CO_2 [11]. The regenerated sorbent produced in the calciner is then sent to the carbonator for a new sorption cycle, while the CO_2 is cooled and compressed for permanent storage after final purification [12].

The majority of the heat used to regenerate the CaO-based adsorbent from $CaCO_3$ and the heat from carbonation reaction is used to generate super-critical steam, which provides additional energy and contribute to the overall energy efficiency of the plant.

The main equipment used for the simulation of Ca – looping process and the main equipment used by super-critical power plant without CO$_2$ capture is described in Table 2. The calcium looping cycle was designed to have a CO$_2$ capture rate of at least 90%.

Table 2. Design characteristics for the main plant units

Plant units	Design characteristics
Boiler	Temperature: 1200 – 1400°C Super-critical steam conditions
Steam (Rankine) cycle	290 bar/582°C with two steam reheats at 75 bar/580°C and 20 bar/580°C
Carbon capture (calcium looping) unit	Carbonation reactor: 550 – 650°C Calcination reactor: 850 – 950°C Gibbs free energy model for both reactors Pressure drop: 0.1 bar
Air Separation Unit (ASU)	Power consumption: 225 kWh/t O$_2$
CO$_2$ conditioning unit - for compression and drying	CO$_2$ final pressure: 120 bar CO$_2$ final temperature: 50°C 4 compression stages
Steam expander	Final expansion pressure: 46 mbar Compressor efficiency: 85%
Heat recovery unit	Minimum temperature difference: 10°C Pressure drop: 2 - 4% of inlet pressure

Economic Evaluation

The simulation performed in ChemCAD offered the necessary data, (mass and energy balances), to assess the overall techno-economic plant performance indicators. The simulation results were used to assess the key techno-economic and environmental plant. The study included capital cost estimations, specific investment costs per kW generated power, operation and maintenance costs, CO$_2$ capture costs, cumulative cash flow etc.

The cases evaluated in this paper:

Case 1 - Super-critical power plant without carbon capture;

Case 2 - Super-critical power plant with post- combustion CO$_2$ capture based on calcium looping cycle [13].

Table 3 presents the main technical and environmental indicators for Case 1 and 2.

Table 3. Plant technical and environmental performances

Main plant data	Units	Case 1	Case 2
Coal flowrate	t/h	156.74	241.74
Coal LHV	MJ/kg	25.17	
Thermal energy of the feedstock - LHV	MWh	1095.87	1690.16
Steam turbine output	MW_e	502.32	686.14
Gross electric power output	MW_e	502.32	686.14
Coal processing power consumption	MW_e	5.47	8.45
Power island power consumption	MW_e	21.98	24.24
CO_2 compressor power consumption	MW_e	0.00	71.81
Total ancillary power consumption	MW_e	27.55	104.51
Net electric power output	MW_e	474.87	581.62
Gross electriclal efficiency	%	45.83	40.59
Net electrical efficiency	%	43.33	34.41
Carbon capture rate	%	0.00	90.00
Specific CO_2 emissions	kg/MWh	800.58	65.27

As it can be seen from Table 3, the power plant with calcium looping generates a net electric power output of nearly 600 MW_e and a carbon capture rate of 90% in the conditions of a process which requires a significant heat duty. The high running temperature of the whole cycle makes possible heat recovery in form of generated steam.

The next step is to make an estimation of the capital costs. The methods used for estimation of the cost of the equipment are quotations from dealers, (used in the final version of the project) and correlations of cost, (used for the analysis of different technological variants of the process). In this case the equations were obtained using cost relations based on the relationship between cost of equipment and the main geometrical characteristics: volume, area, mass or technological: area, flow, etc. [14].The cost of the equipment was estimated using Equation 3.

$$C_E = C_B * (Q/Q_B)^M \qquad (3)$$

Where:

C_E – equipment cost with capacity Q;

C_B – known base cost for equipment with capacity Q_B;

M – constant depending on equipment type.

Table 4. Capital cost and specific investment cost estimations

Units	Scaling Basis	Case 1	Case 2
Solids handling facilities	tonnes of coal/h	41.47	56.16
PF coal boiler	MW_{th} fuel feed	159.65	175.62
Calcium looping unit	MW_{th} calciner	0.00	104.13
CO_2 conditioning	tonnes of CO_2/h	0.00	31.75
Desulphurisation unit (FGD)	kmole/s feed	69.13	84.65
Air separation unit	tonnes of O_2/h	0	124.26
Steam turbine	MW_e gross	146.66	185.3
Utilities and offsite units	25%	104.23	190.46
Total installed cost	**MM Euro**	**521.14**	**952.32**
Owner's cost and contingency	15%	78.17	142.85
Land purchase, permitting etc.	5%	26.06	47.62
Total investment cost	**MM Euro**	**625.37**	**1142.79**
Gross power production	MW_e	502.32	686.14
Net power production	MW_e	474.87	581.62
Investment cost / kW_e (gross)	Euro / kW_e	1244.96	1665.53
Investment cost / kW_e (net)	Euro / kW_e	1316.92	1960.99

Comparing the two evaluated super-critical power plant cases, it can be seen that CO_2 capture by calcium looping cycle implies a significant increase of investment cost, in the range of about 82% increase. All the units have higher capital costs in the second case compared to the case without carbon capture, (due to larger mass and energy flows), in addition there are some new units, e.g. post-combustion CO_2 capture unit by calcium looping, CO_2 processing and drying – which infuence the total investment cost. In the case of CO_2 capture it can be observed an increased value of gross power production, the increase is about 36% comparing with the case without capture. The specific capital investment is increasing with 48% compared to the case without carbon capture.

The next step is the estimation of operation and maintenance (O&M) costs. O&M costs are generally structured in variable and fixed costs relating to their proportionality to the generated power. Variable operating costs are directly proportional to amount of generated power, (e.g. fuel, chemicals, process and boiler feed water, raw materials, calcium sorbent consumed in the process etc.) [15]. Fixed operating costs are mostly independent of the amount of generated power, (e.g. maintenance, direct labor cost, support and overhead cost etc.). Table 5 presents the distributed O&M costs for Cases 1 and 2.

Table 5. Operating and maintenance cost estimations

Fixed O&M Cost	Case 1	Case 2
Annual maintenance cost	18.05	31.77
Direct labor cost	5.6	5.6
Administrative, support & overhead cost	1.68	1.68
Total (MM Euros / yr)	**25.33**	**39.05**
Variable O&M Cost	**Case 1**	**Case 2**
Fuel	65.11	100.41
Auxilliary feedstock	0.00	0.00
Make-up water	0.04	0.05
Catalysts	0.50	0.50
Solvents	0.38	7.50
Chemicals	1.37	1.48
Total (MM Euros / yr)	**67.40**	**109.94**

Conclusion that can be drawn from Table 5 is that the power plant with CO_2 capture is more expensive in terms of O&M costs. Fixed and variable costs have increased values than in the case of the power plant without CO_2 capture and the major differences come from the fuel and annual maintenance costs. The additional fuel consumption comes from lower energy efficiency and the fuel required for the calciner. Superior annual maintenance cost for the power plant with carbon capture comes from the need to repair a more complex design with additional units, (e.g. calcium looping unit, CO_2 conditioning etc.).

Comparing those two evaluated power plant cases, a significant importance must be given to two parameters that can influence the option of choosing one process over the other, meaning the cost of electricity and the costs of CO_2 capture. The net present value, (NPV), method was used to calculate the levelised cost of electricity, (LCOE) and to compare cash inflows with the cash outflows of the processes with or without CO_2 capture. This net present value determines whether or not the process is an acceptable investment.

The CO_2 capture costs – CO_2 removal and avoidance costs – are important to establish if the carbon capture technology used is more profitable than other. CO_2 capture costs are calculated using the levelised cost of electricity, (LCOE) [16], in the case of the plant with CO_2 capture compared with the cost of electricity without CO_2 capture and the specific CO_2 emissions in both cases. The values were obtained with the Equations (4, 5) and the results are summarized in Table 6.

$$CO_2 \text{ removal cost} = \frac{LCOE_{\text{ with CO2 capture}} - LCOE_{\text{ without CO2 capture}}}{CO_2 \text{ removed}} \qquad (4)$$

$$CO_2 \text{ avoided cost} = \frac{LCOE_{\text{ with CO2 capture}} - LCOE_{\text{ without CO2 capture}}}{CO_2 \text{ emissions}_{\text{without CO2 capture}} - CO_2 \text{ emissions}_{\text{with CO2 capture}}} \qquad (5)$$

Table 6. Cost of electricity and CO_2 capture costs

LCOE with CO_2 capture	LCOE without CO_2 capture
7.02 ¢ /kWh	4.55 ¢/kWh
CO_2 emissions with CO_2 capture	CO_2 emissions without CO_2 capture
65.27 kg/MWh	800.58 kg/MWh
CO_2 removal cost	CO_2 avoided cost
27.81 Euro/t	33.89 Euro/t

It can be observed from the results that the difference between specific CO_2 emissions is very large in advantage being the case with CO_2 capture. The differences between the costs of energy advantages the case without CO_2 capture, the difference being about 35%. This is the economic penalty of the carbon capture design. It must be realized from the above economic evaluations that there are significant capital and operational cost penalties for the carbon capture case, (in addition to the energy penalty as presented in Table 3).

Other important economic aspect of the process is the profitability of the plant and the period of time that will be necessary to payback the made capital investment [17-18]. To evaluate this matter, cumulative cash flow is used. Cumulative cash flow represents a financial statement that reflects the inflow of revenue vs. the outflow of expenses resulting from operating, investing and financing activities during a specific time period [19-21].

In our power plant cases with and without carbon capture, the life time of the power plant was 28 years, (3 years for construction and 25 years for operation). Results of the cumulative cash flow analysis are displayed in Figure 3 and state the fact that the payback period is about 11 years. At the end of the plant life, the power plant with CO_2 capture is more productive in terms of cash flow, knowing a rapid growth and a significant difference towards the case without CO_2 capture [22].
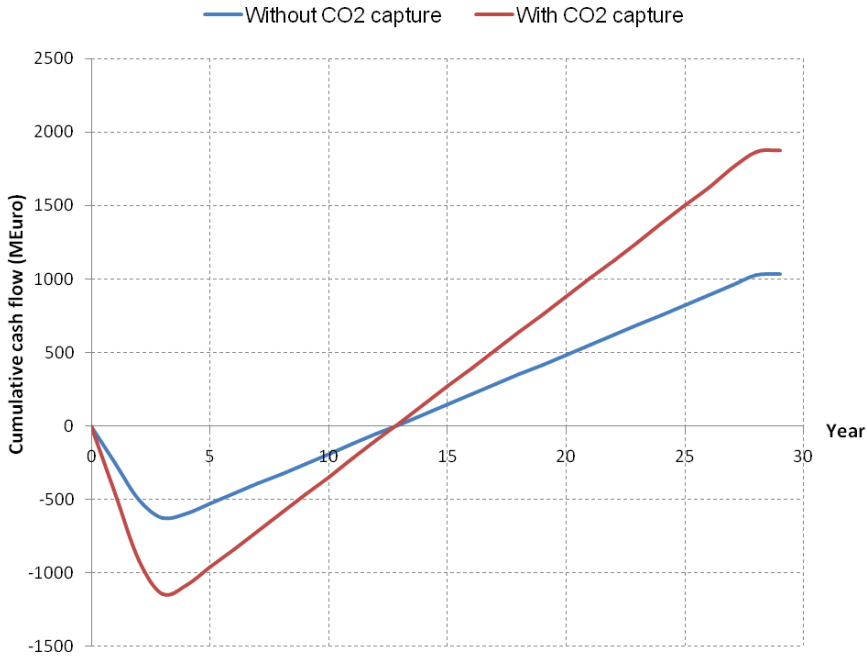
Fig. 3. Cumulative cash flow analysis

CONCLUSIONS

This paper analyzes the techno-economic performances of two power plants in two situations: with and without CO_2 capture. The performance of the CO_2 capture process mainly depends on the flow of CaO coming from the calciner, the make-up flow, and the solid inventory. Carbonate looping process implies an extra capital investment, maintenance costs, and energy penalties comparing with the plant without CO_2 capture. These extra costs mean an increase of 82% of total investment cost, 10% of fixed operating costs (e.g. direct labour), 63% of variable costs (e.g. fuel, chemicals), but bring also a higher profitability after the payback period of the investment and a capture rate of 90%. Those are very promising results which highlights the potential of calcium looping process to significantly reduce CO_2 emissions from atmosphere.

It is certain that carbonate looping process is a new promising carbon capture technology for future power plants over the world, but also, it is certain that are aspects than can be improved and studied.

ACKNOWLEDGEMENTS

REFERENCES

1. A. Woodward, K.R. Smith, D. Campbell-Lendrum, D. Chadee, Y. Honda, Q. Liu, J. Olwoch, B. Revich, R. Sauerborn, Z. Chafe, U. Confalonieri, A. Haines, *The Lancet,* **2014**, *383*, 1185.
2. H. Lindstad, B.E. Asbjornslett, A. H. Stromman, *Energy Policy,* **2012**, *46*, 386.
3. D.C Ozcan, H. Ahn, S. Brandani, *International Journal of Greenhouse Gas Control*, **2013**, *19*, 530.
4. M. Gulbe, *Procedia – Social and Behavioral Sciences*, **2014**, *109*, 935.
5. T. Ming, R. De Richter, W. Liu, S. Caillol, *Renewable and Sustinable Energy Reviews*, **2014**, *31*, 792.
6. T. Gibon, E. Hertwich, *Procedia CIRP*, **2014**, *15*, 3.
7. F. Aldawi, F. Alam, I. Khan, M. Alghamdi, *Procedia Engineering,* **2013**, *56*, 661.
8. A.J. Ma, H.Z. Zhao, *Procedia Environmental Sciences*, **2012**, *13,* 2310.
9. L.M. Romeo, Y. Lara, P. Lisbona, J.M. Escosa, *Chemical Engineering Journal*, **2009**, *147*, 252.
10. G.S. Grasa, J. C. Abanades, M. Alonso, B. Gonzalez, *Chemical Engineering Journal*, **2008**, *137*, 561.
11. S.K. Bhatia, D.D. Perlmutter, *AIChE*, **1983**, *29*, 79.
12. C. Hawthorne, M. Trossmann, P. Galindo Cifre, A. Schuster, G. Scheffknecht, *Energy Procedia*, **2009**, *1*, 1387.
13. J. Strohle, A. Galloy, B. Epple, *Energy Procedia,* **2009**, *1*, 1313.
14. C.C. Cormos, A.M. Cormos, P.S. Agachi, *Chemical Engineering Transactions*, **2013**, *35*, 369.
15. J.M Valverde,P.E Sanchez- Jimenez, L.A . Perez- Maqueda, *Applied Energy,* **2014**, *127*, 161.
16. G. Duelli-Varela, L. Bernard, A.R. Bidwe, V. Stack-Lara, C. Hawthorne, M. Zieba, G. Scheffknecht, *Energy Procedia*, **2013**, *37*, 190.
17. M.E. Diego, B. Arias, M. Alonso, J.C. Abanades, *Fuel,* **2013**, *109*, 184.
18. C.C. Cormos, *Energy*, **2014**, *78*, 665.
19. I. Vorrias, K. Atsonios, A. Nikolopoulos, N. Nikolopoulos, P. Grammelis, E. Kakaras, Fuel, **2013**, *113*, 826.
20. C.C. Dean, J. Blamey, N.H Florin, M.J. Al-Jeboori, P.S. Fennell, *Chemical Engineering Research and Design*, **2011**, *89*, 836.
21. I. Martinez, R. Murillo, G. Grasa, J.C. Abanades, *Energy Procedia*, **2011**, *4*, 1699.
22. C.C. Cormos, A.M. Cormos, *International Journal of Hydrogen Energy*, **2013**, *38,* 2306.